EUSKAL HERRIKO UNIBERTSITATEA
THE UNIVERSITY OF THE BASQUE COUNTRY

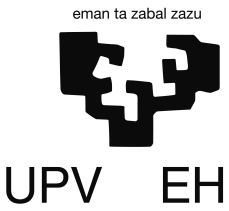


# Atomic and molecular structures on a superconducting surface

Thesis by

**Cristina Mier González**

Supervised by

**Dr. Nicolás Lorente Palacios**

and

**Dr. Deung-Jang Choi**

Donostia-San Sebastián, January 2023

# ACTA DE GRADO DE DOCTOR O DOCTORA
# ACTA DE DEFENSA DE TESIS DOCTORAL

DOCTORANDO/A DON/DÑA. Cristina Mier González

TITULO DE LA TESIS: Estructuras atómicas y moleculares en una superficie superconductora

El Tribunal designado por la Comisión de Postgrado de la UPV/EHU para calificar la Tesis Doctoral arriba indicada y reunido en el día de la fecha, una vez efectuada la defensa por el/la doctorando/a y contestadas las objeciones y/o sugerencias que se le han formulado, ha otorgado por_____la calificación de:

*unanimidad ó mayoría*

| |
|---|
| |

*SOBRESALIENTE / NOTABLE / APROBADO / NO APTO*

Idioma/s de defensa (en caso de más de un idioma, especificar porcentaje defendido en cada idioma):

Castellano _____

Euskera _____

Otros Idiomas (especificar cuál/cuales y porcentaje) _____

En _____a _____de _____de _____

EL/LA PRESIDENTE/A, EL/LA SECRETARIO/A,

Fdo.: Fdo.:

Dr/a: _____ Dr/a: _____

VOCAL 1º, VOCAL 2º, VOCAL 3º,

Fdo.: Fdo.: Fdo.:

Dr/a: _____Dr/a:_____Dr/a:_____

EL/LA DOCTORANDO/A,

Fdo.: _____

Universidad del País Vasco Euskal Herriko Unibertsitatea

NAZIOARTEKO EBAKINTASUN CAMPUSA
CAMPUS DE EXCELENCIA INTERNACIONAL

| TESI ZUZENDARIAREN BAIMENA TESIA AURKEZTEKO | AUTORIZACIÓN DEL/LA DIRECTORA/A DE TESIS PARA SU PRESENTACIÓN |
|---|---|

Zuzendariaren izen-abizenak /Nombre y apellidos del/la director/a:
Nicolas Lorente Palacios
IFZ /NIF: 50712479D

Zuzendariaren izen-abizenak /Nombre y apellidos del/la director/a:
Deung-Jang, Choi
IFZ /NIF: Y3906688Z

Tesiaren izenburua / Título de la tesis:
Atomic and molecular structures on a superconducting surface

Doktorego programa / Programa de doctorado:
Física de Nanoestructuras y Materiales Avanzados

Doktoregaiaren izen-abizenak / Nombre y apellidos del/la doctorando/a:
Cristina Mier González

| | |
|---|---|
| Unibertsitateak horretarako jartzen duen tresnak emandako ANTZEKOTASUN TXOSTENA ikusita, baimena ematen dut goian aipatzen den tesia aurkez dadin, horretarako baldintza guztiak betetzen baititu. | Visto el INFORME DE SIMILITUD obtenido de la herramienta que a tal efecto pone a disposición la universidad, autorizo la presentación de la tesis doctoral arriba indicada, dado que reúne las condiciones necesarias para su defensa. |

Tokia eta data / Lugar y fecha: SAN SEBASTIAN, 4 ENERO 2023

Sin. / Fdo.: Tesiaren zuzendaria / El/La director/a de la tesis

Universidad del País Vasco | Euskal Herriko Unibertsitatea

NAZIOARTEKO BIKAINTASUN CAMPUSA
CAMPUS DE EXCELENCIA INTERNACIONAL

**AUTORIZACION DEL TUTOR/A DE TESIS**

**PARA SU PRESENTACION**

Dr/a. Andrés Arnau Pino como Tutor/a de la Tesis Doctoral: "Estructuras atómicas y moleculares en una superficie superconductora" realizada en el Programa de Doctorado Física de Nanoestructuras y Materiales Avanzados, por el Doctorando Don/ña. Cristina Mier González, y dirigida por el Dr./a Nicolás Lorente Palacios y Dr./a Deung-Jang Choi autorizo la presentación de la citada Tesis Doctoral, dado que reúne las condiciones necesarias para su defensa.

En Donostia- San Sebastián a 9 de enero de 2023

EL/LA TUTOR/A DE LA TESIS

ANDRES ARNAU PINO - 00692057X

Digitally signed by ANDRES ARNAU PINO - 00692057X
DN: c=ES, o=UPV - EHU, ou=Ziurtagiri Profesionala - Certificado Profesional, 2.5.4.97=VATES-Q4818001B, cn=ANDRES ARNAU PINO - 00692057X, givenName=ANDRES, sn=ARNAU PINO, serialNumber=00692057X
Date: 2023.01.09 10:21:55 +01'00'

Fdo.: Andres Arnau Pino_____

Universidad del País Vasco | Euskal Herriko Unibertsitatea

NAZIOARTEKO BIKAINTASUN CAMPUSA
CAMPUS DE EXCELENCIA INTERNACIONAL

## AUTORIZACIÓN DE LA COMISIÓN ACADÉMICA DEL PROGRAMA DE DOCTORADO

La Comisión Académica del Programa de Doctorado en Física de Nanoestructuras y Materiales Avanzados, en reunión celebrada el día _9__ de enero de 2023, ha acordado dar la conformidad a la presentación de la Tesis Doctoral titulada: "Estructuras atómicas y moleculares en una superficie superconductora" dirigida por el/la Dr/a. Nicolás Lorente Palacios y Dr/a. Deung-Jang Choi y presentada por Don/Dña. Cristina Mier González adscrito o adscrita al Departamento Polímeros y materiales avanzados: Física, química y tecnología.

En Donostia- San Sebastián a 9 de enero de 2023

EL/LA RESPONSABLE DEL PROGRAMA DE DOCTORADO

Fdo.: ALEGRIA LOINAZ ANGEL MARIA - 15918091K

Digitally signed by ALEGRIA LOINAZ ANGEL MARIA - 15918091K
Date: 2023.01.09 14:12:43 +01'00'

Universidad del País Vasco | Euskal Herriko Unibertsitatea

NAZIOARTEKO BIKAINTASUN CAMPUSA
CAMPUS DE EXCELENCIA INTERNACIONAL

## AUTORIZACIÓN DEL DEPARTAMENTO

El Consejo del Departamento de Polímeros y materiales avanzados: Física, química y tecnología en reunión celebrada el día _16__ de enero de 2023 ha acordado dar la conformidad a la admisión a trámite de presentación de la Tesis Doctoral titulada: "Estructuras atómicas y moleculares en una superficie superconductora" dirigida por el/la Dr/a. Nicolás Lorente Palacios y Dr/a. Deung-Jang Choi y presentada por Don/ña. Cristina Mier González ante este Departamento.

En Donostia_San Sebastián a __16___ de enero de 2023

VºBº DIRECTOR/A DEL DEPARTAMENTO

AGUSTIN ETXEBERRIA LIZARRAGA - 72434443Z

Firmado digitalmente por AGUSTIN ETXEBERRIA LIZARRAGA - 72434443Z
Fecha: 2023.01.17 10:11:25 +01'00'

Fdo.: _____Agustin Etxeberria Lizarraga__

SECRETARIO/A DEL DEPARTAMENTO

JOSEBA IÑAKI JUARISTI OLIDEN - 34089368X

Firmado digitalmente por JOSEBA IÑAKI JUARISTI OLIDEN - 34089368X
Nombre de reconocimiento (DN): c=ES, o=UPV - EHU, ou=Ziurtagiri Profesionala - Certificado Profesional, 2.5.4.97=VATES-Q4818001B, cn=JOSEBA IÑAKI JUARISTI OLIDEN - 34089368X, givenName=JOSEBA IÑAKI, sn=JUARISTI OLIDEN, serialNumber=34089368X
Fecha: 2023.01.17 10:03:35 +01'00'

Fdo.: Joseba Iñaki Juaristi Oliden

# Contents

# Summary

This Ph.D. thesis studies the physical properties of magnetic impurities and spin chains on $s-$wave superconductors. This is an important field of research that has acquired particular importance in recent years thanks to technological advances in the study of superconducting surfaces at the atomic level. Within the last decade, an important effort in creating and measuring the properties of spin chains on superconductors has been led by the search of Majorana bound states. In particular, this thesis studies two superconductors (Pb and $\beta$-$Bi_2Pd$) and atomic and molecular magnetic impurities that are controllably manipulated on their surface. In addition to experiments, the thesis also deals with theoretical studies of topological phases and under what conditions Majorana bound states can be found.

In 1957, Bardeen, Cooper, and Schrieffer proposed the first microscopic theory able to describe the phenomena of superconductivity, the BCS theory [1]. This theory is based on the idea that below a critical temperature, electrons near the Fermi surface couple, creating the so-called Cooper pairs [2]. In conventional superconductors, electrons form pairs with opposite spin, this type of coupling is known as $s-$wave superconductivity. Consequently, when an external magnetic field is applied, it will favor the alignment of the two spins; when the strength of the magnetic field is larger than the coupling interaction between the electrons, the Cooper pairs break, and superconductivity is suppressed.

However, at microscopic scales, the interplay between superconductivity and magnetic interactions gives rise to interesting phenomena. In particular, as independently described by Yu [3], Shiba [4], and Rusinov [5] in the 1960s, the presence of a single magnetic impurity on a superconductor results in states inside the superconducting gap, known as Yu-Shiba-Rusinov (YSR) states. These in-gap quasi-particle states show electron and hole components. Phenomenologically, YSR states can be understood as a local weakening of the coupling between the electrons in Cooper pairs.

Technical advances in recent decades have enabled the study of systems at the atomic level. In particular, scanning tunneling microscopy (STM) [6] has become a vital tool for studying YSR states. The sub-atomic spatial resolution achieved by STM allows to prove the local density of states of single magnetic atoms and molecules. Using this technique, YSR could be first experimentally observed on Mn and Gd atoms deposited on Nb(100) in 1997 [7].

This thesis is devoted to the study of magnetic impurities on superconducting surfaces using theoretical and experimental tools. In recent years, the study of such systems has been motivated by the search for non-trivial topological states of matter. Indeed, magnetic chains on superconductors have been proposed as potential platforms for the emergence of topological states at the edges of finite systems, known as Majorana fermions [8], [9].

In 1937, Ettore Majorana theoretically discovered Majorana fermions (or Majoranas for short) [10]. These particles are their own antiparticle. This unique feature results in Majoranas having non-Abelian exchange statistics, *i.e.*, upon their exchange, the total wave function is subject to a unitary operation, meaning that, in general, exchange operations of Majorana fermions do not commute. Consequently, their primary interest comes from their potential application in quantum computation. Theoretically proposed protocols that utilize Majorana fermions as building blocks receive the name of topological quantum computers [11], [12]. One of the main drawbacks of current quantum computers is the loss of coherence due to interactions with the environment and local perturbations. However, thanks to the unique properties of Majoranas, topological quantum computers encode information in a non-local way, making these states immune to local disorder and decoherence.

In 2001, Alexei Kitaev developed a simple model where Majorana fermions can emerge [13]. The author proposed a finite 1-D chain of spin-less fermions (or sites). Each site can be expressed as a pair of Majoranas. This pairing can involve Majoranas within the same site (trivial state of the chain), or it may couple Majoranas from neighboring sites (topological state of the chain). In the latter case, two Majoranas are left unpaired at the edges of the chain. The two unpaired Majoranas form one fermionic state, even if they are spatially delocalized. Because of its localization to the edges, this pair gets the name of Majorana bound states (MBS).

The pairing interaction responsible for Cooper pairs makes superconductors natural candidates for experimental realizations of the Kitaev model. However, as mentioned above, the model requires the fermionic quasiparticles to be spinless, and superconductors with such characteristics have never been observed in nature. Within the last decade, several approaches have been proposed to effectively create spinless superconductors that can host MBS [14]–[18]. These models include three main ingredients: $s-$wave superconductivity, magnetic Zeeman interactions, and spin-orbit coupling (SOC).

Spin chains on superconducting surfaces with high SOC are a promising platform. This approach has been developed in the context of STM and the study of YSR states. The atomic manipulation techniques developed with this tool allow crafting default-free atomic chains of several tens of atoms [19]. Attempts to create MBS with this approach have been reported in recent years [20]–[25]. However,

the unambiguous detection of MBS in the lab still remains a challenge.

In this thesis, we aim to develop a theoretical model using realistic parameters able to reproduce real experimental results and simulate the emergence of MBS. Additionally, we experimentally study, with the aid of STM, magnetic molecules on a superconducting surface. As such, the thesis is organized into two main parts: the first part (chapters 1, 2, and 3) focuses on theoretical and numerical results. The second part (chapters 4 and 5) is devoted to the experimental results obtained with STM.

In the first part of the thesis, we develop a theoretical model in the free-electron approximation using Green's functions [26], [27] to simulate magnetic impurities on a bulk superconductor. We model a 2-D superconducting array, the impurities (assuming classical spins) are then located in selected sites of the discrete array and added as a perturbation to the system using Dyson's equation. In this framework, we can easily compute the local density of states. The resulting calculation, using realistic parameters, shows YSR states. We analyze the results for single and two impurities (dimers) in a finite 2-D superconductor. The relative spin orientation in dimers results in drastically different spectra, as ferromagnetic (FM) dimers show hybridization between the YSR states, whereas anti-ferromagnetic (AFM) dimers have a single-atom behavior [28]. This situation is affected when SOC is added to the calculation [29]. Using the same approach, we study spin chains of several tens of atoms. The calculation shows edge states at zero energy in good agreement with the presence of MBS. We further support this possibility by analyzing the spin polarization of the in-gap states [30].

Next, we use the same model to analyze experimental data of Cr atomic chains deposited on the superconductor $\beta$-$Bi_2Pd$ [31]. Two different chain geometries are considered, the results of our calculations agree with the overall measured spectra. We find a drastically different spin arrangements between the two chains. Furthermore, according to our calculations, one configuration presents promising results for the emergence of MBS in longer chains (only 4-atom chains could be crafted in the experiment). However, the unambiguous determination of the topological origin of these edge states requires the computation of the topological invariant. To that end, we develop a procedure to evaluate the winding number of the system Hamiltonian starting from the real-space Green's function used to model the spin chains [32]. Moreover, we show that it is possible to compute the winding number starting from a finite system and using solely numerical calculations. Finally, we study the effect of the finite size of the chains. We find an oscillatory behavior in the energy of the edge states, the obtained period can be rationalized as a moiré pattern emerging from the electronic interactions in the superconductor and the discreteness of the model lattice [33].

In the second part of this work, we conduct an experimental study of a system candidate to show YSR states using low-temperature STM with superconducting tips. We study molecular arrays of nickelocene (Nc), a magnetic molecule with spin $S = 1$, deposited on a Pb (111) single crystal. Nickelocene, previously studied on metallic surfaces [34], [35], shows a significant inelastic signal product of a molecular spin-flip process. We could not find evidence of in-gap states in this system in the tunneling regime. Nevertheless, the use of superconducting tips allows us to measure slight differences in the magnetic anisotropy energy of individual molecules. With this information, we could unravel the absorption of the molecules with respect to the Pb (111) surface [36]. We further studied individual molecules attached at the apex of the tip by bringing the tip close to the superconducting sample. In this regime, we could measure low-resistance tunneling processes in the superconductor-insulating-superconductor junction. Finally, we deposit Fe atoms in this system, single Fe atoms on Pb surfaces show YSR states [37]. When deposited on Nc layers, some Fe atoms seem to migrate below the molecules creating Nc+Fe complexes, this new structure shows YSR states in the tunneling regime.

In summary, this Ph.D. thesis aims to improve our understanding of the physical properties of magnetic impurities in superconducting surfaces. In particular, the emergence of MBS and their behavior in spin chains. To this end, we use theoretical and experimental techniques to study Cr atomic chains on the superconductor $\beta$-$Bi_2Pd$, and nickelocene molecules deposited on a Pb(111) crystal.

# Resumen

Esta tesis doctoral estudia las propiedades físicas de impurezas magnéticas y cadenas de espines en superconductores de onda $s$. Éste se trata de un importante campo de investigación que ha adquirido especial relevancia en los últimos años gracias a los avances tecnológicos en el estudio de superficies superconductoras a nivel atómico. En la última década, un importante esfuerzo en la fabricación y medida de las propiedades de las cadenas de espines en superconductores ha estado motivado por la búsqueda de estados ligados de Majorana. En particular, esta tesis estudia dos superconductores (Pb y $\beta$-$Bi_2Pd$) e impurezas magnéticas atómicas y moleculares que se manipulan de forma controlada en su superficie. Además de los experimentos, la tesis también aborda estudios teóricos de las fases topológicas y en qué condiciones se pueden encontrar estados ligados de Majorana.

En 1957, Bardeen, Cooper y Schrieffer propusieron la primera teoría microscópica capaz de describir los fenómenos de la superconductividad, la teoría BCS [1]. Esta teoría se basa en la idea de que por debajo de una temperatura crítica, los electrones cercanos a la superficie de Fermi se acoplan, creando los llamados pares de Cooper [2]. En superconductores convencionales, los pares de Cooper están comprendidos por electrones con espín opuesto, este tipo de acoplamiento se conoce como superconductividad de onda $s$. En consecuencia, cuando un campo magnético externo es aplicado, éste favorecerá la alineación de los dos espines; cuando la intensidad del campo magnético es mayor que la interacción de acoplamiento, los pares de Cooper se rompen y la superconductividad desaparece.

Sin embargo, a escalas microscópicas, la interacción entre superconductividad e interacciones magnéticas da lugar a fenómenos interesantes. En particular, como describieron de manera independiente Yu [3], Shiba [4] y Rusinov [5] en la década de 1960, la presencia de una impureza magnética en un superconductor da lugar a estados dentro de la banda prohibida superconductora (o *gap* superconductor), conocidos como estados Yu-Shiba-Rusinov (YSR). Estos estados de cuasipartículas muestran componentes de electrón y hueco. Fenomenológicamente, los estados YSR pueden ser interpretados como un debilitamiento local del acoplamiento entre los electrones que forman los pares de Cooper.

Los avances técnicos de las últimas décadas han permitido el estudio de sistemas a nivel atómico. En particular, el microscopio de efecto túnel (STM, por sus siglas en inglés) [6] se ha convertido en una herramienta vital en el estudio de los

estados YSR. La resolución espacial subatómica alcanzada por el STM permite medir la densidad local de estados en átomos y moléculas magnéticas individuales. Utilizando esta técnica, fue posible observar estados YSR experimentalmente por primera vez en átomos de Mn y Gd depositados sobre Nb(100) en 1997 [7].

Esta tesis está dedicada al estudio de impurezas magnéticas en superficies superconductoras utilizando herramientas teóricas y experimentales. En los últimos años, el estudio de estos sistemas ha estado motivado por la búsqueda de estados topológicos no triviales de la materia. En particular, cadenas de impurezas magnéticas en superconductores se han propuesto como plataformas potenciales para la creación de estados topológicos en los bordes de sistemas finitos, conocidos como fermiones de Majorana [8], [9].

En 1937, Ettore Majorana descubrió teóricamente los fermiones de Majorana (o Majoranas para abreviar) [10]. Estas partículas son su propia antipartícula. Esta particular característica hace que los Majoranas tengan estadísticas de intercambio no abelianas, es decir, al intercambiarlas, la función de onda total es sujeta a una operación unitaria, lo que significa que, en general, las operaciones de intercambio de Majoranas no conmutan. En consecuencia, su principal interés proviene de su potencial aplicación en computación cuántica. Los protocolos propuestos que utilizan fermiones de Majorana como componentes básicos reciben el nombre de ordenadores cuánticos topológicos [11], [12]. Una de las principales limitaciones de los ordenadores cuánticos actuales es la pérdida de coherencia debido a las interacciones con el entorno y las perturbaciones locales. Sin embargo, gracias a las propiedades únicas de los Majoranas, los ordenadores cuánticos topológicos codifican la información de forma no local, lo que hace que estos estados sean inmunes al desorden local y a la decoherencia.

En 2001, Alexei Kitaev desarrolló un modelo sencillo en el que pueden emerger fermiones de Majorana [13]. El autor propuso una cadena 1-D finita de fermiones (o sitios) sin espín. Cada sitio se puede expresar como un par de Majoranas. Este emparejamiento puede involucrar Majoranas dentro del mismo sitio (estado trivial de la cadena), o puede acoplar Majoranas de sitios vecinos (estado topológico de la cadena). En este último caso, dos Majoranas quedan no apareados en los bordes de la cadena, éstos forman un estado fermiónico aunque estén espacialmente deslocalizados. Debida a esta localización en los bordes, este par recibe el nombre de estados ligados de Majorana (MBS, en inglés).

La interacción de emparejamiento responsable de los pares de Cooper convierte a los superconductores en candidatos naturales para realizaciones experimentales del modelo de Kitaev. Sin embargo, como ya se ha mencionado, el modelo requiere que las cuasipartículas fermiónicas carezcan de espín. Superconductores con tales características nunca se han observado en la naturaleza. En la última década, se han propuesto varios modelos para crear eficazmente superconductores sin espín que puedan albergar MBS [14]–[18]. Estos modelos incluyen tres ingredientes

principales: superconductividad de onda $s$, interacciones magnéticas de Zeeman y acoplamiento espín-órbita (SOC, en inglés).

Las cadenas de espines en superficies superconductoras con SOC constituyen una plataforma prometedora. Este enfoque se ha desarrollado en el contexto del STM y el estudio de los estados YSR. Las técnicas de manipulación atómica desarrolladas con esta herramienta han permitido la elaboración de cadenas atómicas sin defectos y longitudes de varias decenas de átomos [19]. En los últimos años se han reportado tentativas de crear MBS con este enfoque [20]–[25]. Sin embargo, la detección inequívoca de MBS en el laboratorio sigue siendo un reto.

En esta tesis pretendemos desarrollar un modelo teórico con parámetros realistas capaz de reproducir resultados experimentales y simular MBS. Además, estudiamos experimentalmente, con ayuda del STM, moléculas magnéticas sobre una superficie superconductora. De esta manera, la tesis está organizada en dos partes principales: la primera parte (capítulos 1, 2, y 3) se centra en los resultados teóricos y numéricos. La segunda parte (capítulos 4 y 5) está dedicada a los resultados experimentales obtenidos con STM.

En la primera parte de la tesis, desarrollamos un modelo teórico en la aproximación de electrones libres utilizando funciones de Green [26], [27] para simular impurezas magnéticas en un superconductor. Modelizamos una matriz discreta superconductora bidimensional, y situamos impurezas magnéticas (asumiendo espines clásicos) en sitios seleccionados de la matriz. Su efecto es incluido como una perturbación al sistema utilizando la ecuación de Dyson. En este marco, podemos calcular fácilmente la densidad local de estados. El cálculo resultante, utilizando parámetros realistas, muestra estados YSR. Analizamos los resultados para una y dos impurezas (dímeros) en un superconductor bidimensional finito. La orientación relativa de los espines en los dímeros da lugar a espectros drásticamente diferentes: los dímeros ferromagnéticos (FM) muestran hibridación entre los estados YSR, mientras que los dímeros antiferromagnéticos (AFM) muestran un comportamiento similar al de átomos aislados [28]. Esta situación se ve afectada cuando se añade SOC al cálculo [29]. Utilizando este mismo enfoque, estudiamos cadenas de espín de varias decenas de átomos. El cálculo muestra estados de borde a energía cero, en buen acuerdo con la presencia de MBS. Apoyamos aún más esta posibilidad mediante el análisis de la polarización de espín de los estados dentro del *gap* [30].

A continuación, utilizamos el mismo modelo para analizar datos experimentales de cadenas atómicas de Cr depositadas en el superconductor $\beta$-$Bi_2Pd$ [31]. Se consideran dos cadenas con geometrías diferentes, los resultados de nuestros cálculos concuerdan con los espectros medidos. Los cálculos indican una textura de espín drásticamente diferente entre las dos cadenas. Además, según nuestros cálculos, una de las configuraciones presenta resultados prometedores para la aparición de MBS en cadenas más largas (en el experimento sólo se pudieron elaborar cade-

nas de hasta 4 átomos). Sin embargo, la determinación inequívoca del origen topológico de estos estados de borde requiere el cálculo del invariante topológico. Para ello, desarrollamos un procedimiento para evaluar el índice (*winding number*) del sistema a partir de la función de Green en el espacio real utilizada para modelizar las cadenas de espín [32]. Además, demostramos que es posible calcular el índice a partir de un sistema finito y utilizando únicamente cálculos numéricos. Finalmente, estudiamos el efecto del tamaño finito de las cadenas. Encontramos un comportamiento oscilatorio en la energía de los estados de borde. El período obtenido puede ser racionalizado como un patrón de moiré producto de las interacciones electrónicas en el superconductor y de la red discreta del modelo [33].

En la segunda parte de este trabajo, realizamos un estudio experimental de un sistema candidato a mostrar estados YSR utilizando STM de baja temperatura con puntas superconductoras. Estudiamos islas moleculares de niqueloceno (Nc), una molécula magnética con espín $S = 1$, depositada sobre un monocristal de Pb. El niqueloceno, previamente estudiado en superficies metálicas [34], [35], muestra una gran señal inelástica producto de un proceso de *spin-flip* molecular. No pudimos encontrar evidencias de estados dentro del *gap* superconductor en este sistema en el régimen de túnel. No obstante, el uso de puntas superconductoras nos permite medir ligeras diferencias en la energía de anisotropía magnética de moléculas individuales. Con esta información, pudimos descifrar la absorción de las moléculas con respecto a la superficie de Pb (111) [36]. También estudiamos moléculas individuales absorbidas en el vértice de la punta, acercando la punta a la muestra superconductora. En este régimen, pudimos observar procesos de túnel a baja resistencia en la unión superconductor-aislante-superconductor. Finalmente, depositamos átomos de Fe en este sistema, los átomos de Fe individuales sobre superficies de Pb muestran estados YSR [37]. Cuando se depositan sobre islas de Nc, algunos átomos de Fe parecen migrar bajo las moléculas creando complejos Nc+Fe, esta nueva estructura muestra estados YSR en el régimen de túnel.

En resumen, esta tesis doctoral pretende mejorar nuestra comprensión de las propiedades físicas de las impurezas magnéticas en superficies superconductoras. En particular, la formación de MBS y su comportamiento en cadenas de espín. Para ello, utilizamos técnicas teóricas y experimentales para estudiar cadenas atómicas de Cr sobre el superconductor $\beta$-$Bi_2Pd$, y moléculas de niqueloceno depositadas sobre un cristal de Pb(111).

# Outline

The contents of this thesis are organized as follows:

- Chapter 1 gives an introduction to the topic of MBS in consed matter systems, in particular, spin chains on superconductors.
- In chapter 2 we present the mean-field model using Green's function formalism utilized to model magnetic impurities on superconductors.
- Chapter 3 compiles the main results obtained with the model presented in the previous chapter.
- Chapter 4 reviews the working principle of STM. In particular, the use of superconducting tips.
- In chapter 5, we examine the STM measurements obtained on Nc deposited on Pb (111).

Finally, this thesis contains conclusions and outlook for the presented work as well as an appendix sections where details are given for concrete aspects of our work.

# List of publications

The thesis is supported by the following publications:

Chapter 3: Calculations of spin chains on superconductors.

1. **Cristina Mier**, Jiyoon Hwang, Jinkyung Kim, Yujeong Bae, Fuyuki Nabeshima, Yoshinori Imai, Atsutaka Maeda, Nicolás Lorente, Andreas Heinrich, Deung-Jang Choi. *Atomic manipulation of in-gap states in the $\beta-Bi_2Pd$ superconductor.*
   Physical Review B 104 (4), 045406 (2021)

2. **Cristina Mier**, Deung-Jang Choi, Nicolás Lorente. *Calculations of in-gap states of ferromagnetic spin chains on s-wave wide-band superconductors.*
   Physical Review B 104 (24), 245415 (2021)

3. **Cristina Mier**, Deung-Jang Choi, Nicolás Lorente. *Moiré dispersion of edge states in spin chains on superconductors.*
   Phys. Rev. Research 4, L032010 (2022)

Chapter 5: Nickelocene on Pb(111): STM study with superconducting tips.

4. **Cristina Mier**, Benjamin Verlhac, Léo Garnier, Roberto Robles, Laurent Limot, Nicolás Lorente, Deung-Jang Choi. *Superconducting scanning tunneling microscope tip to reveal sub-millielectronvolt magnetic energy variations on surfaces.*
   The Journal of Physical Chemistry Letters 12 (11), 2983-2989 (2021)

# 1 Majorana fermions in spin chains.

## 1.1 Topology in condensed matter systems

Topology in condensed matter physics has gained increasing attention in recent decades. In mathematics, topology is the branch that studies the geometrical properties that remain invariant under continuous, smooth deformations. The recent connection between topology and physics comes from the topological properties that can be found in the band structure of periodic quantum systems. Since the 1970's topology has been used to theorize and describe new and exotic physical phenomena [38], [39].

A major breakthrough came in 1982 with the discovery of the quantum Hall effect (QHE) [40]. Just like in the classical Hall effect, a transverse current is measured in a metallic system subject to an applied voltage and external magnetic field. However, in the QHE, researchers found that, as the magnetic field increased, the conductance of the transverse current increased in discrete jumps. They were able to relate the different conductance steps with an integer number called a *topological invariant* [38], [41].

Since then, topology and topological invariants were used to characterize other exotic phases of matter, most prominently topological insulators [42]. In 2016, the Nobel Prize in Physics was awarded to physicists who contributed to the development and description of topological phases of matter [38].

The notion of topological phases has been extended to other systems, such as topological superconductors. In this state of matter, one of the most important consequences is the emergence of Majorana fermions. These are zero-energy quasiparticles with equal electron and hole components, implying that it is a particle identical to its own anti-particle [11], [41], [43], [44]. Using common terminology, we call these zero-energy excitations, Majorana fermions despite the fact that they present non-Abelian statistics. Majorana fermions are of special interest in the development of topological quantum computing, as their non-Abelian statistics lay in the core of fault-tolerant quantum computation [11], [12], [44].

In the present chapter, we will review some basics of topological states of matter and topological invariants, with special interest in the emergence of Majorana fermions as described in the Kitaev model [13]. We will see how this toy model can be realized in superconducting systems under the right conditions.

### 1.1.1 Majorana fermions

In 1937 Ettore Majorana proposed an alternative form for the Dirac equation [10]. This representation, using real wave functions, implies that the described particle, unlike electrons and positrons, it is its own anti-particle. Today, these are known as *Majorana fermions*. Neutrinos were proposed as candidates for Majorana fermions. In high energy and particle physics, their detection still remains a challenge [45], [46].

The search for Majorana fermions has, in recent years, expanded to the field of condensed matter physics. In this context, Majorana fermions are not expected to arise as fundamental particles, but rather as emergent excitations [11]. These excitations are usually denoted with the $\gamma$ operator, fulfilling the conditions $\gamma^\dagger = \gamma$ (particle equal to anti-particle) and $\gamma^2 = 1$. As such, it is inaccurate to call a Majorana fermion a particle, since there is no meaning in $\gamma$ being occupied or unoccupied [11], [44]. It is more precise to refer to these modes as "fractionalized", comprising half of a regular fermion. In this way, a pair of Majorana modes, $\gamma_1$ and $\gamma_2$, form a fermionic state, $c = (\gamma_1 + i\gamma_2)/2$, where $c$ has a well-defined occupation number.

The most interesting property of Majorana fermions are their non-Abelian statistics. In some systems, particles whose statistics are not fermionic nor bosonic can arise, these are called anyons. They come in two kinds: Abelian and non-Abelian. Between the two, non-Abelian anyons are the most interesting: Upon their spatial exchange, the final state of non-Abelian anyons is subject to a unitary operation [12], [47], unlike fermions and bosons, for which particle exchange simply results in a multiplication by $-1$ or $+1$, respectively. Consequently, exchange operations of non-Abelian anyons do not commute. Using this property, topological quantum computing algorithms are based on "braiding" operations using non-Abelian anyons [12], [44]. The statistics of Majorana fermions are described by the so-called Ising anyons [47]. Unfortunately, the set of unitary operations of Ising anyons does not constitute a "universal" set of quantum gates [12], [48], as such they need to be supported by additional non-topological operations.

The search for Majorana fermions has focused on superconducting systems. The particle-hole symmetry existing in superconductors makes them natural candidates for experimental realizations. In the Bogoliubov-de Gennes representation [49], the excitations in superconducting systems are described by a quasi-particle operator with electron and hole part. In this representation, the parallel between Majorana fermions and superconducting systems becomes apparent [43], [50]. A system host-

ing Majorana Fermions is referred to as a topological superconductor. One of the simplest models exhibiting topological superconductivity is the Kitaev model [13], it describes a 1-D chain of spinless fermions in one dimension. In the following, we will review the Su-Schrieffer-Heeger model, one of the simplest model exhibiting a non-trivial topological phase. And, in more detail, the Kitaev model.

### 1.1.2 The Su-Schrieffer-Heeger model

One of the most basic models to support topological excitations is the Su-Schrieffer-Heeger (SSH) model [51], on Fig.1.1 (a) we show a sketch of the system. It describes a one dimensional chain with alternating hopping parameters between sites, $v$ and $w$, (orange and blue lines respectively). In this way, the unit cell of the system is composed by two sites, A and B, each can host one state (black and gray balls). A real system described by this structure is, for example, the organic polymer polyacetylene [52].

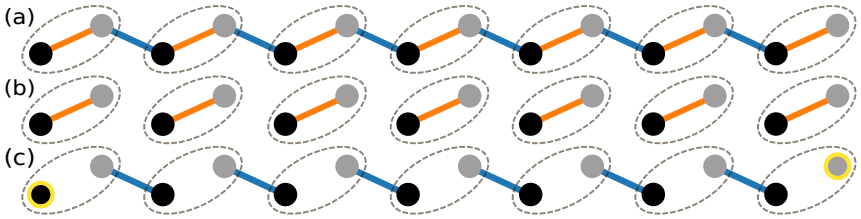


Figure 1.1: SSH chain diagram. (a) The two sites (A and B) are represented by black and gray balls, connected by alternating hopping parameters ($v$ and $w$) in orange and blue. The unit cell of the chain is marked by dashed gray bubbles. (b) Fully dimerized limit $v = 1$, $w = 0$, all sites are paired inside their unit cell. (c) Fully dimerized limit $v = 0$, $w = 1$, the edge sites marked with yellow border are isolated from the rest of the chain, topological state.

The tight-binding Hamiltonian modelling a finite chain of $N$ sites can be written [42]:

$$\hat{H} = v \sum_{n=1}^{N} (|n, B\rangle\langle n, A| + h.c.) + w \sum_{n=1}^{N-1} (|n+1, A\rangle\langle n, B| + h.c.) \tag{1.1}$$

Where *h.c.* stands for *hermitian conjugate*. $|n, A\rangle$ and $|n, B\rangle$ indicate the state of the chain with an electron on the sublattice A or B, respectively. The index $n \in \{1, 2, ..., N\}$ labels the site of the chain. As we can observe from the previous expression, the hopping $v$ connects two sites inside the same unit cell (indicated by the dashed gray balls), whereas $w$ links two sites from different unit cells.

Like in many systems, we can differentiate between *bulk* and *boundary*. In this

case, the bulk is the inside of the chain, while the boundary are the two sites at the ends of the chain. To describe the bulk Hamiltonian, we take advantage of the translational symmetry of the system and applying Bloch's theorem (see Appendix A). We go to the reciprocal space and obtain the dispersion relation of the system:

$$E(k) = \pm\sqrt{v^2 + w^2 + 2vw\cos k} \tag{1.2}$$

Note that the previous dispersion relation is gapped in energy for all $v$ and $w$, except when $v = w$. If we look at the fully dimerized cases in Fig. 1.1 (b) $v = 1$, $w = 0$ and (c) $v = 0$, $w = 1$. We notice that in the second case, there are two sites in the chain that are left out from the Hamiltonian. In this case, we say that the system is in a *topological* state and the two sites left out are *edge states*. More generally, we can verify that for hopping values such that $w > v$, we find ourselves in the topological state of the system. To change the topological character, the system has to go through a *topological phase transition* (TPT) and the energy gap has to close. In the SSH model, this transition occurs when $v = w$.

As we have seen, the topological character of these two different phases appears in the bulk. In the present case, the bulk is defined by the unit cell. Depending on whether we choose the unit cell with its internal bond given by $v$ or $w$, we are choosing a completely different ending when we cut the infinite system to create the finite one. Otherwise, the phases in the infinite system are totally equivalent and indistinguishable.

The SSH model provides one of the most basic systems to show topological edge states, its easy description provides an ideal platform for the study of topological states in 1-D. As we will see in the following, Kitaev's chain follows a very similar description, and many of its properties can be translated into the SSH model. Numerous experimental realizations, have shown the emergence of topological states in this model [53], [54].

### 1.1.3 The Kitaev model

Kitaev's chain is a model proposed by Alexei Kitaev in 2001 [13]. It consists of a 1-D chain of N sites, each occupied by a fermionic particle [43], [55]. The Hamiltonian in real space can be written:

$$\hat{H}_{Kiatev} = -\mu \sum_{n=1}^{N} c_n^\dagger c_n + \sum_{n=1}^{N-1} (\Delta c_n^\dagger c_{n+1}^\dagger - t c_n^\dagger c_{n+1}) + h.c. \tag{1.3}$$

Where $c^\dagger$ and $c$ are creation and annihilation fermion operators, respectively, $\mu$ is the chemical potential of the system, $t$ is the coupling between neighboring sites and the coupling, $\Delta$, couples pairs of fermions. This last parameter, as we will see in the following, is usually identified with the pairing potential in superconductors, responsible for the bonding between electrons forming Cooper pairs. However, it

is important to mention that in the previous equation, the spin is absent, meaning that in real systems $\Delta$ must couple fermions with the same spin. As we will see in 1.2, this type of coupling can not be found in conventional superconductors.

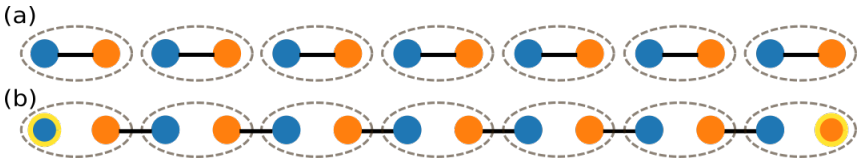


Figure 1.2: Kitaev chain schema. Each site of the chain is represented by a dashed gray bubble, the two Majorana states $\gamma^A$ and $\gamma^B$ are represented by blue and orange balls, the black lines connect adjacent Majorana states forming a fermionic state. (a) Trivial state, Majorana states in the same site are coupled, forming a fermionic state in each site. (b) Topological state, Majoranas from different sites are coupled to each other, leaving two unpaired Majorana (with yellow contour) at the ends of the chain.

### Majorana operators

In order to observe topological states in this model, we have to express the current fermion operators as a function of new operators:

$$c_n = \frac{1}{2}(\gamma_n^A + i\gamma_n^B) \qquad c_n^\dagger = \frac{1}{2}(\gamma_n^A - i\gamma_n^B), \tag{1.4}$$

$\gamma^A$ and $\gamma^B$ are the *Majorana operators*. Any fermionic operator can be decomposed into two Majorana operators [11], [43], because the new representation allows to write the creation and annihilation operators in terms of their real and imaginary parts, Eq. 1.4. In Fig. 1.2, each fermionic site of the chain is represented by a dashed bubble, and the blue and orange balls represent the $\gamma^A$ and $\gamma^B$ Majorana operators. In this representation, we can see how the fermionic chain is decomposed in individual Majorana states. Rewriting Eq. 1.3 in terms of these new operators, we obtain:

$$\hat{H}_{Kitaev} = -i\mu \sum_{n=1}^{N} \gamma_n^A \gamma_n^B + i \sum_{n=1}^{N-1} (i(\Delta + t)\gamma_n^B \gamma_{n+1}^A + i(\Delta - t)\gamma_n^A \gamma_{n+1}^B). \tag{1.5}$$

This model is very similar to the SSH model explained in 1.1.2: we can define the two hopping parameters $v := i(\Delta - t)$ and $w := i(\Delta + t)$ [56] and the real and imaginary parts of the fermionic operators constitute the new bipartite lattice. Similarly, if we look at the case where $\mu = 0$ and $\Delta = t$, in the SSH notation, this corresponds to $v = 0$ and $w = 2$. Here, the Hamiltonian simply becomes:

$$\hat{H}_{Kiatev} = 2it \sum_{n=1}^{N-1} \gamma_n^B \gamma_{n+1}^A. \tag{1.6}$$

We find ourselves in a very similar situation as the one described in the SSH model: two of the Majorana operators ($\gamma_1^A$ and $\gamma_N^B$) are left out of the Hamiltonian, as shown in Fig. 1.3 (b). This is the topological state of the Kitaev chain. The two Majorana states left unpaired at the edges of the chain are called *Majorana bound states* (MBS). Unlike the SSH model, there are not experimental realizations that have proved the emergence of MBS in the lab to the present date.

### Bulk-edge correspondence

As we have discussed in 1.1.2, the study of the bulk Hamiltonian of the SSH model allowed us to identify topological solutions of the system. We want to proceed similarly for the Kitaev chain. For this, we go into the reciprocal space, because k-points are good quantum numbers we can apply Bloch's theorem. We can write the Hamiltonian using the basis $\psi_k = \{c_k, c_{-k}^\dagger\}$:

$$\begin{aligned} \hat{H}(k) =& \frac{1}{2}\sum_k \psi_k^\dagger \hat{H}_{BdG}\psi_k \\ \hat{H}_{BdG} =& (-\mu - 2t\cos k)\tau_x + 2\Delta \sin k \tau_y \end{aligned} \tag{1.7}$$

Where $\tau_{x,y,z}$ denote the Pauli matrices. The previous Hamiltonian is written under the Bogoliubov-de Gennes (BdG) form [49].

Figure 1.3 shows the result of diagonalizing Eq. 1.7 for different chemical potential values. For $\mu = -3$ (Fig. 1.3 (a)), we observe two bands and an energy gap. When we increase to $\mu = -2$ in Fig. 1.3 (b), we observe that the gap has closed, this is the topological phase transition, the topological state of the system changes at this point. For $\mu = -1$, the system is newly gapped, and we find ourselves in the non-trivial topological phase. This transition can also be observed by diagonalizing the Hamiltonian in Eq. 1.3 for a finite chain. The resulting eigenenergies for a 30-site chain are depicted in Fig. 1.3 (d). As the chemical potential is increased, we observe a zero-energy state emerging at $\mu \sim -2$. Indeed, the system is found to be in the trivial phase for $\mu < -2t$ and in the topological state for $\mu > -2t$. As we can see, the properties of the bulk Hamiltonian give information about the finite system, by virtue of the *bulk-edge correspondence* [13]. The bulk-edge correspondence principle states that zero-energy edge states appear when joining two systems of different bulk topology. Then, by knowing the topology of different finite systems, when they are put together, the number of zero-energy edge states is determined.

However, is there a way of knowing the topology of a system for any given parameters without having to look for this gap closing of the bulk Hamiltonian? Indeed, it is possible to define an integer that identifies the different topological phases of a system, this is called a *topological invariant*.

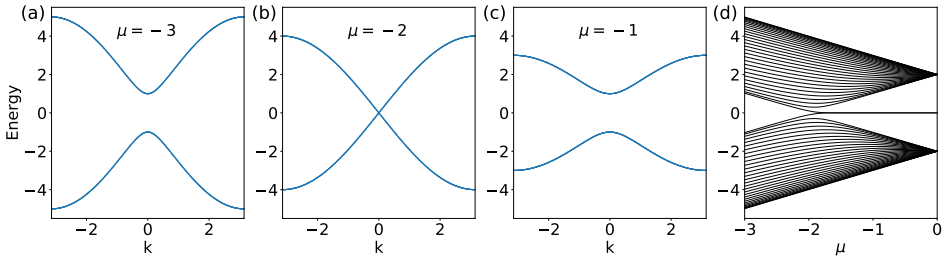


Figure 1.3: (a), (b) and (c) band structure from Eq.1.7 for $\mu = -3, -2, -1$, respectively. The topological phase transition, and gap closing, is observed at $\mu = -2$. (d) Eigenenergies for a finite chain of 30 sites. Parameters: $\Delta = t = 1$, $\mu$ as indicated.

In gapped systems (like insulators and superconductors) it is possible to defined topological invariants based in smooth variations of the Hamiltonian. When creating and edge between different systems, if they are gapped, we expect that we can smoothly change from one to the other. But if the topological invariants are different, this is not possible, because the invariant should be preserved during the smooth evolution. The only way to make the transition possible is by closing the gap at the edge, and as a consequence zero-energy edge states appear. As we will see in the next section, the topological invariant for a given system is defined by the symmetries present in the system.

### 1.1.4 Symmetries and topological classification

Symmetries have an important role in physics, they add restrains to systems, which can be useful because they reduce the degrees of freedom. As we are about to see, symmetries also allow to classify a system, by means of topological invariants. Using the presence or absence of the three main symmetries, we can classify the system in different topological classes. These symmetries are summarized in the following table [57], [58]:

| Symbol | Symmetry | Commutation | Unitary |
|---|---|---|---|
| $\mathcal{T}$ | Time-reversal | $[\hat{H}, \mathcal{T}] = 0$ | Anti-unitary |
| $\mathcal{P}$ | Particle-hole | $\{\hat{H}, \mathcal{P}\} = 0$ | Anti-unitary |
| $\mathcal{C}$ | Chiral | $\{\hat{H}, \mathcal{T}\} = 0$ | Unitary |

Table 1.1: Three main symmetries considered for topological classification of a Hamiltoninan, $\hat{H}$. They are defined by their commutation or anti-commutation with $\hat{H}$, and wheter the symmetry is defined by a unitary or anti-unitary operator.

As we can see in Table 1.1, time-reversal symmetry commutes with the Hamiltonian, *i.e.*, $\mathcal{T}\hat{H}\mathcal{T}^{-1} = \hat{H}$. Particle-hole and chiral symmetries, on the other hand, anti-commute with the Hamiltonian, *i.e.* $\mathcal{P}\hat{H}\mathcal{P}^{-1} = -\hat{H}$[1]. The symmetries are further classified by the unitary or anti-unitary[2] corresponding operators. The three main symmetries and whether their associated operators squares to $\pm 1$ result in the 10-fold symmetry classification, summarized in Table 1.2.

### Time-reversal symmetry

Time-reversal are the conservation laws under time inversion, ($t \rightarrow$ -t). In quantum mechanics, it is defined by an anti-unitary operator. In general, time-reversal operators can be expressed under the following from:

$$\mathcal{T} = U\mathcal{K} \tag{1.8}$$

where $U$ is a unitary operator and $\mathcal{K}$ denotes the complex-conjugation operator. A Hamiltonian with time-reversal symmetry satisfies the following relation $\mathcal{T}\hat{H(k)}\mathcal{T}^{-1} = \hat{H(-k)}$.

An important case is the one of spin 1/2 systems, time-reversal symmetry on this case is defined as $\mathcal{T} = i\sigma_y\mathcal{K}$. This is the most commonly known time-reversal symmetry in physics. In this case, $\mathcal{T}^2 = -1$.

### Particle-hole symmetry

Also known as charge conjugation symmetry, particle-hole is the symmetry conserved when we exchange particles and anti-particles, in our case, electrons and holes. It is defined by the anti-unitary operator:

$$\mathcal{P} = \sigma_x\mathcal{K} \tag{1.9}$$

The particle-hole symmetric Hamiltonian satisfies $\mathcal{P}\hat{H}(k)\mathcal{P}^{-1} = -\hat{H}(-k)$. It is worth mentioning that every BdG Hamiltonian is particle-hole symmetric by construction.

### Chiral symmetry

Geometrically, chirality refers to the symmetry existing between an object and its mirror image. In physical systems, a natural way for chirality to emerge is to

[1]Some authors use the term *chiral symmetry* to refer to any symmetry satisfying $\{\hat{H}, \mathcal{C}\} = 0$, however, in our case we use the term chiral symmetry to refer to an anti-symmetric relation defined by a unitary operator.

[2]Note that the definition of anti-unitary operator is a bijective operation $U : H_1 \longrightarrow H_1$ in a complex space $H_1$ such that $< Ux, Uy > = < \overline{x, y} >$ and it does not necessary mean that $U^2 = -1$. For example, $\mathcal{T} = \mathbf{1}\mathcal{K}$, is an anti-unitary operator such that $\mathcal{T}^2 = 1$.

have a sublattice defined, this is why this symmetry is also referred to as sublattice symmetry. The operator defining the so-called chiral symmetry is the one composed by the two previous ones:

$$\mathcal{C} = \mathcal{T} \cdot \mathcal{P} \tag{1.10}$$

It satisfies the following relation $\mathcal{C}\hat{H}(k)\mathcal{C}^{-1} = -\hat{H}(k)$. It is possible for a system that $\mathcal{T}$ and $\mathcal{P}$ are broken buy still $\mathcal{C}$ is satisfied [58].

| class | $\mathcal{T}$ | $\mathcal{P}$ | $\mathcal{C}$ | d=1 | 2 | 3 |
|---|---|---|---|---|---|---|
| A | | | | $\mathbb{Z}$ | | |
| AI | 1 | | | | | |
| AII | -1 | | | | $\mathbb{Z}_2$ | $\mathbb{Z}_2$ |
| AIII | | | 1 | $\mathbb{Z}$ | | $\mathbb{Z}$ |
| BDI | 1 | 1 | 1 | $\mathbb{Z}$ | | |
| C | | -1 | | | $2\mathbb{Z}$ | |
| CI | 1 | -1 | 1 | | | $2\mathbb{Z}$ |
| CII | -1 | -1 | 1 | $2\mathbb{Z}$ | | $\mathbb{Z}_2$ |
| D | | 1 | | $\mathbb{Z}_2$ | $\mathbb{Z}$ | |
| DIII | -1 | 1 | 1 | $\mathbb{Z}_2$ | $\mathbb{Z}_2$ | $\mathbb{Z}$ |

Table 1.2: 10-fold symmetry classification, according to time-reversal ($\mathcal{T}$), particle-hole ($\mathcal{P}$) and chiral ($\mathcal{C}$) symmetries. $d$ denotes the dimensionality of the system.

#### Classification

The presence or absence of these three symmetries and depending on the square of the operators ($\mathcal{U}^2 = \pm 1$) permits to perform a topological classification of the electronic structure. We can classify the system on 10 different topological classes. In Table 1.2 we show the classification in symmetry classes as a function of the three aforementioned symmetries [58].

For the Kitaev chain Hamiltonian, we can define the generalized time reversal operator $\mathcal{T} = \mathbb{1}\mathcal{K}$, in this case $\mathcal{T}^2 = 1$. Particle-hole symmetry is preserved by every BdG Hamiltonian by construction, the operator defined by Eq. 1.9 and it satisfies $\mathcal{P}^2 = 1$. Then, the chiral operator is $\mathcal{C} = \mathcal{T} \cdot \mathcal{P} = \sigma_x$, and $\mathcal{C}^2 = 1$. Thus, as we can observe on Table 1.2, the system falls into the BDI class. The SSH chain previously discussed is also included in the BDI class. In the next section, we take a closer look into this topological class and the corresponding invariant used to describe the different topological phases.

### 1.1.5 Topological invariants

As we have seen in the previous section, the symmetries of a system allow us to classify it in a specific topological class. Each class has a topological invariant associated to it, taking values as specified in Table 1.2. The Kitaev and SSH models

fall into the BDI class, the topological invariant in this case takes values in the set of integer numbers, $\mathbb{Z} = \{... - 2, -1, 0, 1, 2, ...\}$.

Assuming that the topology of the system is well represented by the two lower-energy bands, because they are the ones that will close the gap first, then we can write the Hamiltonian as $\hat{H}(k) = \vec{d}(k)\vec{\tau}$, where $\vec{\tau}$ is the basis of the Pauli matrices. Because any $2 \times 2$ matrix can be expressed as a linear combination of the Pauli matrices and the identity matrix.

### Winding number

Due to the chiral symmetry of the SSH and Kitaev models, the component $d_z(k) = 0$. As such, the hamiltonian can simply be written [42]:

$$\hat{H}(k) = \begin{pmatrix} 0 & d_x(k) - id_y(k) \\ d_x(k) + id_y(k) & 0 \end{pmatrix} \tag{1.11}$$

The $\vec{d}(k)$ vector, describes a closed trajectory in the $(d_x, d_y)$ plane. The topology of this loop is characterize by the *winding number* [42], [59]:

$$w = \frac{1}{2\pi} \int_{1\mathcal{BZ}} d\theta(k) \tag{1.12}$$

Where $\theta(k)$ is the angle described by the $\vec{d}(k)$ vector in its trajectory. The winding number counts the number of turns that the trajectory completes about the origin in the first Brillouin zone (positive for anti-clockwise trajectories and negative for clockwise). Hence, this number must take values in $\mathbb{Z}$, as expected.

To evaluate the winding number, we can define the following formula, $z(k) = \exp i\theta(k) = \vec{d}(k)/|\vec{d}(k)|$, from this the winding number can be obtained by evaluating:

$$w = \int_0^{2\pi} \frac{dz(k)}{z(k)} \tag{1.13}$$

Applying the $z(k)$ expression, we find:

$$w = \frac{1}{2\pi} \int_{-\pi/a}^{\pi/a} dk (d_x \frac{d}{dk} d_y - d_y \frac{d}{dk} d_x), \tag{1.14}$$

The cases where $w = 0$ the system is in the topologically trivial state, for $w = \mathbb{Z}\backslash\{0\}$, the system is in a non-trivial topological state.

### Q topological invariant

By considering a lower symmetry class, such as the D class in 1-D, we can define a different topological invariant. The associated topological invariant in that case

is:

$$Q = Sgn[Pf(\hat{H}(k=0)) \cdot Pf(\hat{H}(k=\pi))] \tag{1.15}$$

Where $Pf$ denotes the Pfaffian of the Hamiltonian, which is easily evaluated $Pf(\hat{H}(k=0)) = \det(A(k))$. $Q$ takes values in $\mathbb{Z}_2 = \{-1, 1\}$[3]. It can be shown that $Q$ and the winding number are related by the expression,

$$Q = (-1)^w \tag{1.16}$$

in other words, $Q$ gives the parity of the winding number. These two invariants will be used in the following to determine the topological phase of our system. But first, we will review some superconductivity basics, and how the excitations in these systems are closely related to Majorana fermions.

## 1.2 Theory of superconductivity

As already mentioned in the introduction to this chapter, the particle-hole symmetry existing in superconductors makes them natural candidates for experimental realization of MBS. Indeed, as explained in 1.1.3, the pairing parameter $\Delta$ in the Kitaev model, is usually identified with the pairing parameter in superconductors. In this section, we review the basics of the BCS theory of superconductivity, as well as the Bogoliubov-de Gennes equations.

### 1.2.1 General considerations

Superconductivity was first observed in 1911 by Heike Kamerlingh Onnes while doing experiments on mercury at low temperatures. He found that below a critical temperature the resistance of the mercury sample dropped to zero. In 1933 Walther Meissner and Robert Ochsenfeld discovered that superconductors expel applied magnetic fields, this is called the Meissner effect. In 1957 John Bardeen, Leon Cooper, and John Robert Schrieffer proposed the first microscopic theory for superconductivity, the BCS theory [1].

Bardeen, Cooper and Schrieffer postulated that superconductivity had its origin in the coupling of electrons forming *Cooper pairs* [2], as the result of an attractive interaction between electrons. This interaction, can have different origins. In conventional superconductors, it is the result of the electron-phonon interaction [60], this is represented in Fig. 1.4. The pairing of electrons leads to a new ground state below a certain critical temperature. This ground state is formed by the condensation of all Cooper pairs such that no single-particle state is possible. As a consequence, single-particle states become available only after breaking Cooper pairs. The energy to break the Cooper pair is called the superconducting gap, $\Delta$. Since the ground state is conducting, the presence of the excitation gap leads

[3]Strictly $\mathbb{Z}_2$ refers to the quotient group $\mathbb{Z}/(2\mathbb{Z})$ know as the cyclic group with two elements, this group is isomorphic to the set $\{0, 1\}$ with the addition modulo 2.

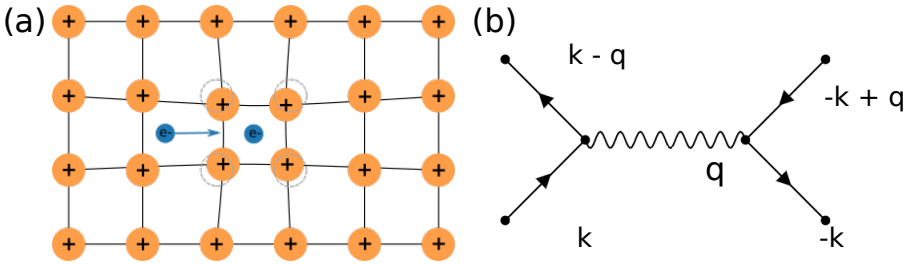


Figure 1.4: Electron-phonon interaction. (a) The lattice of positive ions is displaced due to the presence of an electron, a second electron is attracted due to the excess of positive charges. (b) Feymann diagram of electron-phonon interaction. Here the two electrons exchange a virtual phonon.

to non-decaying currents as first observed in 1911. Furthermore, assuming an isotropic pairing leads to Cooper pairs whose two-particle wave function can be well represented by the first spherical harmonic about the center of the Cooper pair. This s-wave approximation leads to a singlet pairing of the electronic spins to maintain the antisymmetry of the Cooper pair wave function as dictated by the Pauli principle. As a consequence, the BCS ground state is formed by spinless particles that trend to break under the presence of a magnetic field. In order to minimize the energy of the system, the magnetic field is then expelled giving rise to the Meissner effect. Indeed, this theory was able to explain all the known phenomena characterizing superconductors. Bardeen, Cooper and Schrieffer received the Nobel Prize in Physics for this theory in 1972.

### 1.2.2 BCS theory

#### Cooper pairs

Cooper showed that, at low temperature, an attractive interaction can bind pairs of electrons near the Fermi surface. This is true no matter how weak the interaction is, making the Fermi sea of electrons unstable. The two particle wave function can be written:

$$\psi(\vec{r}_1, \sigma_1, \vec{r}_2, \sigma_2) = e^{i\mathbf{kR}}\phi(\vec{r}_1, \vec{r}_2)\chi_{\sigma_1,\sigma_2} \tag{1.17}$$

Where $\phi(\vec{r}_1, \vec{r}_2)$ is the orbital part and $\chi_{\sigma_1,\sigma_2}$ is the spin part. $\mathbf{k}$ and $\mathbf{R}$ are the center of mass and total momenta, respectively. Cooper showed that the lowest energy state is reached when the momenta of the two electrons are opposite $\vec{k}_2 = -\vec{k}_1$, *i.e.*, $\mathbf{k} = 0$ [61], [62]. To satisfy the Pauli exclusion principle and the indistinguishability of the electrons, the total wave function of the pair has to be antisymmetric with respect to electron exchange. If we assume the orbital part of the Cooper pair to be an even function $\phi(\vec{r}_1, \vec{r}_2) = -\phi(\vec{r}_1, \vec{r}_2)$, then spin wave

function must be a singlet (total spin $S = 0$):

$$\chi_{\sigma_1,\sigma_2} = \frac{1}{\sqrt{2}}(|\uparrow\downarrow\rangle - |\downarrow\uparrow\rangle) \tag{1.18}$$

Conventional superconductors show this singlet coupling, and are known as $s$-wave superconductors. Alternatively, if the orbital part, $\phi(\vec{r}_1, \vec{r}_2)$ is an odd function, the Cooper pairs must couple in a triplet spin state ($S = 1$):

$$\chi_{\sigma_1,\sigma_2} = \begin{cases} |\uparrow\uparrow\rangle \\ \frac{1}{\sqrt{2}}(|\uparrow\downarrow\rangle + |\downarrow\uparrow\rangle) \\ |\downarrow\downarrow\rangle \end{cases} \tag{1.19}$$

This type of Cooper pair coupling in known as $p$-wave superconductivity. And it lies at the core of experimental realizations of Majorana fermions in condensed matter systems. As it couples electrons with the same spin.

### BCS Hamiltonian

The pairing Hamiltonian of a conventional superconductor induces the electron-electron interaction described in 1.2.2. This interaction appears as a scattering term that takes the pair of electrons with momentum: $(\vec{k}', -\vec{k}') \rightarrow (\vec{k}, -\vec{k})$.[4] We use creation ($c^\dagger_{k\sigma}$) and annihilation ($c_{k\sigma}$) operators to write the Hamiltonian, they respectively create and destroy an electron with momentum $\vec{k}$ and spin $\sigma$. The BCS Hamiltonian writes:

$$\hat{H} = \sum_{k\sigma} \xi_k c^\dagger_{k\sigma} c_{k\sigma} + \frac{1}{N} \sum_{kk'} V_{kk'} c^\dagger_{k\uparrow} c^\dagger_{-k\downarrow} c_{-k'\downarrow} c_{k'\uparrow}. \tag{1.20}$$

Where $\sigma = \uparrow, \downarrow$ is the spin index. $\xi_k = \epsilon_k - E_F$ is the electron energy relative to the Fermi level, $E_F$. $N$ is the number of electrons and $V_{kk'}$ is the interaction potential. Using the mean field approximation, the Hamiltonian is converted to:

$$\hat{H}^{MF} = \sum_{k,\sigma} \xi_k c^\dagger_{k\sigma} c_{k\sigma} - \sum_k \Delta^*_k c_{-k\downarrow} c_{k\uparrow} - \sum_k \Delta_k c^\dagger_{k\uparrow} c^\dagger_{-k\downarrow}. \tag{1.21}$$

Where the gap of the superconductor is given by the expectation value of the Cooper pair creation and annihilation operators:

$$\begin{aligned} \Delta_k &= -\frac{1}{N} \sum_{-k} V_{kk'} < c_{-k'\downarrow} c_{k'\uparrow} >, \\ \Delta^*_k &= -\frac{1}{N} \sum_{-k} V_{kk'} < c^\dagger_{k'\uparrow} c^\dagger_{-k'\downarrow} > . \end{aligned} \tag{1.22}$$

[4] In the following, we drop the vector symbol in $\vec{k}$ and simply write $k$ to denote the reciprocal space wave vector.

### 1.2.3 Bogoliubov quasiparticles

As shown independently by Bogoliubov [63] and Valantin [64] the mean field Hamiltonian in Eq. 1.21 can be diagonalized by applying the following linear transformation:

$$\begin{aligned} c_{k\uparrow} &= u_k \gamma_{k\uparrow} + v_k \gamma^{\dagger}_{-k\downarrow} \\ c^{\dagger}_{-k\downarrow} &= -v^{*}_k \gamma_{k\uparrow} + u^{*}_k \gamma^{\dagger}_{-k\downarrow} \end{aligned} \tag{1.23}$$

This transformation is commonly known as *Bogoliubov transformation.*

The creation and annihilation operators in Eq. 1.21 can be replaced by the Bogoliubov transformation 1.23. The cross-diagonal terms of the Hamiltonian ($\gamma^{\dagger}_{k\uparrow}\gamma^{\dagger}_{-k\downarrow}$ and $\gamma_{-k\downarrow}\gamma_{k\uparrow}$ terms) in the mean field Hamiltonian will be cancelled if the coefficients $u_k$, $v_k$ are such that:

$$|u_k|^2 = \frac{1}{2}\Big(1 + \frac{\xi_k}{\sqrt{\xi_k^2 + |\Delta|^2}}\Big); \qquad |v_k|^2 = \frac{1}{2}\Big(1 - \frac{\xi_k}{\sqrt{\xi_k^2 + |\Delta|^2}}\Big). \tag{1.24}$$

In the new basis, the Hamiltonian is diagonal and can be expressed under the form:

$$\hat{H}^{MF} = E_0 + \sum_{k\sigma} E_k \gamma^{\dagger}_{k\sigma}\gamma_{k\sigma}. \tag{1.25}$$

$E_0$ is the energy of the ground state, and $E_k$ is the dispersion relation of the eigenstates defined by the Bogoliubov transformation. The second term gives an increase in energy of the ground state in terms of $\gamma^{\dagger}_k\gamma_k$. As such, the $\gamma_k$ operator describes the elementary quasiparticle excitations of the system, commonly known as *Bogoliubov quasiparticles.* Their dispersion relation:

$$\pm E_k = \pm\sqrt{\xi_k^2 + |\Delta|^2} \tag{1.26}$$

By inverting the Bogoliubov-Valantin transformation (Eq. 1.23), we find the expression for the Bogoliubov quasiparticle creation operators:

$$\begin{aligned} \gamma_{k\uparrow} &= u^{*}_k c_{k\uparrow} - v_k c^{\dagger}_{-k\downarrow}, \\ \gamma^{\dagger}_{-k\downarrow} &= u_k c^{\dagger}_{-k\downarrow} + v^{*}_k c_{k\uparrow}. \end{aligned} \tag{1.27}$$

As shown in the previous expression, the Bogoliubov quasiparticles are a coherent superposition of creation and annihilation electron operators, making these quasiparticles a combination of electron and hole. The superconducting gap, $\Delta$, is the minimum energy required to have Bogoliubov excitations. The transformation in Eq. 1.27 highlights the electrons-hole symmetry existing in superconductors. Figure 1.5 (a) depicts the $u_k$ and $v_k$ probabilities as a function of $\xi_k$. As shown, in the high-energy limit ($E >> \Delta$), the Bogoliubov quasiparticles behave as particles: for negative $\xi_k$, in the limit $|v_k|^2 = 1$, and for positive energies $|u_k|^2 = 1$, *i.e.*, the quasi-particles become hole and electron, respectively.

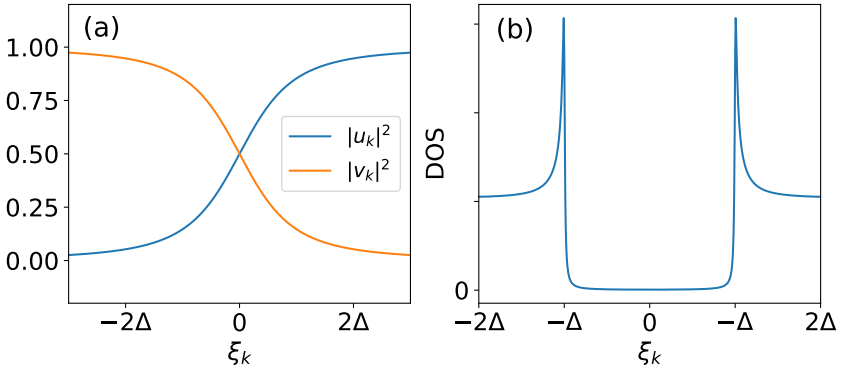


Figure 1.5: Density of states of a superconductor. (a) Coherence probabilities $|u_k|^2$ and $|v_k|^2$ as a function of $\xi_k$. (b) Density of states of a superconductor as obtained from Eq. 1.30.

As it can be noted, the Bogoliubov transformation is the same as the one utilized in the Kitaev model (section 1.1.3) to express the fermion states as Majorana operators in Eq. 1.4. Indeed, Majorana bound states are Bogoliubov quasi-particle with equal electron and hole part [43], which implies that they can *only* exist at zero energy, $\xi_k = 0$.

### Superconducting density of states

To compute the superconducting density of states, $N_s(E)$, we can use the dispersion relation of the Bogoliubov quasi-particles and equating: $N_s(E)dE = N_n(\xi)d\xi$. Since $E_k^2 = \Delta^2 + \xi_k^2$, and assuming that the normal-metal density of states is constant and equal to the metal's density of state at the Fermi energy, $N_n(\xi) = N(0)$, we find [61]:

$$\frac{N_s(E)}{N(0)} = \frac{d\xi_k}{dE} = \begin{cases} \frac{E}{\sqrt{E^2-\Delta^2}} & (E > \Delta) \\ 0 & (E < \Delta) \end{cases} \tag{1.28}$$

As we can see from the previous expression, at $E = \Delta$, we expect to have a divergent state density. To better fit the experimental data and the measured density of states. Dynes introduced a damping factor, such that $E \to E + i\Gamma$ [65], [66]. Which takes into account the pair braking during tunneling processes [61]. In this way, the density of states is written:

$$N_s(E) = \frac{E + i\Gamma}{\sqrt{(E + i\Gamma)^2 - \Delta^2}} \tag{1.29}$$

Alternatively, the superconducting density of states can be obtained from the Bogoliubov quasiparticles probabilities [49]:

$$N_s(E) = \frac{1}{N}\sum_k \Big[|u_k|^2\delta(E-E_k) + |v_k|^2\delta(E+E_k)\Big] \tag{1.30}$$

Figure 1.5 (b) is the superconducting density of states, calculated from Eq. 1.30. At $\xi_k = \Delta$ we can observe the coherence or *quasi-particle peaks*.

### 1.2.4 Bogoliubov-de Gennes equations

The Hamiltonian in Eq. 1.21 expressed in the reciprocal space, can not properly describe a non-uniform system, as $k$ is not a good quantum number. As such, it is more convenient to us to express the mean-field Hamiltonian in real space:

$$\hat{H}^{MF} = \sum_{ij\sigma}\big(-\mu c^\dagger_{i\sigma}c_{i\sigma} - t_{ij}c^\dagger_{i\sigma}c_{j\sigma}\big) + \sum_i\big(\Delta_i c^\dagger_{i\uparrow}c^\dagger_{i\downarrow} + \Delta^*_i c_{i\downarrow}c_{i\uparrow}\big) \tag{1.31}$$

where $t_{ij}$ accounts for the hopping terms. Due to the four component Nambu spinor that we use as our base, we need to define a spin-generalized Bogoliubov transformation:

$$\begin{aligned} c_{i\uparrow} &= \sum_n u_{ni\uparrow}\gamma_{n\uparrow} + v^*_{ni\uparrow}\gamma^\dagger_{n\downarrow}, \quad c_{i\downarrow} = \sum_n u_{ni\downarrow}\gamma_{n\downarrow} + v^*_{ni\downarrow}\gamma^\dagger_{n\uparrow} \\ c^\dagger_{i\uparrow} &= \sum_n u^*_{ni\uparrow}\gamma^\dagger_{n\uparrow} + v_{ni\uparrow}\gamma_{n\downarrow}, \quad c^\dagger_{i\downarrow} = \sum_n u^*_{ni\downarrow}\gamma^\dagger_{n\downarrow} + v_{ni\downarrow}\gamma_{n\uparrow} \end{aligned} \tag{1.32}$$

Our goal is to find the $u_{n\sigma}$ and $v_{n\sigma}$ coefficients that diagonalizes the mean field hamiltonian in Eq. 1.31. The equations relating these coefficients with the eigen energies of the system are the so-called Bogoliubov-de Gennes (BdG) equations [49]. In the following, we explain how to obtain these equations (the details are shown in Appendix A).

We first need to calculate the commutation relations of the creation and annhiliation operators with the mean-field Hamiltonian, $[\hat{H}^{MF}, c^{(\dagger)}_{i\sigma}]$. With the aid of the anti-commutation relations of the fermionic operators $\{c_\nu, c_\mu\} = \{c^\dagger_\nu, c^\dagger_\mu\} = 0$ and $\{c_\nu, c^\dagger_\mu\} = 1$, we find:

$$\begin{aligned} [\hat{H}^{MF}, c_{i\uparrow}] &= \sum_j (t_{ij} + \delta_{ij}\mu)c_{j\uparrow} + \Delta_i c^\dagger_{i\downarrow} \\ [\hat{H}^{MF}, c_{i\downarrow}] &= \sum_j (t_{ij} + \delta_{ij}\mu)c_{j\downarrow} - \Delta_i c^\dagger_{i\uparrow} \\ [\hat{H}^{MF}, c^\dagger_{i\uparrow}] &= \sum_j -(t_{ij} + \delta_{ij}\mu)c^\dagger_{j\uparrow} - \Delta^*_i c_{i\downarrow} \\ [\hat{H}^{MF}, c^\dagger_{i\downarrow}] &= \sum_j -(t_{ij} + \delta_{ij}\mu)c^\dagger_{j\downarrow} + \Delta^*_i c_{i\uparrow} \end{aligned} \tag{1.33}$$

We now require that the $\gamma_{n\sigma}^{(\dagger)}$ operators diagonalize the Hamiltonian from Eq. 1.31. So that:

$$\hat{H}^{MF} = E_0 + \sum_n E_{n\uparrow}\gamma_{n\uparrow}^\dagger\gamma_{n\uparrow} + E_{n\downarrow}\gamma_{n\downarrow}^\dagger\gamma_{n\downarrow} \tag{1.34}$$

We obtain the commutators of the diagonalized Hamiltonian, $[\hat{H}^{MF}, c_{i\sigma}^{(\dagger)}]$. Equating them to the commutators in Eq. 1.33 and comparing the coefficients of the $\gamma_{n\sigma}^{(\dagger)}$ operators, we find the BdG equations:

$$\begin{aligned}
u_{ni\uparrow}E_{n\uparrow} &= \sum_j -(t_{ij} + \delta_{ij}\mu)u_{nj\uparrow} - \Delta_i v_{ni\downarrow} \\
u_{ni\downarrow}E_{n\downarrow} &= \sum_j -(t_{ij} + \delta_{ij}\mu)u_{nj\downarrow} + \Delta_i v_{ni\uparrow} \\
v_{ni\uparrow}E_{n\downarrow} &= \sum_j (t_{ij} + \delta_{ij}\mu)v_{nj\uparrow} + \Delta_i^* u_{ni\downarrow} \\
v_{ni\uparrow}E_{n\uparrow} &= \sum_j (t_{ij} + \delta_{ij}\mu)v_{nj\downarrow} - \Delta_i^* u_{ni\uparrow}
\end{aligned} \tag{1.35}$$

Defining $h_\sigma u_{ni\sigma} = \sum_j -t_{ij}u_{nj\sigma} - \mu u_{ni\sigma}$, we can white the equations under matrix form:

$$\begin{pmatrix} h_\uparrow & 0 & 0 & -\Delta_i \\ 0 & h_\downarrow & \Delta_i & 0 \\ 0 & \Delta_i^* & -h_\uparrow & 0 \\ -\Delta_i^* & 0 & 0 & -h_\downarrow \end{pmatrix} \begin{pmatrix} u_{ni\uparrow} \\ u_{ni\downarrow} \\ v_{ni\uparrow} \\ v_{ni\downarrow} \end{pmatrix} = E_n \begin{pmatrix} u_{ni\uparrow} \\ u_{ni\downarrow} \\ v_{ni\uparrow} \\ v_{ni\downarrow} \end{pmatrix} \tag{1.36}$$

From the BdG equations, we can easily show the following statement: For a solution $(u_{i\uparrow}, u_{i\downarrow}, v_{i\uparrow}, v_{i\downarrow})^T$ of Eq. 1.36 with eigen energy $E$. There is always a solution with eigen energy $-E$, $(v_{i\uparrow}^*, v_{i\downarrow}^*, u_{i\uparrow}^*, u_{i\downarrow}^*)^T$ (see Appendix B for more details).

## 1.3 Experimental realizations: Spin chains on superconductors

As it has been discussed, the Kitaev chain is a theoretical model for realizing Majorana bound states. Superconducting systems are natural candidates due to the superconducting pairing potential. Unfortunately, a 1-D superconductor with pairing potential and absence of spin does not exist in nature. This could be effectively achieved by the resulting set of low-energy excitations after fully polarizing the system (for example by applying an external magnetic field), but superconductivity has never been observed in such conditions [55]. Spinless superconductor are systems where the Cooper pairs are formed with only one spin degree of freedom. As discussed in 1.2.2, this forces the orbital function of the pair to be an odd function, resulting in $p-$wave superconductivity.

Realizations of $p$-wave superconductivity have been proposed in the later years. One major breakthrough came from the work by Fu and Kane [14], they showed

a way of engineering $p-$wave superconductivity induced by the proximity effect of a $s-$wave superconductor in the surface of topological insulators. In the following years, several works focused on the Rashba semiconductor model [15]–[18]. In this approach, the presence of a Rashba spin-orbit coupling along with the breaking of the time-reversal symmetry (for example, by a Zeeman field), allows the system to enter a similar non-trivial state as the one shown by Fu and Kane.

Inspired by these theoretical works, experimental realizations [67] of MBS have focused on 1-D systems that combine three main ingredients: superconductivity, spin-orbit coupling (SOC) and magnetic Zeeman interactions. Semiconducting nanowires with high SOC and proximitized superconductivity [68]–[72] are one of the main approaches. The presence of topological states is detected by a zero-bias anomaly in transport measurements. This signal corresponds to a resonant Andreev reflection due to the presence of a MBS [43]. A peak of unitary quantized conductance, $G = 2e^2/\hbar$ is expected to appear at zero energy when the system is in the topological phase. Unfortunately, transport measurements do not allow to spatially resolve the emergence of MBS at both edges of the wire. Additionally, disorder in the device may result in the appearance of zero bias signals when the system is in the trivial state [73], [74].

In recent years, spin chains on superconducting surfaces with high SOC have also gained attention [20], [22]–[25], [75]. This approach has been developed in the context of scanning tunneling microscopy (STM). This tool, allows for precise control in the assembly of atomic structures [76]. In this way, 1-D structures of magnetic atoms can be crafted without any defects [19], [23], [28], [31]. Moreover, spatially resolved spectroscopy is possible in STM, which enables to observe the presence of the MBS at both ends of the chain.

This thesis focuses on the study of magnetic impurities in superconductors, as such, we are more interested on the second approach because it allows us to study these effects on the atomic scale, using both experimental and theoretical tools especially developed for atomistic studies.

In this section, we present and analyze the tight-binding model describing a 1-D superconducting system with Zeeman interaction and SOC. This is an effective model of a ferromagnetically ordered spin chain on a superconductor, but it equivalently describes a semiconductor nanowire with proximitized superconductivity and an external magnetic field. This simple model, although it employs unrealistic parameters, will help us understand more realistic models and experimental results in the following.

### 1.3.1 1-D bulk Hamiltonian

We start from the Hamiltonian of a 1-D superconducting system in real space, we write the mean-field Hamiltonian from Eq. 1.31. For the single-particle interac-

tions, we only consider the chemical potential of the system and a hopping term connecting neighboring atoms:

$$\hat{H}_{BCS} = \sum_i \big[ -\mu c^\dagger_{i\sigma} c_{i\sigma} - t(c^\dagger_{i\sigma} c_{i+1\sigma} + h.c.)\big] + \sum_i \big[\Delta c^\dagger_{i\uparrow} c^\dagger_{i\downarrow} + \Delta^* c_{i\downarrow} c_{i\uparrow}\big]. \quad (1.37)$$

Where $\mu$ is the chemical potential of the system, $t$ represents the hopping parameter between neighboring sites and $\Delta$ is the local pairing potential, we assume that it is real, $\Delta = \Delta^*$, and that it is site independent $\Delta_i = \Delta$ [8].

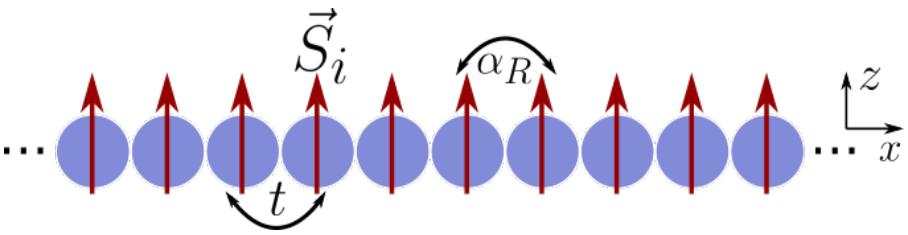


Figure 1.6: Tight-binding model of a ferromagnetic chain in a 1-D superconductor. The chain is assumed to be oriented along the $x$ direction. $t$ couples first-neighbor sites and the $\alpha_R$ is the effective Rasha coupling strength. The impurities spins are oriented along the $z$ direction.

The Rashba spin-orbit interaction [77] is the result of spin-orbit coupling, and the symmetry breaking that occurs in surfaces. As electrons move, they experience an effective magnetic field (the Rashba field), proportional to their momentum and perpendicular to their movement [78]. In one dimension, can be expressed by the following Hamiltonian[5]:

$$\hat{H}_{Rashba} = i\frac{\alpha_R}{2a} \sum_{j\sigma\sigma'} \big[c^\dagger_{j+1\sigma} (\sigma_y)_{\sigma\sigma'} c_{j\sigma'} + h.c.\big]. \quad (1.38)$$

Where $\alpha_R$ is the Rashba coupling strength and the factor $2a$ comes from the discretization of the system that replaces the appearing spatial gradients by finite differences in the discrete grid. This Hamiltonian, is an effective hopping term that couples neighboring sites with opposite spin.

Finally, we want to add magnetic impurities to the chain. This is modeled by the local $s-d$ Hamiltonian:

$$\hat{H}_{impurity} = J \sum_i \big[\vec{S}_i \cdot \vec{s}(i)\big]. \quad (1.39)$$

Where $J$ is the coupling strength between the magnetic impurities and the hosting material, $\vec{S}_i$ is the spin of the localized impurities in site $i$ and $\vec{s}(i)$ is the spin

[5]The Rashba spin-orbit interaction is discussed in more detail in chapter 2.

operator of the conduction electrons that interact with the magnetic impurities. In this study, we limit ourselves to ferromagnetic spin chains, *i.e.* the spins of all the impurities have the same orientation, perpendicular to the chain's axis. In this case, all the sites will have the same magnetic interaction and the term will simply be $J \cdot S$. We now add all previous terms together and express it using the notation $|i\rangle$ representing the i-site of the chain, each site is modelled with the 4-component Nambu $\psi_i = (c_{i\uparrow}, c_{i\downarrow}, c^\dagger_{i\uparrow}, c^\dagger_{i\downarrow})$.

$$\begin{aligned}\hat{H}_{total} = &\sum_i^N \big[ -\mu\tau_z\sigma_0 + \Delta\tau_y\sigma_y + J\cdot S\tau_z\sigma_z \big] |i\rangle\langle i| + \\ &\sum_i^N \big[ (-t\tau_z\sigma_0 + i\frac{\alpha_R}{2a}\tau_z\sigma_y) |i+1\rangle\langle i| + h.c. \big]\end{aligned} \tag{1.40}$$

The Pauli matrices $\tau_{x,y,z,0}$ and $\sigma_{x,y,z,0}$ operate in the particle-hole and spin sectors, respectively[6]. The previous Hamiltonian describes the spin chain of $N$ sites in real space. But we are interested in the case of an infinite 1-D chain. To this end, we move to the reciprocal $k$-space, so we are able to obtain the band structure of the system. Again, applying Bloch's theorem, we define the unit cell of a single atomic site. A complete basis is given by the 4-Nambu components $\psi_k = \{\hat{c}_{k\uparrow}, \hat{c}_{k\downarrow}, \hat{c}^\dagger_{-k\uparrow}, \hat{c}^\dagger_{-k\downarrow}\}$. The resulting Hamiltonian matrix is a $4\times 4$ matrix for each $k$ point:

$$\hat{H}(k) = \tag{1.41}$$
$$\begin{pmatrix} -\mu + JS - 2t\cos k & -2i\alpha\sin k & 0 & -\Delta \\ 2i\alpha\sin k & -\mu - JS - 2t\cos k & \Delta & 0 \\ 0 & \Delta & \mu - JS + 2t\cos k & 2i\alpha\sin k \\ -\Delta & 0 & -2i\alpha\sin k & \mu + JS + 2t\cos k \end{pmatrix}$$

We diagonalize the previous Hamiltonian in the first Brillouin zone of the spin chain, $k \in [-\frac{\pi}{a}, \frac{\pi}{a}]$ where $a$ is the distance between spins, and plot the resulting band structure. We set $\Delta = 0.5$ and $\mu = t = 1$, we add the Rashba interaction and magnetic exchange coupling separately to better observe their effect in the band structure. In Fig. 1.7, we plot the resulting bands for four different cases: In Fig. 1.7 (a) we see two bands with an energy gap, here magnetic and Rashba interactions are zero, so the two bands are doubly degenerated. We add the magnetic interaction and, as shown in Fig. 1.7 (b), the two bands split, breaking Kramer's degeneracy. In Fig. 1.7 (c) we solely add the Rashba interaction, the two bands split in the k-vector, lifting the spin degeneracy [18], [43], [72]. Finally, in Fig. 1.7

[6] All the Pauli matrices products in Eq. 1.40 are, in fact, Kronecker products. They are expressed in the compact notation $\tau_i \otimes \sigma_i = \tau_i\sigma_i$. The resulting matrix has $4\times 4$ dimension. We keep this notation throughout the thesis

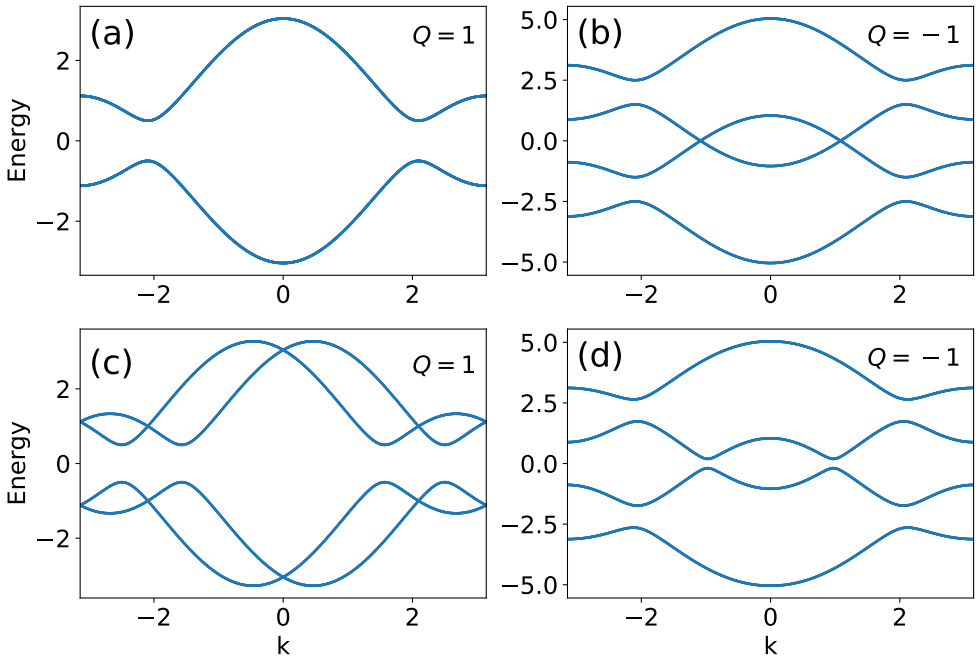


Figure 1.7: Band structure of a one dimensional spin ferromagnetic chain in a superconductor. Parameters: $\mu = 1.0$, $t = 1.0$, $\Delta = 0.5$. (a) No magnetic or Rashba interaction $JS = 0.0$, $\alpha_R = 0.0$. (b) Magnetic interaction alone $JS = 2.0$, $\alpha_R = 0.0$. (c) Rashba interaction alone $JS = 0.0$, $\alpha_R = 0.5$, (d) Magnetic and Rashba interaction $JS = 2.0$ and $\alpha_R = 0.5$.

(d) both magnetic and Rashba interactions are present, when compared to (b) we observe that the two bands crossing at zero energy split, opening a new gap in the system. This gap opening marks the topological phase transition to a non-trivial state.

The topological invariant, $Q$, is evaluated as indicated by Eq. 1.15, for all cases in Fig. 1.7. The system is in a topological state in (b) and (d), however, only (d) is a gapped system, meaning that in this case topological edge states will be able to emerge. The difference between Fig. 1.7 (b) and (d) is the respective absence and presence of the Rashba spin-orbit interaction. When added, the Rashba term, opens the topological gap in the system. $Q$ is obtained by evaluating the Pfaffian in $k = 0$ and $k = \pm\frac{\pi}{a}$, at these high symmetry points, the Rashba interaction vanishes, meaning that the presence or absence of the Rashba interaction has no effect on the topological phase of the system. However, its presence is required to reopen the gap and have MBS emerging in the spin chain [8].

### 1.3.2 Topological phase diagram

Topological phase diagrams are of special interest when studying the topological phases of a system. The topological invariant is evaluated as a function of two parameters and represented as a 2-D map in the parametric space. This allows us to easily identify the topological phases of the system depending on the parameters.

In Fig. 1.8, we show the topological phase diagrams of a ferromagnetic spin chain in a superconductor as a function of the magnetic exchange interaction ($J \cdot S$) and the chemical potential ($\mu$). Figure 1.8 (a) shows the topological invariant, $Q$, where the $Q = 1$ (yellow) areas correspond to the trivial phases and the $Q = -1$ (purple) areas are the topologically non-trivial. This is in good agreement with the winding number in Fig. 1.8 (b), here $w = 0$ is the trivial phase while we can differentiate two topological phases, $w = \pm 1$. As we mentioned before, $Q$ gives the parity of the winding number, in this sense, $Q$ allows distinguishing trivial from topological phases, but it carries less information than the winding number. The winding number sign indicates the direction of the $\vec{d}$ vector, and it allows distinguishing two types of MBS emerging at the ends of finite chains [79]. Finally, Fig. 1.8 (c) is not a topological invariant, but the energy gap of the system. As discussed in previous paragraphs, the topological phase transition occurs only if there is a gap closing. The dark purple areas of the map correspond to a zero energy gap. As we can observe in Fig. 1.8, the places where $Q$ and the winding number change value, perfectly match with the gap closings of the system in panel (c).

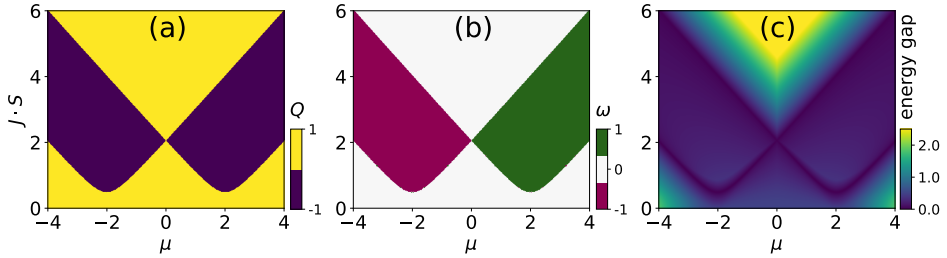


Figure 1.8: Topological phase diagrams as a function of $JS$ and $\mu$. (a) Topological invariant, $Q$. The yellow (purple) areas mark the trivial (topological) phases. (b) Winding number, $w$. The white areas correspond to trivial phases, while green and magenta are two distinct topological phases. (c) Energy gap of the system, the topological phases transitions always coincide with a zero gap. Parameters: $\Delta = 0.5$, $t = 1$ and $\alpha_R = 0.5$.

The topological phase transition, observed in Fig. 1.8, is given by the following

relation:

$$J \cdot S = \sqrt{(\pm 2t - \mu)^2 + \Delta^2}. \tag{1.42}$$

The two branches correspond to the two possible gap closing points of the bands: $k = 0, \pm\pi$. One centered at $\mu = 2t$ and the other one at $\mu = -2t$. The topological order parameter, $\Delta$, marks the minimum of $J \cdot S$ delimiting the topological area. For large $|\mu|$, $J \cdot S$ is linear with $\mu$ explaining the shape of the curves delimiting the topological area.

### 1.3.3 Finite chains

In the previous paragraph, we studied the bulk Hamiltonian of the spin chain. This allowed us to identify the topological phases of the system. Thanks to the bulk-edge correspondence, when we move to the case of a finite system, the topological phases of the system should result in MBS at the edges of the chain.

We go back to the real space Hamiltonian from Eq. 1.31. We define a finite 1-D system with $N$ sites, modeling the superconductor, and we select the middle $N_j$ sites to host the magnetic impurities. The resulting matrix has a size of $4N \times 4N$:

$$\begin{pmatrix} M_{11} & M_{12} & \dots & M_{1N} \\ M_{21} & M_{22} & & \\ \vdots & & \ddots & \vdots \\ M_{N1} & & \dots & M_{NN} \end{pmatrix} \tag{1.43}$$

Where each $M_{ij}$ is a $4 \times 4$ matrix as written in Eq. 1.36:

$$M_{i,i} = \begin{pmatrix} -\mu + JS & 0 & 0 & -\Delta \\ 0 & -\mu + JS & \Delta & 0 \\ 0 & \Delta & \mu - JS & 0 \\ -\Delta & 0 & 0 & \mu + JS \end{pmatrix}, \quad M_{i,i+1} = \begin{pmatrix} -t & \alpha_R & 0 & 0 \\ -\alpha_R & -t & 0 & 0 \\ 0 & 0 & t & -\alpha_R \\ 0 & 0 & \alpha_R & t \end{pmatrix}$$

The $JS$ component is present only on the sites where we have a magnetic impurity, being zero elsewhere. The matrix from Eq. 1.43 acts on the $4N$-component vector:

$$\hat{\phi}_n = (c_{1\uparrow}, c_{1\downarrow}, c^\dagger_{1\uparrow}, c^\dagger_{1\downarrow}, ..., c_{i\uparrow}, c_{i\downarrow}, c^\dagger_{i\uparrow}, c^\dagger_{i\downarrow}, ..., c_{N\uparrow}, c_{N\downarrow}, c^\dagger_{N\uparrow}, c^\dagger_{N\downarrow})^T \tag{1.44}$$

#### Solving the equations

We want to solve the BdG equations for the Hamiltonian in 1.43. To this end, we numerically, diagonalize the $4N \times 4N$ matrix. For an eigenenergy, $E_n$, the resulting eigenvectors are of the form

$$\hat{\phi}_n = (u_{1\uparrow}, u_{1\downarrow}, v_{1\uparrow}, v_{1\downarrow}, ..., u_{i\uparrow}, u_{i\downarrow}, v_{i\uparrow}, v_{i\downarrow}, ..., u_{N\uparrow}, u_{N\downarrow}, v_{N\uparrow}, v_{N\downarrow})^T$$

We select the following parameters: $\Delta = 0.5$, $t = 1$, $\mu = 2$, $JS = 2$ and $\alpha_R = 0.5$. If we take a look at the phase diagrams in Fig. 1.8, we can easily see that this corresponds to a topological phase, as such, MBS emerge in this system. After diagonalizing the matrix, we select the eigenstate with energy closest to zero. Because, we are now solving a finite system the energy of the Majorana mode is not exactly zero by a small amount [80]. Figure 1.9 (a)-(b) depicts the resulting modulus square of $u_{i\uparrow,\downarrow}$ for the corresponding eigenvector, as a function of the sites in the system. The vertical black dashed lines mark the edges of the magnetic impurity chain. As we can observe, $|u_{\uparrow,\downarrow}|^2$ reach their maximum at the edges, and they drop to zero as we move to the middle of the chain or outside. Since this is a Majorana mode, the coefficients satisfy $|u| = |v|$, equal electron and hole part. However, we can note that the two spin $\uparrow, \downarrow$ coefficients do not have the same amplitude. This fact highlights one of the main differences with the Kitaev chain: the spin chain is not a spinless system, and the MBS emerging in this case have some spin component [30].

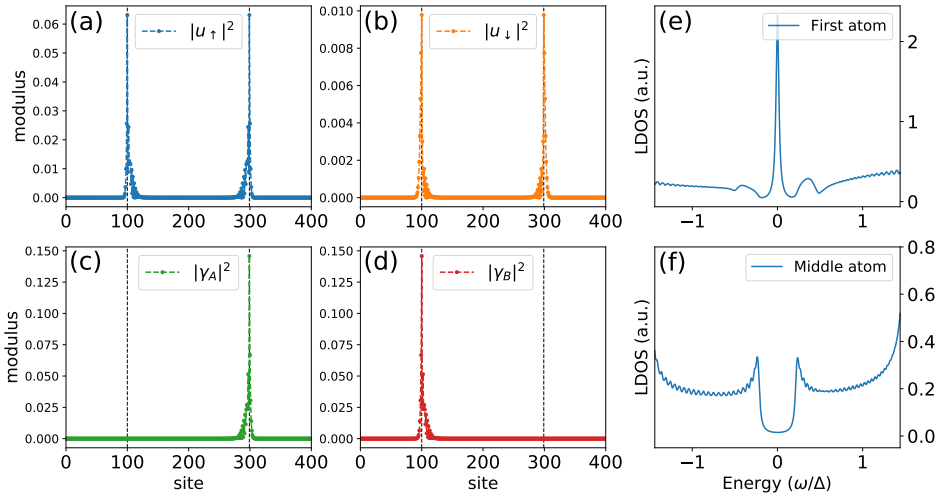


Figure 1.9: Finite chain of magnetic impurities in a superconductor. (a)-(b) Modulus square of $u_{i\uparrow}$ and $u_{i\downarrow}$ as a function of site. (c)-(d) Modulus square of the Majorana wave functions, $\gamma_A$ and $\gamma_B$. (e) and (f) LDOS at the end and middle of the chain, respectively, as a function of energy. Parameters: $\Delta = 0.5$, $t = 1$, $\mu = 2$, $JS = 2$ and $\alpha_R = 0.5$. 400 superconducting sites and 200 magnetic impurities.

We also want to observe the Majorana probability distribution in the chain, and verify that have two different modes ($\gamma_A$ and $\gamma_B$). To this end, we need to make a unitary transformation of the Hamiltonian to express it in the Majorana repre-

sentation:

$$\begin{aligned} \hat{c}_\uparrow &= \frac{1}{2}(\hat{\gamma_\uparrow^A} + i\hat{\gamma_\uparrow^B}), \quad \hat{c}_\downarrow = \frac{1}{2}(\hat{\gamma_\downarrow^A} + i\hat{\gamma_\downarrow^B}) \\ \hat{c}_\uparrow^\dagger &= \frac{1}{2}(\hat{\gamma_\uparrow^A} - i\hat{\gamma_\uparrow^B}), \quad \hat{c}_\downarrow^\dagger = \frac{1}{2}(\hat{\gamma_\downarrow^A} - i\hat{\gamma_\downarrow^B}) \end{aligned} \tag{1.45}$$

Or under matrix form:

$$\hat{U} = \mathbb{I}_N \otimes \frac{1}{\sqrt{2}} \begin{pmatrix} 1 & 0 & 1 & 0 \\ 0 & 1 & 0 & 1 \\ i & 0 & -i & 0 \\ 0 & i & 0 & -i \end{pmatrix} \tag{1.46}$$

We apply the previous unitary transformation to the eigen vector, $\hat{\phi}_n$. Figure 1.9 (c)-(d) show the resulting modulus square of the $\gamma_A$ and $\gamma_B$ coefficients using the same parameters as previously mentioned. As observed, each of these reach the maximum at the edge of the chain, but in opposite sites. Showing that these correspond to the two Majorana bound states.

We can also calculate the local density of states (LDOS) from the electron and hole coefficients:

$$\rho_{i\sigma}(E) = \sum_n \left[ |u_{i\sigma}|^2 \delta(E_n - E) + |v_{i\sigma}|^2 \delta(E_n + E) \right] \tag{1.47}$$

The total LDOS being $\rho_i = \rho_{i\uparrow} + \rho_{i\downarrow}$. On Fig. 1.9 (e) and (f) we have plotted the local density of states at the edge (e) and the centre (f) of the magnetic chain. We can clearly observe a pronounced peak at zero energy that correspond to the Majorana bound state, at the opposite end of the chain, the corresponding spectrum perfectly matches the one in Fig. 1.9 (e). When we look at the spectrum in the middle of the chain (Fig. 1.9) (f), we observe an absence of this peak and an energy gap.

This example of a finite chain, shows the main characteristics of MBS in ferromagnetic spin chains: (i) The two bound states are well localized at the ends of the 1-D system, and their wave function probability goes to zero as we move away from the edges. (ii) The MBS show some spin component different from zero, and its value is the same at both ends. (iii) The MBS appears as a pronounced peak at zero energy when we look at the LDOS at the edges of the chain. The parameters used in this tight-binding study are non-realistic. For instance, the bandwidth is unrealistically of the order of the superconducting gap, $\Delta$). Nevertheless, these properties remain true when we look at more realistic models, as we will see in chapters 2 and 3.

### Effect of the Rashba spin-orbit coupling

As briefly discussed in 1.3.1, the Rashba coupling has no effect in the topological phase of the spin chain. However, in order for MBS to emerge in finite ferromagnetic spin chains, this interaction is required [81], [82].

To better show this effect, in Fig. 1.10 we have plotted the 30-lowest energy levels for a 150-atom spin chain as a function of the magnetic exchange interaction ($J \cdot S$), for two distinct cases: In Figure 1.10 (a) the Rashba strength is $\alpha_R = 0.5$ while in Fig. 1.10 (b) it is zero. We have also plotted the topological invariant, $Q$ to indicate the topological phase of the system. Keeping the same color code as in Fig. 1.8 (a), the non-trivial phase ($Q = -1$) correspond to the purple area. As observed, the presence or absence of Rashba coupling does not affect the topological invariant.

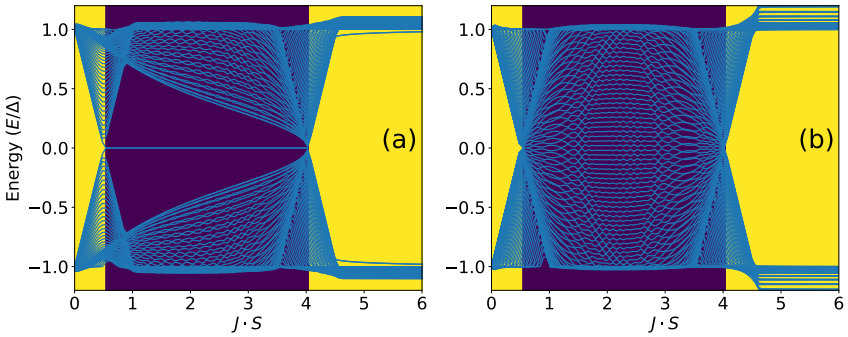


Figure 1.10: Calculated energy spectrum for a 150-atom spin chain on 300-site superconducting 1-D system. The topological phase is indicated with the purple areas ($Q = -1$) and the trivial correspond to the yellow ($Q = 1$). Parameters: $\Delta = 0.5$, $t = 1$, $\mu = 2$, $JS = 2$, (a) $\alpha_R = 0.5$ and (b) $\alpha_R = 0$

However, if we look at the energy levels, both situations are strikingly different. In Fig. 1.10 (a) we can observe a solution at zero energy once the system enters the topological phase. This zero energy state is protected from the rest of the states by a topological gap [8]. As $J \cdot S$ increases, the gap is reduced, until the system reaches a trivial phase again and the energy levels split to higher energies. For magnetic interaction values in the window, $0.5 \leqslant J \cdot S \leqslant 4.0$, there is a MBS arising in this system, topologically protected from the higher energy states. In Fig. 1.10 (b), however, when the system is in the topological phase, no zero-energy state can be found. Even if there are zero-energy crossings between the levels, a new energy gap does not open in the topological region, preventing MBS to emerge. This is due to the absence of Rashba coupling in the system. As recently reported, higher SOC can lead to a larger topological gap [83], as a result, MBS are better

protected from finite-energy states.

**Conclusions**. In this first chapter, we have reviewed how the search Majorana fermions have become a prominent topic in condensed matter physics. Experimental realizations of the Kitaev model focus around superconducting systems with spin-orbit and magnetic interactions. In this thesis, we focus on the study of spin chains in superconductors. In 1.3, using a tight-binding model, we show how MBS can arise in this type of system and compute the corresponding topological invariant. Using non-realistic parameters, we could observe the main physical characteristics that the topological edge states should exhibit in finite spin chains on superconductors. In the following, we will present a more realistic model, where we implement the BdG equations using a Green's functions approach.

# 2 Yu-Shiba-Rusinov states: Green's functions formalism.

**Superconductivity and magnetic impurities: YSR states.** When a metal in the superconducting state is subjected to an external magnetic field, the applied field is expelled from the material. This is known as the Meissner effect. However, for a sufficiently high field, superconductivity is suppressed. Similarly, magnetic impurities have a big effect on superconductors at the microscopic scale. As independently shown by Yu [3], Shiba [4] and Rusinov [5], the exchange interaction caused by a single magnetic moment leads to the appearance of local in-gap states, the Yu-Shiba-Rusinov (YSR) states. The emergence of these sates can be understood as a local weakening of the Cooper pairs' pairing, resulting in quasi-particle states appearing at energies $E < \Delta$. The study of YSR states is key in the study of topological states emerging in spin chains, as the hybridization of such states and consequential formation of the so-called YSR-bands can lead the system to enter the topological phase.

In the present chapter, we study YSR states by means of a theoretical approach that utilizes single-electron Green's functions. This method allows to easily obtain the local density of states (LDOS) of the modeled system. We study in-gap states in a 2-D finite superconductor, created by single impurities, dimers, and finally we simulate a ferromagnetic spin chain to observe the emergence of edge states. The model utilizes realistic parameters that can be compared with experiments. Studies of impurities in superconductors have shown that non-magnetic impurities have a minimal effect on the superconducting energy gap, only for a high density of impurities, the superconductor is better described in the dirty limit [84]. On the other hand, magnetic impurities have a strong effect, as they break the time-reversal symmetry, and locally suppress the superconducting order parameter. As such, the LDOS in the vicinity of the impurity is greatly affected. In the original YSR states theoretical description [3]–[5] the spin is assumed to be classical[1]. As such, the impurity's spin is fixed and cannot fluctuate, simplifying the theoretical treatment. The exchange field is a local magnetic field centered on the impurity that will attract electrons with opposite spins and repel electrons with their spin

[1] In the classical spin limit, the spin is assumed to be large ($S \to \infty$), but the total interaction should be finite, $J \to 0$, $JS$ =finite. Under these conditions, the spin does not experience internal transitions and only acts as a scattering center for external particles.

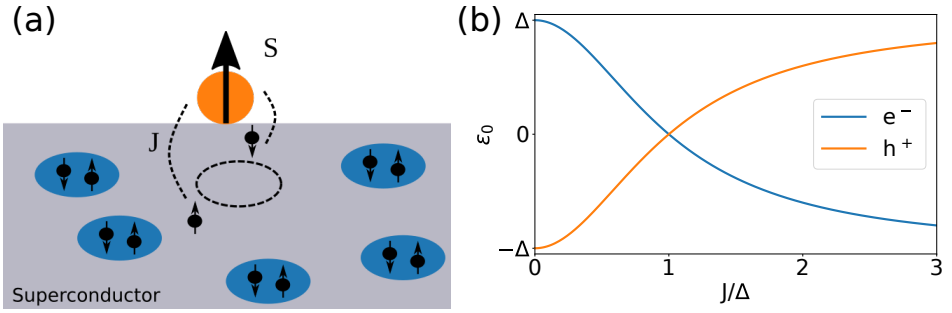


Figure 2.1: Emergence of YSR bound states on a superconductor. (a) Cooper pair braking due to the presence of a magnetic impurity. (b) Energy of the YSR bound states (Eq. 2.1) as a function of the exchange interaction, $J$.

aligned with the impurity's one (see Fig. 2.1 (a)), similar to the Meissner effect. The resulting exchange field is a consequence of the classical-spin approximation and is given by the exchange interaction of the Kondo Hamiltonian representing the impurity-substrate interaction times the impurity spin.

The solutions of the Hamiltonian for a purely magnetic impurity, with a classical spin oriented along the $z$ direction, yields a bound state of energy $\epsilon_0$ inside the superconducting gap ($\epsilon_0 < \Delta$):

$$\epsilon_0 = \Delta \frac{1-\alpha^2}{1+\alpha^2}, \qquad \alpha = \pi N_0 J S. \tag{2.1}$$

Where $J$ is the exchange interaction between the magnetic impurity and the electrons from the substrate, $S$ is the spin of the impurity and $N_0$ is the normal density of states of the superconductor. The previous equation shows the energy for a single YSR bound state. A second state will emerge with opposite sign. YSR states are usually referred to in plural. However, it is more correct to think about one single state with electron and hole components following the Bogoliubov description of superconducting quasiparticle states.

From a phenomenological point of view, the effect of the magnetic impurity can be understood as a polarization of the Cooper pairs in the superconductor. The exchange interaction reduces locally the pairing potential, "weakening" the Cooper pair and inducing a bound state at energy $|\epsilon_0| < \Delta$. The first experimental detection of YSR bound states were obtained in tunneling measurements using scanning tunneling microscopy, on Mn and Gd atoms deposited on Nb [7].

For very large exchange fields, the Cooper pair can break, and the impurity becomes efficiently screened by the electrons. This leads to a different ground state of the impurity + superconductor system. A change of many-body ground state

is usually described as a quantum phase transition (QPT) [85]. The YSR-states energy from Eq. 2.1 is plotted in Fig. 2.1 (b) as a function of the exchange interaction, $J$. As we can observe, as $J$ increases, the energy of the YSR lowers. At a critical $J_c$ value, the bound state crosses the Fermi level and electron and hole components change sign. At this crossing point, the ground state of the system is no longer the $\Phi_{BCS}$, but one with a YSR bound state. The crossing corresponds to the QPT of the system.

## 2.1 Green's functions

In the previous chapter, we studied the emergence of Majorana edge states in a superconductor using a simple tight-binding model. However, in order to obtain realistic results that use energy gaps and bandwidths that can be compared with experiments, we need to take a different approach.

Green's functions are widely used in physics, like in the investigation of many-body systems. They can be viewed as operators describing the propagation of a perturbation in the system. Green's functions are also interesting because they contain information about the system that can be directly compared with experiments, for instance, the density of states.

### 2.1.1 Spin chains on wide band superconductors

For our model, we aim to simulate a bulk superconductor with magnetic impurities on its surface. Beyond their superconducting transition, superconductors behave as normal metals. Usually, materials that become $s-$wave superconductors have a large electron band in their metallic state. The usual values show a superconducting gap thousands of times smaller than the metallic band. Additionally, an energy mismatch also exists between the typical exchange interaction values (in the eV range) and the superconducting order parameter (usually in the meV range). These different energy scales call for a different modelling approach from the tight-binding model presented in chapter 1, or the ones used, for example, to treat semiconducting nanowires with proximitized superconductivity [18], [86], where the energy scales are comparable.

The typical approach for modelling a wide-band superconductor is to use a free-electron approximation [9], [26]–[28], [87], [88] using Green's functions. The next step is to add the effect of the magnetic impurities. For this, one can stick to the Green's function approach and add the effect of the impurities by solving the Dyson equation [26]–[28] (equivalently the T matrix approach [87], [89]), or obtain the wave function by applying the Lippmann-Schwinger approach [9], [88].

In our model, we follow the theory developed by Flatté and Byers [26], [27] for a discrete grid. We use single-particle Green's functions to describe a BCS super-

conductor using the BdG equations. With the aid of the Dyson equation, we add the effect of local magnetic impurities to the system, as well as the effect of the Rashba spin-orbit coupling. These two interactions can be added to the system as a single-particle self-energy term.

### 2.1.2 Single particle Green's functions

We will start by discussing single-particle Green's functions for one-particle Hamiltonians, where the Green's function becomes the resolvent of the Hamiltonian. In this context, the features of the resolvent can be easily shown as we do in the following.

#### Propagator

The Green's function associated with the Schrödinger equation:

$$\big[i\hbar\frac{\partial}{\partial t} - \hat{H}\big]\psi(\vec{r},t) = 0 \tag{2.2}$$

is defined by the solution to:

$$(i\hbar\frac{\partial}{\partial t}\psi(\vec{r},t) - \hat{H})G(\vec{r},t,\tilde{\vec{r}},t') = \delta(\vec{r}-\tilde{\vec{r}})\delta(t-t') \tag{2.3}$$

Where $\hat{H}$ is a time-independent Hamiltonian. In this context, $G(\vec{r},t,\tilde{\vec{r}},t')$ is called a *propagator*. Taking into account the time evolution and assuming $t < t'$. The propagator is the operator that yields the system's wave function at $t'$ if the wave function is known at $t$:

$$\psi(\vec{r},t') = \exp\big[-i\hat{H}(t'-t)/\hbar\big]\psi(\vec{r},t) \tag{2.4}$$

Where we can define the propagator or Green's operator,

$$G^{+}(t'-t) = -i\theta(t'-t)e^{-i\hat{H}(t'-t)/\hbar} \tag{2.5}$$

here $\theta(\tau)$ is the step function. The + index, indicate that the previous expression correspond to the retarded Green's operator. The advanced operator ($G^{-}$) can be obtained similarly, but with $t' < t$.

In case the Hamiltonian is time-independent, the Green's function only depends on the time difference, $t'-t$, in this case it is convenient to Fourier transform into the frequency domain:

$$G^{+}(\omega) = \int_{-\infty}^{\infty} G(t'-t)e^{i\omega(t'-t)}dt' = -i\int_{t}^{\infty} e^{i(\omega-H/\hbar)/(t'-t)}dt' \tag{2.6}$$

Using time translational invariance, we can take $t = 0$. To make the integral converge, we let $\omega \to \omega + i\eta$ where $\eta = 0^{+}$ is a positive infinitesimal. After solving the integral, we find:

$$G^{+}(\omega) = \frac{1}{(\omega - H/\hbar + i\eta)} \tag{2.7}$$

$G^+(\omega)$ is known as the resolvent operator. The poles of the corresponding Green's function, coincide with the discrete eigenenergies of the Hamiltonian $H$, and vice-versa, as can be seen from Eq. 2.7. The density of states can be obtained from the imaginary part [90]:

$$N(\omega) = \mp\frac{1}{\pi} Tr\{Im\{G^{\pm}(\omega)\}\} \tag{2.8}$$

that is trivially shown by using the Cauchy equality $\frac{1}{\omega+i\eta} = \frac{p}{\omega} - i\pi\delta(\omega)$ where $p$ stands for the principal part of the implicit integration.

### Non-interacting electrons

We now want to look at the particular case of non-interacting electrons, at zero temperature, and calculate the corresponding $k$-space Green's function. In this case, the Hamiltonian is simply:

$$\hat{H} = \sum_{nk} \xi_{nk}\psi_{nk}(\vec{r}) \tag{2.9}$$

Where $k$ takes values in the first Brillouin zone and $n$ is the band index (this index could represent also, for example, the spin state of the excitation). We can express the $\psi(\vec{r})$ as field operators:

$$\psi^{\dagger}(\vec{r}) = \sum_{nk} \psi^{*}_{nk}(\vec{r}) c^{\dagger}_{nk}, \tag{2.10}$$

and so the Hamiltonian can be written:

$$\begin{aligned} \hat{H} &= \int d\vec{r}\psi^{\dagger}(\vec{r})\hat{H}\psi(\vec{r}) = \sum_{nk,mp} \langle\psi_{nk}|H|\psi_{mp}\rangle| \, c^{\dagger}_{nk}c_{mp} \\ &= \sum_{nk,mp} \xi_{nk}\delta_{nk,mp}c^{\dagger}_{nk}c_{mp} = \sum_{nk} \xi_{nk}c^{\dagger}_{nk}c_{nk} \end{aligned} \tag{2.11}$$

Using the time dependence of the $c$ operators: $c_{nk}(t) = c_{nk}e^{-i\xi_{nk}t}$ and $c^{\dagger}_{nk}(t) = c^{\dagger}_{nk}e^{i\xi_{nk}t}$. And the definition from Eq. 2.5 ($/\hbar = 1$ unless otherwise specified):

$$G^+(nk, t-t') = -i\theta(t-t')e^{-i\xi_{nk}(t-t')} \tag{2.12}$$

We perform Fourier transform to obtain the corresponding propagator of the free electron Hamiltonian:

$$\begin{aligned} G^+(nk,\omega) =& -i\int_{-\infty}^{\infty} dt\, \theta(t-t')e^{i\omega(t-t')}e^{-i\xi_{nk}(t-t')\eta(t-t')} \\ =& \frac{1}{\omega - \xi_{nk} + i\eta} \end{aligned} \tag{2.13}$$

Using Cauchy's expression: $\frac{1}{\omega+i\eta} = \frac{p}{\omega} - i\pi\delta(\omega)$ where $p$ stands for the principal part when this expression appears in the integration over the continuum states,

(we reintroduce $\hbar$ for clarity in the following expressions):

$$G(k,\omega) = \sum_n \left(\frac{p}{\omega - \xi_{nk}/\hbar} - i\pi\delta(\omega - \xi_{nk}/\hbar)\right) \tag{2.14}$$

We now want to find the function in real space. Using that $|nk\rangle$ is a complete basis $\mathbb{1} = \sum_{nk} |nk\rangle\langle nk|$:

$$\begin{aligned} G(\vec{r},\tilde{\vec{r}},\omega) = \langle\vec{r}|\, G(\omega)\, |\tilde{\vec{r}}\rangle &= \sum_{nk,mp} \langle\vec{r}|nk\rangle\langle nk|\, G(\omega)\, |mp\rangle\langle mp|\tilde{\vec{r}}\rangle \\ &= \sum_{nk} \psi_{nk}(\vec{r}) G(k,\omega) \psi^*_{nk}(\tilde{\vec{r}}) \end{aligned} \tag{2.15}$$

Replacing $G(k,\omega)$ by Eq. 2.14, we arrive at the final expression:

$$G(\vec{r},\tilde{\vec{r}},\omega) = \sum_{nk} \left( p\frac{\psi_{nk}(\vec{r})\psi^*_{nk}(\tilde{\vec{r}})}{\omega - \xi_{nk}/\hbar} - i\pi\psi_{nk}(\vec{r})\psi^*_{nk}(\tilde{\vec{r}})\delta(\omega - \xi_{nk}/\hbar) \right). \tag{2.16}$$

### Density of states

Let us define the local density of states, $\rho(\vec{r}_0,\omega)$:

$$\rho(\vec{r}_0,\omega) = \sum_{nk} |\psi_{nk}(\vec{r_0})|^2 \delta(\omega - \xi_{nk}/\hbar). \tag{2.17}$$

If we look at the expression, we found for $G(\vec{r},\vec{r}',\omega)$ in Eq. 2.16, we can write the LDOS as:

$$\rho(\vec{r}_0,\omega) = -\frac{1}{\pi} Im(G(\vec{r}_0,\vec{r}_0,\omega)). \tag{2.18}$$

The density of states, $N(\omega)$, can be calculated by integrating the previous expression over $\vec{r}$:

$$\begin{aligned} N(\omega) = \int d\vec{r}\rho(\vec{r},\omega) &= -\frac{1}{\pi}\int d\vec{r}\, Im(G(\vec{r},\vec{r},\omega)) \\ &= -\frac{1}{\pi} Im \sum_k G(k,\omega) = \sum_{nk} \delta(\omega - \xi_{nk}/\hbar). \end{aligned} \tag{2.19}$$

In this section, we have reviewed how to obtain the retarded Green's function for free electrons, as defined in Eq. 2.5. We have also seen how we can easily obtain the density of states from the imaginary part of the real-space Green's function (Eq. 2.18 and 2.19). In the following, we will obtain the retarded Green's function of a BCS superconductor, described by the mean-field Hamiltonian, presented in chapter 1.

### 2.1.3 Green's function for a BCS superconductor

Using the Green's function results from the previous section, we want to calculate the corresponding Green's function for a BCS superconductor. This will allow us to compute the corresponding local density of states. As we discussed in 1.2, the mean-field BCS Hamiltonian, can be expressed in the 4-component Nambu spinor basis [49], [91]:

$$\psi_k = \begin{pmatrix} c_{k\uparrow} \\ c_{k\downarrow} \\ c^\dagger_{-k\uparrow} \\ c^\dagger_{-k\downarrow} \end{pmatrix} \tag{2.20}$$

Using Pauli matrices, $\tau$ and $\sigma$, the BCS Hamiltonian in this basis, can be expressed under the following form [91]:

$$H_{BCS} = \xi_k \tau_z \sigma_0 + \Delta \tau_y \sigma_y \tag{2.21}$$

Where $\tau_{0,x,y,z}$ act in the particle-hole space and $\sigma_{0,x,y,z}$ act in the spin space. Assuming that $\Delta$ is real and homogeneous in the superconductor, $\Delta_{ij} = \Delta\delta_{i,j} = \Delta$ such that we recover the s-wave superconductor condition $\Delta_k = \sum_j \Delta_{0,j} e^{ik\cdot(r_0 - r_j)} = \Delta$. Thanks to the one-particle character of the BCS Hamiltonian, we can simply apply the propagator equation 2.7 to obtain the Green's function of the superconductor:

$$G_{BCS}(k,\omega) = \frac{1}{\omega^2 - \xi_k^2 - \Delta^2} \begin{pmatrix} \omega + \xi_k & 0 & 0 & -\Delta \\ 0 & \omega + \xi_k & \Delta & 0 \\ 0 & \Delta & \omega - \xi_k & 0 \\ -\Delta & 0 & 0 & \omega - \xi_k \end{pmatrix} \tag{2.22}$$

The goal is to obtain the Green's function in real space, $\hat{G}_{BCS}(\vec{r}, \tilde{\vec{r}}, \omega)$. As shown in 2.1.2, we can change the basis by evaluating the following expression:

$$\begin{aligned} &\sum_{k,k'} \langle \vec{r}|k\rangle \langle k| \, G_{BCS}(k,\omega) \, |k'\rangle \langle k'|\tilde{\vec{r}}\rangle \\ &= \sum_{k,k'} \psi_k(\vec{r}) G_{BCS_{kk'}}(k,\omega) \psi^\dagger_{k'}(\tilde{\vec{r}}) \\ &= \frac{1}{(2\pi)^3} \int e^{ikr} G_{BCS}(k,\omega) dk \end{aligned} \tag{2.23}$$

To solve Eq. 2.22 we need to evaluate two different integrals:

$$I_1 = \frac{1}{(2\pi)^3} \int \frac{e^{ikr}\Delta}{\omega^2 - \xi_k^2 - \Delta^2} dk \tag{2.24}$$

$$I_2 = \frac{1}{(2\pi)^3} \int \frac{e^{ikr}(\omega + \xi_k)}{\omega^2 - \xi_k^2 - \Delta^2} dk \tag{2.25}$$

Where $r = |\vec{r} - \tilde{\vec{r}}|$ is the distance between sites. It can be shown that [9], [91] (details are provided in Appendix B):

$$I_1 = -\frac{\pi N_0 \Delta}{k_F r\sqrt{\Delta^2 - \omega^2}} \sin k_F r \times e^{-\sqrt{\Delta^2-\omega^2}\frac{r}{\pi\xi\Delta}} \tag{2.26}$$

$$I_2 = -\frac{\pi N_0}{k_F r}(\cos k_F r + \frac{\omega}{\sqrt{\Delta^2 - \omega^2}} \sin k_F r) \times e^{-\sqrt{\Delta^2-\omega^2}\frac{r}{\pi\xi\Delta}} \tag{2.27}$$

Finally, the resulting matrix writes:

$$G_{BCS}(\vec{r}, \vec{r'}, \omega) = -\frac{\pi N_0}{k_F r} e^{\frac{-\sqrt{\Delta^2-\omega^2}r}{\pi\xi\Delta}} \times \tag{2.28}$$

$$\begin{pmatrix} \cos k_F r + \frac{\omega}{\sqrt{\Delta^2-\omega^2}} \sin k_F r & 0 & 0 & \frac{-\Delta}{\sqrt{\Delta^2-\omega^2}} \sin k_F r \\ 0 & \cos k_F r + \frac{\omega}{\sqrt{\Delta^2-\omega^2}} \sin k_F r & \frac{\Delta}{\sqrt{\Delta^2-\omega^2}} \sin k_F r & 0 \\ 0 & \frac{\Delta}{\sqrt{\Delta^2-\omega^2}} \sin k_F r & -\cos k_F r + \frac{\omega}{\sqrt{\Delta^2-\omega^2}} \sin k_F r & 0 \\ \frac{-\Delta}{\sqrt{\Delta^2-\omega^2}} \sin k_F r & 0 & 0 & -\cos k_F r + \frac{\omega}{\sqrt{\Delta^2-\omega^2}} \sin k_F r \end{pmatrix}$$

Where $N_0$ is the normal electronic density, $k_F$ is the Fermi wave vector, and $\xi = \frac{k_F}{\pi\Delta m_{eff}}$. The energy variable, $\omega = \omega' + i\Gamma$, where $\Gamma$ is the Dynes parameter [65]. The imaginary part of $\hat{G}_{BCS}(\vec{r}, \vec{r}, \omega)$ gives the one particle density of states at the coordinate $\vec{r}$. As it can be noted, the Green's function has an oscillatory behavior with $k_F r$.

We solve Eq. 2.28 on a finite array of sites modeling the superconductor. In Fig. 2.2 (a) we show an example of a 2-D array with dimensions $N_x = N_y = 5$, each $G_{BCS}(r_i, r_j, \omega)$ is modeled by the $4 \times 4$ Green's function in Eq. 2.28. For a 2-D case, the full matrix has a size of $4N_xN_y \times 4N_xN_y$. For the case of a homogeneous superconductor, the distance between sites, $r$, is fixed by the lattice parameter, $a$, such that $r = |r_i - r_j| \times a$.

The density of states can be directly obtained by looking at the imaginary part of Eq. 2.28, as discussed in 1.2.4, the four-component BdG equations are redundant, so it is enough to look at only two of their components to obtain the DOS. In our model, we are projecting the DOS into the sites of the finite array, in this way, we refer to this quantity as projected density of states (PDOS). This expression writes:

$$\rho(\vec{r}_i, \omega) = -\frac{1}{\pi} Im[G_{1,1}(\vec{r}_i, \vec{r}_i, \omega) + G_{4,4}(\vec{r}_i, \vec{r}_i, -\omega)]. \tag{2.29}$$

As shown by the Abrikosov-Gorkov equations (see 2.1.4), after the corresponding analytical continuation to real times (frequencies), each of the components from Eq. 2.29 gives us the PDOS for spin up ($G_{11}$) and down ($G_{44}$) components. Figure 2.2 (b) depicts the resulting PDOS obtained on a finite 2-D array with

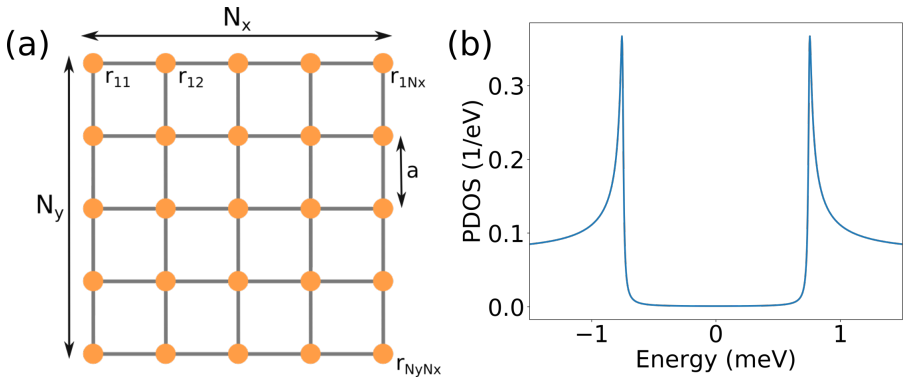


Figure 2.2: (a) 2-D square lattice modeling a superconductor, the size is $N_x \times N_y$. The distance between sites is the lattice parameter, $a$. (b) PDOS as obtained from Eq. 2.29 for a superconducting 2-D lattice. Parameters: $\Delta = 0.75$ meV, $k_F = 0.183\ a_0^{-1}$, $a = 3.36$ Å and $\Gamma = 0.01$ meV. Modeling the superconductor $Bi_2Pd$.

dimension $N_x = N_y = 8$, with parameters: $\Delta = 0.75$ meV, $k_F = 0.183\ a_0^{-1}$. The parameters used here are found to correctly described the superconductor $Bi_2Pd$ [28]. The Dynes parameter is set to be: $\Gamma = 0.01$ meV to reproduce the experimental data. As observed, the PDOS shows the characteristic coherence peaks at energy $\pm 0.75$ meV.

### 2.1.4 Abrikosov-Gorkov equations

As expressed in Eq. 2.18, the local density of states is obtained from the imaginary part of the resulting Green's function. Expressing the Green's function in the imaginary-time space with the Abrikosov equations shows how we obtained the correct density of states after the corresponding analytical continuation.

The Nambu operators in the imaginary time space:

$$\hat{\Psi}_i(\tau) = \begin{pmatrix} \hat{c}_{i\uparrow}(\tau) \\ \hat{c}_{i\downarrow}(\tau) \\ \hat{c}^{\dagger}_{i\uparrow}(\tau) \\ \hat{c}^{\dagger}_{i\downarrow}(\tau) \end{pmatrix}, \qquad \hat{\Psi}^{\dagger}_i(\tau) = \begin{pmatrix} \hat{c}^{\dagger}_{i\uparrow}(\tau) & \hat{c}^{\dagger}_{i\downarrow}(\tau) & \hat{c}_{i\uparrow}(\tau) & \hat{c}_{i\downarrow}(\tau) \end{pmatrix} \tag{2.30}$$

The Heisenberg operators are defined:

$$\hat{c}^{(\dagger)}_{i\sigma}(\tau) = e^{\tau \mathcal{H}/\hbar} \hat{c}^{(\dagger)}_{i\sigma} e^{-\tau \mathcal{H}/\hbar}. \tag{2.31}$$

Where $\tau$ is the imaginary time ($\tau = it$) and $\mathcal{H}$ is the Hamiltonian of our model. With this the Green's function is defined as

$$\mathcal{G}(i, \tau; j, \tau') = - < T_\tau \hat{\Psi}_i(\tau) \otimes \hat{\Psi}_j(\tau') > \tag{2.32}$$

Where $T_\tau$ is the time-ordering operator, more explicitly the previous equation becomes

$$\mathcal{G}(i,\tau;j,\tau') = -\theta(\tau-\tau') < \hat{\Psi}_i(\tau)\otimes\hat{\Psi}_j^\dagger(\tau') > +\theta(\tau'-\tau) < \hat{\Psi}_j^\dagger(\tau')\otimes\hat{\Psi}_i(\tau) > \quad (2.33)$$

Where $< ... >= \sum_n \frac{e^{-\beta E_n}}{Z} \langle n| ... |n\rangle$ is, the thermal average over all states $|n\rangle$ and $Z$ is the canonical partition function ($Z = \sum_n e^{-\beta E_n}$). With this, we can explicitly calculate some of the components.

$$\mathcal{G}_{11}(i,\tau;j,\tau') = -\theta(\tau-\tau') \underbrace{< \hat{c}_{i\uparrow}(\tau)\hat{c}_{j\uparrow}^\dagger(\tau') >}_{I_1} + \theta(\tau'-\tau) \underbrace{< \hat{c}_{j\uparrow}^\dagger(\tau')\hat{c}_{i\uparrow}(\tau) >}_{I_2} \quad (2.34)$$

It can be shown that (see Appendix B for details):

$$\begin{aligned} I_1 &= \sum_s (e^{-E_s(\tau-\tau')/\hbar} u_{i\uparrow}^s u_{j\uparrow}^{s*} f(-E_s) + e^{E_s(\tau-\tau')/\hbar} v_{i\uparrow}^{s*} v_{j\uparrow}^s f(E_s)) \\ I_2 &= \sum_s (e^{E_s(\tau'-\tau)/\hbar} u_{j\uparrow}^{s*} u_{i\uparrow}^s f(E_s) + e^{-E_s(\tau'-\tau)/\hbar} v_{j\uparrow}^s v_{i\uparrow}^{s*} f(-E_s)) \end{aligned} \quad (2.35)$$

So that,

$$\begin{aligned} \mathcal{G}_{11}(i,\tau;j,\tau') = &-\theta(\tau-\tau') \sum_s (e^{-E_s(\tau-\tau')/\hbar} u_{i\uparrow}^s u_{j\uparrow}^{s*} f(-E_s) + e^{E_s(\tau-\tau')/\hbar} v_{i\uparrow}^{s*} v_{j\uparrow}^s f(E_s)) \\ &+\theta(\tau'-\tau) \sum_s (e^{E_s(\tau'-\tau)/\hbar} u_{j\uparrow}^{s*} u_{i\uparrow}^s f(E_s) + e^{-E_s(\tau'-\tau)/\hbar} v_{j\uparrow}^s v_{i\uparrow}^{s*} f(-E_s)) \end{aligned} \quad (2.36)$$

We now go back to the frequency domain:

$$\mathcal{G}_{11}(i,j,i\omega_n) = \int_0^{\beta\hbar} d\tau e^{i\omega_n\tau} \mathcal{G}_{11}(i,j,\tau) \quad (2.37)$$

$$\begin{aligned} &= -\sum_n \left[ u_{i\uparrow}^n u_{j\uparrow}^{n*} f(-E_n) \int_0^{\beta\hbar} d\tau e^{(i\omega_n - E_n/\hbar)\tau} + v_{i\uparrow}^{n*} v_{j\uparrow}^n f(E_n) \int_0^{\beta\hbar} d\tau e^{(i\omega_n + E_n/\hbar)\tau} \right] \\ &= -\sum_n \left[ \frac{u_{i\uparrow}^n u_{j\uparrow}^{n*}}{i\omega_n - E_n/\hbar} f(-E_n)\big(e^{\beta\hbar(i\omega_n - E_n/\hbar)} - 1\big) \right. \\ &\quad \left. + \frac{v_{i\uparrow}^{n*} v_{j\uparrow}^n}{i\omega_n + E_n/\hbar} f(E_n)\big(e^{\beta\hbar(i\omega_n + E_n/\hbar)} - 1\big) \right] \\ &= \sum_n \left[ \frac{u_{i\uparrow}^n u_{j\uparrow}^{n*}}{i\omega_n - E_n/\hbar} + \frac{v_{i\uparrow}^{n*} v_{j\uparrow}^n}{i\omega_n + E_n/\hbar} \right] \end{aligned} \quad (2.38)$$

Similarly, we can be show that $\mathcal{G}_{44}(i,j,i\omega_n)$, in the frequency domain:

$$\mathcal{G}_{44}(i,j,i\omega_n) = \sum_n \left[ \frac{u_{i\downarrow}^{n*} u_{j\downarrow}^n}{i\omega_n + E_n/\hbar} + \frac{v_{i\downarrow}^n v_{j\downarrow}^{n*}}{i\omega_n - E_n/\hbar} \right] \quad (2.39)$$

And the local density of states can be calculated using the analytical continuation, as:

$$\rho_{i\uparrow}(E) = -\frac{1}{\hbar\pi}\{\mathcal{G}_{11}(i,i,i\omega_n \to E/\hbar + i0^+)\} \tag{2.40}$$

$$\rho_{i\downarrow}(E) = -\frac{1}{\hbar\pi}\{\mathcal{G}_{44}(i,i,-i\omega_n \to -(E/\hbar + i0^+))\} \tag{2.41}$$

In this way, the total local density of states is obtained $\rho_i(E) = \rho_{i\uparrow}(E) + \rho_{i\downarrow}(E)$, which coincides with the expression written in Eq. 2.29.

## 2.2 Magnetic impurities on a BCS superconductor

As discussed above, the presence of magnetic impurities in a superconductor results in the formation of YSR states. When several impurities assemble, their in-gap states can overlap forming in-gap bands, also called YSR-bands [9], [24], [92], [93]. When the impurity chain forms and helical spin ordering, it has been shown that the bands can enter a topological superconductivity phase and, as a result, MBS can emerge at the edges of the chain [8], [9], [94]. The presence of spin-orbit coupling can induce this helical spin ordering in ferromagnetic chains [87], [95], [96].

Here, we study the emergence of YSR-states by means of the Green's function formalism. We add the effect of the magnetic impurities and the Rashba interaction as self-energies in the Dyson equation. We first study the simple case of single impurities and two impurities in proximity.

### 2.2.1 Perturbations with Green's functions

To obtain the BCS Green's functions, we can simply apply the equations for free electrons, as describe in 2.1. However, to add the effect of the magnetic impurities and the Rashba coupling, we need to add a perturbation to the system. As we will see in the following, by describing these perturbations as mean-field Hamiltonians, the Dyson equation allows us to obtain the total Green's function of the system.

#### Dyson equation

Our goal is to find the corresponding Green's function of a Hamiltonian $H = H_0 + H_1$, where $H_0$ is unperturbed (in our case $H_0 = H_{BCS}$) and $H_1$ is the perturbation to the system (in our case the magnetic impurities and the Rashba interaction that are treated as one-particle potentials). To obtain the corresponding Green's function of the total Hamiltonian, we want to express it in terms of $G_0$ and $H_1$. For this, we start by writing the Green's functions:

$$\begin{aligned} G_0(\omega) =& (\omega - H_0)^{-1} \\ G(\omega) =& (\omega - H)^{-1} \end{aligned} \tag{2.42}$$

The total Green's operator, then:

$$\begin{aligned} G(\omega) &= \big(\omega - H_0 - H_1\big)^{-1} = \big[(z - H_0)\big(1 - (z - H_0)^{-1}H_1\big)\big] \\ &= \big[1 - (\omega - H_0)^{-1}H_1\big]^{-1}(\omega - H_0)^{-1} \\ &= \big(1 - G_0(\omega)H_1\big)^{-1}G_0(\omega) \end{aligned} \tag{2.43}$$

Expanding $(1 - G_0H_1)^{-1}$, we write:

$$G = G_0 + G_0H_1G_0 + G_0H_1G_0H_1G_0 + ... \tag{2.44}$$

In a more compact form, we find:

$$G = G_0 + G_0H_1G \tag{2.45}$$

The previous expression is the so-called *Dyson equation* [90], [97]. By applying basic algebra it can be shown that:

$$G = \big[G_0^{-1} - H_1\big]^{-1} \tag{2.46}$$

In this context, $H_1$ is referred to as the *self-energy*, and it models the effect of interactions on the unperturbed Green's operator. In the following, we will see how we can apply the Dyson equation to add magnetic impurities to the superconductor.

### 2.2.2 Adding magnetic impurities

The first term we add to the self energy, is the one describing the magnetic impurities. As discussed, the BCS superconductor is modelled as a finite array, and the impurities will be located in selected sites of the array, being able to create different structures.

#### Kondo Hamiltonian

Similar to the magnetic term in 1.3.1, the magnetic impurities are described using the Kondo model, the Hamiltonian in this case is [9]:

$$\hat{H}_{impurity} = \sum_{j}^{N}(J_j\vec{S_j}\cdot\vec{\alpha} - K_j\tau_z\sigma_0) \tag{2.47}$$

Where $J$ is the magnetic strength coupling of the impurity and $\vec{S}_j$ is its spin. For $J > 0$ values, the exchange field will attract electrons with opposite spin, and repel electrons with parallel spin, this is the antiferromagnetic interaction. For $J < 0$, the interaction is ferromagnetic, attracting electrons with the same spin. $\vec{\alpha}$ is the electron-spin as expressed in the Nambu basis: $\vec{\alpha} = \frac{1+\tau_z}{2}\vec{\sigma} + \frac{1-\tau_z}{2}\sigma_y\vec{\sigma}\sigma_y$ where $\vec{\sigma}$ is the spin operator [98]. $\vec{S}_j$ is assumed to be classical and, in principle, can be oriented in any direction of the 3-D space, $\vec{S_j} = (S_{j,x}, S_{j,y}, S_{j,z})$

$= S(\sin\theta_j \cos\phi_j, \sin\theta_j \sin\phi_j, \cos\theta_j)$, although recent studies have reported effects of quantum spins in superconductors [99]–[101]. $K$ accounts for the non-magnetic potential scattering due to the Coulomb interaction.

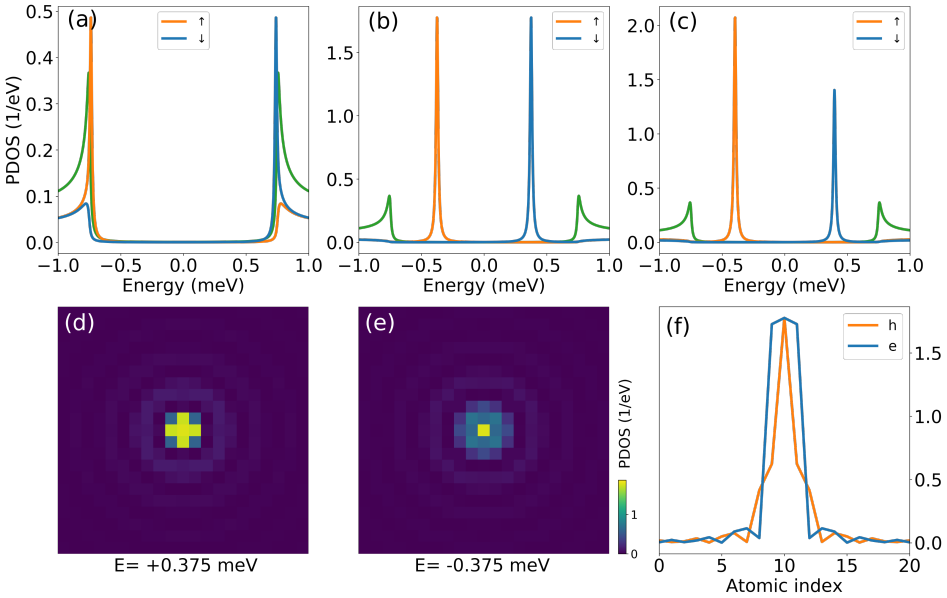


Figure 2.3: (a)-(c) Spin-resolved PDOS calculated on a single magnetic impurity located at the center of a 21 × 21 superconducting lattice. (a) $J = 0.3$ meV, $K = 0.0$, (b) $J = 2.0$ meV, $K = 0.0$, (c) $J = 2.0$ eV, $K = 2.0$ eV. (d), (e) 2-D maps of the spatial distribution of the electron and hole components, respectively, of the spectra shown in (b). (f) Electron/hole PDOS along the middle row of the 2-D-array shown in (d) and (e). Superconductor parameters same as in Fig. 2.2.

We numerically solve the Dyson equation (Eq. 2.46), by setting $G_0 = G_{BCS}$ and $H_1 = H_{impurity}$, modelling a single impurity located at the center of a superconducting 2-D array. The impurity spin is chosen to be $S = 5/2$ corresponding, for example, to a Chromium atom. The magnetic moment is set to be aligned along the $\vec{z}$ axis, perpendicular to the surface. We evaluate the spectral function or PDOS as written in Eq. 2.29. Figure 2.3 (a)-(c) shows the resulting spectra, $\rho_\uparrow$ (in blue) and $\rho_\downarrow$ (in orange), the total spectrum is the sum of both components. In Fig. 2.3 (a) the magnetic coupling is $J = 0.3$ eV and no scattering potential ($K = 0$). For comparison, we have depicted (in green) the spectra obtained on a clean superconductor with the same size. By comparing the two spectra, the presence of in-gap states can be only noted by a narrowing of the superconducting gap in the orange + blue curve. These states become more apparent as we increase

the exchange coupling.

Figure 2.3 (b) shows the calculated PDOS with $J = 2.0$ eV, as we can see, two peaks corresponding to a YSR state are present inside the energy gap. The coherence peaks have vanished from the spectra. The two YSR peaks emerge at a symmetric energy of $\pm 0.375$ meV, and they have equal electron and hole components. We can also see that the YSR states are fully spin polarized [102], [103]. The electron (hole) component, visible at positive (negative) energy, is spin-down(up) polarized. As expected from AFM coupling, the magnetic impurity attracts electrons with opposite spin polarization. To break the spectral symmetry, we add a potential scattering term to the system. Figure 2.3 (c) shows the obtained PDOS with the same parameters as Fig. 2.3 (b), but with $K = 2.0$ eV. As we can appreciate, the YSR peaks have shifted to a slightly different energy ($\pm 0.396$ meV) but, most notably, the spectra now show an asymmetry between electron and hole components. The scattering Coulomb term, repels the electrons, reducing its spectral height.

The 2-D maps, shown in Fig. 2.3 (d) and (e), represent the spatial distribution of the electron an hole components, as calculated in (b). As we can see, the YSR states extend in space far from the impurity. As we can observe, the electron and hole spatial distributions do not match, even in the absence of a potential scattering term. They both show their maximum height at the location of the magnetic atom, but they decay with some phase shift [102]. Figure 2.3 (f) gives more insight into the electron/hole spatial distribution, this figure shows a cut of the PDOS along the $x$ direction of the 2-D array. We observe the maximum of both electron and hole at the center of the array (where is impurity is located), and the spatial miss-match between the two can be better observed.

### Quantum phase transition

As first pointed out by Sakurai [104], a large magnetic exchange interaction leads to a level crossing between two ground states [98]. In this transition, the spin quantum number of the ground state changes from zero to $\pm 1/2$, and the parity of the ground state changes. This transformation receives the name of *quantum phase transition* (QPT) [85], [98], [105]. In an $s-$wave superconductor, this results in a local breaking of Cooper pairs. As a consequence, beyond some critical coupling $J > J_c$, the impurity spin becomes partially screened. This transition occurs, when the in-gap states cross at zero energy, and the electron and hole components interchange.

For a single impurity, using the same parameters as Fig. 2.4, we study the evolution of the YSR states as we vary the exchange coupling, $J$. Figure 2.4 (a)-(c) show the results for an impurity without potential scattering ($K = 0.0$). In Fig. 2.4 (a) we depict the magnetic coupling versus the YSR-state energy. We can observe

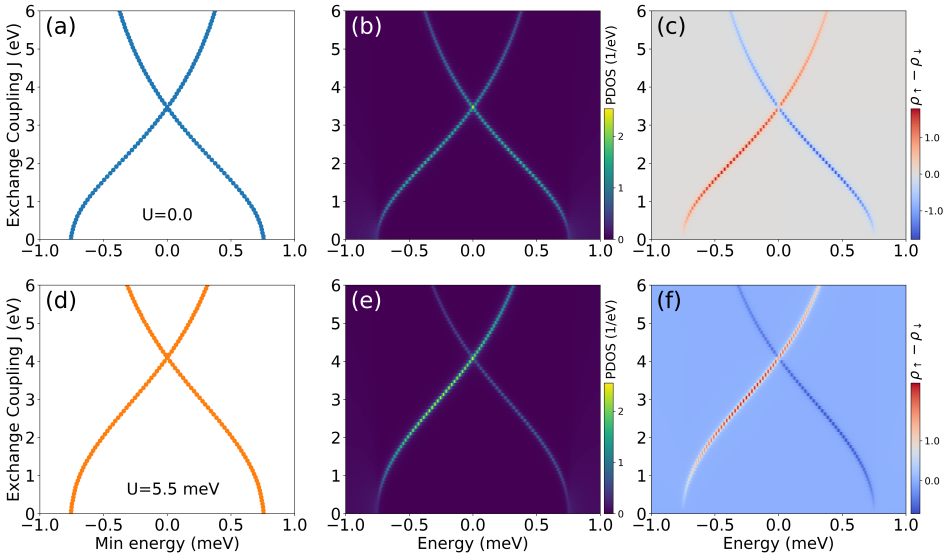


Figure 2.4: Quantum phase transition for a single magnetic impurity. (a)-(c) $K = 0.0$ meV. (d)-(f) $K = 5.5$ meV. (a),(d) Exchange energy, $J$ versus energy peak position. (b),(e) PDOS 2-D map as a function of $J$ vs energy. (c),(f) Spin $z$ component 2-D map. Parameters: Same Fig. 2.3 (b) and (c), only varying $J$.

a crossing of the two peaks at $J = 3.48$ eV, coinciding with the value extracted from Eq. 2.1, by setting $\alpha = 1$. The calculated behavior of the in-gap states coincides with the one shown in Fig. 2.1. To obtain more information about the quantum phase transition, Fig. 2.4 (b) and (c) show 2-D maps of the PDOS and the $\rho_z = \rho_\uparrow - \rho_\downarrow$ spin polarization of the states, respectively. The PDOS is particle/hole symmetric, since there is no potential scattering in this calculation. We obtain more information when we look at the spin component. We can observe that the spin polarization inverts at the transition. Indeed, at the QPT, the spin polarization is expected to flip [106], [107].

Figure 2.4 (d)-(f) shows analogous results to the upper row, but with potential scattering $K = 5.5$ eV. As we can observe, the $J_c$ has shifted to higher values, observing the QPT at $J \sim 4.0$ eV. In Fig. 2.4 (e) we can again note the electron/hole asymmetry due to the presence of $K$, the spin components switch again at the QPT.

### 2.2.3 Adding Rashba spin-orbit coupling

When electrons move in an electric field, they experience a magnetic field in their rest-frame. This field induces a momentum-dependent Zeeman energy called spin-

orbit coupling (SOC). The Hamiltonian describing this interaction:

$$\hat{H}_{SOC} \sim \mu_B(\vec{E} \times \vec{p}) \cdot \vec{\sigma} \tag{2.48}$$

Where $\mu_B$ is the Bohr magneton and $\vec{p}$ is the electron's momentum. Rashba SOC arises as a consequence of inversion symmetry to be broken (for example on surfaces). This symmetry breaking can be added as an electric field, $\vec{E} = E_z\vec{z}$, that breaks the symmetry in the $\vec{z}$ axis. With this condition, the SOC Rashba interaction takes the form [77], [108]:

$$\hat{H}_{Rashba} = \frac{\alpha_R}{\hbar}(\vec{z} \times \vec{p}) \cdot \vec{\sigma} \tag{2.49}$$

As such, when electrons flow along the $\vec{x}$ axis with a well-defined $\vec{p}$, they experience an effective magnetic field along $\vec{y}$, the Rashba field [78]. $\alpha_R$ is the Rashba parameter, it measures the strength of the Rashba SOC. The highest $\alpha_R$ values have been measured on Bi compounds: for Bi/Ag alloys an $\alpha_R \approx 3.0$ eV-Å has been experimentally measured [109], on BiTeI $\alpha_R = 3.8$ eV-Å was obtained [110].

We want to add this Rashba interaction to our discrete lattice model (see Appendix C for details). Rewriting Eq. 2.49 more explicitly:

$$\hat{H}_{Rashba} = \frac{\alpha_R}{\hbar}(p_y\sigma_x - p_x\sigma_y) \tag{2.50}$$

The momentum operator is related to the differential operator:

$$\hat{p}_x = -i\hbar\frac{\partial}{\partial x} \qquad \hat{p}_y = -i\hbar\frac{\partial}{\partial y} \tag{2.51}$$

Using finite differences and the following discretization of the 2-D space as $|i,j\rangle = |x = ia, y = ja\rangle$ states where $a$ is the lattice parameter, the momentum operators become [111]:

$$\hat{p}_x = -i\hbar\frac{|i+1,j\rangle\langle i,j|}{2a} \qquad \hat{p}_y = -i\hbar\frac{|i,j+1\rangle\langle i,j|}{2a} \tag{2.52}$$

So the Rashba Hamiltonian can be written:

$$\hat{H}_{Rashba} = \frac{\alpha_R}{2a}\sum_{i,j}\Big[\big(|i+1,j\rangle\langle i,j| \times i\sigma_y\big) - \big(|i,j+1\rangle\langle i,j| \times i\sigma_x\big)\Big] + h.c. \tag{2.53}$$

Where the state $|i,j\rangle$ indicates the site $i$ in the $x$ direction and the site $j$ in the $y$ direction. $a$ is the lattice parameter of the material. The previous Hamiltonian couples states at nearest neighbors sites and with different spin. As such, the Rashba SOC can be understood as a hopping term that includes a spin flip in the electron. Equation 2.53 can be written more explicitly, in terms of the creation and annihilation operators:

$$\hat{H}_{Rashba} = \frac{i\alpha_R}{2a}\sum_{i,j,\sigma,\sigma'}(c^{\dagger}_{i+1,j\sigma}\sigma_y c_{i,j,\sigma'} - c_{i,j+1,\sigma}\sigma_x c_{i,j,\sigma'} + h.c.) \tag{2.54}$$

Finally, to obtain the total Green's function of the system, we solve Dyson's equation (Eq. 2.46) by taking the impurity and the Rashba term together in the self-energy term:

$$\hat{H}_{Self} = \hat{H}_{impurity} + \hat{H}_{Rashba} \tag{2.55}$$

The $\hat{H}_{impurity}$ term is a local term, only found at the lattice sites where the magnetic impurities are located. The $\hat{H}_{Rashba}$ term, on the other hand, is present everywhere in the superconducting lattice. The effect of the Rashba term for a single impurity is rather small, to better observe its effect we instead look at the case of a pair of magnetic impurities (or dimers).

### 2.2.4 Magnetic dimers

We now take a look at the case of two magnetic impurities located next to each other in the center of the superconducting array. For this structure, it is also interesting to consider the relative spin arrangement existing between the two impurities within our classical-spin model. We investigate two cases: a ferromagnetically ordered dimer (both spins are parallel to each other) and anti-ferromagnetic pair (the spins are antiparallel, oriented in opposite directions).

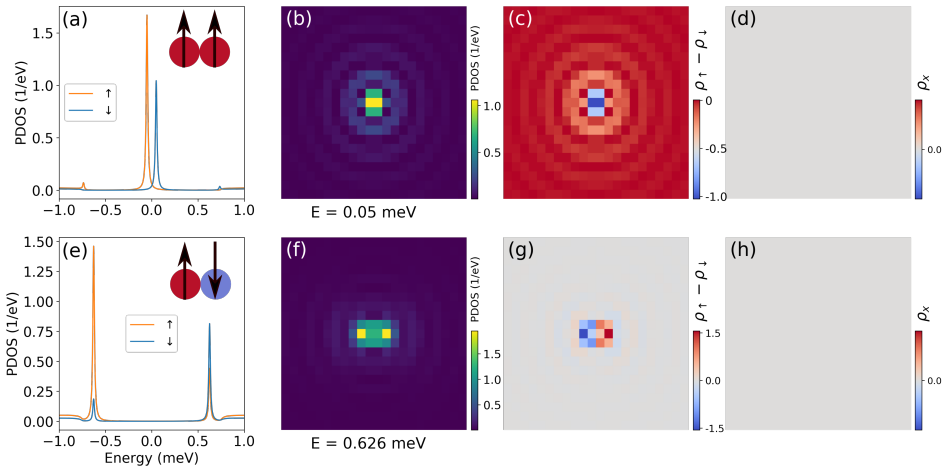


Figure 2.5: Impurity dimer with no Rashba SOC. (a)-(d) FM dimer and (e)-(h) AFM dimer. (a),(e) PDOS obtained on the first atom. The blue (orange) curve is the $\rho_\downarrow$ ($\rho_\uparrow$) component. (b),(f) PDOS spatial distribution of the electron component at the indicated energy. (c),(g) Density of spin along $z$. (d),(h) Density of the transversal spin component, $\rho_x$. Parameters: $\Delta = 0.75$ meV, $k_F = 0.183$ $a_0^{-1}$, $a = 3.36$ Å, $\Gamma = 0.01$ meV, $J = 1.8$ eV, $K = 2.0$ eV and $\alpha_R = 0.0$. All shown densities are in units of 1/eV.

Figure 2.5 shows the result for the FM dimer (upper row) and AFM ordering (lower row). Figures 2.5 (a), (e) depict the PDOS obtained on the first atom of the pair, in blue (orange) we show the $\rho_{i\downarrow}$ ($\rho_{i\uparrow}$) component, the total PDOS is simply the sum of the two. In the FM case, we can observe four peaks: one pair at $\pm 0.15$ meV and, with a much reduced height, at second pair at $\pm 0.74$ meV. In contrast, in Fig. 2.5 (e) we observe only two peaks. This difference is due to the YSR hybridization expected for FM atomic dimers. Indeed, the states split into the symmetric and anti-symmetric combination of the one impurity YSR states [28], [29]. However, for the AFM ordered dimer, the expected behavior is single-atom like. Since the quasi-particles attracted by the two impurities have opposite spin, the hybridization in this case is weaker and only a small energy shift can be observed when compared to the single-impurity spectrum in Fig. 2.3 (c) [27]–[29]. As we will see in the following, this behavior changes in the presence of SOC. Also, we can see that the in-gap states of the FM dimer are fully spin polarized, the negative (positive) YSR states only show spin up (down) components. In the AFM spectrum, however, we can observe spin up and down components on both in-gap peaks due to the presence of the neighboring atom with opposite spin direction.

The 2-D maps in Fig. 2.5 (b), (f) show the spatial distribution of the PDOS at the indicated energy, corresponding to the electron component of the YSR state. For the FM case, the maximum can be observed at the position of the dimer, while for the AFM dimer, the maximum is reached at the neighbor sites of the magnetic atoms. In the remaining maps, we show the spin distribution at the same energy. Figures 2.5 (c), (g) show the $\rho_{iz} = \rho_{i\uparrow} - \rho_{i\downarrow}$ spin distribution. We can observe a big difference between the two cases: In the FM dimer, the spin of the YSR state in both atoms is the same, with a majority of spin down component. In the AFM case, the polarization of the in-gap state is opposite on the two atoms, due to the opposite spin direction of the pair: in the spin-up (down) atom the majority of electrons show spin-down (up) polarization. Finally, we also study the transverse, or in-plane spin component, $\rho_x$. It can be obtained from the non-diagonal components in the Green's function:

$$\rho_x(\vec{r}_i, \omega) = -\frac{1}{\pi} Im[G_{1,4}(\vec{r}_i, \vec{r}_i, \omega) + G_{4,1}(\vec{r}_i, \vec{r}_i, \omega)] \tag{2.56}$$

Figures 2.5 (d), (h) show the transverse spin component distribution. As we can see, for both cases, there is no in-plane polarization component.

Figure 2.6 shows similar results as Fig. 2.5, but we have added the Rashba interaction, with $\alpha_R = 3.0$ eV-Å. The spectra in Fig. 2.6 (a) shows small difference compared to the $\alpha_R = 0.0$ case: there are still four peaks visible, but they have slightly shifted to different energies. For the AFM dimer, on the other hand, we can observe that, as the Rashba SOC is added to the system, the two peaks have now split into four (Fig. 2.6 (e)), indeed, the presence of SOC allows for anti-parallel spins to hybridize [112], as experimentally observed for Mn dimers on Nb [29].

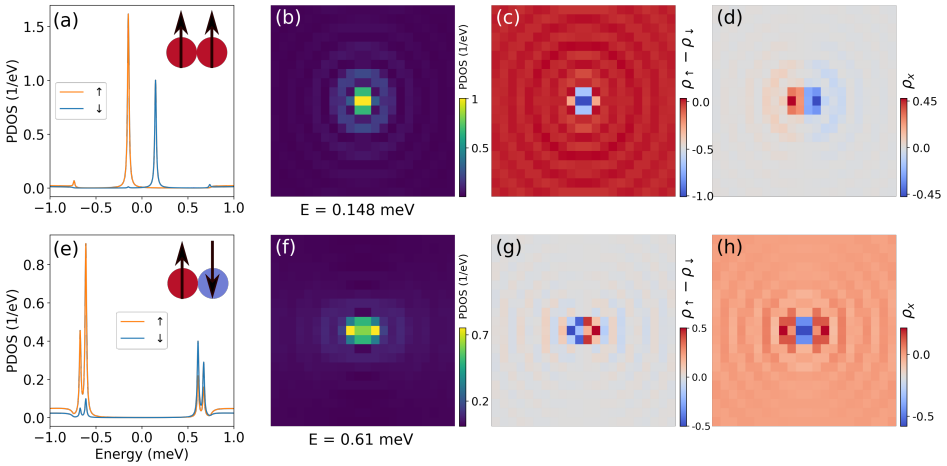


Figure 2.6: Impurity dimer with Rashba SOC. (a)-(d) FM dimer and (e)-(h) AFM dimer. (a),(e) PDOS obtained on the first atom. The blue (orange) curve is the $\rho_\downarrow$ ($\rho_\uparrow$) component. (b),(f) PDOS spatial distribution at the indicated energy. (c),(g) Density of spin along $z$. (d),(h) Density of the transversal spin component, $\rho_x$. Parameters: Same as Fig. 2.5 and $\alpha_R = 3.0$ eV-Å. All shown densities are in units of 1/eV.

The 2-D maps, show similar behavior as in Fig. 2.5. Most notably, we can now observe a non-zero transverse spin component ($\rho_x$) in Fig. 2.6 (d) and (h). The PDOS distribution in Fig. 2.6 (b), (f) does not differ a lot from the corresponding case in Fig. 2.5 For the FM dimer, the transverse spin is opposite in each of the impurities and shows an antisymmetric behavior in the rest of the array. In the AFM pair, the in-plane spin component has a symmetric distribution around the dimer. Overall, the presence of the Rashba SOC, results in a mixture of the spin components, allowing, for example, for the AFM YSR states to hybridize.

## 2.3 Spin chains on a superconductor

Finally, we want to build a chain with several impurities on a superconducting surface. The realization of MBS in spin chains follows two main approaches. The first one is the so called *diluted chain limit*. The YSR states created by the impurities can hybridize, resulting in the YSR bands. These bands can go into a topological phase, and host MBS on their edges [9], [88], [93], [113], [114]. The second approach is the *dense impurity limit*, here magnetic impurities are coupled to each other and superconductivity is induced by proximity effect into the chain. The chain may enter the topological phase when a non-collinear spin texture is present in the chain. This may result from RRKY interaction or spin orbit coupling [94],

[115], [116]. The last approach is similar to the experimental realizations using semiconducting nanowires.

In our Green's function model, we find ourselves on the diluted chain limit. In this section, we will simulate a chain of magnetic impurities using the same model used to simulate single impurities and dimers in 2.2. We aim to observe the emergence of MBS using realistic parameters which can be realized on experimental set-ups.

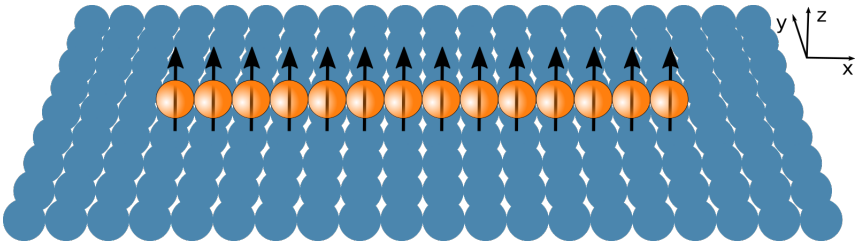


Figure 2.7: Spin chain on a superconductor. The superconducting surface is modelled, by a discrete 2-D array represented by blue balls in the figure. The magnetic impurities, represented by the orange balls, are placed along the $x$ direction forming the chain. The arrows represent the spin state of the impurities, in this figure, we can observe the spins ferromagnetically coupled and pointing along the $\vec{z}$ axis, perpendicular to the superconducting surface.

### 2.3.1 Modeling and plotting

Figure 2.7 depicts the geometry of the modelled system: the blue balls represent the atoms of the BCS superconductor, each of them is one site of the lattice. The orange balls are the magnetic atoms. They are located at the center of the superconducting surface. The chain is placed along the $\vec{x}$ direction. The arrows represent the spin of the impurities. Here the arrows are pointing along the $\vec{z}$ axis, perpendicular to the surface creating a FM chain, however the spins can point in any other direction in the 3-D space, as explained in 2.2.2.

We solve Dyson's equation for a FM spin chain with 27 magnetic impurities on a 2-D superconducting array of $35 \times 11$ sites. Figure 2.8 shows the results of the calculation. In Fig. 2.8 (a) we depict the spectrum obtained on one of the edge atoms of the chain, we can easily notice a pronounced peak at zero energy as well as other in-gap states at higher energies. A key feature of MBS is their spatial distribution in finite systems. In a 1-D system, such as a spin chain, MBS are expected to arise localized at the edges of the chain [8], [117]. To observe this, on Fig. 2.8 (b) we plot the PDOS of the chain at $E = 0.0$ as a function of the atomic site along the $x$ axis. The red dashed lines mark the limits of the atomic chain, we leave a margin

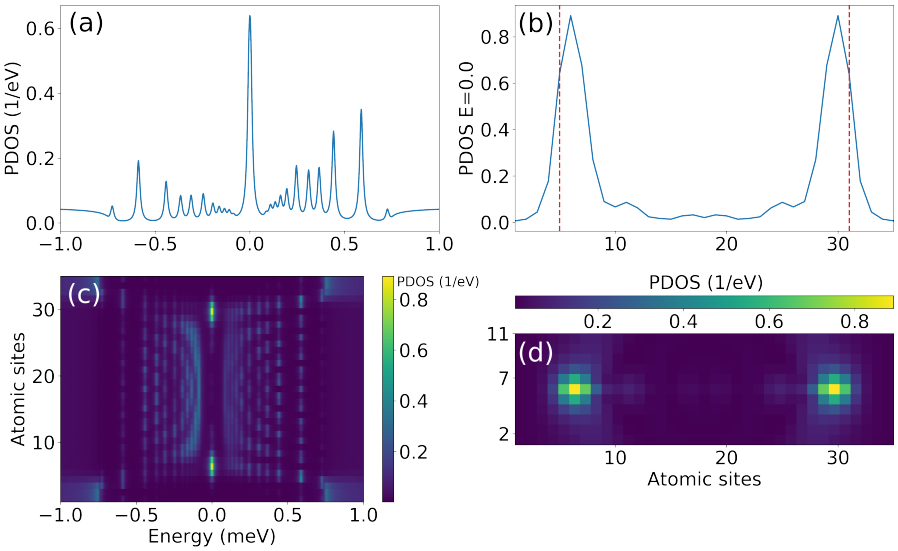


Figure 2.8: Spin chain on a superconductor. (a) PDOS energy spectrum on the first atom of a 27-atom chain. (b) PDOS profile at zero energy along the $x$-axis of the magnetic chain, red dashed lines mark the edges of the spin chain, these coincide with PDOS maximum. (c) Spectra as a function of atomic site along $x$ direction. (d) Spatial distribution of PDOS at E=0.0 in the 2-D array. Parameters: $\Delta = 0.75$ meV, $k_F = 0.183\ a_0^{-1}$, $a = 3.36$ Å, $\Gamma = 0.01$ meV, $J = 1.7$eV, $K = -2.0$ eV and $\alpha_R = 3.0$ eV-Å.

of 4 sites of clean superconductor on both sides. We observe how the PDOS at zero energy reaches its maximum close to the edges, and it rapidly decays as we move toward the center of the chain and outside. Note that the PDOS does not go down to zero inside the chain. This is due to the finite size of the chain [80]. The MBS wave functions have some overlap, resulting in the finite PDOS inside the chain. To gain more insight into the spatial distribution of the rest of the states, in Fig. 2.8 (c) we plot the spectra as a function of the atomic site along the $x$ direction. We can easily distinguish the two zero-energy edge states at both ends of the chain. Additionally, in this plot we can observe an energy gap around the chain, this is the so-called *topological gap* [8], that protects the MBS from mixing with finite energy states. Other in-gap states can be observed outside this gap along the chain. Figure 2.8 (d) is a 2-D map of the PDOS at $E = 0.0$ everywhere in the 2-D array, the localized zero energy states can again be observed here.

All the features shown in Fig. 2.8 are in good agreement with the presence of MBS, however they are necessary but not sufficient conditions to have topological edge states. Indeed, trivial in-gap states can emerge at zero energy on spin chains [25], [118]. MBS arise when the system enters a topological phase, however,

this can not be simply identified by looking at the density of states. As we will see in the following, the spin polarization can help us determine if the system has gone through a topological phase transition.

### 2.3.2 Topological phase transition and spin polarization of MBS

Unlike Majoranas in the Kitaev model, MBS in spin chains are spin polarized. They are expected to have a characteristic spin signature, providing further information that can help distinguish MBS from other trivial zero-energy edge states [30], [119]–[122]. In experimental realizations, the development of spin-polarized (SP)-STM [123], [124], gives an extra tool that can be utilized to further characterize zero-energy states in spin chains [21]. It has been argued, that the $\rho_z$ component (perpendicular to the chain) is expected to be the same for the two edge states, additionally, their transversal spin component, $\rho_x$, is the same with opposite sign [30]. Furthermore, the spin of the YSR bands along the chain is also helpful to identify the topological phase. When the system goes through a topological phase transition (TPT) the lower energy YSR bands switch their spin polarization [119]. With this in mind, by slowly tuning the parameters and monitoring the spin state of the in-gap states of the chain, we can observe this transition, and hence, identify the topological phase of the chain.

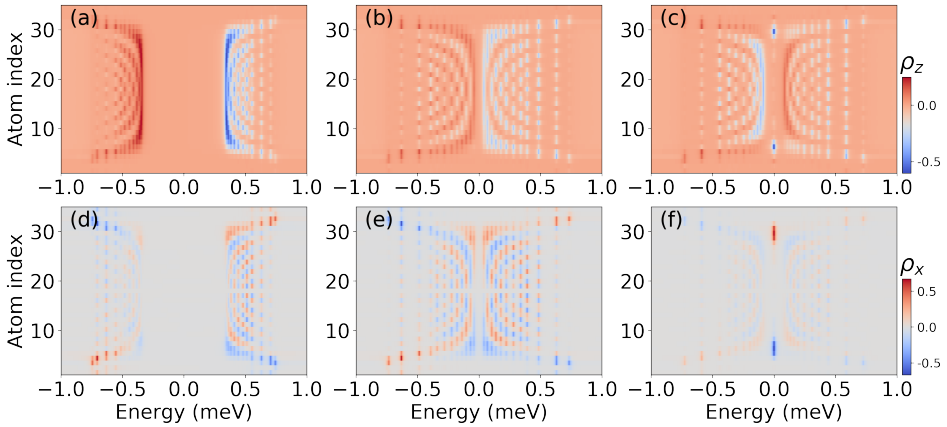


Figure 2.9: TPT in spin chain. (a)-(c) $S_z$ spin component along the chain axis for $J = 1.0$ eV, $J = 1.5$ eV and $J = 1.7$ eV, respectively. (d)-(f) Same as (a)-(c) but $S_x$ spin component. All shown densities are in units of 1/eV. Other parameters: Same as Fig. 2.8.

The energy-resolve $z$ spin density can be easily obtained as shown in 2.2.2, $\rho_z = \rho_\uparrow - \rho_\downarrow$. And the transverse spin component ($\rho_x$) is obtained from Eq. 2.56. In

Fig. 2.9 we plot the spin components $\rho_z$ (upper row) and $\rho_x$ (lower row) for different exchange interaction ($J$) values, keeping the rest of parameters from Fig. 2.8. Fig. 2.9 (a) and (d) correspond to the case where $J = 1.0$ eV. For this value, the lowest energy YSR states are found at $\sim \pm 0.2$ meV and no in-gap states are present near zero energy. Figure 2.9 (a) shows the $\rho_z$ spin component, as we can see, the lowest YSR states have opposite spin components, the negative energy band has a positive polarization and the states at positive energy are spin-down polarized. The $\rho_x$ polarization shows an alternating behavior between the YSR bands. We now increase the magnetic interaction to $J = 1.5$ eV, in Fig. 2.9 (b) and (e) we can observe in-gap states very close to zero energy. As discussed in chapter 1, the closing of the energy gap is a necessary condition to have a TPT, this is what we can observe here. Also, the $\rho_z$ spin polarization of the bands decreases as they approach zero energy. For even higher exchange interaction ($J = 1.7$ eV), in Fig. 2.9 (c) and (f) we can observe two edge states at zero energy, well localized at the chain's ends (the parameters in this case coincide with Fig. 2.8). Their $\rho_z$ spin component coincides, while the transverse component, $\rho_x$, is the same but with opposite sign. These signatures are in good agreement with the presence of MBS [30]. To have further evidence of a TPT, we can also look at the spin polarization of the low energy YSR states. By comparing the $\rho_z$ component on Fig. 2.9 (a) and (c) we can observe that the spin sign of the YSR states closer to zero are interchanged, this is a signature of a TPT [119]. Assuming the system was initially in a trivial phase, we can conclude that the parameters used in the calculation in Fig. 2.8 correspond to a topological phase.

However, as pointed out in Ref. [30], these spin signatures are still necessary but not sufficient conditions to have topological superconductivity. Furthermore, in real experiments, the exchange coupling $J$ cannot, in general, be modified in the same fashion as shown in Fig. 2.9. So identifying this transition is, in general, not possible. As we viewed in chapter 1, the topological state of the system can only be identified by evaluating a topological invariant.

**Conclusions.** In the present chapter, we have described a Green's functions-based model to describe a BCS bulk superconductor. By means of the Dyson equation, the effect of magnetic impurities and Rashba SOC can be added to the system. We have reviewed some results on single impurities as well as magnetic dimers, allowing to observe the effect of the Rashba term. As observed, the presence of SOC, allows for YSR states in AFM dimers to hybridize. Following the same approach, we simulated a 27-atom spin chain on a superconducting surface. We studied the emergence of zero-energy edge states and how the spin polarization shows good agreement with the presence of MBS and a topological phase transition of the system.

In the following, we will use the Green's function model to reproduce real experimental results on magnetic spin chains in superconductors. We will also develop a method to evaluate the topological invariant starting from the Green's functions,

allowing us to identify topological regions using realistic parameters.

# 3 Calculations of spin chains on superconductors

**Introduction.** Topological edge states are expected to arise in ferromagnetic spin chains on superconducting surfaces under the right conditions [20]–[24], [93], [125]–[128]. In chapter 2, we introduced the free-electron model used to describe a bulk superconductor with magnetic impurities. This formalism allowed us to compute the PDOS, and observe the emergence of presumably topological edge states in ferromagnetic spin chains. In the present chapter, we will focus on two goals: (i) Using our model, reproduce experimental results of spin chains on a superconducting surface. (ii) Develop a method to evaluate the topological invariant of the system, allowing us to unambiguously identify the topological phase.

The present chapter is organized as follows: In 3.1 we show a direct application of the model by reproducing experimental measurements on Cr spin chains in the superconductor $\beta$-$Bi_2Pd$. These findings are published in Phys. Rev. B 104, 045406 [31]. In 3.2 we present a method to obtain the Hamiltonian $\hat{H}(k)$ of the spin chain+superconductor system starting from the real space Green's function. In 3.3 we discuss the evaluation of the topological invariant and a topological phase diagram that will allow us to easily identify the topological phases. These results were published in Phys.Rev.B 104, 245415 [32]. Finally, in 3.4 we discuss the finite size effects of spin chains and the consequential emergence of energy oscillations as we vary the length of the chain. These finding were published in Phys.Rev. Research **4**, L032010 [33].

## 3.1 Chromium atoms on $Bi_2Pd$

The Green's function model described in chapter 2 can be utilized to reproduce measurements performed on real systems using scanning electron tunneling microscopy (STM)[1]. In the following, we will compare the results obtained with our model with measurements on chromium atoms deposited on the $\beta$-$Bi_2Pd$ superconductor [31].

[1] Scanning tunneling microscopy is discussed in detail in chapter 4.

### 3.1.1 Measurements with STM

$\beta$-$Bi_2Pb$ is an s-wave superconductor with critical temperature of $T_c = 5.4$ K [129], the crystal structure consists of alternating bilayers of bismuth and monolayers of palladium atoms [129], [130]. When the crystal is cleaved, the exposed surface is Bi terminated, forming a square lattice with parameter $a = 3.36$ Å. Chromium atoms are deposited at temperature $\leqslant 20$ K [31] onto a $Bi_2Pb$ sample, cleaved *in-situ* in ultra-high vacuum conditions. As reported in previous studies, the Cr atoms get absorbed on hollow sites of the Bi surface [28]. Atomic lateral manipulation using the STM tip allows for building different atomic arrangements. In particular, we focus on chains of atoms (denoted as $Cr_n$ where $n$ is the number of atoms) along different orientations with respect to the Bi lattice and, hence, different distance between the impurities.

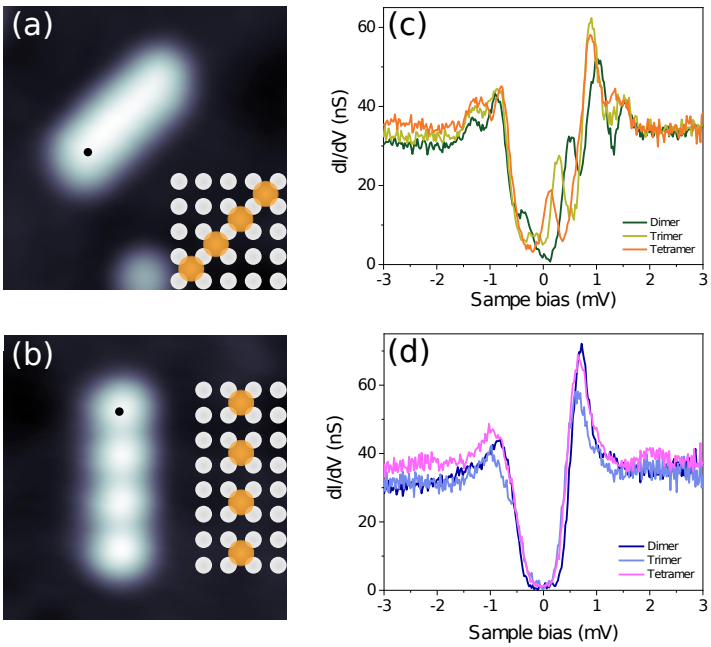


Figure 3.1: Scanning tunneling spectroscopy on Cr chains. (a) Topography image of $Cr_4$ of the $d = \sqrt{2}a$ chain. The black dot indicates the atoms when the STS is measured (b) Same as (a) for the $d = 2a$ chain. Insets in (a) and (b) show the Cr atoms (orange balls) over the Bi lattice. (c) Spectra obtained for $Cr_2$, $Cr_3$ and $Cr_4$ for chain in (a). (d) Same as (c) for chain in (b).

Measurements are carried out at a temperature of $T = 30$ mK, using a metallic PtIr tip [31]. Figure 3.1 shows scanning tunneling spectroscopy (STS) obtained on

the edge atom of small Cr chains on $\beta$-$Bi_2Pd$ for lengths between 2 and 4 atoms. Figure 3.1 (a) and (b) show the topography images of the four-atom, or tetramer, with two different orientations. The inset figures depict the geometry of the Cr chains (in orange) on the $\beta$-$Bi_2Pd$ surface. The chain in Fig. 3.1 (a) is built along the $< 110 >$ direction of the Bi square lattice, the distance between Cr atoms in this case is $d = \sqrt{2}a$. The chain in Fig. 3.1 (b) is built along the $< 100 >$ direction by keeping the Cr atoms at a distance of $d = 2a$. In Fig. 3.1 (c) and (d) we have plotted the scanning tunneling spectroscopy (STS) obtained in the edge atom (marked as a black dot in panels (a) and (b)) of dimer ($Cr_2$), trimer ($Cr_3$) and tetramer ($Cr_4$). The three curves in Fig 3.1 (c) show a clear in-gap YSR state. As the chain's length increases from 2 to 4 Cr atoms, we can observe that the in-gap state, shifts closer to zero energy. On the other hand, the spectra obtained on the $d = 2a$ spaced chain, looks very similar for dimer, trimer and tetramer: the presence of YSR states in this structure can only be noted by the asymmetry in the quasi-particle peaks.

Previous work on Cr dimers on $\beta$-$Bi_2Pd$, point to a different arrangement of the magnetic moments depending on the spatial configuration of the Cr atomic structures. In particular, authors conclude that dimers built with distance $d = \sqrt{2}a$ show a ferromagnetic spin ordering, whereas dimers with distance $d = 2a$ are coupled anti-ferromagnetically [28]. These findings are based in the presence or absence of hybridized in-gap states. We keep this in mind, to reproduce the experimental results with the Green's functions model. However, Rashba SOC was not taken into account in the study presented in [28], which, as we saw in 2.2.4, can induce hybridization between the YSR states in AFM structures.

### 3.1.2 Comparison with Green's function model

We model the Cr spin chains on $\beta$-$Bi_2Pd$ in the independent-atom limit using our Green's function model. Density functional theory (DFT) calculations show that Cr atoms have been found to have no electronic levels at the Fermi energy and negligible direct interactions, even for Cr atoms located a unit cell apart [28], which justifies this approach. The calculations will allow us to gain more insight into the behavior YSR states. We create a superconducting lattice and select specific locations to place the magnetic impurities and reproduce the structures' geometry shown in Fig. 3.1 (a) and (b).

The magnetic impurities are modelled as discussed in 2.2.2, the spin is assumed to be classical, and, in principle, it can be oriented anywhere in the 3-D space. We fit the spectrum of a single magnetic impurity. Figure 3.2 (a) shows the measured STS for a single Cr atom on $\beta$-$Bi_2Pd$. The simulated spectrum is depicted in Fig. 3.2 (b), from which we obtain the following parameters: the exchange interaction is estimated to be $J \approx 2$ eV, the potential scattering is taken as $K = 5.5$ eV to reproduce the electron/hole asymmetry. Finally, the Rashba SOC is modeled as discussed in 2.2.3, we use a Rashba SOC strength of $\alpha_R \approx 1.8$ eV, which

is estimated from DFT calculations, and in good agreement with Bi-terminated surfaces [131].

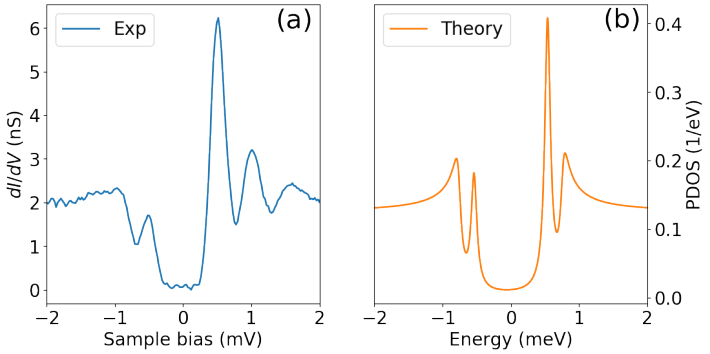


Figure 3.2: Single Cr spectra on $Bi_2Pd$. (a) Experimental spectrum measured with STM. (b) Calculated spectrum using the Green's functions model. Parameters: $\Delta = 0.75$ meV, $J = 1.9$ eV, $K = 5.5$ eV and $\alpha_R = 0.0$.

**The case of $d = \sqrt{2}a$ - $< 110 >$ spin chains**

Figure 3.3 shows 2-D maps of the spectra along the chain for $Cr_2$, $Cr_3$ and $Cr_4$ in the case of atomic chains built with $d = \sqrt{2}a$ distance, *i.e.*, along the $< 110 >$ direction of the Bi lattice. In Fig. 3.3 (a)-(c) we show the experimental $dI/dV$ spectra measured along the chain's axis. For the dimer, we can observe two YSR extended states: one at lower energy, with maximum DOS in the middle of the structure and a second one at an energy close to the quasi particle peaks of the superconductor with a minimum in the center of the structure. The overall spatial distribution of the YSR states is maintained for the trimer and tetramer. However, as the length increases, the YSR state at low energy, moves toward zero.

This behavior, is well reproduced by the theoretical calculation shown in Fig. 3.3 (d)-(f). Additionally, the calculations allow us to better distinguish YSR states found at higher energies, located at the edges of the chain. These are more easily observed at positive energies. The overall, distribution of the YSR states on $Cr_2$, $Cr_3$ and $Cr_4$ is well reproduce by our calculations, including the electron-hole asymmetry, achieved by choosing an adequate potential scattering. In order to properly reproduce the position of the YSR bands, the magnetic exchange coupling is increased from $J = 2.0$ eV for the dimer, $J = 2.1$ eV for trimer, and $J = 2.3$ eV for the tetramer. This tuning of the parameter may be justified by an increase of the magnetic hybridization of the magnetic impurities with the surface due to a geometrical rearrangement as the number of atoms increases, resulting in larger couplings, but this is speculative, and we have no evidence to support it other than the computed YSR spectra better reproduce the experimental one.

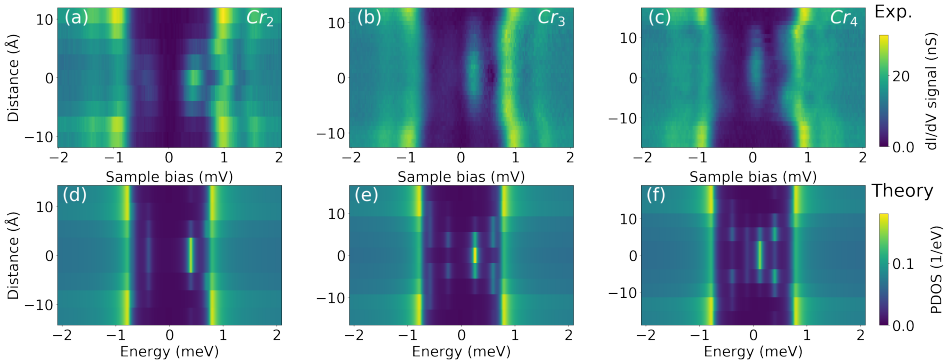


Figure 3.3: Experimental $dI/dV$ (a)-(c) and theoretical local density of states (d)-(f) on Cr chains on $Bi_2Pd$ built on the diagonal direction of the Bi lattice. (a)-(c) Experimental dI/dV spectra obtained along the chain for (a) dimer, (b) trimer and (c) tetramer. (d)-(f) Calculated PDOS along the chain for (d) dimer, (e) trimer and (f) tetramer. Fitting parameters: $\Delta = 0.75$ meV, $K = 5.5$ meV, $k_F = 0.15$ $a_0^{-1}$, $\Gamma = 0.01$ meV and the magnetic coupling (d) $J = 2.0$ eV, (e) $J = 2.1$ eV and (f) $J = 2.3$ eV.

A background signal coming from the superconducting hosting material is also added to the calculated spectra to better reproduce the experiments. This can be justified by the fact that, in the experimental set-up, the STM tip is not sharp enough, so DOS coming from the $\beta$-$Bi_2Pd$ surface is also measured.

The spin arrangement of the magnetic atoms is set to be ferromagnetic, with the spins pointing perpendicular to the surface. Other arrangements, such antiferromagnetic and spin helices with different periods, were also calculated. But FM ordering showed the best agreement with the experiments, as predicted in Ref. [28]. In the experimental set-up, longer chains than 4 atoms along this particular direction could not be built, as the Cr atoms tend to form clusters at this interatomic distance.

**The case of $d = 2a$ - $< 100 >$ spin chains**

Unlike the $d = \sqrt{2}a$, the $d = 2a$ chains built along the $< 100 >$ direction are far enough so that atoms do not clusterize so easily, and chains up to 12 atoms could be built. However, in this case, we cannot observe any obvious structure inside the superconducting gap, even as the length of the chain is increased. The evolution is depicted in Fig. 3.4 (a)-(h), here the spectra along the chain's axis are depicted for selected chain's lengths ranging from $Cr_2$ to $Cr_{12}$. Due to the presence of YSR states, the chains show a smaller energy gap than the superconducting gap of $2\Delta$, being $\Delta = 0.75$ meV. Additionally, the chains show an even smaller superconduct-

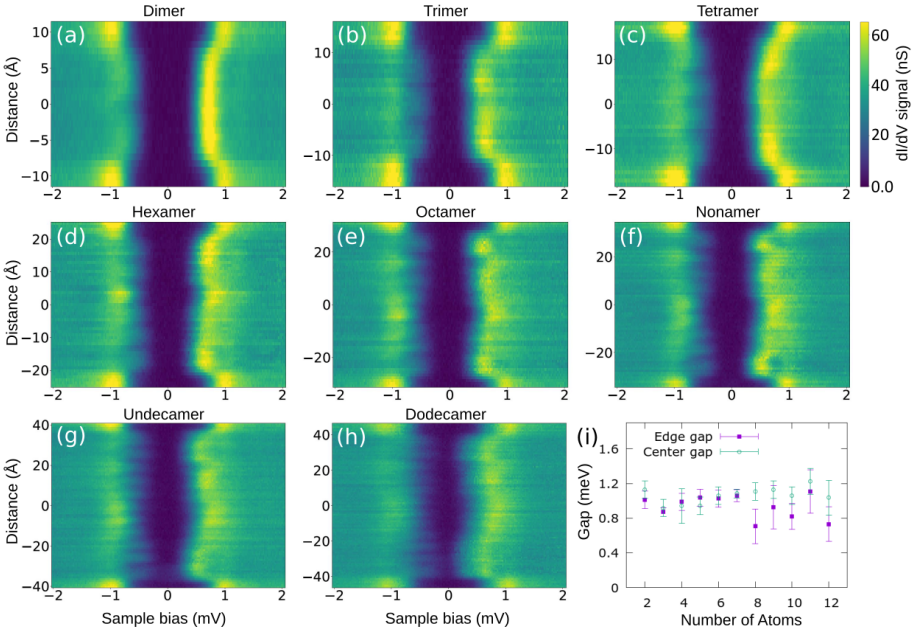


Figure 3.4: $dI/dV$ signal measured for the $d = 2a- < 100 >$ Cr chains. For $n = 2$ (a), $n = 3$ (b), $n = 4$ (c), $n = 6$ (d), $n = 8$ (e), $n = 9$ (f), $n = 11$ (g) and $n = 12$ (h). (i) Shows the evolution of the energy gap measured in the edge atom of the chain (purple marker) and in the center (green marker) versus the number of atoms in the chain.

ing gap at the edge atom compared to spectra in the center of the structure (see Fig. 3.4 (i)), this is particularly notable for chains longer than 8 atoms, however this gap closing remains constant for longer chains, indicating that a complete closing of the gap cannot take place, and hence, no topological phase transition is expected in these chains. A closer look into the spectra at negative energies, reveals a modulation in the in-gap states that matches the number of atoms present in the chain, this means that each atom gives rise to a YSR state that does not hybridize with the neighboring YSR states, as expected in AFM spin structures on superconductors.

As concluded by the absence of hybridization between the YSR states for atomic dimers in this configuration [28], the spin ordering is expected to be AFM for these chains. However, with the addition of Rashba spin-orbit coupling into the model and a higher number of atoms, the simulated AFM 12-atom chain (shown in Fig. 3.5 (b)) does not resemble the experimental spectra of the dodecamer in Fig. 3.5 (a). As we can see in the calculated PDOS, two edge states emerge close to zero energy, these features are absent in the experimental data. Indeed, as

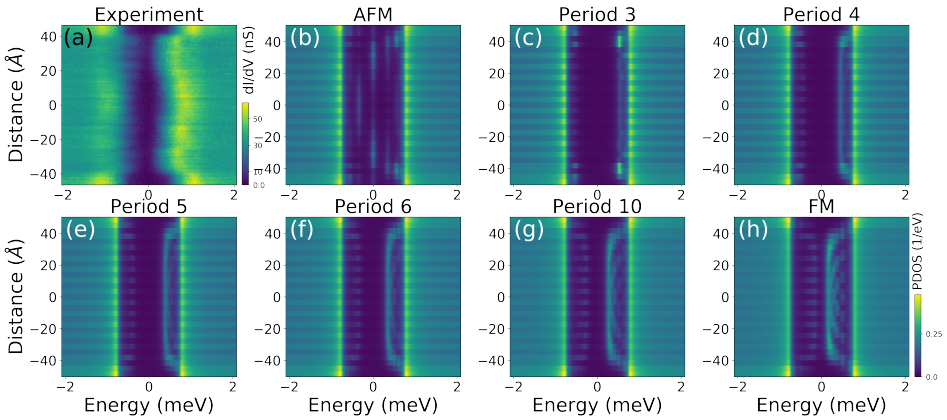


Figure 3.5: (a) Experimental STS spectra along the chain's axis of the $Cr_{12}$ (b)-(h) 12-atom calculations with different spin ordering and period.

discussed in Ref. [29] the presence of spin-orbit coupling induces splitting due to hybridizations forming the YSR bands for AFM chains, so a slightly different approach is needed to reproduce the experimental data.

To obtain a spin configuration that better reproduces the measurements, we model a non-collinear spin texture [132] and compare with the 12-atom chain measurements. We define a spin helix going along the chain, and we study the resulting spectra obtained for different helix periods. As mentioned in 2.2.2, the imputies' spin can be oriented everywhere in the 3-D space, $\vec{S_j} = (S_{j,x}, S_{j,y}, S_{j,z}) = S(\sin\theta_j \cos\phi_j, \sin\theta_j \sin\phi_j, \cos\theta_j)$. With this in mind, the spin helix is defined by varying the $\theta$ coordinate between sites. Fig. 3.5 (b)-(h) show the obtained PDOS for 12-atom chains with different period spin helices. The periodicity number indicate the number of atoms until the spin configuration is repeated, so period 2 corresponds to AFM spin ordering, period 3 corresponds to a $120^{\text{o}}$ angle with the neighboring spin, and infinite period is FM. As we can observe, the period 3 and period 4 configurations, show an overall good agreement with the experiments: the in-gap states result in a narrowing of the energy gap, and edge states reduce the gap at the edges of the chain. This is an indication that the presence of spin-orbit coupling in this system, induces a more complex spin texture than the one found for $d = 2a$ dimers in Ref. [28]. On the other hand, non-collinear spin DFT calculations, including spin-orbit interactions, show that the preferred spin arrangement in this chain is AFM coupling. Spin-polarized-STM measurements could shed more light into the spin configuration of these atomic spin chains [133].

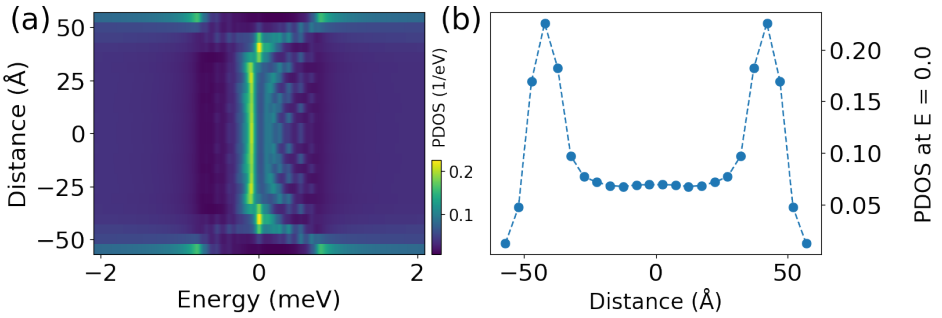


Figure 3.6: MBS signatures in 20 atom $d = \sqrt{2}a-$ $< 110 >$ chain. (a) color map of the PDOS along the chain's axis. (b) Profile of the PDOS at zero energy along the chain's axis. Fitting parameters: Same as Fig. 3.3 and $J = 2.5$ eV.

### 3.1.3 MBS in Cr chains on Bi2Pd

As seen in Fig. 3.3, the $d = \sqrt{2}a-$ $< 110 >$ chains exhibit in-gap states moving to zero as the chain's length increases. This is a good indication for the emergence of MBS in longer chains. Since chains longer than 4 atoms could not be experimentally realized, we performed calculations for longer chains. In Fig. 3.6 we plot the calculated 20-atom chain along the $< 110 >$ direction for the same parameters as in Fig. 3.3 and $J = 2.5$ eV. Fig. 3.6 (a) shows the PDOS along the chain's axis, exhibiting two edge states at zero energy, and an energy gap inside the chain. Fig. 3.6 (b) depicts the profile of the PDOS at zero energy along the chain, as we can see, the zero-energy states are localized at the edge atoms, however, inside the chain the PDOS does not go down to zero due to the finite size of the system.

The features in Fig. 3.6 are in good agreement with the presence of MBS states. As discussed in 2.3.2, the spin polarization of the in-gap states can help us identify if a TPT has taken place, and potentially distinguish MBS from zero-energy trivial states [30], [119]. In Fig. 3.7, we plot the evolution of the two spin components, $\rho_z$ and $\rho_x$, as we increase the magnetic coupling interaction, $J$. Fig. 3.7 (a) and (d) correspond to an exchange interaction of $J = 2.1$ eV, here we see an energy gap in the spectra but no edge states, the YSR band at positive (negative) energy is spin-down (up) polarized. At $J = 2.3$ eV (Fig. 3.7 (b) and (e)), the energy gap is virtually zero, and it reopens at $J = 2.5$ eV (Fig. 3.7 (c) and (f)). Two edge states at zero energy become apparent, showing opposite polarization for the spin density along the x direction, $\rho_x$ and parallel $\rho_z$ component. The $z$-polarization of the YSR bands in the middle of the chain reverses when comparing Fig. 3.7 (a) and (c), and only on the later the edge states can be observed. This behavior is in good agreement with a TPT. Indicating that the edge states in Fig. 3.6 are topological.

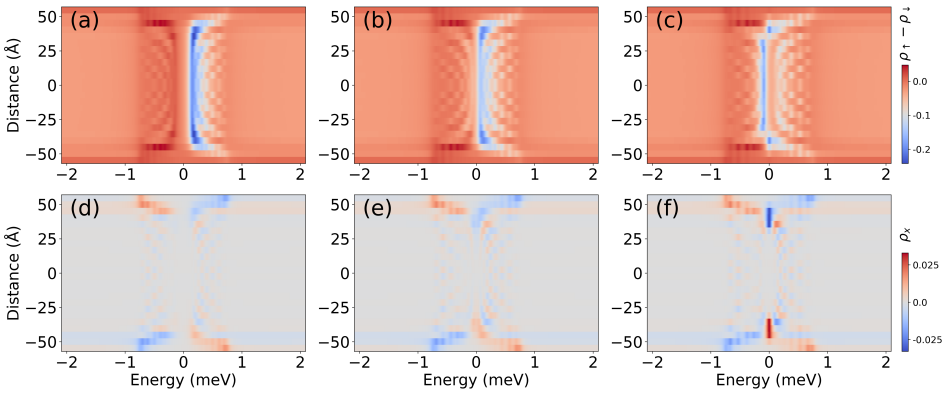


Figure 3.7: Topological phase transition on Cr atoms on $\beta$-$Bi_2Pd$ as we increase the exchange interaction, $J$. The three columns correspond to three different J values, $J = 2.1$ eV, $J = 2.3$ eV and $J = 2.5$ eV. (a)-(c) Shows color maps of the perpendicular spin density, $\rho_z$ as a function of the chain's length versus energy. (d)-(f) Transversal spin density, $\rho_x$.

The number of atoms in the chain is decisive for the formation of MBS [117]. The calculations in Fig. 3.6, are performed for a 20-atom chain, but shorter chains may suffice to host topological edge states. The emergence of edges in the chain can be observed in Fig. 3.8, we show the evolution of the PDOS as we vary the chain's length from $Cr_5$ to $Cr_{20}$. According to this calculation, for chains as short as 8 atoms, edge states can already be distinguished at zero energy.

### 3.1.4 Summary

In this section, using the Green's functions model described in chapter 2, we were able to obtain the PDOS of magnetic impurities in a superconducting surface. In particular, we could reproduce experimental results obtained with STM on Cr atoms deposited on $\beta$-$Bi_2Pd$. The different arrangement of short spin chains lead to striking different behavior of the YSR states. With our model, we are able to reproduce the PDOS, and to better understand the spin configuration. We have observed that the spectra on $d = \sqrt{2}a-$ $< 110 >$ chains is in good agreement with the calculations when the spin ordering is chosen to be ferromagnetic [28]. However, the $d = 2a-$ $< 100 >$ chains calculations do not show a good agreement when the spin configuration is set to be AFM, as anticipated. The different period spin helix calculation points to a more complex spin texture for these chains.

The measurements, show a fast gap closing in the $d = \sqrt{2}a-$ $< 110 >$ Cr chains, as the number of atoms in the chain increases. Calculations in 20-atoms structures, using similar parameters to model the experimental data, show features in good

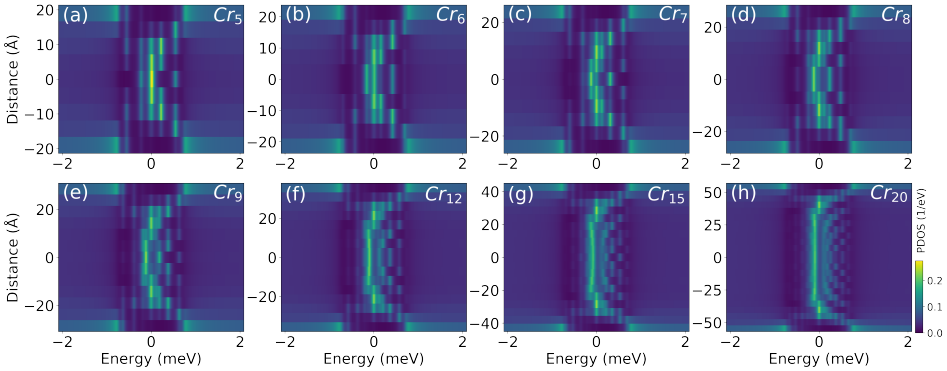


Figure 3.8: Evolution of the in-gap states for the $d = \sqrt{2}a$ chains. The parameters are set such that the system is in a topological state, (a)-(h) show the spectra for $Cr_n$ chains from $n = 5$ to $n = 20$. For $n = 8$, edge states can already be distinguish.

agreement with the presence of MBS. In fact, we could already observe Majorana-like edge states for 8-atoms chains. Additionally, a study of the spin components as we vary the magnetic exchange interaction, $J$, points to the presence of a TPT [31]. All of these features are in good agreement with a topologically non-trivial state of the system. However, as already discussed, they are all necessary but not sufficient conditions [30].

## 3.2 Green's functions in k-space

As explained in chapter 1, topological invariants serve to identify the topological phase of a system. These depend on its topological class, which is determined by its symmetries. In particular, we saw that for the BDI class in 1-D, the relevant topological invariant is the *winding number*. In the case of an infinite magnetic chain on a superconductor, the winding number takes values in $-1, 0, 1$. And phase diagrams that help us identify the topological phase become particularly useful.

In chapter 2, we described a model based on Green's functions capable of obtaining the density of states of magnetic chains on a superconductor. In particular, as discussed in 3.1, we could reproduce the experimental results of Cr chains on $\beta$-$Bi_2Pd$. For some parameters, we could find signatures indicative of the presence of MBS. However, to be certain that the studied system is in the topological phase, we need to compute the topological invariant. In this section we will see how to obtain the winding number starting from the Green's functions model described in chapter 2.

### 3.2.1 BCS superconductor in k-space

We are interested in studying the topological properties of 1-D spin chains. In order to calculate the topological invariant, we will obtain the bulk Hamiltonian of the system. In this first section, we will see how to go from our Green's function in real space back to the reciprocal $k$-space. The reason to do this is that in the approximations performed to obtain the real-space Green's function, the properties of the original Hamiltonian in k-space, Eq. 2.21, are strongly modified. The Nambu basis in the reciprocal space is:

$$\psi_k = \begin{pmatrix} c_{k\uparrow} \\ c_{k\downarrow} \\ c^{\dagger}_{-k\uparrow} \\ c^{\dagger}_{-k\downarrow} \end{pmatrix} \tag{3.1}$$

Where, $k$ is the wave-vector of the plane-wave basis function $\phi_k(r) = e^{i\vec{k}\cdot\vec{r}}/\sqrt{V}$, $V$ is the normalization volume and $\vec{r}$ are the spatial-coordinate vectors.

Starting from the Green's function in real space, we can go to $k$-space by applying the following Fourier transform:

$$G_{BCS}(\vec{k},\omega) = \sum_{\vec{R}} G_{BCS}(R,\omega) e^{i\vec{k}\cdot\vec{R}}. \tag{3.2}$$

Where $G_{BCS}(R,\omega)$ is the Green's function in real space and the sum is to all the sites. This sum can be solved analytically, as done in Ref [134] and Ref [117]. In terms of the 4-component Nambu basis (Eq. 3.1), we obtain:

$$\begin{aligned} G_{BCS}(\vec{k},\omega) = \frac{\pi N_0}{2k_F a} L_+(k)\tau_z\sigma_0 + \left( \frac{\omega}{i\sqrt{\Delta^2-\omega^2}} L_-(k) - \frac{\pi N_0}{\sqrt{\Delta^2-\omega^2}} \right) \tau_0\sigma_0 \\ + \frac{\pi N_0}{\sqrt{\Delta^2-\omega^2}} \left( \frac{\pi}{i2k_F a} L_-(k) - 1 \right) \tau_y\sigma_y \end{aligned} \tag{3.3}$$

Where the function $L_{\pm}(k)$ is defined as:

$$\begin{aligned} L_{\pm}(k) =& F(-\xi + i(k_F + k)) + F(-\xi + i(k_F - k)) \\ & \pm F(-\xi - i(k_F + k)) \pm F(-\xi - i(k_F - k)) \end{aligned} \tag{3.4}$$

And where $F(x) = log(1 - e^x)$.

Alternatively, we can also evaluate the Fourier transform in Eq. 3.2 numerically, for a finite but large system such that we can approximate the behavior in the center of the chain to the behavior in an infinite system. In the previous chapter, we studied 2-D systems containing the magnetic impurities, however, when studying spin chains, we can simply consider finite 1-D systems thanks to the locality of the interactions and to our interest in the behavior of the band structure along

the chain. This allows us to easily evaluate Eq. 3.2.

We have computed Eq. 3.2 numerically for a 1-D superconductor of a finite number of sites and compared it to the analytical solution obtained from Eq. 3.3. In Fig. 3.9, we plot the density of states for both (a) numerical calculation and (b) analytical expression. Similar to the real-space calculation, the density of states is obtained from the imaginary part of the retarded Green's function:

$$\rho(\omega) = -\frac{1}{\pi} ImG_{BCS}(\vec{k}, \omega + i0^{+}) \tag{3.5}$$

The two cases show good agreement, even for short systems, the numerical calculation in Fig. 3.9 (a) was obtained from a system of 101 sites. The superconducting energy gap is clearly visible for $|E| < 0.75$ meV, along with the quasi-particle peaks. The parameters used are $a = 3.36$ Å, $k_F = 0.15\ a_0^{-1}$ and $\Delta = 0.75$ meV, values used to describe $Bi_2Pd$.

We can also observe a cutoff in the density of states when $k > k_F$. This is observable when $k_F$ is smaller than the Brillouin zone $\pi/a$. These $k$ values behave pathologically, and beyond this $k$ value the system is not well described. The density of states becomes well behaved when $k_F > \pi/a$. If we think in terms of real space, this shows that the theory is not good when the $r$ values in real space are small, but is well behaved when the distances considered are rather big. The reason for this is the long-distance limit taken in the evaluation of the analytical real-space Green's function. The approximation is good when we consider spin chains in the diluted limit [9], [92], [113], [114], where the distance between impurities is of the same order as the Fermi wavelength of the superconductor.

### 3.2.2 Effective Hamiltonian

The next step is to add the effect of the magnetic impurities to the Green's function. To this end, we can solve Dyson's equation to obtain the full $G(\vec{k}, \omega)$ function of the infinite system. Similar to the real-space calculation, the total Green's function can be obtained:

$$G(\vec{k}, \omega) = G_{BCS}(\vec{k}, \omega) + G_{BCS}(\vec{k}, \omega)\Sigma(\vec{k}, \omega)G(\vec{k}, \omega). \tag{3.6}$$

To include the effect of the impurities in the system, we model their effect, as explained in the previous chapter, as the Kondo Hamiltonian:

$$\hat{H}_{impurity} = \sum_{j}^{N} (-K_j \tau_z \sigma_0 + J_j \vec{S_j} \cdot \vec{\alpha}) \tag{3.7}$$

Where $K_j$ is non-magnetic potential interaction and $J_j$ is the magnetic exchange interaction of impurity $j$. All the matrices in Eq. 3.6 are $4 \times 4$ operators, $\Sigma(\vec{k}, \omega)$ is the self-energy term accounting for the effect of the impurities. Due to the locality

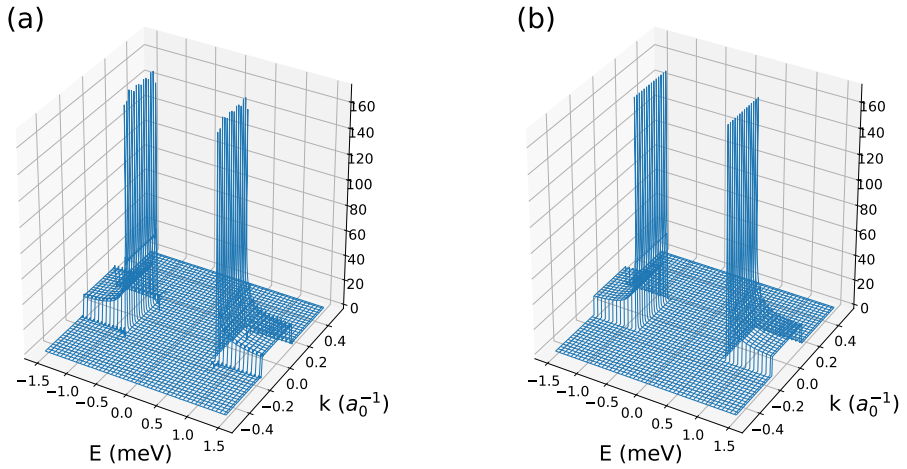


Figure 3.9: Density of states obtained for a superconductor. (a) From numerical Fourier transform (Eq. 3.2) for a 1-D system with 101 sites. (b) Analytical calculation (Eq. 3.3). Parameters: $a = 3.36$ Å, $k_F = 0.15\ a_0^{-1}$, $N_0 = 0.037/eV$, Dynes broadening $\Gamma = 0.01$ meV and $\Delta = 0.75$ meV. A cut in the density of states is visible for values $k > k_F = 0.15\ a_0^{-1}$.

of the spins and assuming they are identical and ferromagnetically ordered, this term can be easily calculated in the reciprocal space:

$$\Sigma_{imp}(\vec{k},\omega) = \sum_{\vec{R}} \langle \vec{R}|\hat{H}_{impurity}|0\rangle e^{i\vec{k}\cdot\vec{R}} = -K\tau_z\sigma_0 + J\vec{S}\cdot\vec{\alpha}, \tag{3.8}$$

Where the matrix element $\langle \vec{R}|\hat{H}_{impurity}|0\rangle$ is only evaluated between the 0 and $\vec{R}$ unit cells of the periodic system. We also need to add the effect of the spin-orbit coupling to the self-energy term. In chapter 2, we showed that the Rashba coupling acted effectively as a hopping term between neighboring sites with opposite spin. Doing the transformation into a 1-D $k$-space lattice, and expressing in the Nambu $k$ basis, we find:

$$\Sigma_{SOC}(\vec{k},\omega) = 2\alpha_R \sin(\vec{k}a)\tau_z\sigma_y \tag{3.9}$$

We solve Dyson's equation, by setting $\Sigma(\vec{k},\omega) = \Sigma_{inp}(\vec{k},\omega) + \Sigma_{SOC}(\vec{k},\omega)$ (Eq. 3.6) to obtain the total Green's function, $G(\vec{k},\omega)$. From this expression, we want to compute the Hamiltonian of the infinite spin chain, $H(\vec{k})$. But as we will see, this is not a simple task. The $G_{BCS}$ function is not a resolvent in the Nambu space, as such inverting the Green's function, $G(\vec{k},\omega)$, to find the bulk Hamiltonian [135], does not work:

$$\hat{H}(\vec{k}) \neq -G^{-1}(\vec{k},\omega=0) \tag{3.10}$$

Instead, we take into account that we are looking for the poles of the Green's function near $\omega = 0$. Then, we can expand the inverse Green's functions about 0

in the $\omega$ variable, approximately find the zero of the inverse of the Green's function and thus, find the poles of the Green's function:

$$0 = G^{-1}(\vec{k},\omega) \approx G^{-1}(\vec{k},\omega=0) + \left(\frac{\partial G^{-1}(\vec{k},\omega)}{\partial\omega}\right)^{-1}_{\omega=0} \omega. \tag{3.11}$$

This equation gives the poles of the Green's function near the Fermi energy, $\omega = 0$. Then these values of $\omega$ correspond to the bands near the Fermi energy, because *the bands are the poles* of the Green's function. The bands, expressed as the eigenvalues of the Hamiltonian, are then obtained [32]:

$$\hat{H}(\vec{k}) = -\left(\frac{\partial G^{-1}(\vec{k},\omega)}{\partial\omega}\right)^{-1}_{\omega=0} G^{-1}(\vec{k},\omega=0) \tag{3.12}$$

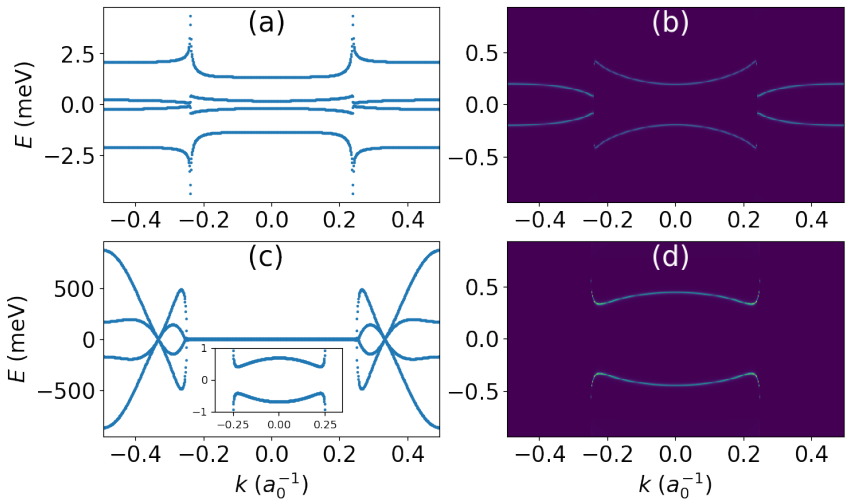


Figure 3.10: (a) and (c) Band structure obtained from Eq. 3.6, using the analytical Green's function from Eq. 3.6. (b) and (d) Resulting PDOS from the imaginary party of the Nambu Green's function. Parameters: $J = 2.5$eV, $\Delta = 0.75$ meV, $N_0 = 0.037$/eV, $\alpha = 3.0$ eV-Å $K = 5.5$ eV, $a = 3.36$ Å. (a) and (b) $k_F = 0.75\ a_0^{-1}$, (c) and (d) $k_F = 0.25\ a_0^{-1}$.

The bands in $\hat{H}(\vec{k})$ are in a matrix shape, expressed in the original Nambu basis, to find the actual *in-gap* bands, we need to diagonalize the total matrix.

In Fig. 3.10 (a) we obtain 4 bands, as the result of diagonalizing the $4 \times 4$ Hamiltonian form Eq. 3.12. Calculations on a single impurity, solving for the in-gap states analytically or using the above procedure, show that only the lower-energy states are good approximations of the actual in-gap state. In this calculation

$k_F = 0.75\ a_0^{-1}$, but the Brillouin zone is $(-\frac{\pi}{a}, \frac{\pi}{a}) \approx (-0.49, 0.49)a_0^{-1}$. Meaning, that we will have folding in the band structure, this is visible in the discontinuity at $k = \frac{2\pi}{a} - k_F \approx \pm 0.24\ a_0^{-1}$. Despite this fact, the bands behave properly, and the lower bands perfectly match the density of states in Fig. 3.10 (b). Figure 3.10 (c) and (d) are obtained with the same parameters but with $k_F = 0.25\ a_0^{-1}$. As we can observe in Fig. 3.10 (c), for $k > k_F$ values, the bands go to very high energies, as the Green's function is not defined for this $k$ range. As a consequence, these points fail to describe the system. The inset in Fig. 3.10 (c) shows the zoomed-in bands for smaller energies, the two lower bands perfectly match the PDOS depicted in panel (d).

## 3.3 Topological invariants

We have seen that we can compute the Green's functions in the reciprocal space for infinite and finite chains, also we are able to obtain the renormalized Hamiltonian. Our next goal is to evaluate a topological invariant that defines the topological phase of the system. As discussed in chapter 1 and reported in previous works [59], [136], a chain of magnetic impurities in a 1-D superconducting system belongs to the BDI topological class due to its symmetries. The relevant topological invariant in the case is the winding number ($w$). In the following, we will find a procedure to evaluate this number for infinite and finite chains, using numerical calculations.

### 3.3.1 Winding number evaluation

As previously discussed, a 1-D infinite chain on a superconductor has chiral (or sublattice) symmetry. As a consequence, the Hamiltonian can be rewritten under the following form:

$$H(k) = \begin{pmatrix} 0 & A(k) \\ A^\dagger(-k) & 0 \end{pmatrix} \tag{3.13}$$

Where $A$ is a $2 \times 2$ matrix in the spin sector. This representation is retrieved by performing a change of basis to the Majorana representation, and express it in terms of the Majorana operators $\gamma = (\hat{c} \pm \hat{c}^\dagger)/\sqrt{2}$. For a $2 \times 2$ Hamiltonian, Eq. (3.13) can be written as:

$$H(k) = d_x(k)\tau_x + d_y(k)\tau_y, \tag{3.14}$$

where the change of basis has permitted us to have a zero component of $\tau_z$, because $\tau_z$ anticommutes with the Hamiltonian and defines the chiral symmetry of the system [42]. The vector $\vec{d} = (d_x, d_y)$ defines a closed trajectory in the complex plane in the first Brillouin zone. As discussed in chapter 1, the winding number, $w$, is defined as the number of complete turns described by $\vec{d}$ about zero, as such, $w \in \{\mathbb{Z}\}$. However, for a 1-D system such as a spin chain on a superconductor, $w$ is takes values in $\{-1, 0, 1\}$ [59]. The winding number can be evaluated:

$$w = \frac{1}{2\pi} \int_{-\pi/a}^{\pi/a} dk (d_x \frac{d}{dk} d_y - d_y \frac{d}{dk} d_x), \tag{3.15}$$

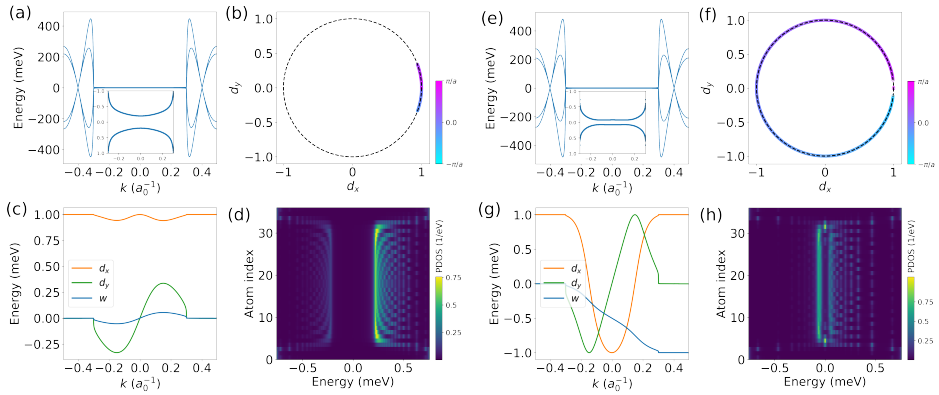


Figure 3.11: Calculations for ferromagnetic spin chains in trivial (a)-(d) and topological (e)-(h) state. (a), (e) Calculated band structure with 4 bands, insets show the two lower energy bands where we can observe the trivial (a) and topological (e) gap. (b), (f) Normalized $\vec{d}(k)$ as $k$ is varied. To facilitate the visualization of the trajectory, $k$ values go from $-\pi/a$ (in cyan) to $\pi/a$ (in magenta). (c), (g) Evolution of $d_x$ (orange), $d_y$ (green) and $w(k)$ (blue) as a function of $k$. (d), (h) Finite 30 atomic chain calculation with same parameters as the analytical one. We plot the PDOS in 2-D map as a function of the atomic site in the chain versus the energy. Parameters: (a)-(d) $J = 2.0$ eV and (e)-(h) $J = 2.7$ eV, $K = 5.5$ eV and $\alpha_R = 3.0$ eV-Å, the Fermi vector is $k_F = 0.3a_0^{-1}$, and the spin is $S = 5/2$, the metal density of states at the Fermi energy is $N_0 = 0.037$/eV and $\Delta = 0.75$ meV.

where $\vec{d}$ has been previously normalized. Mathematically equivalent expressions can be obtained by using the trajectories in the complex plane of $z = Det(A)/|Det(A)|$ as shown in Refs. [59] and [42]. But they involve the evaluation of the $log(z)$ that plagues the computation with numerical problems due to artificial discontinuities caused by the logarithm's branch cut. Expression 3.15 however, is numerically simple and accurate to evaluate.

Although $w$ is the good topological invariant for 1-D systems, we want to compare with numerical calculations in 2-D superconducting systems. We have modeled the Rashba interaction for a two dimensional system, however, the relevant interaction allowing the formation of MBS involves only the SOC along the chain, and the perpendicular coupling has a minimal effect. As such, the Rashba is an effective 1-D interaction [96]. Additionally, our calculations have a highly local character, meaning that the chain sites are unaffected by the presence of sites in the perpendicular direction. As a result, the winding number still can describe the topological state of the 2-D spin chain accurately.

To exemplify this calculation, we compute the bands and corresponding $\vec{d}$ vector for two cases in an infinite chain, Fig. 3.11 shows the results. Figure 3.11 (a)-(d)

correspond to a spin chain on a superconductor in the trivial phase. Figure 3.11 (a) shows the band structure, in this case $k_F = 0.3\ a_0^{-1}$. As previously noted, for $k > k_F$ the band structure is unreliable, the inset shows a zoom for $k \leqslant k_F$, and the two lower energy bands are depicted, here the trivial energy gap can be observed. Figure 3.11 (b) and (c) show the evolution of $\vec{d}$, in (b) we have depicted the trajectory of the normalized vector in the complex plane in the range of the first Brillouin zone. Using a gradient of colors, we indicate the evolution from $k = -\frac{\pi}{a}$ (cyan) to $k = \frac{\pi}{a}$ (magenta). As shown, $\vec{d}$ oscillates about $(1.0 + 0\mathrm{i})$, and does not complete any turn about zero. The same behavior can be extracted from panel (c). Here, we have depicted the $d_x$ (orange curve) and $d_y$ (green curve) components versus $k$, we notice that for $k > k_F$ these quantities do not show any evolution, further supporting the fact that for high $k$ values, the bands fail to describe the system and, hence, these points do not contribute to the topological character. However they could contribute, and this contribution would be spurious. In the same plot, we also show the cumulative value of $w$ (blue curve). This number is obtained by evaluating the following expression for every $k$ point:

$$w(k) = \frac{1}{2\pi} \int_{-\pi/a}^{k} dk' (d_x \frac{d}{dk'} d_y - d_y \frac{d}{dk'} d_x), \tag{3.16}$$

It shows some evolution for $|k| < k_F$, but its value goes back to zero at the end of the first Brillouin zone, resulting in $w = 0$ for this particular case. To check how this topological phase translates into finite system, in Fig. 3.11 (d) we plot the PDOS of a 30-atom spin chain on a 2-D superconductor. The plot is a color map of the atomic sites versus energy and the PDOS is indicated by the color map. As shown in this case, the lowest energy in-gap states are found at $\sim 0.2$ meV all along the chain, but no edge state close to zero energy is observed. On the other hand, Fig. 3.11 (e)-(h) correspond to a topologically non-trivial phase of the infinite chain. The parameters are kept the same as for Fig. 3.11 (a)-(d) and we have simply increased the magnetic coupling, from $J = 2.2$ eV to $J = 2.7$ eV. The band structure in (e) again, gives unrealistic values for $|k| > k_F$. As shown in the in-set, we observe two in-gap bands at lower energy for $|k| < k_F$. In Fig. 3.11 (f), we show the evolution of the $\vec{d}$ vector. In this case, it completes a clockwise turn about zero, resulting in a winding number of $w = -1$. This can be further noticed by looking at the evolution of $d_x$, $d_y$ and $w$ versus $k$ (Fig. 3.11 (g)). Again, all the evolution is limited to the $k$ points, $|k| < k_F$. We observe, how $w$ evolves from zero to $-1$. We conclude that this corresponds to a topological phase of the system. To further verify this, in Fig. 3.11 (h) we plot the PDOS for a finite chain using the same parameters. In this case, two edge states emerge at zero energy. The topological character of the system proves that these are MBS.

Apart from the winding number, a lower-symmetry topological invariant, may also be calculated. The $\mathbb{Z}_2$ topological invariant is obtained from the Pfaffian of the system. For a chiral Hamiltonian written as in Eq. 3.13 the Pfaffian can be easily evaluated using $Pf[H(k)] = Det[A(k)]$. And the $\mathbb{Z}_2$ topological invariant,

$Q$, becomes:

$$\begin{aligned} Q &= sgn\left[Pf[H(k=0)] \times Pf[H(k=\pi/a)]\right] \\ &= sgn\left[d_x(k=0) \times d_x(k=\pi/a)\right] \end{aligned} \tag{3.17}$$

Obviously, this topological invariant carries less information than the winding number, as it only takes values in $\mathbb{Z}_2 = \{-1, 1\}$. It only indicates whether the system is in the trivial ($Q = 1$) or topological ($Q = -1$) phase. The winding number, on the other hand, distinguishes two different topologically non-trivial phases ($w = \pm 1$). However, $Q$ is easier to obtain, as it only evaluates the Hamiltonian in two $k$ points, making this invariant more convenient to calculate in certain situations. Equation 3.17 is valid when we have a high $k_F$ value. However, when $k_F$ is smaller than the first Brillouin zone, as we have already described, the $k$ points such that $|k| > k_F$ are not reliable, in those cases the Pfaffian in $k = \pi/a$ is instead evaluated in $k^*$ close to $k = k_F$.

The winding number can be particularly difficult to evaluate, as a high number of $k$ points is needed. The value is highly dependent on the evolution on $\vec{d}$, and it rapidly changes at $k = k_F$ due to the drastic changes of the band structure at this $k$ point. To avoid errors, we have systematically increased the number of $k$-points and followed the evolution of the different topological invariants to reach a coherent description of the topological character of the studied phases.

In the previous calculations, we have obtained the effective Hamiltonian (Eq. 3.12) for a 1-D infinite spin chain on a superconductor, starting from the analytical Green's function. The winding number can be then easily computed from expression Eq. 3.15. And the topological phase, found for the infinite system, corresponds to the emergence of zero-energy states in finite systems. The band structure is only relevant for $k$ values $|k| < k_F$. In the case that we use a $k_F$ bigger than the 1st Brillouin zone, the band folding solves this problem, so all $k$ points properly describe that system.

### 3.3.2 Topological phase diagrams

In the following, we want to apply the topological invariant calculation, and do a systematic evaluation as we change the parameters of the system. The goal is to be able to map the parameter space, so that we can easily identify the topological regions of the system.

Figure 3.12 shows the resulting phase diagrams as we study the phase space by varying three different parameters versus the Fermi vector. We systematically evaluate both $Q$ and $w$, as well as the energy gap, that we obtain from the band structure. Figure 3.12 (a)-(c) shows color maps of the energy gap, the red and blue color respectively indicate $Q = 1$ and $Q = -1$. So the areas with a positive

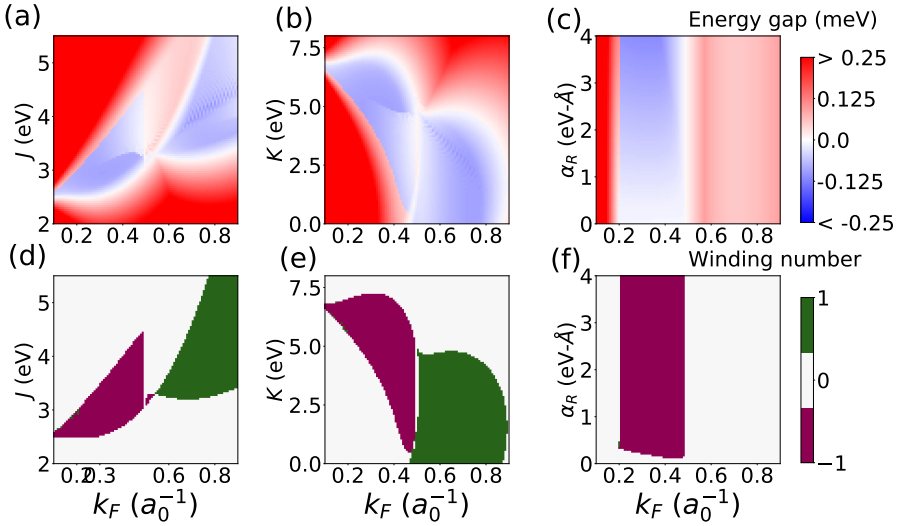


Figure 3.12: Phase diagrams obtained for a ferromagnetic spin chain with normal-metal DOS at the Fermi energy $N_0 = 0.037$/eV, $\Delta = 0.75$ meV and spin $s = 5/2$. (a)-(c) Energy gap of the system multiplied by the $\mathbb{Z}_2$ topological invariant, $Q$, allowing for differentiation of trivial ($Q = 1$) and topological ($Q = -1$) phases. (d)-(f) Winding number. The green areas correspond to $w = -1$ (cases like the one shown in Fig. 3.11 (f)) and the magenta areas to $w = 1$, here the winding vector, $\vec{d}$ completes a turn in the opposite direction. (a) and (d) Phase diagrams as a function of the Kondo coupling $J$ versus the Fermi wave vector of the system $k_F$, with potential scattering $K = 5.5$ eV and Rashba coupling $\alpha_R = 3.0$ eV-Å. (b) and (e) Phase diagrams as a function of the potential scattering, $K$ versus $k_F$ with Kondo coupling $J = 3.0$ eV and Rashba coupling $\alpha_R = 3.0$ eV-Å. (c) and (f) Phase diagrams as a function of the Rashba coupling, $\alpha_R$ versus $k_F$ with Kondo coupling $J = 3.0$ eV and potential scattering $K = 5.5$ eV.

gap (in red) correspond to the trivial phase, and the negative gaps (in blue), are topologically non-trivial. We can also observe that in the transition between the two phases, when the system undergoes a TPT, the energy gap goes to zero (in white). Indeed, in order to have a change in the topological character, a gap closing is required [42], [43].

If we look at Fig. 3.12 (a), magnetic coupling, $J$ versus $k_F$, we can easily distinguish two branches where the gap closes. One is the gap closing occurring at $k = 0$ going from $k_F \sim 0.1\ a_0^{-1}$ to $k_F \sim 0.75\ a_0^{-1}$, and at the second one is the gap closing at $k = \pi/a$ visible at low values of $J$ for $k_F > 0.5\ a_0^{-1}$. In other cases, however, the gap closing at a TPT can be difficult to observe. For example, in Fig. 3.12 (a) for Fermi vector values such that $k_F < 0.5\ a_0^{-1}$ and $J$ couplings going from $\sim 2.5$ eV to $\sim 4.5$ eV, the topological character changes, but we do not see a

clear zero gap in this area. Here, the gap closes at a $k^*$ point close to $k_F$, but this transition is very abrupt, requiring a high number of k-points and a fine tuning of the parameters to properly observe the gap closing.

Figure 3.12 (d) shows the same phase diagram, but here we plot the winding number, $w$. The magenta and green areas correspond to $w = -1$ and $w = 1$ topological phases, respectively. While the white areas are trivial. As expected, the $w = \pm 1$ areas perfectly match the topological $Q = -1$ areas from panel (a). This is true for the three phase diagrams in Fig. 3.12. A similar behavior is observed in panels (b) and (e), these are the phase diagrams of the potential scattering, $K$ versus $k_F$. Again, there are two easily observed white branches corresponding to the gap closings at $k = 0, \pi/a$, while the transition at $k^*$ requires a high number of $k$ points to be distinguished.

It is interesting to note, the big effect that the potential scattering, $K$-term in Eq. 3.7, has on the topology of the spin chain. The effect of magnetic coupling, $J$ is known to be necessary, as exchange interaction is required to have in-gap states, as such, we can observe on panels (a) and (d) from Fig. 3.12 that no topological phase is obtained for $J = 0$. Potential scattering, on the other hand, is not necessary for the system to enter the topological phase, as we can observe in panels (b) and (e) topological regions for $K = 0$. However, it has an important effect on the topology. If we look again at Eq. 3.7, $K$ is an on-site term that has a similar effect as a chemical potential in the system. This will shift the on-site energies of the sites, and have a big effect on the topological phase.

Figure 3.12 (c) and (f) show the phase diagrams as a function of the Rashba coupling strength, $\alpha_R$, versus $k_F$. Overall, we notice that the topological state is independent of $\alpha_R$, and the system is on the topological phase for $0.2a_0^{-1} < k_F < 0.5a_0^{-1}$. This is in good agreement with the definition of $Q$, Eq. 3.17, since the term Rashba banishes at $k = 0, \pm\pi/2$, the topological phase should not depend on the presence or absence of spin-orbit coupling. However, if we pay closer attention to Fig. 3.12 (f), we can observe that the system is in the trivial state for small values of $\alpha_R$. Indeed, topological phases on ferromagnetic chains can *only* be achieved on systems with Rashba interaction, even if $\alpha_R$ is infinitesimally small [81], [82]. The previous remark shows that Eq. 3.17 should not be blindly applied. Moreover, in Fig. 3.12 (e) we can see that the topological gap becomes bigger with an increasing $\alpha_R$, giving better protection to the MBS arising in finite systems [125].

The number of MBS that emerge on a finite system is given by the difference in the winding number at the domain wall between regions with different topological phase, $|w_1 - w_2|$ [114]. With the consequence that an interface carrying two Majoranas could be created between two superconductors with $w = 1$ and $w = -1$. Up to now, we have only observed the emergence of MBS in ferromagnetic chains with $w = \pm 1$. As such, finite spin chains in a superconductor, will host one MBS

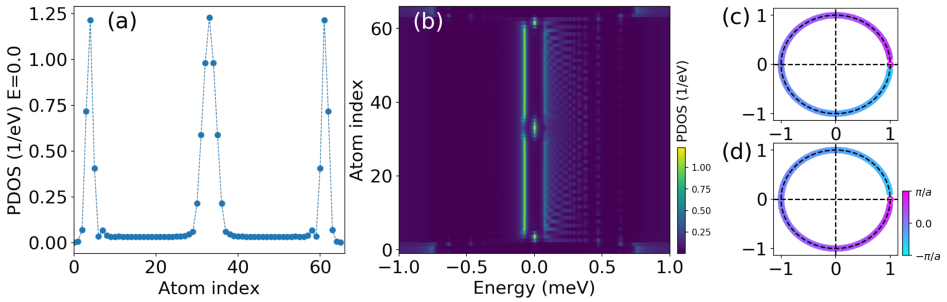


Figure 3.13: Chain with $\alpha_R = 3.0$ eV-Å in the first half and $\alpha_R = -3.0$ eV-Å in the other half. (a) PDOS profile at $E = 0$ along the chain. (b) Color map of PDOS along the chain's axis versus energy. The state at E=0 found in the middle of the chain is constituted by two MBS. (c)-(d) Winding number computer in the firs and second half of the chain, respectively. Parameters: Exchange interaction $J = 2.7$ eV, potential scattering $K = 5.5$ eV, the Fermi vector is $k_F = 0.3\ a_0^{-1}$

on each end. However, if we look at the phase diagrams in Fig. 1.8, there are some regions where there's an abrupt change in $w$. Particularly, in Fig. 1.8 (d) and (e) when $k_F$ is close to $\pi/a$, there are regions with $w = 1$ and $w = -1$ very close to each other. An interface between two superconductors of very different electron density, such that one has a $k_F < \pi/a$, and the other one has $k_F > \pi/a$, a spin chain straddling the interface will have a change of winding number of 2, and hence present two MBS at the interface.

Alternatively, the sign of the $\alpha_R$ parameter changes the sign of $w$ [137]. Like this, in the domain wall of a spin chain with two different spin orbit coupling interactions, we expect two MBS to arise. The behavior of a ferromagnetic spin chain in the presence of Rashba SOC can be compared to a non-collinear spin chain [9], [138], following this analogy, a chain with two $\alpha_R$ sections with different sign can be compared to a non-collinear spin chain with a domain wall separating two sections with opposite chirality [114], [137]. This situation is depicted in Fig. 3.13. Here, we have plotted a 60-atom chain, with $\alpha_R = 3.0$eV-Å on one half of the chain and $\alpha_R = -3.0$ eV-Å in the other. Figure 3.13 (a) shows the PDOS profile at zero energy and along the chain. As observed, there are two edge states localized at the ends and another state in the middle of the chain. This can also be observed in Fig. 3.13 (b), the color map clearly shows a zero energy state at the domain wall between the two sections of the chain. Figure 3.13 (c) and (d) show the winding number calculation with different sign of $\alpha_R$. As it can be noted, the $\vec{d}$ trajectory is completed in opposite directions in each case.

### 3.3.3 Numerical calculations

So far, we have obtained the effective Hamiltonian and computed the topological invariants, for an infinite ferromagnetic spin chain on a superconductor. In a similar spirit, as Fig. 3.9, we want to obtain all previous calculations for a finite system, using purely numerical approach, and compare it to analytical results. Our goal is to study the validity of our calculations of finite spin chains on 2-D superconductors [31], like the results presented in 3.1. We have verified that the dimensionally does not drastically affect the emergence of edge states in finite systems, our calculations in 2-D superconductors show that the DOS of in-gap states decay in only 5 sites perpendicular to the chain, and the resulting spectra does not differ a lot compared to 1-D simulations. Similarly, in 3-D systems, the addition of extra layers does not affect the overall DOS distribution of in-gap states. This is largely due to the presence of the Rashba interaction being limited to the first superconducting layer in our calculations.

#### Numerical evaluation of topological invariants

Figure 3.14 shows the numerical calculation for a finite spin chain. Figure 3.14 (a), (b) and (d) are obtained for a 30 atom impurity chain on a 2-D superconductor. In order to be able to compute the band structure of the system by solely numerical means, we need to simulate a long enough chain. Figure 3.14 (c), (e) and (f) were obtained from a 1001-atom chain in a 1-D superconductor with the same parameters.

Figure 3.14 (a) shows the spectra on the first atom of the chain. The 30-atom chain is located at the center, of a 2-D rectangular superconducting array with dimensions $N_x = 36$ and $N_y = 5$ sites. The exchange coupling is $J = 3.5$ eV, the potential scattering amplitude is $K = 5.5$ eV, Rashba coupling is $\alpha_R = 3.0$ eV-Å and the Fermi vector is $k_F = 0.7a_0^{-1}$. By looking at the topological phase diagram in Fig. 3.12 (a), we can come to the conclusion that these parameters yield a topological solution with winding number $w = 1$. Figure 3.14 (b) shows PDOS along the chain's profile at zero energy. As shown, the zero-energy states are well localized at the chain's ends. More information about the spatial distribution of the in-gap states is found in Fig. 3.14 (d). We can again see the zero-energy states at the ends of the spin chain, and a small energy gap that separates them from the rest of in-gap states. The resulting band structure obtained for a finite chain is shown in Fig. 3.14 (c).

We obtain $G(\vec{k}, \omega)$ from the real-space Green's function $G_{i,j}(\omega)$ by using a finite Fourier transform (Eq. 3.2), and a sufficiently high number of atoms in a 1-D finite system. We then calculate the $k$-resolved Hamiltonian from the renormalized Green's function, Eq. (3.12). In red, we plot the numerical results, and for comparison the analytical band structure for an infinite chain is plotted as black dashed lines. The two show good agreement, but it can be improved by using even longer spin chains, and increasing the number of $k$ points in the calculation.

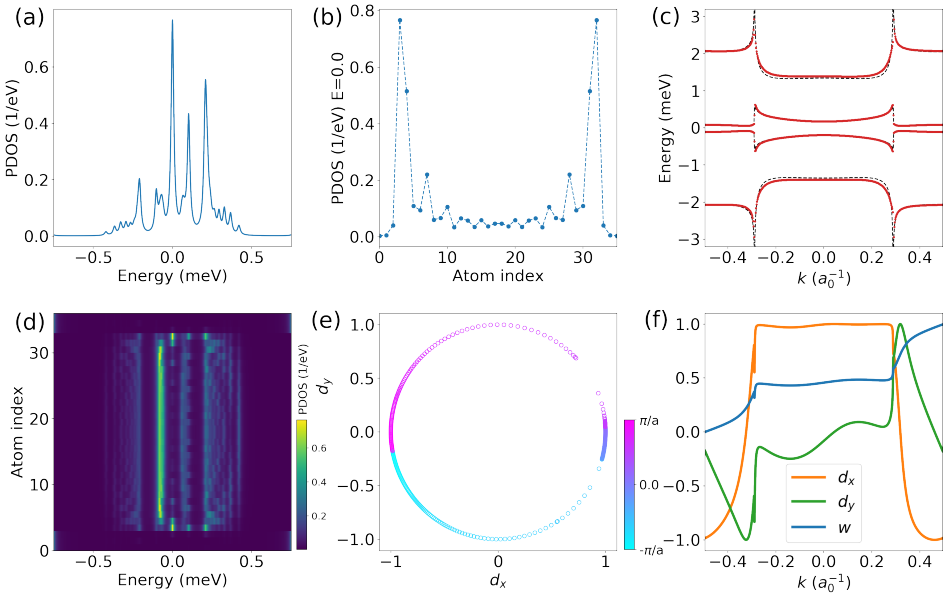


Figure 3.14: Numerical results of 30-atom impurity chain of a 2-D superconductor with dimensions $N_x = 36$ and $N_y = 5$. (a) Spectrum obtained on the first atom of the chain. (b) PDOS at zero energy along the chain's axis. (c) Renormalized bands, analytical calculation (black dashed lines) and numerical result (in red) for a 1001-atom chain in a 1-D superconductor. (d) PDOS spectra along the 30 atom chain. (e) Corresponding trajectory of winding vector $\vec{d}$, the color bar shows the $k$-points where $\vec{d}(k)$ is evaluated. (f) $d_x$, $d_y$ and cumulative winding number $w(k)$, Eq. (3.16) as a function of $k$. Parameters: $\Delta = 0.75$ meV, $N_0 = 0.037$/eV, $k_F = 0.7\ a_0^{-1}$, $\alpha = 3.0$ eV-Å $J = 3.5$ eV, $K = 5.5$ eV.

Figures 3.14 (e) and (f) depict the evolution of the $\vec{d}$ vector and winding number for the above case. As we can see, $\vec{d}$ completes a turn about zero in the positive direction, resulting in $w = 1$ and proving the topological origin of the edge states in the 30-atom chain. The evolution of $d_x$, $d_y$ and $w$ is depicted in Fig. 3.14 (f). It is interesting to note here that $d_x$ and $d_y$ are not perfectly symmetrical for positive and negative values of $k$. This is again, due to numerical problems. The asymmetry can be reduced by taking sufficiently small $\omega$ steps that improves the numerical precision of the derivative in Eq. (3.12). Also, small oscillations can appear in these curves due to the Fourier transform from the finite-chain in real space to $k$-space, Fig. 3.14 (f).

The agreement between the numerical calculation and the analytical solution is of special interest, because it shows that the band structure and topological invari-

ants of a system can be calculated from a finite system and by means of purely numerical calculations.

### Numerical phase space

We have seen that it is possible to determine the topological character of a system from numerical calculations on a finite system. Compared to the analytical approach, it requires a much higher computational power, but a big advantage of the finite-system calculation, is that we can directly observe the emergence of edge states when entering the topological phase, whereas the infinite chain calculation only gives information about the bulk system. Moreover, for a long-enough chain, the middle of the chain should be a good approximation of the bulk system. With this in mind, we want to explore the phase space by looking at the in-gap states of the bulk and edges of the system. And, again, compare the numerical and analytical approaches.

We aim to study how the edge states emerge, also we wish to observe when the TPT occurs as we vary one of the parameters of the system. The calculations are performed in finite system, and we look at the PDOS in the edge and the middle of the chain. For comparison, we also obtain the resulting in-gap states in an infinite chain, this will help us distinguish edge states from purely bulk states. To do so, we obtain the Green's function in $k$ space, $G(\vec{k}, \omega)$, and we Fourier transform to real space, such that the PDOS of the infinite system can be evaluated.

In Fig. 3.15, we have plotted the bulk and edge states as a function of the exchange interaction, $J$, for a fixed value of the potential scattering $K = 5.5$ eV (Fig. 3.15 (a)-(c)) or as a function of the potential scattering, $K$, for a fixed value of $J = 3.0$ eV (Fig. 3.15 (d)-(f)) for a 30-atom spin chain. The region between the red dashed lines indicate the topological phase as extracted from the phase diagrams in Fig. 3.12.

Figure 3.15 (a) and (b) show the evolution of the edge and middle atom, respectively, as a function of $J$. As observed, for an increasing $J$, the in-gap states move to zero until they cross, closing and reopening the gap. The crossing coincides with the change in topological character, this is the TPT at $J \sim 2.7$ eV. If we look at the edge atom, Fig. 3.15 (a), the topological phase also coincides with the emergence of an edge state at zero energy. In the middle of the chain (Fig. 3.15 (b)) we observe a closing of the gap and reopening, as the system enters the topological phase. This can be compared with Fig. 3.15 (c), which corresponds to the infinite system calculation. We can observe a good agreement between (b) and (c), showing that some states in (b) are not bulk states but rather a result of the finite length of the chain. The TPT can also be observed in (c) at the same $J$ value.

As the exchange interaction increases, the energy gap starts to close again and

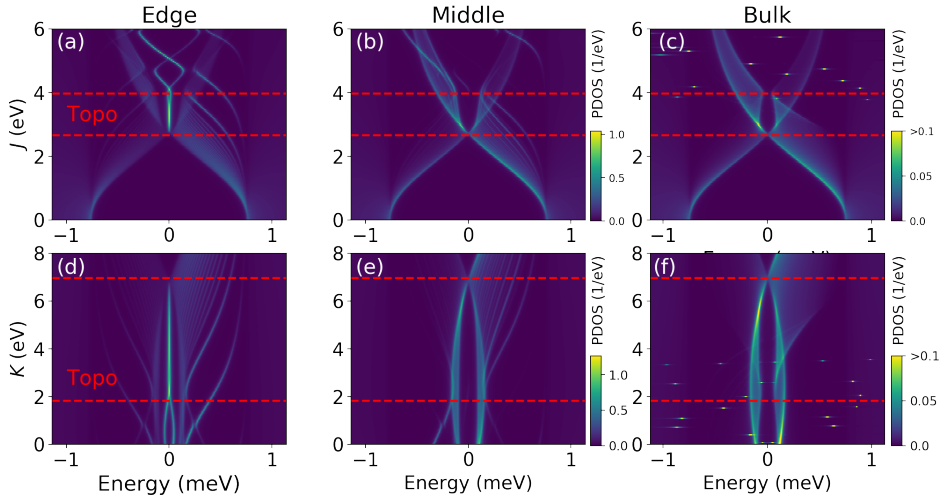


Figure 3.15: Evolution of in-gap states at the edges and at the center of the chain ((a) and (b) respectively) as a function of the couplings for exchange $J$ for a fixed value of the potential interaction matrix element $K = 5.5$ eV and potential $K$, for fixed $J = 3.0$ eV ((d) and (e)) interactions. For comparison, the states at the center of an infinite chain from an analytical calculation are also shown in (c) and (f). As expected, the agreement between the spectra at the mid-site of the finite chain (b) and the site of the infinite chain (c) is excellent, as well as between (e) and (f). The main differences are due to long-range edge states that are absent from the infinite chain. Red dashed lines indicate the TPT as obtained from phase diagrams in Fig. 1.8. Topologically non-trivial phases are found between the two horizontal lines. Parameters: $\Delta = 0.75$ meV, $N_0 = 0.037$/eV, $k_F = 0.4\ a_0^{-1}$, $\alpha = 3.0$ eV-Å, the finite chains ((a), (b), (d) and (e)) are 30-atom long. The PDOS is in (1/eV) units.

at $J \sim 4.0$ eV, there is a new TPT, Fig. 3.15 (b) and (c). We observe a narrowing of the gap, but the gap closing is difficult to observe because a high number of k-points and $J$ values is required to observe this gap closing. As a consequence, we find a zero-energy edge mode between $J = 2.7$ and $J = 4.0$ eV that clearly signals the topological phase, Fig. 3.15 (a).

A similar situation can be observed for the potential scattering study (Fig. 3.15 (d)-(f)). Here, the first TPT is more difficult to distinguish (at $K \sim 2.0$ eV), while the transition at $K \sim 7.0$ eV is easily observed, and perfectly matches the loss of the edge state in Fig. 3.15 (d). The good agreement between numerical and analytical solutions, further supports the validity of numerical calculations for topological studies.

We can also note the finite-size effects on the edge states. In Fig. 3.15 (a) we can observe how the edge state begins to split before the system enters the trivial state at $J \sim 4.0$ eV. This is a direct consequence of the finite length of the chain. We have verified, that for longer chains, this small splitting is shifted to $J$ values closer to the TPT. The above calculations show, overall, a very good agreement between analytical and purely numerical calculations on finite systems, showing that topological properties can be studied in finite-system calculations. In the following, we will take a closer look at the finite-size effects that the spin chains have on the edge states.

## 3.4 Finite-size effects on spin chains in a superconductor

As we have discussed so far in this thesis, MBS in ferromagnetic spin chains are expected to arise at zero energy, however, as we could already observe in Fig. 3.15, the topological edge state shows some splitting. Indeed, the chain's length is a critical parameter for the emergence of MBS in topological phases of the system [128]. And, due to the finite length of the chains, the spatial overlap existing between the two MBS, results in a shift of the edge states from zero to a finite energy [69], [80], [128], [139], [140]. Furthermore, MBS in finite systems can interact with each other but also with other in-gap states [141], which can lead to a periodic oscillation of these edge states [24], [33], [128].

In the following, we will study these edge states at finite energy in finite-size spin chains and study how they evolve as we vary the size of the chain.

### 3.4.1 Energy oscillation and topological state

In 3.3.2 we obtained the phase diagram for spin chains in a superconductor, here, we want to study the parameter space and observe how edge states evolve with the chain's length. Figure 3.16 shows the $J$ vs $k_F$ phase diagram as depicted in Fig. 3.12. Here, we have selected four pairs of parameters (indicated by different shapes in the inset) and obtain their spectra at the edge atom of a finite chain, as we vary its length.

The phase diagram depicts the winding number as computed in 3.3.1. The white areas are the trivial phase, while the magenta and green areas correspond to $w = \pm 1$. Figure 3.16 (a) is a trivial case. As we can see, the lowest-energy in-gap states are found at $\sim 0.3$ meV, and they remain at this energy as the number of atoms increases. Figure 3.16 (e) shows the spatial distribution for the lowest-energy state for a chain of 100 atoms. As we can observe, the in-gap states are distributed along the chain and not localized at the ends.

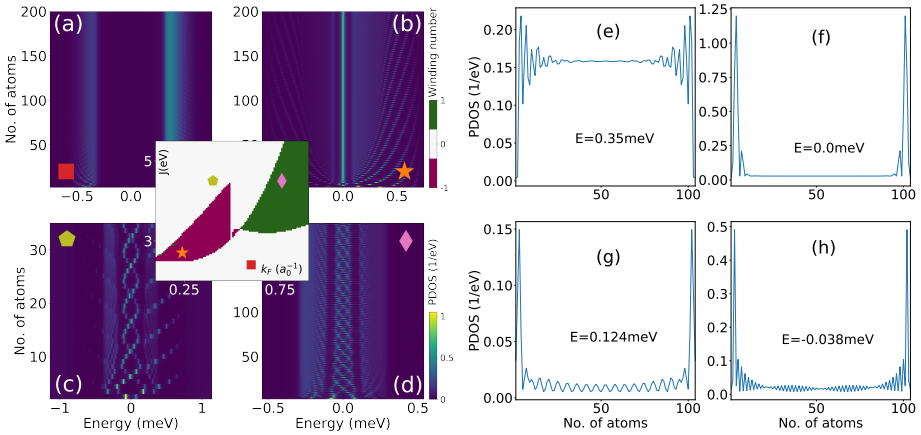


Figure 3.16: (a)-(d) Evolution of edge states as a function of the number of atoms in the spin chain. Inset: Topological phase diagram. We selected 4 pairs of parameters: exchange interaction ($J$) and Fermi vector ($k_F$), as indicated by the different shapes in the phase diagram. (e)-(h) Corresponding spatial distribution of the PDOS along the chain's axis for a fixed length of 100 atoms. Other parameters: $\Delta = 0.75$ meV, $N_0 = 0.037$/eV, $\alpha_R = 3.0$ eV-Å $K = 5.5$ eV and $a_c = 3.36$ Å.

On the other hand, Fig. 3.16 (b) corresponds to a topological phase ($w = -1$), here we see that for chains as short as 5 atoms, there's a strong peak at zero energy. As the length of the chain is increased, the edge state remains at zero energy. The PDOS profile along the chain's axis in Fig. 3.16 (f) show that these states are very localized at the edges, as expected for MBS. Figure 3.16 (c) shows a different behavior, in this case the edge states oscillate in energy around zero with a period of $\sim 5$ atoms, and panel (g) shows that these states are also well localized at the edges. Here, the winding number ($w = 0$) indicates that this is a trivial state of the chain.

Finally, Fig. 3.16 (d) also shows an oscillatory behavior, but in this case the system is in a topological phase ($w = 1$). The period here is about 60 atoms, and two different branches are observed, which can be separated between even and odd number of atoms (see Fig. 3.17 (a) and (b)). This behavior is completely compatible with the experimental findings of topological spin chains [128]. In the present study, we have observed energy oscillations of the edge states in spin chains, however, the topological phase of the system cannot be related with the emergence of the oscillations, because we have observed them for trivial and topological states.

### 3.4.2 Moiré periodic oscillations

The period of the oscillations in Fig. 3.16 is not straight forward to rationalize. Particularly, Fig. 3.16 (d) presents an even-odd effect with the number of atoms

in the chain. Figure 3.17 (a) and (b) show the split oscillations from Fig. 3.16 (d) in even and odd number of atoms. From these plots, we can see a clearer period of $\sim 105$ atoms.

In the presence of impurities, Friedel oscillations emerge in their vicinity on conducting surfaces [142], in particular also on superconductors [5], [102]. These oscillations follow the relation $\cos(2k_F r + \delta)$, where $k_F$ is the Fermi wave vector, $r$ is the distance to the impurity and $\delta$ is a phase shift [5]. However, if we try to rationalize the oscillations in Fig. 3.16 with this equation, we find that the observed periods are much larger than the expected. To understand the resulting periodicity, we need to take into account the periodical effect of the interaction between spins in superconductors. This oscillation follows $E_J = -\Delta \sin(k_F r)/k_F r e^{-r/\xi}$ [9]. Additionally, we need to consider the periodicity emerging from the discrete lattice distance between spins ($a_c$) [33]. To take into account this discretization, we need to apply a mask function, $f(r)$, to the $E_J$ relation, making non-zero only the values at a $n \times a_c$ distance, with $n \in \mathbb{N}$. To approximate this function, we can take its first harmonic, $f(r) \approx \cos(2\pi r/a_c)$. Then, the energy of the in-gap states with our model will follow

$$E_{YSR}(r) = E_J \times f(r) \tag{3.18}$$

To understand the periodicity, we simply take the oscillatory part from the previous equation:

$$\sin(k_F r) \times \cos(\frac{2\pi r}{a_c}) = \frac{1}{2}\big[\sin(k_F r - \frac{2\pi r}{a_c}) + \sin(k_F r + \frac{2\pi r}{a_c})\big] \tag{3.19}$$

In this expression, we can observe two oscillatory terms, one with high frequency, $k_1 = k_F r + \frac{2\pi r}{a_c}$, responsible for the even-odd effect: this frequency is too high to be visible in our discrete-lattice model, as such, this fast oscillation results in an alternating signal between even and odd sites. The lower frequency of $k_2 = k_F r + \frac{2\pi r}{a_c}$, results in the longer range oscillations.

To better illustrate this model, we solve a simple case where we only consider two sites in the system, *i.e.* an impurity dimer at different inter-impurity distances. We vary the distance in a continuous fashion to obtain the spectra as a function of the impurities distance, shown in Fig. 3.17 (c), the fast oscillation does not allow to properly observe the period. The inset shows a zoomed-in area for inter-impurities distance from 25 to 27.5 $a_c$, here we can verify that, as expected, the period of these oscillations coincides with the frequency in $E_J$. To retrieve the period observed in Fig. 3.17 (a) and (b), we have to select inter-impurity distances that are sites of the underlying superconducting atomic lattice, such that $r = n \times a_c$ with $n \in \mathbb{N}$. This is exactly what is depicted in Fig. 3.17 (d), the period of the oscillations observed here perfectly matches the chain calculation in Fig. 3.16 (d). Finally, we split the resulting structure into even and odd number of atoms (Fig. 3.17 (e) and (f), respectively). Note that the energies in the two-sites model are not

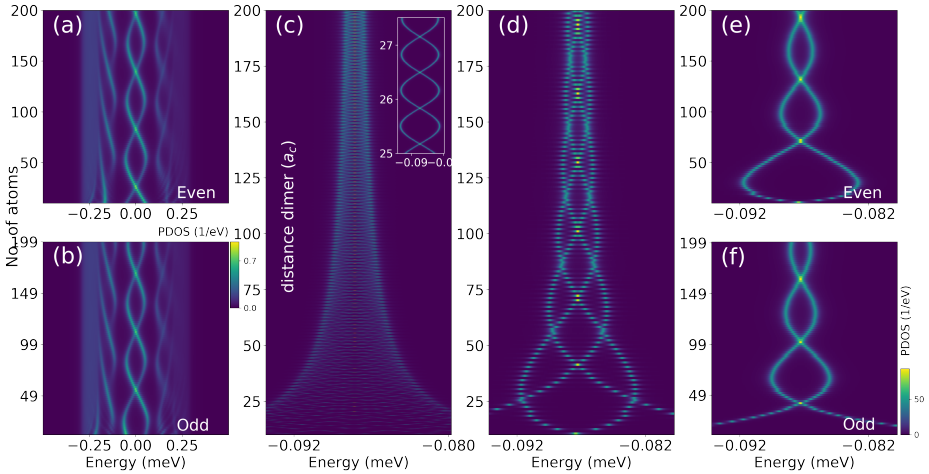


Figure 3.17: Comparison of spin chain and magnetic dimer. (a), (b) Projected density of states in the edge atom as we vary the number of atoms in the chain for even (a) and odd (b) number of atoms, combining (a) and (b) we recover Fig. 3.16 (d). (c)-(f) Dimer PDOS as we vary the distance between the two sites. (c) The distance between the two impurities is varied in a continuous fashion, the inset shows a zoomed in for distances between 25-27 $a_0$. (d) Selected distances extracted from (c) corresponding to integer numbers of $a_0$ and split between even (e) and odd (f) numbers. Comparing (a), (b) and (e), (f) we arrive at the conclusion that the periodicities perfectly match.

around zero, but we expect this behavior not to be energy dependent, and the interactions leading to these oscillations are the same regardless of the state's energy.

By comparing Fig. 3.17 (a) and (b) for the spin chain versus Fig. 3.17 (e) and (f) corresponding to the two impurity model. We can observe that the period on both cases is the same. We conclude that the resulting period is the one of a moiré pattern, product of the interaction between the substrate-mediate oscillations, with a spatial frequency of $k_F$ and the lattice discretization with a wave vector of $2\pi/a_c$. As a consequence, the resulting periodicity highly depends on $k_F$ and $a_c$.

The dependence of the oscillations with $a_c$ and $k_F$ can be used to tune their periodicity. Figure 3.18 show the resulting spectra for different $a_c$ values (a)-(c) and $k_F$ (d)-(f), only for odd number of atoms in the chain. As expected for moiré patterns, slight changes in any of the parameters, lead to highly different periodicities. In particular, as shown in Fig. 3.18 (b) and (e), it is possible to tune the parameters in a way that the obtained period is long enough, so that the edge

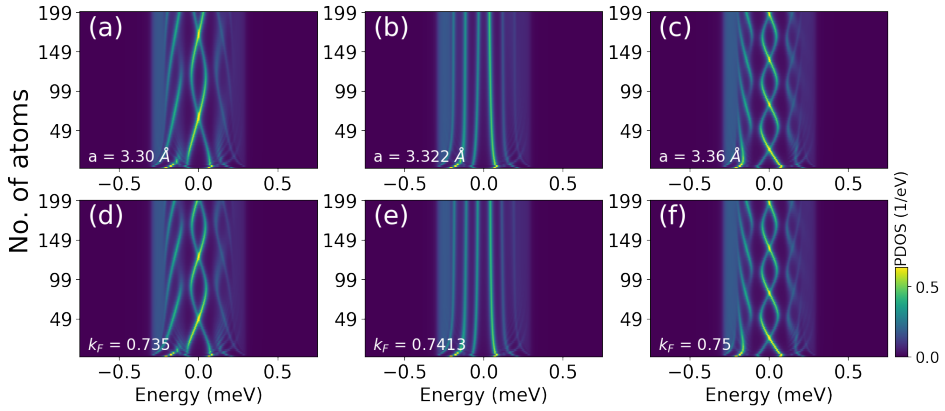


Figure 3.18: Oscillations observed for odd-number spin chains. (a)-(c) for different lattice parameters, $a$ and $k_F = 0.75\ a_0^{-1}$. (d)-(f) for different wave vectors, $k_F$ and $a = 3.36$ Å.

states do not evolve as the number of atoms varies. The edge states in Fig. 3.18 all correspond to topological phases of the system. Thanks to the underlying moiré pattern, we are able to tune these topological edge states to a regime where they are found a fixed and non-zero energy, regardless of the spin chain's length [33].

**Conclusions.** Throughout this chapter, we have reviewed some applications of the Green's function model presented in chapter 2. As shown in 3.1, this model provides a realistic framework able to reproduce experimental data. We explained the YSR states present on Cr spin chains on $\beta$-$Bi_2Pd$, and predicted the emergence of Majorana-like edge states in the same system.

In 3.2, starting from the real space Green's function, we were able to derive an effective Hamiltonian in the reciprocal space, the band structure that we obtained from diagonalizing the Hamiltonian allowed us to compute the topological invariants for infinite systems, as described in 3.3. Furthermore, we could extend the calculation to finite-size systems, and we performed a topological invariant calculation from a purely numerical approach.

Finally, in 3.4, we studied how the finite size of topological spin chains results in non-zero edge states. In particular, we observed how these edge states oscillate in energy as the spin chain's length is varied. We rationalized the period of these oscillations as a moiré pattern resulting from the discrete nature of the superconducting lattice and the spin-spin interaction transmitted through the substrate.

# 4 Scanning tunneling microscopy and experimental techniques

**Introduction.** Scanning tunneling microscopy (STM) was developed by Gerd Binnig and Heinrich Rohrer in the IBM Zurich Research Laboratory in 1981 [6], [143], allowing to observe surfaces with atomic precision for the first time. This major break through in the development of nanoscience, granted the two scientists the Nobel prize in 1986. The first great achievement of this new technique, was to spatially observed the $7 \times 7$ reconstruction on Si(111) [144], being able to resolve the surface down to their individual atoms. Following the STM, other techniques were developed, such as the atomic force microscope (AFM), developed by Binnig a few years later [145].

In the present chapter, we will review the working principle and main concepts behind scanning tunneling microscopy, as well as the use of superconducting tips in STM. All the experimental results in this thesis were obtained with the aid of this technique.

## 4.1 Scanning tunneling microscopy: basics

### 4.1.1 Working principle

Scanning tunneling microscopy relies on the principle of a small current existing between a sharp metallic tip, with an applied bias, and a conducting sample that are brought in proximity, with a vacuum barrier existing between the two. This current, in principle prohibited by classical physics at low bias, is a result of the quantum tunneling effect. The resulting flow of electrons tunneling through the vacuum barrier is the so-called *tunneling current*.

Bardeen described a model for electronic tunneling in a metal-insulator-metal junction [146]. After the development of STM, Tersoff and Hamann [147] derived a simplified tunneling model taking into account the geometry of the STM system (a sharp metallic tip and flat surface). In the Bardeen model, Fermi's golden rule shows that the tunneling process from an initial state ($t$) into a final state ($s$), where $t$ and $s$ denote, for example, tip and sample, respectively, is given by the

transition probability per unit time [148]:

$$\Gamma_{ts} = \frac{2\pi}{\hbar}|M_{ts}|^2\delta(\epsilon_s - \epsilon_t), \tag{4.1}$$

where $|M_{ts}|$ is the tunneling matrix element, which depends on the geometry of the tip, the distance to the sample the electronic wave functions of both surface and tip and the connecting potential. The Dirac delta function in the previous expression, shows that tunneling is only allowed between same-energy states (elastic process). The tunneling current will be $e\Gamma_{ts}$, where $e$ is electron's change.

To calculate the total tunneling current from tip to sample, we integrate over all energies taking into account the occupation of the electronic states. The occupation is defined by the Fermi-Dirac distribution $f_{t,s}(\epsilon) = (1 + \exp[\epsilon/k_BT])$. Electrons can only tunnel from occupied (described by $f(\epsilon)$) to unoccupied states $((1 - f(\epsilon)))$. As such, the flow of electrons tunneling from tip to sample is given by the expression:

$$I_{t\to s} = \frac{4\pi e}{\hbar}\int_{-\infty}^{\infty} d\epsilon\rho_t(\epsilon - eV)\rho_s(\epsilon)f_t(\epsilon - eV)(1 - f_s(\epsilon))|M_{ts}|^2, \tag{4.2}$$

where $\rho_{s(t)}$ is the density of states of the sample (tip), there is a factor 2 coming from spin degeneracy. Note that we have set a potential difference, $V$, between tip and sample (as depicted in Fig. 4.1 (a)). To obtain the total tunneling current, we also need to take into account the flow of electrons going from the sample to the tip, $I_{s\to t}$. The tunneling current is then calculated as the difference between the two $I_T = I_{t\to s} - I_{s\to t}$. Finally, we obtain:

$$I_T = \frac{4\pi e}{\hbar}\int_{-\infty}^{\infty} \rho_t(\epsilon - eV)\rho_s(\epsilon)\Big[f_t(\epsilon - eV) - f_s(\epsilon)\Big]|M_{ts}|^2. \tag{4.3}$$

As we can see in the previous expression, and as sketched in Fig. 4.1 (a), the applied bias ($V$), makes electrons tunnel from filled to empty states between tip and sample.

### 4.1.2 Imaging with STM

To obtain a topographic image using STM, we take advantage of the high dependence of the tunneling current with the tip-sample distance ($z$). As reported by Binning and Rohrer [6], the tunneling current decays exponentially with $z$. We scan the area that we intend to map by moving the tip in the $x - y$ plane. The measured tunneling current is subject to a feed-back loop. In this way, when scanning over an area, the feed-back tries to maintain the tunneling current constant to a given set point by varying $z$. This correction is achieved by the piezoelectric components attached to the tip. Piezoelectric materials can shrink or extend under voltage. In this way, the tip-sample distance is recorded. The ensemble of tip positions over the sample while keeping the tunneling current constant creates

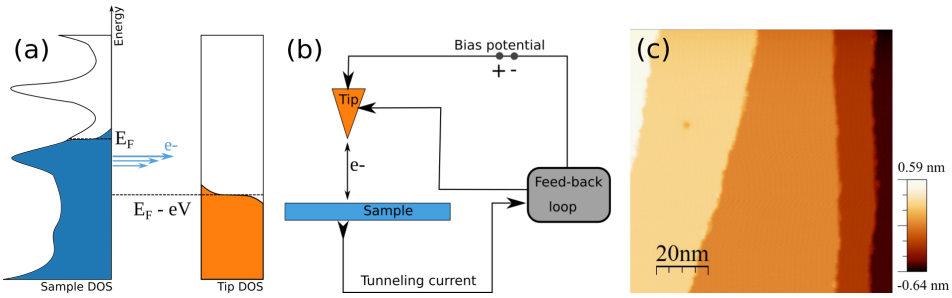


Figure 4.1: STM working principle. (a) Electrons can tunnel from filled states of the sample to empty states in the tip, due to the energy difference, $eV$. Here, we are considering a substrate with a complex density of states (DOS) while the tip is assumed to have a constant DOS about the Fermi energy. Both sample and tip are assumed to be kept at the same temperature, $T$, that leads to the thermal occupation represented in colors. (b) Schematics of the STM set-up. The potential difference generates a tunneling current between tip and sample. In the constant-current mode, the tunneling is kept constant by a feed-back loop that acts on the tip's height with respect to the sample. (c) Constant-current image obtained on a clean Pb(111) surface, with a current set point $I = 200$ pA and $V = -200$ mV.

the experimental topography map. The movement in $x - y$ is also achieved by piezoelectric components. In Fig. 4.1 (b) we depict a sketch of the STM set-up. This scanning mode is called *constant current*, as the feed-back works to maintain a constant current in the sample-tip junction.

Alternatively, we can also scan an area with the feed-back off, in this case the tip-sample distance is kept constant and, as we scan over an area, the set-up will record a varying tunneling current. The topography is retrieved by looking at the current map. This mode is called *constant height*. Between the two, the constant-current mode is most commonly used for acquiring topography images. Figure 4.1 (c) shows a constant-current map with size 100 nm×100 nm of a Pb(111) crystal obtained with a current set-point of $I = 200$ pA. As observed, the topography shows several atomic-sized terraces.

### 4.1.3 Scanning tunneling spectroscopy

As we can see in Eq. 4.3, the tunneling current carries information about the DOS of the local area directly under the tip. Meaning that the local density of states (LDOS) of the sample can be probed by measuring the tunneling current at different biases. This is called scanning tunneling spectroscopy (STS). In the following, we will see how the LDOS can be directly extracted from tunneling measurements.

We go back to the expression of the tunneling current in Eq. 4.3. By assuming that the matrix element, $M$, is constant. We have that:

$$I_T \propto \int_{-\infty}^{\infty} \rho_t(\epsilon - eV)\rho_s(\epsilon)\Big[f_t(\epsilon - eV) - f_s(\epsilon)\Big]d\epsilon \tag{4.4}$$

And we calculate the derivative with respect to the bias voltage, $V$.

$$\begin{aligned}\frac{\partial I_T}{\partial V}|_V \propto \int_{-\infty}^{\infty} d\epsilon\Big[ &- \rho_s(\epsilon)\rho_t'(\epsilon - eV)f_t(\epsilon - eV) \\ &- \rho_s(\epsilon)\rho_t(\epsilon - eV)f_t'(\epsilon - eV) \\ &+ \rho_s(\epsilon)\rho_t'(\epsilon - eV)f_s(\epsilon)\Big]\end{aligned} \tag{4.5}$$

If we assume that the DOS of the tip remains constant, then the derivative with respect to $V$ is $\rho_t' = 0$. The first and third component in Eq. 4.5 become zero. Also, in the limit where the temperature goes to zero, the derivative of the Fermi-Dirac function, becomes simply a delta distribution. $f'(\epsilon)_{T\to 0} = \delta(\epsilon)$. Like this, Eq. 4.5 simply becomes:

$$\frac{\partial I}{\partial V}|_{V_{bias}} \propto \rho_t(\epsilon) \int_{-\infty}^{\infty} \rho_s(\epsilon)\delta(\epsilon - eV)d\epsilon = \rho_t\rho_s(eV) \tag{4.6}$$

As we can see, $\frac{\partial I}{\partial V}$ is proportional to the density of states of the sample at energy $eV$. By keeping the tip at a constant height, *i.e.* feed back is off, and sweeping the tunneling voltage while measuring the current, we obtain the $I(V)$ curve. By performing a numerical derivation, we can obtain the $\frac{\partial I}{\partial V}$ signal. However, in experiments, due to mechanical vibrations, external electromagnetic noise and noise from the amplifier electronics, this signal turns out to be very noisy. In this way, in experimental set-ups, the $\frac{\partial I}{\partial V}$ is directly measured with the aid of a lock-in amplifier.

### Lock-in measurements

As previously discussed, the goal of STS is to measure the derivative of the tunneling current with respect to the applied bias, $\partial I/\partial V$. To this end, we can use the lock-in technique. The idea behind this, is that by applying a small oscillating modulation to the voltage, the measured current will also oscillate, the amplitude of this modulated current carries information about the slope of the $I(V)$ curve, in other words, its derivative. This measurement drastically reduces the signal-to-noise ratio compared to the numerical derivation of the $I(V)$ signal [148].

The modulation added to the input voltage is $V_m \cos(\omega_{ref}t + \theta)$, where $V_m$ is the modullation amplitude, $\omega_{ref}$ is the known reference frequency, and $\theta$ is an unknown phase. The tunneling current is then,

$$I = I(V + V_m \cos\omega_{ref}t + \theta) \tag{4.7}$$

If $V_m$ is taken to be small enough ($V_m << V$), we can do a Taylor expansion of the previous expression:

$$\begin{aligned} I(V + V_m \cos \omega_{ref} t + \theta) = I(V) + a_1 \frac{\partial I}{\partial V} V_m \cos(\omega_{ref} t + \theta) \\ + a_2 \frac{\partial^2 I}{\partial V^2} V_m \cos(2\omega_{ref} t + \theta) + ... \end{aligned} \tag{4.8}$$

To detect the first harmonic, $\omega_{ref} t$, the previous expression is multiplied by a reference modulation signal $V' \cos(\omega_{ref} t + \phi)$, with same frequency as the modulation and phase $\phi$. The signal measured by the lock-in is the first term of the Taylor expansion:

$$\frac{\partial I}{\partial V}|_{lock-in} = V' \cos(\omega_{ref} t + \phi) \times \left[ a_1 \frac{\partial I}{\partial V} V_m \cos(\omega_{ref} t + \theta) \right] \tag{4.9}$$

Which can be rewritten as:

$$\frac{\partial I}{\partial V}|_{lock-in} = a_1 \frac{V'}{2} \frac{\partial I}{\partial V} V_m \Big[ \cos(\theta - \phi) + \cos(2\omega_{ref} t + \theta + \phi) \Big] \tag{4.10}$$

As we can see, the out-put signal has two components: a DC component proportional to $\frac{\partial I}{\partial V} \cos(\theta - \phi)$ and an AC signal of frequency $2\omega_{ref}$. By doing a time average of the signal, only the DC component is filtered out. Note that for all other signals with frequency ($\omega \neq \omega_{ref}$) the DC component is zero. Additionally, the result is proportional to the cosine of the phase difference between the input and reference signal. This phase can be adjusted to maximize the amplitude of the output [148].

### Inelastic electron tunneling spectroscopy (IETS)

The electron tunneling discussed up to now involves only elastic processes, *i.e.* electrons tunneling between tip and sample conserving their energy (see Fig. 4.2 (a)). However, electrons can tunnel from one side to the other of the vacuum barrier, losing part of their kinetic energy and promoting the system into a higher-energy state. These type of processes receive the name of *inelastic tunneling*, and can be used to probe discrete energy states of the system. Inelastic tunneling spectroscopy (IETS) has been used, for example, to probe vibrational modes on molecules [149]–[151] or spin excitations on single magnetic moments [152], [153] such as molecules [34] and atoms [154], [155].

As we vary the voltage, the elastic flow of electrons contributes linearly to the total tunnel current. However, the inelastic processes open a new channel that will induce changes in the slope of the $I(V)$ curve. The inelastic channel opens when electrons have a sufficiently high energy, $eV \geqslant E_i$. Above this energy threshold, the additional inelastic current is added to the tunneling current. The total current

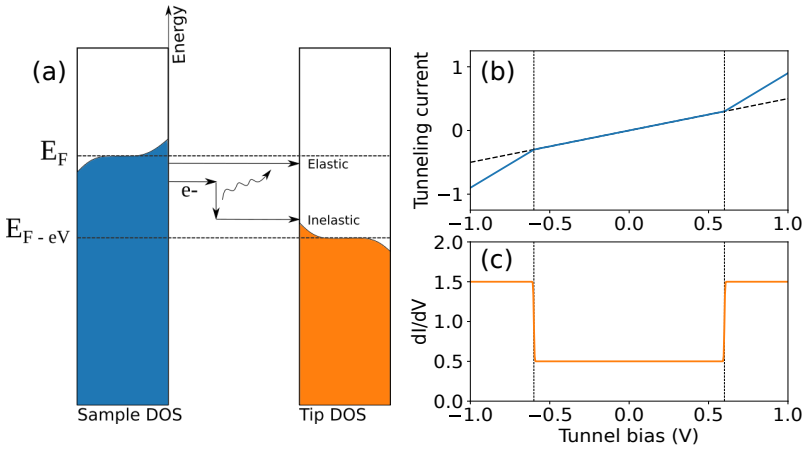


Figure 4.2: Inelastic electron tunneling spectroscopy. (a) Tunneling electrons flowing from the sample to tip in elastic and inelastic processes. In the elastic tunneling, the electron conserves its energy. In the inelastic case, the electron loses some of its energy and tunnels to a lower-energy state. (b) Total tunneling current (blue line) obtained from Eq. 4.12, the change in the slope coincides with the opening of the inelastic channel. For comparison, the elastic current is also depicted (black dashed line). (c) Numerical derivative of (b), the changes in the $I(V)$ slope result in steps in the $dI/dV$ spectra.

will be the combination of both elastic and inelastic processes, $I_T + I_e + I_i$:

$$I_T = \sigma_e V + \frac{\sigma_i}{e}\int \Big[f(\epsilon - eV + E_i)(1 - f(\epsilon)) + f(\epsilon)(1 - f(\epsilon - eV - E_i))\Big]d\epsilon \quad (4.11)$$

where $\sigma_{e(i)}$ is the elastic (inelastic) conductance. The two terms in the previous expression are the electron flow from tip to sample and vice versa. The previous integral can be analytically solved:

$$I_T = \sigma_e V + \sigma_i\left[\frac{(V - E_i/e)\tilde{f}(eV - E_i)}{\tilde{f}(eV - E_i) - 1} + \frac{(V + E_i/e)\tilde{f}(-eV - E_i)}{\tilde{f}(-eV - E_i) - 1}\right] \quad (4.12)$$

where $\tilde{f}(\epsilon) = exp(\epsilon/k_B T)$. Figure 4.2 (b) shows the resulting tunneling current with an inelastic channel corresponding to an excitation of energy $E_i = 0.6$eV. The elastic current is depicted as the black dashed line ($I = \sigma_e V$), beyond the threshold, we see a change in the slope and an increasing total current, due to the opening of the inelastic channel. Figure 4.2 (c) shows the derivative of the tunneling current. As we can observe, the change in slope becomes a step-like feature in the $\partial I/\partial V$ spectra at bias $E_i/e$. These abrupt changes in conductance allow us to easily detect excitations in the system.

### 4.1.4 Experimental set-up

The microscope used in this thesis is a low-temperature STM from Omicron kept under ultra-high-vacuum (UHV) conditions. The system is located at l'Institut de Physique et Chimie des Matériaux de Strasbourg (IPCMS), in France. A picture of the system is shown in Fig. 4.3 (a), indicating the main components. The UHV system consists in two chambers: the preparation and STM chambers, separated by gate valves. Both chambers are equipped with a turbo-molecular pump and an ionic pump. The base pressure in the preparation chamber is kept in the range of $10^{-10}$ mbar and in the STM chamber at $10^{-11}$ mbar. Additionally, titanium sublimation pumps (TSP) are periodically used to help keep the vacuum conditions. A third chamber, the load-lock, is connected to the preparation chamber, this one can be exposed to ambient pressure and it is used to insert or remove samples from the system.

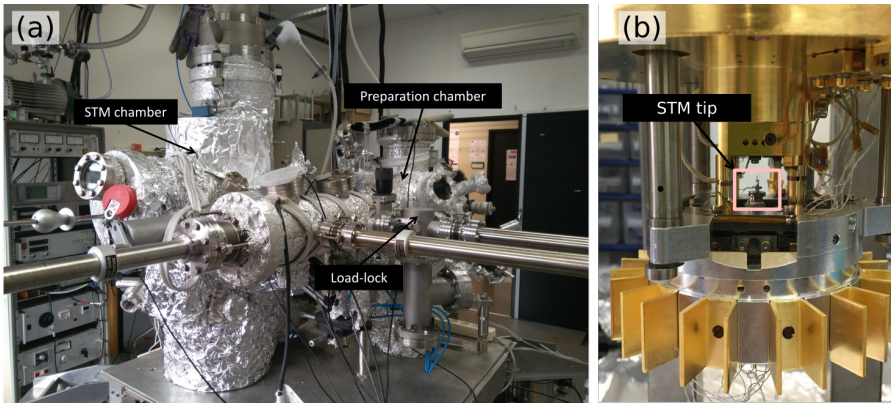


Figure 4.3: STM system used in this thesis at IPCMS in Strasbourg. (a) UHV system with its main components labelled: STM and preparation chambers and load-lock. (b) STM head outside the STM chamber, the STM tip is framed with a pink square.

The preparation chamber is equipped with a sputtering gun and heating stage used for sample preparation. The samples used in this thesis are Pb(111) single crystals. To achieve a clean surface, we perform several sputtering annealing cycles. We use tungsten tips, also prepared by $Ar^+$ sputtering. In Fig. 4.3 (b) we can see the STM stage outside the UHV system, the tip is marked by a pink square. Samples are placed on top of the tip, in the sample stage.

A cryostat with 3.5L of capacity is located directly on top of the STM head, when filled with liquid helium, the temperature in the microscope reaches 4.5 K. For measurements, the temperature can be further reduced by pumping on the

cryostat. When the pump is working at full power, the temperature reaches 2.5 K, all the measurements reported in the present and next chapter were acquired at this temperature, unless otherwise specified.

## 4.2 Scanning with superconducting tips

As discussed in 4.1.3, STS is used to measure the LDOS of the sample. In the case we use a tip with a flat DOS around the Fermi energy, the energy resolution of the spectroscopy will be limited by the Fermi-Dirac distribution, and a high energy resolution can be only achieved at very low temperatures. As we will see in the following, the use of superconducting tips in STM [156], [157], can increase the energy resolution of the measured STS [158], [159].

### 4.2.1 Tunneling between superconductors

As previously discussed in 4.1.1, the tunneling current between tip and sample is given by the Eq. 4.3, this expression depends on the DOS of both tip an sample. As explained in chapter 1 (1.2.3), the DOS of a superconductor is well described by the Dynes formula [65]:

$$\rho_{sc}(\epsilon) = N_0 Re\Big[\frac{\epsilon + i\Gamma}{\sqrt{(\epsilon + i\Gamma)^2 - \Delta^2}}\Big], \tag{4.13}$$

where $i\Gamma$ is a damping factor, known as the *Dynes parameter* [65], [66]. It accounts for the pair breaking that occurs under a finite current during tunneling processes [61].

#### Metal-superconductor tunneling

In case we are studying a superconducting sample with a metallic tip, the tunneling current can be easily obtained by replacing the superconducting DOS in Eq. 4.3.

$$I_{ns} \propto \int_{-\infty}^{\infty} \frac{\rho_{sc}(\epsilon)}{N_0}\Big[f(\epsilon) - f(\epsilon + eV)\Big]d\epsilon. \tag{4.14}$$

From this expression, we can see that electrons will be able to tunnel when the bias is $|eV| > \Delta_1$. This situation is sketched in Fig. 4.4 (a), the sign of the bias is not relevant, since creating a hole or an electron in the superconductor requires the same energy. The $\partial I/\partial V$ signal, as discussed in 4.1.3, is proportional to the LDOS of the sample.

#### Superconductor-superconductor tunneling

In the case where we have superconducting materials on both electrodes, the tunneling current expression becomes more complex. Replacing the superconducting

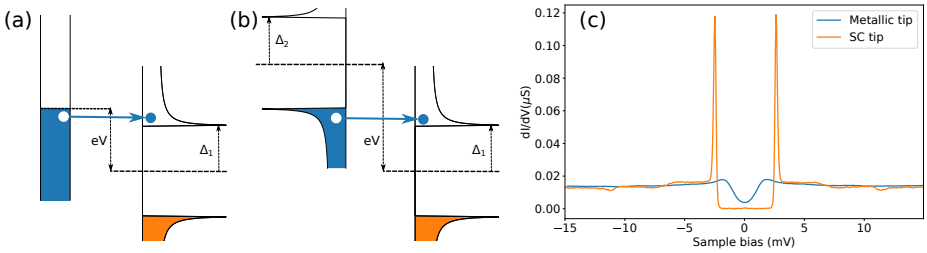


Figure 4.4: Electron tunneling between metal-superconductor and two superconductors. (a) Current tunneling from a metalic tip to a superconducting sample. Electrons can tunnel when the bias potential is $eV > \Delta_1$. (b) In case tip and sample are superconducting, the potential requiered is $eV > |\Delta_1 + \Delta_2|$, this energy is enough to create a hole in one side and an electron in the other. (c) STS measurements on Pb(111) crystal with a metallic W tip (blue curve) and Pb coated superconducting tip (orange curve) at T=2.5K.

density of states in Eq. 4.3, we get:

$$I_{ss} \propto \int_{-\infty}^{\infty} \frac{|\epsilon|}{\sqrt{\epsilon^2 - \Delta_1^2}} \frac{|\epsilon + eV|}{\sqrt{(\epsilon + eV)^2 - \Delta_2^2}} \Big[ f(\epsilon) - f(\epsilon + eV) \Big] d\epsilon. \tag{4.15}$$

From the previous equation, we observe that no current can flow from one side to the other until $|eV| = \Delta_1 + \Delta_2$. At this bias, the energy is enough to create a hole in one side and an electron on the other. The tunneling process is depicted in Fig. 4.4 (b).

The derivative, $\frac{\partial I}{\partial V}$, is given by Eq. 4.5. In the case of a superconducting tip, we cannot make the assumption of $\rho_t' = 0$. We need to explicitly evaluate the three terms. So the conductance between a sample and a superconducting tip is proportional to:

$$\begin{aligned} \frac{\partial I}{\partial V} \propto & \int_{-\infty}^{\infty} -e \left. \frac{\partial \rho_t}{\partial V} \right|_{\epsilon - eV} \rho_s(\epsilon) \Big[ f_t(\epsilon - eV) - f_s(\epsilon) \Big] d\epsilon \\ & + \int_{-\infty}^{\infty} -e \rho_t(\epsilon - eV) \rho_s(\epsilon) \left. \frac{\partial f}{\partial V} \right|_{\epsilon - eV} d\epsilon \end{aligned} \tag{4.16}$$

The derivative of Eq. 4.13 can be calculated analytically (find the expression in Appendix D), and the resulting $\partial I / \partial V$ from Eq. 4.16 can be evaluated numerically. This calculation can be used to compare with experimental results.

Compared to the metal-superconductor tunneling, the signal now is not proportional to the DOS of the sample. Rather, the resulting signal is a convolution with the DOS of the tip, mainly shifting all features in the sample by the superconducting gap of the tip, $\Delta_{tip}$. This convolution, on the other hand, is what gives the

enhanced energy resolution to the superconducting tip measurements. In order to properly study the energy resolved spectroscopy, the spectra obtained need to be deconvoluted to remove the effect of the tip.

### 4.2.2 Spectroscopy with Pb tips

For most of the measurements shown in this thesis, we used a Pb-coated STM tip. Lead is one of the highest $T_c$ elemental superconductors, with a critical temperature of $T_c = 7.19$ K [160]. The superconducting pairing potential of Pb at T=0 is $\Delta = 1.35$ meV.

#### Tip preparation

STM measurements were performed using tungsten tips. They are prepared by chemically etching tungsten wires, using a solution of NaOH [161]. Resulting in sharp-end tips. To improve the sharpness and removing impurities, tips are also sputtered with $Ar^+$ ions, before being inserted in the STM head.

Next, we coat the W tip with some superconducting material. To this end, we prepare clean Pb(111) crystal by doing several sputtering/annealing cycles. For sputtering, we set an Argon pressure of 1.0E-6 mbar and apply 700 V. With these conditions, we measure an emission current of $\sim$1.5 $\mu$A. We then anneal the sample at a maximum temperature of 425 K. The result is a clean Pb surface, as shown in Fig. 4.1 (c). We coat the tip with some Pb, by indenting the tip onto the surface. We move the tip several nanometers into the surface until it crashes. We keep a bias voltage of 10 V during this process, and then move several micrometers in the $x$-$y$ coordinates to get some Pb into the tip. The result is a superconducting tip with a slightly smaller $\Delta$ than the bulk Pb.

#### Experimental STS with Pb tips

Figure 4.4 (c) depicts experimental $\partial I/\partial V$ measurements obtained with a Pb-coated tip, as explained in the previous paragraph, compared with STS obtained with a metallic tip on clean Pb(111) crystal. Both spectra were obtained at T=2.5 K, the blue curve corresponds to the measurement with a metallic W tip, the superconducting gap can be observed, but the features are smeared due to the finite temperature. The orange curve, is obtained at the same conditions using a Pb-coated tip. In this case, the quasi-particle peaks can be easily distinguished, the total energy gap is found to be $\Delta = \Delta_{tip} + \Delta_{Pb} \approx 2.6$ meV, indicating a superconducting gap $\Delta_{tip} < \Delta_{Pb}$, as expected. Other features at higher energy can be observed as well. For instance, the electron-phonon steps at $\approx \pm 6$ meV and $\approx \pm 10.5$ meV [162], that correspond to the electron-phonon modes of the bulk Pb, found at around 4.4 and 8.5 meV [163], [164].

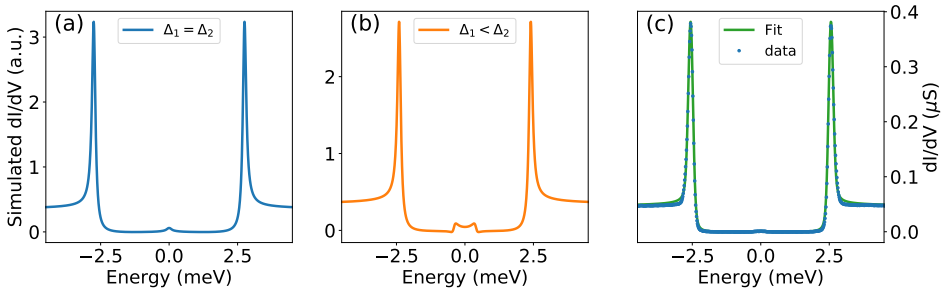


Figure 4.5: Numerical simulation of $\partial I/\partial V$ spectra between two superconductors. (a) $\partial I/\partial V$ with $\Delta_1 = \Delta_2 = 1.35$ meV, and $T = 4.0$ K, thermal tunneling feature is visible at $eV = 0$. (b) Same as (a) but $\Delta_1 = 1.0$meV, and $\Delta_2 = 1.35$meV. Two thermal features are visible at $eV = \pm|\Delta_1 - \Delta_2| = 0.35$meV. (c) $\partial I/\partial V$ spectra measured with Pb tip on Pb(111) surface (blue dots) at a measured temperature of $T = 2.5$ K. Simulated spectra with using Eq. 4.16 and Gaussian noise. Parameters: $\Delta_{sample} = 1.35$meV, $\Delta_{tip} = 1.185$meV, $\Gamma = 0.05$meV, $T = 2.5$K and $\sigma = 2.7E-6$.

#### Simulated dI/dV between two superconductors

As already mentioned, Eq. 4.16 can be numerically evaluated to simulate the $\partial I/\partial V$ signal between two superconductors (see Appendix D for more details). Figure 4.5 shows simulated $\partial I/\partial V$ signals between two superconductors. Figure 4.5 (a) shows the conductance spectra between two superconductors with $\Delta_1 = \Delta_2 = 1.35$ meV. The resulting curve shows two sharp features at $eV = \pm|\Delta_1 + \Delta_2|$, as well as a small peak at zero energy, this corresponds to thermally excited quasi-particles. In Fig. 4.5 (b) the thermal feature arises as two sharp peaks, at $eV = \pm|\Delta_1 - \Delta_2|$, at this voltage the filled states at $\Delta_1$ can tunnel to the available states in $\Delta_2$ [61]. The temperature for the two electrodes in Fig. 4.5 (a) and (b) is $T = 4.0$ K, the thermal features become more apparent as we increase the temperature.

Figure 4.5 (c) shows the measured superconducting gap obtained on a Pb(111) crystal with a Pb-coated tip (blue dots). Using the numerical calculation, we can fit this spectrum with good agreement. The temperature is set to $T = 2.5$ K, as measured in the STM stage, and the tip's pairing potential is set to $\Delta_{tip} = 1.185$ meV. To better fit the quasi-particle peaks in the measured spectra, we also add a Gaussian noise signal to the simulated conductance.

### 4.2.3 Low-resistance tunneling processes

The tunneling processes between two superconductors described in 4.2.2 are valid when the superconducting-insulating-superconducting (S-I-S) junction is in the weak-coupling limit, *i.e.* the STM junction resistance is high (in the range of $M\Omega$). However, in strongly-coupled junctions (when the junction resistance drops to the $k\Omega$ range), new processes emerge. In this section, we review the multiple

Andreev reflections and Josephson effect.

### Andreev reflections

*Andreev reflections* were first described by A.F. Andreev in 1964 [165]. Essentially, in a normal-superconducting (N-S) interface, an incident electron with energy $E < \Delta$ cannot go through the barrier as a quasi-particle of the system because there are no quasi-particle states inside the superconducting gap. Instead, the electron is reflected as a hole as depicted in Fig. 4.6 (a). In this way, a charge of $2e$ is transferred to the BCS condensate in the superconductor [61], [166].

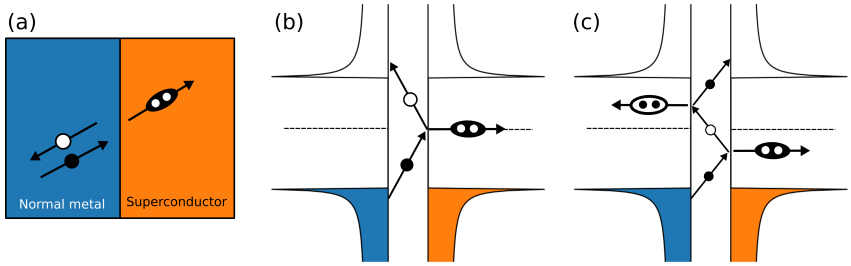


Figure 4.6: (a) Schematic of an Andreev reflection at a normal/superconductor interphase. (b) Single Andreev reflection in a S-I-S junction. (c) Multiple Andreev reflection with order $n = 3$. Tunneling electrons are represented by black balls and holes as white balls. Cooper pairs are depicted as black bubbles with two white dots inside. Adapted from Ref. [167].

An Andreev reflection between two superconductors with same superconducting gap, $\Delta$, is sketched in Fig.4.6 (b), here an incoming electron with energy $2\Delta > |eV| > \Delta$ from superconductor 1, reaches the interface of superconductor 2. Since there are no electron-states available in this side, the process can only occur if the electron is Andreev reflected as a hole. The reflected hole tunnels back in the opposite direction, to superconductor 1, where empty (hole) states are available. After this process, a total of 2 electron charges have tunneled from superconductor 1 to superconductor 2.

A similar process is possible, involving higher-order reflections, these are called *multiple Andreev reflections* (MAR). The reflected hole from Fig. 4.6 (b) can be again Andreev reflected at the interface with superconductor 1, as an electron-like quasiparticle. This process annihilates a Cooper pair in superconductor 1. This situation is depicted in Fig. 4.6 (c) and at the end of this process a total of three elementary charges tunnel across the junction.

These multiple reflection processes result in resonant peaks in the $\partial I/\partial V$ spec-

tra inside the superconducting gap. The threshold for this higher order processes to occur is given by the following relation:

$$eV_T \geqslant \frac{2\Delta}{n} \tag{4.17}$$

where $n-1$ is the number of Andreev reflections occurring in the junction, and $n$ the total number of elementary charges tunneling from one superconductor to the other.

### Josephson effect

The tunneling of Cooper pairs between superconductors was predicted by Brian Josephson in 1962 [168], [169]. He studied a system composed by two bulk superconductors separated by a thin barrier (S-N-S), today known as a Josephson Junction, in hopes of finding a physical quantity which would allow measuring the phase difference between the two superconductors ($\Delta\phi$). This phase was introduced in the Gizburg-Landau theory as a global phase of the wave-function describing the superconducting electrons [166].

The superconducting phase was first highlighted by the findings of Josephson. He predicted the existence of a supercurrent between two superconductors at zero bias voltage, driven by the phase difference existing between the two:

$$I_s = I_c \sin \Delta\phi \tag{4.18}$$

This is known as the DC Josephson effect, and it was measured experimentally by Anderson and Rowell in 1963 in thin films [170]. $I_c$ is the critical current, the maximum current supported by the junction, and it depends on the temperature, the superconducting gap, $\Delta$ and the resistance of the junction, $R_T$ [171]:

$$I_c = \frac{\pi\Delta}{2R_T} \tanh \frac{\Delta}{k_B T} \tag{4.19}$$

Josephson also predicted a superconducting phase evolution as a function of the applied voltage:

$$\frac{d\Delta\phi}{dt} = \frac{eV}{\hbar} \tag{4.20}$$

This is known as the AC Josephson effect, and it generates an alternating current of amplitude $I_c$ and frequency $\nu = 2eV/h$.

When we use superconducting STM tips, the two previous phenomena can be measured when the junction resistance is low enough. Figure 4.7 shows the STS obtained using a Pb-coated tip on a Pb crystal at two different junction resistances. The blue curve is obtained at a resistance of 0.5 MΩ, here we observe the coherence peaks and a superconducting gap of $\sim 2.6$ meV. The junction resistance can be reduced by increasing the tunneling current, which brings the tip closer to

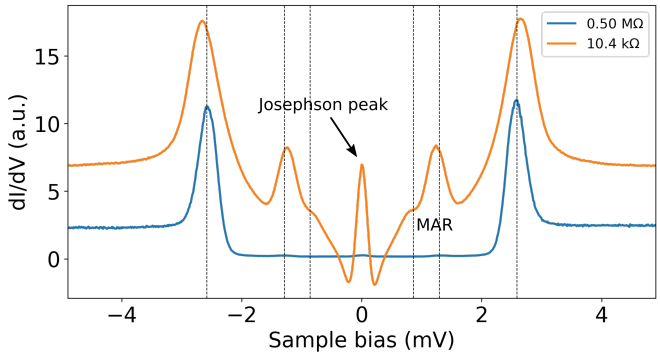


Figure 4.7: dI/dV spectra measured on a Pb crystal with Pb coated tip at $T = 2.5$ K. The dI/dV spectra are shifted for clarity. The blue curve was measured at $R_N = 0.5$ MΩ, showing only the quasi-particle peaks. The orange curve was obtained at $R_N = 10.4$ kΩ showing MAR and Josephson supercurrent.

the sample. The orange curve in Fig. 4.7 was measured at a resistance of 10.4 kΩ. As we can see, in-gap states arise under these conditions. We can observe a peak at zero bias that corresponds to the Josephson current. At higher energies, we can also see two features corresponding to Andreev reflections, showing second and third order MAR. The dashed black lines indicate the expected MAR energies as written in Eq. 4.17. The observed peaks are in good agreement with their expected energies. We can also note that, as the resistance of the junction has decreased, the coherence peaks get broader.

**Conclusions.** As we have reviewed in this chapter, STM is a powerful tool to study metallic samples down to the atomic level. The high spatial resolution allows to image the topography of the sample with a high precision, and to measure the LDOS at selected locations in the sample. The use of superconducting tips and samples, results in convoluted spectra that, in return, allows for a higher energy resolution, otherwise only achieved at mK temperatures. At low resistance junctions, new phenomena arise only observable in superconducting systems: MAR and Josephson supercurrent.

# 5 Nickelocene on Pb(111): STM study with superconducting tips

**Nickelocene on metallic surfaces.** Metallocene molecules consist on a metallic center, usually from one of the middle elements on the $3d$ row (V, Cr, Mn, Fe, Co, Ni) [172]. And two cyclopentadienyl rings ($C_5H_5$, noted as Cp) parallel to each other and on opposite sides of the metallic atom, this structure is sketched in Fig. 5.1 (a). Ferrocene ($FeCp_2$) was the first metallocene molecule discovered in the 1950s [173], [174], with other compounds soon following. Their discovery helped to develop the field of organometallic compounds. Several macroscopic averaging studies on ferrocene [175], [176] and nickelocene ($NiCp_2$) [177]–[179] tried to unravel their absorption on metallic surfaces, in particular on Ag and Cu crystals. More recently, local probe studies [180], [181] allowed to study metallocene molecules down to the single-molecular level and to better understand their absorption into metallic surfaces.

In recent years, the interest on metallocence compounds, has grown in the context of molecular spintronics. Due to the magnetic anisotropy existing in these systems, distinct spin-dependent energy levels can be individually addressed [182]. In this thesis, we focus on the study of nickelocene (noted as Nc in the following). Nc has been previously studied with the aid of STM on normal metallic surfaces [35], [181], [183]. Due to its electronic configuration, Nc has a spin $S = 1$, as shown by several studies [172], and an uniaxial magnetic anisotropy, making the spin's ground state to be perpendicular to the Nc molecular axis. For our study, we change the metallic substrate by a superconducting one. In particular, we will study the absorption and molecular excitations of Nc on a superconducting Pb (111) crystal.

Metallocene molecules exhibit two distinct configurations depending on the relative orientation of the two Cp rings. Usually, a small energy barrier separates the eclipse ($D_{5h}$ symmetry) and the staggered ($D_{5d}$ symmetry) configurations [184]. In the former, the two Cp rings show the same rotation with respect to the molecular axis (Fig. 5.1 (a)), in the later the rings show a relative rotation of 36°. For Nc, DFT calculations in the gas phase show that the eclipsed geometry is 23 meV lower in energy, making this the preferential configuration upon absorption in a

metallic surface [181].

STS studies on Nc deposited Cu(100) [34], [185], [186], Ag(110) [35] and Cu(111) [183] show a big inelastic step in conductance. This molecular excitation corresponds to the promotion from the Nc ground state $|S = 1, m_z = 0\rangle$ to the doubly degenerated $|S = 1, m_z = \pm 1\rangle$ excited state. Due to the spin 1 of Nc, this signal constitutes a direct measurement of the magnetic anisotropy. The magnetic properties of Nc are robust, as their signatures remain unchanged in different metallic environments, for example, when the molecule is absorbed into the STM tip [35], [185]. At low junction resistances, the $dI/dV$ spectra of Nc-terminated tips drastically change showing a peak at zero bias. This transition corresponds to a molecular spin switching from $S = 1$ to $S = 1/2$ [185], [186]. Other metallocene molecules have also been studied on Cu substrates such as, ferrocene [180], [187] and cobaltocene ($CoCp_2$) [188].

In the present chapter, we investigate Nc deposited on a Pb(111) crystal. With the aid of a STM superconducting tip, we were able to resolve small variations in the anisotropy of the molecule. We also compare the measurements obtained on molecules on the surface and absorbed in the tip's apex. Thanks to that information, we could unravel the absorption of molecular islands with respect to the Pb (111) lattice. The main findings presented in this chapter were published in The Journal of Physical Chemistry Letters 2021 12 (11) [36]. Additionally, low junction resistance measurements using a Nc-termiated tip allow observing some characteristic superconducting tunneling processes.

## 5.1 Sample preparation

The STM system used in the present study is presented in 4.1.4. The molecules are deposited on clean Pb(111) crystal after several sputtering and annealing cycles, as described in 4.2.2.

### 5.1.1 Molecular deposition

The molecules are kept in solid state as powder and the deposition is carried out in UHV conditions, following a similar procedure as the one used for depositing on Cu(100) [34], [181]: a small amount of Nc powder is placed inside a ceramic crucible. The crucible is then inserted in the loadlock of the STM system and transferred to the preparation chamber. At low pressure, the molecules sublimate [190]. To control the molecular flux, a lid is placed to cover the crucible with a hole in the center of about 1mm diameter. For deposition, the crucible is placed right in front of the valve separating the preparation and STM chambers. The sample is kept in the STM stage at LHe temperature (about 4.4 K), we take it out and place it also in front of the valve, to maximize the exposure to the molecular flux. Deposition is performed by opening the gate valve separating the

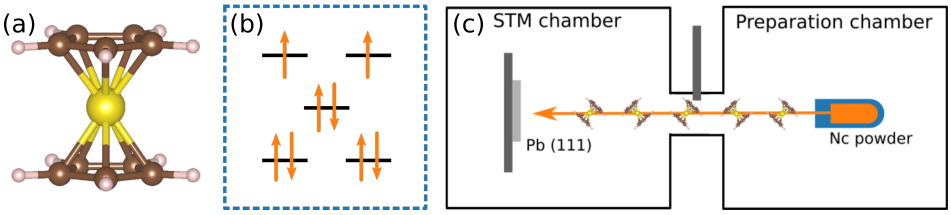


Figure 5.1: (a) Nickelocene structure in the eclipse configuration. Different color balls represent atomic species: Nickel (yellow), Carbon (brow) and Hydrogen (pink). (b) Electronic configuration of the $3d^8$ electrons in Nc. (c) Schema of Nc deposition between preparation and STM chambers under UHV conditions. Adapted from Ref. [189].

two chambers (as depicted in Fig. 5.1 (c)), for times under 1 minute, depending on the coverage we want to achieve.

The pressure in the preparation chamber during deposition ranges from $5.0 \cdot 10^{-7}$ to $10^{-6}$ mbar. If the measured pressure is found to be too low, after transferring the crucible into the preparation chamber, we can increase the molecular flux by slightly heating the crucible with the aid of the annealing filament from the preparation stage.

### 5.1.2 Nc islands on Pb (111)

Self-assemble arrays of magnetic molecules [191], [192] are governed by molecule-molecule and molecule-substrate interactions [193]. This may lead to ordered arrays with magnetic domains and non-collinear magnetic arrangements. On Pb(111) van der Waals forces are the main contribution in molecular absorption [194]–[197], and complex magnetic textures can be expected. Nc has been found to form ordered molecular islands on Cu crystals [34], [181], similar arrangements were also reported for ferrocene [180].

As it was previously observed on Cu crystals, Nc molecules are absorbed on the Pb(111) surface with one of their Cp rings bonded to the surface and the other one exposed to vacuum [181]. As a result of this configuration, in the STM topography, the molecules appear as ring shaped (see Fig. 5.2 (d)-(f)). In the resulting sample, we find big patches of molecules forming molecular islands of sizes about several tens of nanometers with a height of 3.5 Å. Unlike Cu(100), we could not find isolated molecules [181] in the Pb(111) surface. Nevertheless, depending on the deposition conditions, we could achieve different degrees of order in the molecular islands.

Figure 5.2 shows different molecular-island configurations. To control the resulting

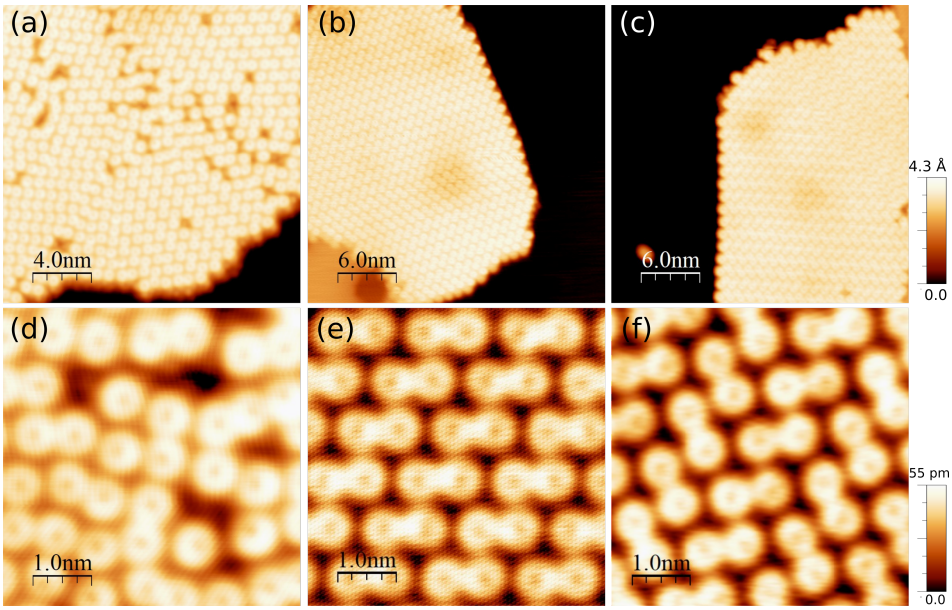


Figure 5.2: Constant current scans of Nc layers on Pb(111) with different configurations on Pb (111) (a) Disordered Nc island on Pb(111), the image was obtained using the parameters I=80pA, V=-20mV. (b) *Paired* phase I=20pA, V=-60mV. (c) *zig-zag* phase I=40pA, V=-80mV. (d) I=60pA, V=-20mV. (e) I=20pA, V=-20mV. (f) I=8pA, V=-20mV.

molecular arrangement, we found that the sample's temperature during deposition is critical. The molecular layers in Fig. 5.2 (a) and (d) are prepared by taking the sample out of the STM head and holding it with the wobble stick in vacuum for about 3 min before deposition. This results in rather disordered islands. Fig. 5.2 (b) and (c) are achieved by proceeding similarly, but in this case, we park the sample on a samples' carousel at room temperature for $\sim$ 2 minutes before deposition. This makes the sample to thermalize faster, resulting in a higher temperature for deposition. As we can observe, the resulting islands show an ordered configuration.

On Pb(111), the ordered Nc islands are mainly present in two different phases [36]: Figure 5.2 (b) and (e) coincides with the *paired* configuration previously observed in Cu samples [181]. The second phase is also formed by pairs of molecules (or dimers), but they are arranged by alternating their direction between rows, we call this phase *zig-zag*, and it is shown in Fig. 5.2 (c) and (f). Both arrangements can be found within the same island, showing domains of one of the two. The *compact* Nc layers observed on Cu(100) [181] can also be found on Pb(111), but they are much less common than the other two.

## 5.2 STS on Nc with superconducting tips

### 5.2.1 Magnetic properties

As previously mentioned, Nc has spin $S = 1$ and it possesses an uniaxial magnetic anisotropy (denoted as $D$), with $D = 3.2$ meV in gas phase [198]. IETS measurements on Cu(100), also found $D = 3.2$ meV in agreement with X-ray magnetic circular dichroism (XMCD) spectra on the same sample [34]. The effective spin Hamiltonian of the system can be written:

$$\hat{H} = D\hat{S}_z^2 \tag{5.1}$$

The ground state is $|S = 1, m_z = 0\rangle$, where $m_z$ is the magnetic quantum number projected onto the molecular axis, perpendicular to the Cp rings. The two degenerate states are $|S = 1, m_z = \pm 1\rangle$. Eclipse Nc has a crystal field with symmetry $D_{5h}$, hence it energetically favors the triplet $S = 1$ state than the single $S = 0$ configuration. The zero-field splitting of Nc [198], leads to a positive anisotropy, $D$, making $|S = 1, m_z = 0\rangle$ the ground state of the system. This spin Hamiltonian allows us to find the magnetic anisotropy energy (MAE) as the molecular spin changes orientation.

Studies on metallic Cu [34], [185] and Ag [35] crystals have proven that Nc conserves its magnetic properties when they are absorbed into a metallic surface, even when the molecule is absorbed on different metallic environments, such as the apex of the STM tip [34], [183]. As we will see in the following, the overall magnetic properties of Nc are also preserved when deposited on Pb (111).

### 5.2.2 Spin excitation in Nc

All the STS measurements shown in this chapter were obtained using superconducting Pb tips [199], prepared as explained in 4.2.2 and carried out at a temperature of $T = 2.5$ K. We measure STS spectra by placing the STM on top of Nc islands. Figure 5.3 (a) shows a Nc paired island on Pb(111), the blue and orange stars indicate the positions where we have acquired the STS. Since we are interested in the spin excitations of Nc, we limit our study to meV energy range. The resulting spectra are shown in Fig. 5.3 (b). The blue curve corresponds to the spectrum obtained on a clean Pb surface, here we can observe a superconducting gap of $\Delta \sim 2.55$meV that corresponds to $\Delta_{Pb} + \Delta_{tip}$, where $\Delta_{Pb} = 1.35$ meV. Using a superconducting tip, means that all the obtained spectra will be convoluted by the superconducting DOS, mainly shifting all the features by the corresponding energy gap, $\Delta_{tip}$.

The orange curve in Fig. 5.3 (b) was obtained on the Nc layer. As shown, the superconducting gap is not affected by the presence of the molecule, and the coherence peaks are found at the same energy. Additionally, we can observe a symmetrical

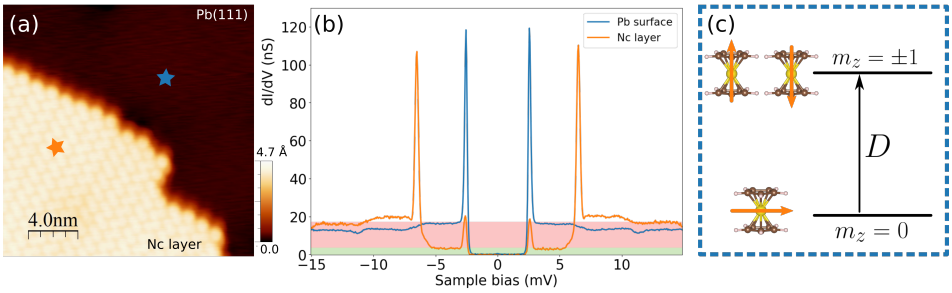


Figure 5.3: IETS signal of Nc coming from spin excitation. (a) Nc layer on Pb(111), the stars mark the places where we take STS. The image was taken for the following parameters: I=50 pA, V=-80 mV. (b) STS obtained on Pb surface (blue curve) and on Nc layer (orange curve). Feed-back was opened at V=-15mV, I=200pA. The spectrum on Nc shows a step signal, at $V = \pm 6.5$ mV accompanied by two narrow peaks, corresponding to the spin excitation depicted in (c). The elastic (inelastic) conductance is marked as green (red) area.

conductance step at $\sim \pm 6.5$ meV, due to an inelastic channel opening. The steps are accompanied by a replica of the quasi-particle superconducting peaks. This signal corresponds to the spin excitation depicted in Fig. 5.3 (c). The system goes from the ground state, $|S = 1, m_z = 0\rangle$, to the excited state, $|S = 1, m_z = \pm 1\rangle$. The spectra are then a measurement of the anisotropy parameter, $D$. As previously mentioned, in Cu(100) researchers found found $D = 3.2$ meV [34], and on Ag(110) $D \sim 3.8$meV [35]. In our case, to obtain the anisotropy parameter, $D$, we have to remove the value of the superconducting gap, so $D = 6.5 - 2.55 = 3.95$ meV [36]. However, as we will see in the following, small variations in $D$ can be measured thanks to the use of superconducting tips.

Something worth noting in the Nc spectra is the ratio between the elastic (indicated as the green area in Fig. 5.3 (b)) and elastic (red area) channels. We found this ratio to be about $\sim 4$, making the spin-flip of Nc a highly-efficient tunneling process [34]. The striking difference between the two channels can also be observed in the topography images, Fig. 5.4 (a) shows the resulting topography with an applied bias above the magnetic anisotropy ($eV > D$) in this case the inelastic channel is open. In contrast, Fig. 5.4 (b) correspond to a sample bias, such that $eV < D$. In this case, we can not image the ring of the molecules, and in the topography, Nc appears as a ball. We can also observe some signal coming from the space between the pairs of molecules. As we will discuss in the following, this signal is coming from the laying down Nc that form the molecular island structure [36], [181].

Another particular aspect about Nc is that, in order to measure its spin excitation, we do not require an insulating layer to decouple the molecule from the metallic

surface. This is usually the case when studying spin excitations on single magnetic entities. Insulating layers such as MgO [200], [201] or $Cu_2N$ [155] are often used to protect the spin excitation from scattering events. The Nc high stability and anisotropy, do not require this decoupling from the metallic environment [34].

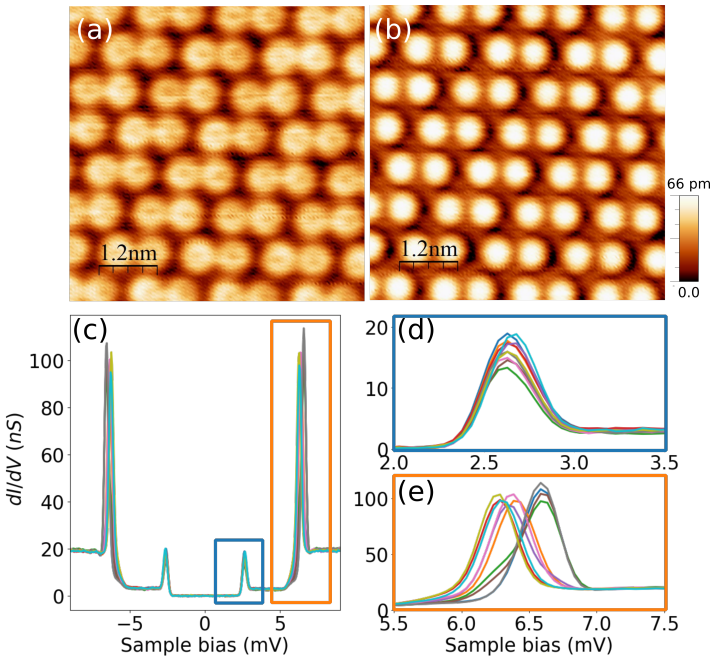


Figure 5.4: (a)-(b) Constant-current topography scans on a paired Nc island with tunneling current I=20pA, and (a) inelastic channel open (V=20mV) and (b) inelastic channel closed (V=5mV). (c) Measured spectra on 10 different molecules within the same paired layer. (d) Zooming in the superconducting gap peak (blue square in (c)). (e) Zooming in the IETS peak (orange square in (c)).

### 5.2.3 Small anisotropy variations

As explained in 4.2.2, the use of a superconducting STM tip leads to a higher energy resolution [154], [158], [159], [195] when performing bias spectroscopy. It allows us to detect small energy variations in the sub-meV range [36], that normal metallic tips are not able to resolve above mK temperatures. With this in mind, we measure STS on several Nc molecules from the paired molecular layer shown in Fig. 5.4 (a) and (b). The resulting spectra are plotted together in Fig. 5.4 (c). We can again distinguish the superconducting gap and, at higher energies, the inelastic step corresponding to the spin excitation. However, if we look carefully, there are some small variations in the IETS peak's position depending on the target molecule. Figure 5.4 (d) zooms in the superconducting gap quasi-particle peak

on different molecules, we can observe the same position for the peak regardless of the molecule ($\pm 2.55 \pm 0.02$ mV), showing again that superconductivity is not affected by the presence of Nc. Figure 5.4 (e) zooms in the IETS peaks, as we can see, there are variations in the peaks' position not present in Fig. 5.4 (d). The IETS peaks are found for energies between 6.2mV - 6.6mV. We trace back these variations to slight changes of the environment of each molecule, resulting in different magnetic anisotropy energies. Note that we are only able to observe these variations thanks to the use of superconducting tips.

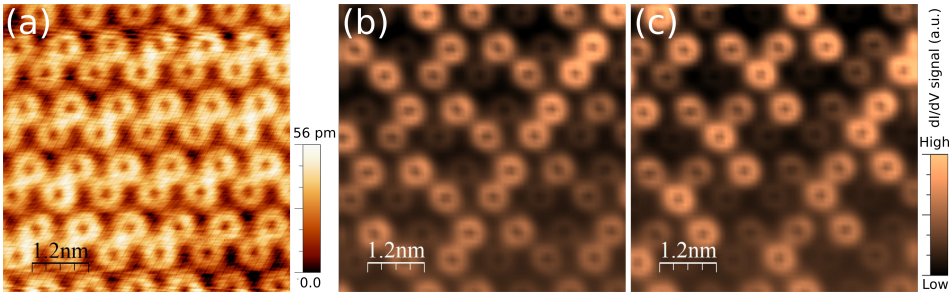


Figure 5.5: dI/dV maps on of Nc paired layers. (a) Constant current topography of Nc paired layer, $I = 20$pA, $V = -30$ mV. (b) $dI/dV$ signal map of the same area in (a) at $V = -6.3$ mV. (c) Same as (b) but $V = -6.5$ mV.

To gain more insight into the spatial distribution of the anisotropy variations, we perform $dI/dV$ maps. Figure 5.5 (a) shows the topography of a paired Nc island that we map. We place the tip on one of the Nc, and set the same feed-back parameters used for STS, we then open the feed-back loop and change the bias at which we would like to do the mapping. We perform constant height scans of the same area as we record the $dI/dV$ signal of the lock-in. By looking at the MAE variations observed in this layer, we select $V = -6.3$ mV and $V = -6.5$ mV as the two distinct biases, the resulting maps are shown in Fig. 5.5 (b) and (c), respectively. The bright molecules, correspond to the Nc with a matching IETS peak at the corresponding bias, while the dark molecules have a different inelastic peak energy position. As we can observe, there is a quasi-periodic pattern shown in the $dI/dV$ maps. The two scans are complementary to each other. This reveals, an underlying structure in the Nc layers, presumably caused by the interaction with the Pb (111) substrate.

In the following, we will try to unravel the difference between these molecules. And how the structure observed in the $dI/dV$ maps relates to the anisotropy of the molecules. To this end, we now study Nc on a different environment: picked up on the STM tip.

## 5.3 Nc-terminated superconducting tip

As already mentioned, Nc preserves its magnetic properties when absorbed in the apex of the STM tip. Indeed, several studies using Nc-terminated STM tip have been reported [34], [35], [183]. In this section, we will see that it is also possible to absorb a Nc molecule on a Pb-coated tip, and we will study the Pb (111) surface with a superconducting and Nc-terminated tip.

### 5.3.1 Picking up Nc

Molecules found on highly ordered layers (see Fig. 5.2 (b) and (c)) are difficult to pick up due to the molecule-molecule interaction that creates the molecular ordered layer. However, Nc found at the edges of disordered islands (see Fig. 5.2 (d)), can be absorbed by bringing the STM tip close enough to the sample. To this end, we perform a constant current scan over the target molecule at low bias ($\sim$ 5mV). We then start increasing the tunneling current, when we reach $\sim$ 200 pA, the molecule is picked up at the tip's apex. This can be noted by a sudden change in the topography. It is also possible to pick-up Nc by scanning at low bias (around 5 mV) over disordered islands, but in this way we do not control the target molecule which is picked up.

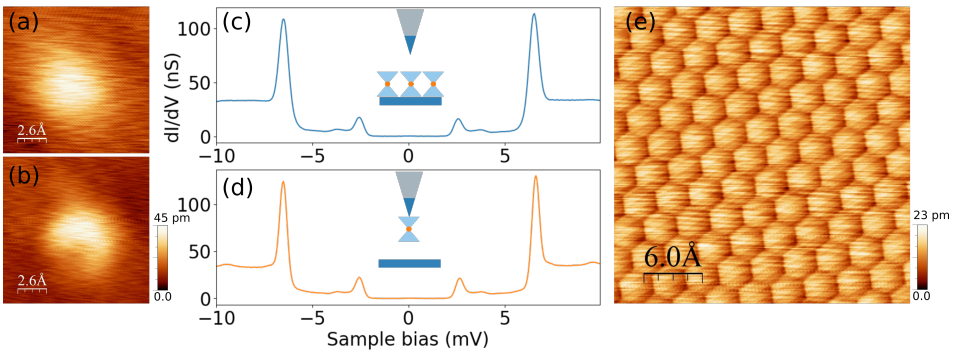


Figure 5.6: Superconducting, Nc-terminated tip. (a)-(b) STM constant current image of a Fe atom absorbed on Pb (111) with (a) *clean* supercondcuting tip and, (b) Nc-terminated tip. (c)-(d) STS spectra measured on Nc layer and on clean Pb (111) surface using a Nc tip, respectively. (e) Constant current STM image showing atomic resolution of the surface obtained with Nc absorbed on the tip's apex, $I = 80$ pA, $V = -15$ mV.

The presence of a Nc molecule at the tip's apex can be noted by the counter image in the topography of single objects. Figure 5.6 (a) and (b) show constant current topography images of single Fe atoms absorbed on Pb (111). Figure 5.6 (a) was

obtained with a *clean* superconducting tip, the atom appears as a round object on the lead surface. Figure 5.6 (b) was obtained after absorbing a Nc molecule at the tip's apex. As shown, the half-moon shape can be assigned to a tilted Nc absorbed onto the apex of the tip [34].

### 5.3.2 STS with Nc-terminated tip

Next, we measure STS with the Nc-terminated tip. Figure 5.6 (c) and (d) show a comparison between spectra measure on a Nc island with a Pb tip, and STS obtained with a Nc tip on clean Pb (111) surface. As we can observe, the two spectra are almost identical. The IETS peaks can be found roughly at the same sample bias, showing that the magnetic properties of Nc on Pb (111) surface are conserved when transferred to the tip's apex.

Another interesting feature observed with the Nc-terminated tip, is that it gives an enhanced spatial resolution, allowing to resolve the atomic structure of the surface [202]. Figure 5.6 (e) shows a constant-current topography image of the Pb (111) surface, feed-back parameters are I=80 pA and V = -15 mV. These atomic-resolution images can only be obtained by bringing the tip close enough to the surface, setting a low-enough bias ($\leqslant$ 20 mV). The resulting hexagonal lattice is in good agreement with the (111) crystal orientation of the Pb sample.

#### Sensing MAE variations

As discussed in 5.2.3, the Nc layer shows small energy variations depending on the measured molecule. With the aid of a Nc tip, we will try to sense these small changes in the anisotropy on the Pb (111) surface. Figure 5.7 (f) shows the atomic resolution image obtained with a Nc-terminated tip. From the topography, we can distinguish the four highly symmetric absorption sites on Pb (111): top (blue dot), bridge (red dot) and the two hollow sites. To further distinguish between the two later, we can observe a higher contribution coming from the hcp site (green dot) due to the presence of the atom below that site [202], allowing us to distinguish it from the fcc hollow site (orange dot).

By increasing the tunneling current we bring the tip close to the surface, Fig. 5.7 (c) shows the current ($I$) as a function of the tip displacement ($z$). The $I(z)$ curve gives information about the molecule-surface interaction. As the tip approaches the surface, the current increases exponentially until $\sim$ 70 nA. At this current, we can observe instabilities due to the Nc-sample interaction. Moreover, the forward and backward sweeps reveal a hysteresis behavior, indicating a rearrangement of the Nc at the tip's apex. The $I(z)$ curve shown in Fig. 5.7 is found to be reproducible with different Nc-terminated tips.

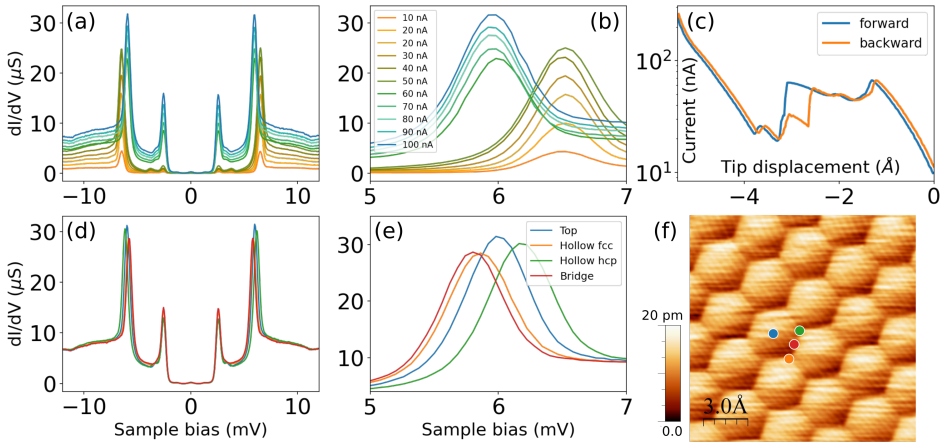


Figure 5.7: Anisotropy sensing with Nc tip. (a) Spectra measured on top position of the Pb (111) surface with increasing tunneling current vañues from I= 10 nA to I=100 nA. (b) Zooming in the data in (a). (c) Forward and backward sweeps of tunneling current versus tip displacement, the tip is placed on top position, and the bias is set to be 15mV. (d) Spectra obtained on different abortion sites with Nc-terminated tip. Feedback is open at $I = 100$ nA and $V = 15$ mV. (e) Zooming in the data of (d), we can observe the different MAE values depending on the absorption site. (f) Atomic resolution image of the Pb (111) surface. $I = 70$ pA, $V = -15$ mV.

Figure 5.7 (a) shows the measured spectra on a top site (blue dot in Fig. 5.7 (f)) as the tip approaches the sample. We can, reproducibly, observe the IETS peaks at $\sim$ 6.5mV and the superconducting gap. As the current increases, we observe an increased signal coming from the quasi-particle peaks. Figure 5.7 (b) zooms in Fig. 5.7 (a) around the IETS peak bias. The peak's energy remains constant up to 70 nA, where a jump of about $\sim$ 0.5 mV can be seen, possibly due to a change in the Nc configuration. This change in energy is too large compared to the small MAE variations observed on the Nc layer in Fig. 5.4. The change in the $I(z)$ curve occurred at $\sim$ 70 nA, and the two distinct IETS peaks values, indicate that the interaction Nc-surface results in two distinct absorption configurations of the molecule at the tip apex [36].

Figure 5.7 (d) shows acquired spectra at a current of $I = 100$ nA, on the four absorption sites. At this current, the molecule-surface interaction is high. Zooming in Fig. 5.7 (e), the colors of the curves coincide with the dot colors in the atomic resolution image. We can observe small anisotropy variations depending on the site we measure with the molecular tip. We can distinguish three different MAE values, as the two hollow sites show a very similar peak position. These values are also found to be reproducible. The difference in MAE between the sites

is found to be up to 0.4 mV. Matching with the variations observed on the Nc islands from Fig. 5.4 (e). Note that these smalls variations in energy are only possible to observe thanks to the use of a superconducting STM tip. With this information, in the following we will unravel the structure of the Nc islands and their orientation with respect to the Pb (111) surface.

## 5.4 Unraveling the structure of Nc islands on Pb(111)

### 5.4.1 DFT calculations of nickelocene

Density functional theory (DFT) has been a key tool for understanding the geometry of Nc on Cu (100) [181] as well as other metallocene molecular layers such as ferrocene [180]. In these studies, the authors found that the molecular islands are composed by a combination of standing up and laying down molecules. As such, we expect the molecular islands in Pb(111) to have a similar geometry. The DFT calculations were performed by the group using the VASP code [203].

Figure 5.8 shows the simulated molecular arrangement of Nc molecules, the structure is a combination of vertical and horizontal molecules. The horizontal molecules are usually not visible in topography images, however, in scans at bias below the inelastic channel ($|V| \leqslant 6.5$ mV), some signal is visible in between the vertical Nc coming from the horizontal ones (see Fig. 5.4 (b)). As we can observe in Fig. 5.8 (a), the unit cell is composed by two vertical and two horizontal Nc. Figure 5.8 (b) shows the structure modeling the zig-zag configuration, in this case the unit cell has doubled in number of molecules. Figures 5.8 (d) and (e) show the corresponding simulated STM images of the two configurations. As we can see, they show good agreement with the paired and zig-zag configurations observed in the sample, even when we are not considering the Pb (111) surface. For comparison, Fig. 5.8 (c) and (f) shows the supercell consisting on the paired structure together with the Pb surface, it comprehends a total of 12 molecules. To find the relative orientation of the molecular layer with the (111) surface we perform scanning at low tunneling bias with a Nc-terminated tip near the edge of an island, the atomic resolution granted by the molecular tip, allows us to find an angle of $47-48^{\circ}$ between the dimerization direction of the Nc layer and the $[\bar{1}01]$ direction of the Pb crystal.

According to the calculations without substrate, the paired and zig-zag configurations are not far in energy, in good agreement with both configurations being present in the same proportion on the sample. The binding energy is found to be 0.438 eV for the paired configuration and 0.425 eV for the zig-zag one without substrate. Including the substrate may not change the difference in energy between the two phases because the interaction with the substrate is mainly due to small van der Waals interactions.

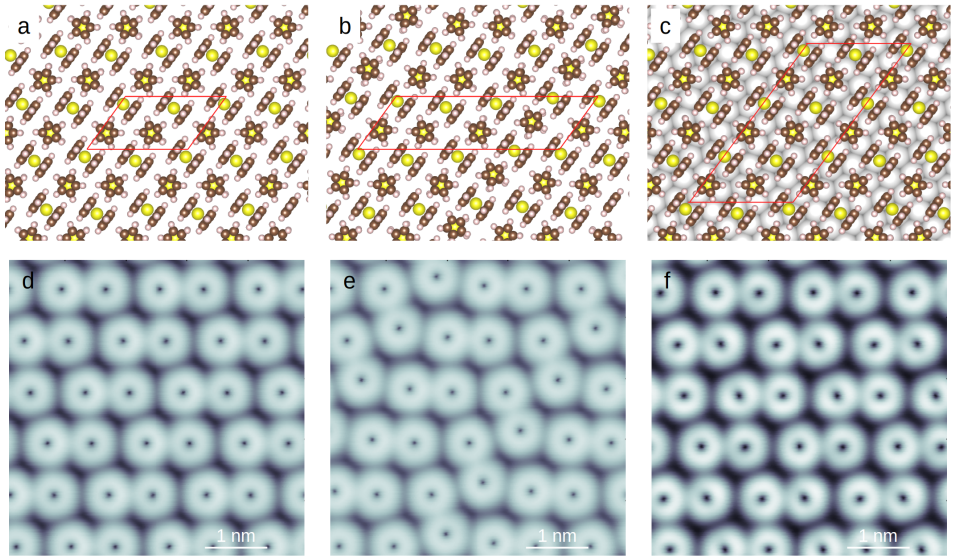


Figure 5.8: DFT calculated Nc layers. (a) Molecular structure of a paired Nc island, in the gas phase the supercell is composed by two vertical and two horizontal Nc molecules. (b) Same as (a) but for the zig-zag arrengement. (c) Supercell composed by the paired molecular layer and the Pb (111) surface. (d)-(f) Corresponding simulated STM topography.

### 5.4.2 Nc structure on Pb (111)

To further optimized the supercell, the molecular layer can be shifted laterally over the Pb (111) surface. This is done so that the molecule at the origin of the molecular supercell occupies the top, hcp, fcc and bridge sites. The final DFT supercell is proposed such that it matches (i) the relative orientation with the surface found in the experiment, (ii) the simulated topography showing the dimer structure observed in the paired islands, and (iii) the quasi-periodic pattern observed on the $dI/dV$ maps in Fig. 5.5 (b)-(c). With these previous constrains, the proposed supercell is shown in Fig. 5.9 (c).

Figure 5.9 (a) and (b) shows two $dI/dV$ maps corresponding to the topography in Fig. 5.4 (a) at $V = 6.6$ mV and $V = 6.0$ mV, respectively. In order to reproduce the quasi-periodic pattern, observed in Fig. 5.9 (a)-(b), the unit cell is chosen with the first atom centered in a fcc site. In this configuration, we can rationalize the $dI/dV$ patterns by realizing there are no molecules absorbed on top position. By looking at the MAE values obtained with the Nc-tip, in Fig. 5.7 (e), we observe that the molecules on hcp sites, show higher energy IETS peak. In Fig. 5.9 (c), we have marked with blue circles on the supercell the standing up molecules in this

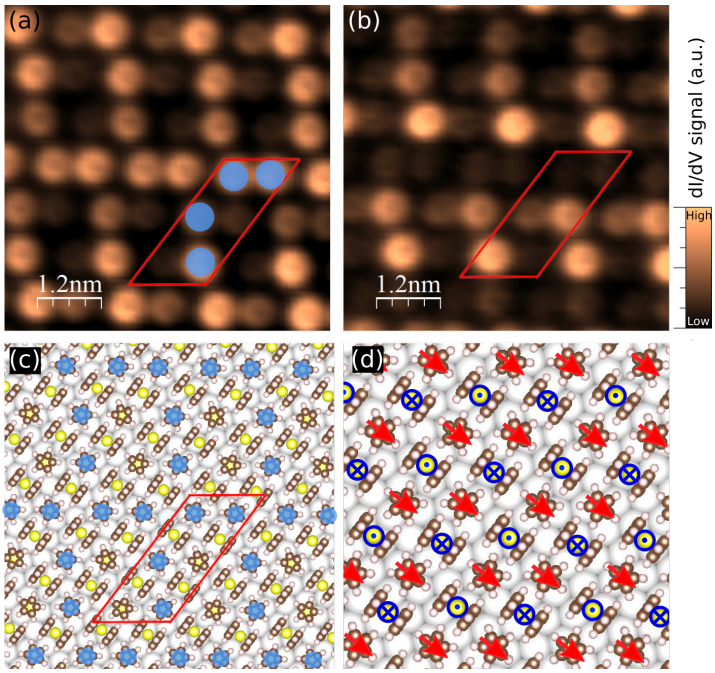


Figure 5.9: (a) Constant-height $dI/dV$ map at $V = 6.6$ mV, corresponding to the topography shown in Fig. 5.4 (a). (b) Same as (b) but $V = 6.0$mV. (c) Supercell for molecular islands on Pb (111). Blue circles indicate the vertical molecules absorbed on hollow hcp sites. (d) Spin texture of the Nc paired layer, as obtained from DFT calculations. Vertical molecules couple ferromagnetically (in-plane red arrows), and horizontal ones anti-ferromagnetically (blue crosses and points represent inward/outward spins).

position, the resulting pattern coincides with the bright molecules from Fig. 5.9 (a), the $dI/dV$ map at higher bias. The remaining molecules in the supercell are absorbed on hollow fcc and bridge, which show a similar MAE, as measured with the Nc tip. Their position matches the bright molecules from the lower bias $dI/dV$ map (Fig. 5.9 (b)). The angle with the surface is 48.7°, which matches the value found experimentally. The supercell is defined by the vectors $(5, -1)$ and $(3, 7)$ which form an angle of 53.9° in good agreement with the experimental value $50 \pm 4°$. The structure also shows some incommensurability with the surface, which translates into the quasi-periodic pattern observed in the experimental $dI/dV$ maps.

Finally, DFT calculations were also used to evaluate intermolecular magnetic interactions in the paired configuration. Using non-collinear spin configurations, minimizing the energy and fitting a generalized Heisenberg exchange tensor. The

spin configuration shown in Fig. 5.9 (d) is found. The vertical molecules show a ferromagnetic spin coupling (red arrows) in the same row. While the horizontal Nc are anti-ferromagnetic, sketched as vectors pointing in and out of the substrate. This study shows that a non-collinear spin arrangement is expected in these Nc molecular patterns [204].

## 5.5 Contact measurements with Nc tip

As we have discussed, Nc is a magnetic molecule with a defined magnetic moment corresponding to a spin $S = 1$. As such, when absorbed on a superconducting surface, one could expect to observe YSR states [3]–[5], [7]. However, the spectra shown until now do not have any in-gap features. The emergence of YSR states mainly depends on the magnetic exchange interaction, $J$, of the impurity with the electrons in the superconductor. This interaction depends on the magnetic species and the surface, but it may be tuned, for example, by controlling the distance between the molecule and the surface, resulting in different molecule/substrate hybridization [195].

With this in mind, we perform STS measurements with a Nc-terminated superconducting tip as we increase the tunneling current, bringing the tip closer to the Pb surface. We found this configuration to be more stable that approaching the tip to the molecules in the layers. In this situation, the junction resistance drops and because our tip is superconducting, we also expect strong coupling effects to arise, such as multiple Andreev reflections and the Josephson effect (see 4.2.3 and 4.2.3).

### 5.5.1 Multiple Andreev reflections

We pick-up a Nc molecule as explained in 5.3. The presence of the molecule at the apex is verified by taking STS on bare Pb(111), showing the typical IETS peaks of the spin-flip in Nc (blue curve in Fig. 5.10 (b)). We first characterize the tip-substrate junction as we approach the tip to the surface. Figure. 5.10 (a) shows the measured conductance as a function of the tip displacement, $G(z)$, in a semi-logarithmic scale. In the forward sweep (blue curve) we observe an exponential increase of the conductance, until the curve jumps at $\sim 1.0\ G_0$ (where $G_0 = 7.748 \times 10^{-5}$ S is the quantum of conductance) to a different regime where the conductance increases more slowly, we refer to this region as *contact*. We perform spectroscopy in these conditions on the clean Pb surface. The backward sweep (orange curve) shows a big hysteresis in the tip's movement, due to strong molecule-surface interactions.

Figure 5.10 (b) shows the measured STS using a Nc-terminated tip in contact regime compared with the spectrum measured in tunneling regime. As observed,

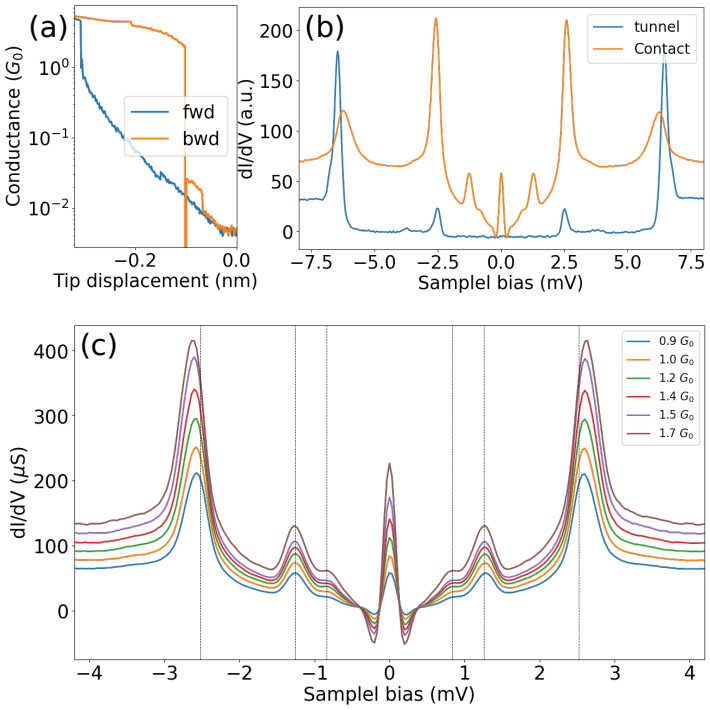


Figure 5.10: STS in contact measurements with a superconducting Nc-terminated tip. (a) G(z) curve of the Nc-terminated tip on Pb surface. Feed-back is opened at $I = 200$ pA, $V = 3.0$ mV. (b) Comparison between tunnel ($G = 1.7 \times 10^{-3}$ $G_0$) and contact ($G = 0.9$ $G_0$) regime, the $dI/dV$ signal is in arbitrary units, allowing to compare the two curves. (c) Contact measurements for conductance values between 0.9-1.7 $G_0$. The black dashed lines mark the expected MAR resonant peaks bias, $2\Delta/n$. Where $\Delta = \pm 2.52$ meV is the superconducting gap, as obtained in tunneling regime.

the two curves are strikingly different. In the high-conductance regime, the inelastic signal coming from the spin flip at $\sim 6.0$ mV is diminished in favor of the quasi-particle peaks of the superconductor and the in-gap features. However, we cannot observe the effect reported on Cu where the molecular spin is reduced to $S = 1/2$ due to the surface-molecule interactions in the contact regime [185]. The most remarkable difference with the tunneling regime is the presence of in-gap states in the orange spectrum. Figure 5.10 (c) shows several spectra in the contact regime for an increasing junction conductance ($G = 0.9 - 1.7$ $G_0$) in the $\pm 4.5$ mV bias range. In the tunneling regime, we measured a superconducting gap of $\pm 2.52$ mV for this particular tip (marked as black dashed lines). As we can observe, the quasi-particle peaks are broadened in the high-conductance regime due to the increased inter-electrode coupling.

We observe two pairs of symmetrical in-gap features and a pronounced zero-bias peak in the contact regime. The finite-energy peaks correspond to multiple Andreev reflections. In Fig. 5.10 (c) we have marked with black dashed lines the expected $2\Delta/n$ energy values. As we can see, under these conditions, we are able to resolve the $n = 2, 3$-order Andreev reflections. The zero-bias peak corresponds to the Josephson supercurrent, we can see how the conductance increases as we approach the Nc-terminated tip closer to the sample. In the following, we will study the Josephson effect in this junction more closely. Note that, even if we are able to resolve in-gap features in the contact regime, we cannot find evidence of the presence of YSR states in this system.

### 5.5.2 Josephson current

In the spectra from Fig. 4.6 (c), we can observe a prominent zero-bias peak, corresponding to the dc-Josepson effect. The Josephson energy, $E_J$, depends on the resistance of the junction, $R_N$:

$$E_J = \frac{\pi\hbar}{4e^2}\frac{\Delta(T)}{R_N}\tanh\frac{\Delta(T)}{2k_BT}. \tag{5.2}$$

Where $\Delta(T)$ refers to the temperature-dependent gap of the superconductors. From this expression, the critical current of the junction is given by $I_c = 2eE_J/\hbar$. Generally, in high-resistance junctions ($R_N \sim 100$ MΩ), $E_J$ is much smaller than the thermal energy of the system [171]. As the resistance of the junction decreases (for example, by bringing the tip closer to the surface), $E_J$ increases. In our case, we are able to bring the Nc-terminated tip close to the surface until we reach a junction resistance of only a few $k\Omega$, without destroying the superconductivity of the tip to a regime where thermal fluctuation interfere with the Josephson effect, $k_BT \sim E_J$.

Figure 5.11 (a) shows the measured $I-V$ curves for junction resistances between $2-4$ kΩ. In this regime, $E_J$ is comparable with the thermal energy. The $I-V$ characteristics can be expressed under the following form [205]:

$$I(V) = \frac{I_c^2 Z_{env}}{2}\frac{V}{V^2+V_p^2}, \tag{5.3}$$

where $V_p = (2e/\hbar)Z_{env}k_BT_n$, and $Z_{env}$ is the impedance of a resistor, used to model the Johnson noise [206], [207] at temperature $T_n$. The solid lines in Fig. 5.3 (a) are the fitting of the data using Eq. 5.3, where the parameters are $V_p$ and $A \equiv I_cZ_{env}/2$. As we can observe the solid lines are only able to fit the experimental points, for small bias in the ±0.2 mV range. This is due to the fast increase of quasi-particle current with bias that ovecomes the slow $1/V$ decrease of Cooper pair tunneling. The small slope of the linear $I-V$ close to zero, reflects the departure of the Cooper-pair current from the ideal Josephson current. This is due to

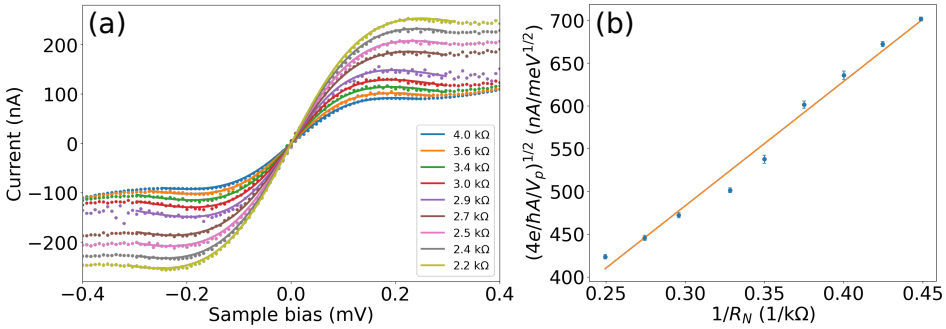


Figure 5.11: Josephson $I-V$ curves for Nc-terminated superconducting tip. (a) Low-bias $I(V)$ curves for $k\Omega$ resistance junctions. The dots represent the experimental data and the solid lines are the fitting usign Eq. 5.3. (b) Linear fit of the extracted parameter $B \equiv \sqrt{(4e/\hbar)A/V_p}$ versus $1/R_n$. From the slope we can extract $V_p$ and $T_n$ of the system.

the Josephson energy being comparable to the thermal energy, as Eq. 5.3 describe the $I(V)$ curves in the limit of strong thermal fluctuations [205].

Nevertheless, the extracted $V_p$ values from each curve can be plotted versus $1/R_N$. The resulting points are plotted in Fig. 5.11 (b), which can be fit by a linear dependence. Error bars are comparable to the markers' size. From its slope we can extract the effective temperature and from the magnitude of the current we obtain the impedance of the system. From this set of measurements we obtain $T_n = 24.648 \pm 0.693$ K and $Z_{env} = 205.5 \pm 22.5$ Ω, describing the Johnson noise in our STM set-up.

## 5.6 Nc and Fe atoms

Finally, we add Fe atoms to the sample. Our goal is to study if the magnetic properties of Nc can be affected by the presence of a Fe atom modifying the in-gap electronic structure, and whether the atoms can form new structures with the molecular Nc layers.

### 5.6.1 Fe on Pb(111): YSR states

The Pb(111) sample obtained after the Nc deposition, shows patches of molecular islands, and also big areas of clean lead. On this sample, we deposit Fe atoms. The atomic evaporation is performed *in situ* by keeping the sample in the STM stage. A window connects the microscope with an evaporator containing three different metallic filaments (Fe, Ni and Cr). The Fe atoms can be directly evaporated into the Pb (111) crystal at LHe temperature. We deposit by opening the STM shield,

connecting to the evaporator for times between 30-60 s. The resulting sample is shown in Fig. 5.12 (a).

The Fe coverage is $< 1\%$, and individual Fe atoms can be found on the Pb (111) surface. Among these, we can distinguish two different species: most of the atoms (around 90 %) show a corrugation of $30.0 \pm 3.6$ pm and have a rather elongated shape (Fig. 5.12 (c)), we call them type I Fe following Ref. [37], the remaining atoms (10 %) show a higher corrugation, $55.0 \pm 9.0$ pm, and have a more round appearance, shown in Fig. 5.12 (b). We refer to them as type II Fe after [37].

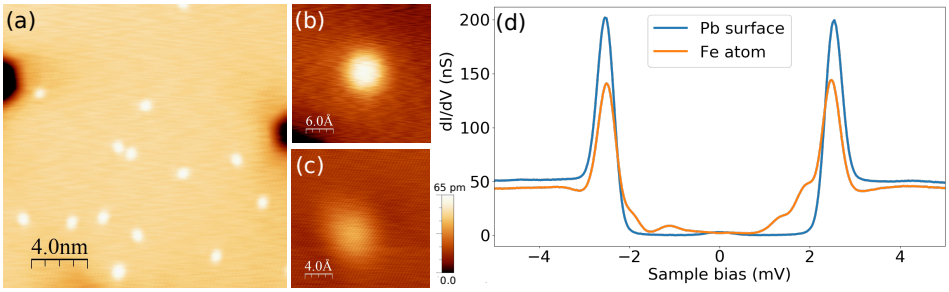


Figure 5.12: Fe atoms deposited on Pb(111). (a) Constant current topography image showing a Pb (111) clean area after the Fe atomic evaporation, I=60 pA, V = 80 mV. (b) Constant current image of single type II Fe atom, I = 60 pA, V = 40 mV. (c) Type I Fe atom, I = 60 pA, V=40 mV. (d) STS measured on clean Pb surface (blue curve) and obtained on type II Fe atom (orange curve).

As reported by previous studies [37], Fe on Pb (110) crystals shows in-gap features. The resulting spectra at low biases is depicted in Fig. 5.12 (d). Spectra over 40 atoms were recorded, type I Fe atoms do not show any in gap feature and the spectra at low biases is indistinguishable from the Pb surface. On the other hand, the higher-corrugation Fe atoms (type II) show in-gap states in the tunneling regime. The orange curve in Fig. 5.12 (d) was obtained by placing the STM tip in the center of a type II Fe atom. The spectrum shows two pairs of in-gap states at $\pm 1.8$ mV and $\pm 1.3$ mV corresponding to two YSR-states. As reference, we also plot the spectrum measured on clean Pb surface with the same tip (blue curve). The energy position of the YSR states is found to be reproducible in other type II Fe atoms.

As we showed in 5.3, the Nc-terminated tip allows for atomic resolution of the surface. This high spatial resolution can help us determine the Fe atoms absorption in the Pb (111) surface. Figure 5.13 (a) shows a constant current image showing the two types of Fe atoms in the sample, close to a surface cavity. These

cavities are the result of Ar embedded in the surface during the sputtering process, resulting in surface bubbles [208]–[210]. The shape of these cavities follow the crystal facets of the (111) crystal, as such, they present a hexagonal shape. Figure 5.13 (b) shows a scan of the same area but with a Nc-terminated tip. As we can see, the scan now shows atomic resolution. The Fe atoms also have a very different appearance, probably due to the current tunneling through the molecular orbitals of the Nc.

In order to determine the absorption position of the atoms, we try to match the atomic pattern of the Pb (111) crystal with a triangular lattice. Figure 5.13 (c) zooms in an area around the type-II Fe, with an over imposed lattice with parameter $a = 3.27$ Å. Which is $< 10\%$ error compared to Pb (111) surface parameter, $a = 3.5$ Å [211]. The center of the balls is assumed to be the top position and the rotation of the lattice is adjusted to better match the pattern. As we can see, the center of the Fe atoms falls in a location that matches a hollow site of the lattice.

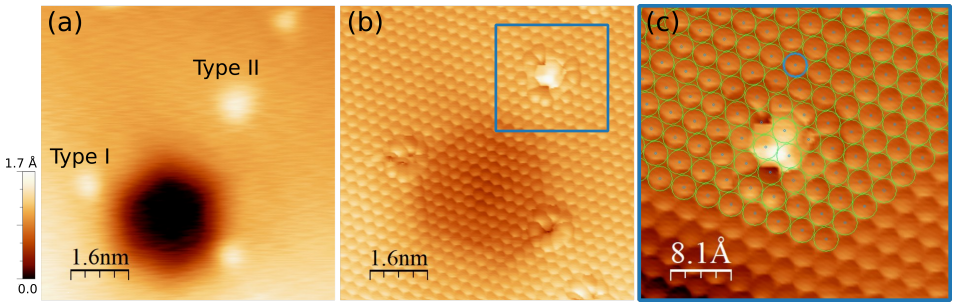


Figure 5.13: Fe atoms on Pb (111) surface. (a) Constant current scan of Fe atoms on Pb surface, feed-back parameters I=60 pA, V=50 mV, the two types of Fe atoms are visible. (b) same as (a) but the superconducting tip is now Nc-terminated, I=200pA, V = 10mV. (c) Zoomed in area from (b), with a triangular lattice over imposed matching the resulting triangular lattice of the (111) surface.

### 5.6.2 Nc tip and Fe atom

The next step we take is to use the Nc-terminated STM tip to study the interaction between the molecule and the type II Fe atoms. As shown by previous studies on Cu (100) with a Nc-terminated tip, the presence of a Fe adatom, induces a splitting of the degenerate excited states of Nc seen in the $dI/dV$ spectra as the tip approaches the magnetic adatom [183]. Similarly, using cobaltocene-terminated tips the presence of a Fe atom, induces a splitting of the Kondo peak of cobaltocene [188]. As such, we expect the Fe atom to magnetically couple with the Nc molecule at the apex of the tip.

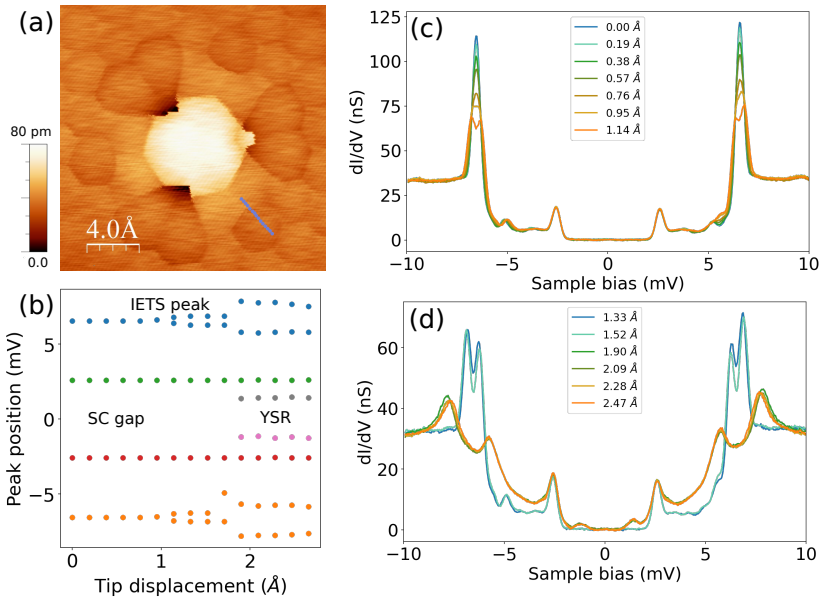


Figure 5.14: Fe atom on Pb (111) measured using a Nc-terminated superconducting tip. (a) Constant current image recorded on a type-II Fe atom with a Nc-terminated tip, $I = 200$ pA, $V = 10$ mV. (b) Peaks position versus tip displacement as obtained from spectra in (c) and (d). (c)-(d) Measures STS as we move the tip toward the Fe atom, the measured positions are depicted as crosses in (a).

Figure 5.14 (a) shows the topography of the Fe atom obtained with a Nc molecule at the tip's apex, with tunneling parameters $I = 200$ pA and $V = 10$ mV. In this configuration, we have atomic resolution of the Pb (111) surface. The Fe atom appears as a bright area in the hexagonal lattice with a corrugation of $\sim 40$ pm. Scanning over Fe atoms with a molecular tip is particularly difficult due to the strong atom-Nc interactions. Some areas appear as dark spots due to instabilities of the tip's Nc. To observe the effect of the magnetic atom, we perform STS as we approach laterally toward the center of the atom (the measured positions are marked with blue dots in Fig. 5.14 (a)). Figures 5.14 (c) and (d) show the resulting spectra. The curves are measured in the $\pm 10$ mV range. The blue curve in Fig. 5.14 (c) shows the usual STS signal of a Nc-terminated tip: at $\sim \pm 6$ mV we observe the inelastic spin-excitation signal, the superconducting energy gap at $\pm 2.6$ mV and no in-gap states. This spectrum does not show any features induced by the presence of the Fe atom, and it is indistinguishable from STS recorded on a clean Pb surface with molecular tip, away from the Fe atom. We label the spectrum as $x = 0.0$, found at a distance of 8.2 Å to the center of the Fe atom. The lateral tip displacement, $x$, is indicated in the legend for the rest of the curves. As

the tip approaches the Fe atom, the IETS peaks start reducing their height until we observe a splitting of the peaks at $x = 1.14$ Å (Fig. 5.14 (c)).

The splitting of the IETS peak, results from the degeneracy breaking of the two excited states of Nc. Indeed, the exchange interaction between Fe and Nc, lifts the degeneracy between the two states, $|S = 1, m_z = +1\rangle$ and $|S = 1, m_z = -1\rangle$ [183]. Figure 5.14 (d) shows the spectra as we keep moving the tip toward the magnetic atom. As we can see, the splitting gets bigger, this coincides with the emergence of YSR states inside the superconducting gap. The splitting suffers a jump between $x = 1.52$ Åand $x = 1.9$ Å (Fig. 5.14 (d)). From this point, the splitting becomes constant, indicating a maximum degeneracy lifting.

Figure 5.14 (b) summarizes the peaks' energy positions. The green and red dots correspond to the coherence peaks, which remain at constant bias throughout. The orange and blue and dots are the inelastic peaks. In this graph we can better observe how the IETS peaks split, a small splitting of sub-meV rapidly becomes an energy difference of $\sim 2$ meV. This splitting coincides with the presence of YSR states inside the gap (gray and pink dots). This splitting remains constant as we keep approaching the tip. This set of measurements is found to be reproducible with different Nc tips and on different Fe atoms. We also perform measurements by bringing the tip close to the Fe atom vertically in the $z$ coordinate, as performed in Cu(100) [183]. However, in that case, we cannot see any variation in the splitting of the IETS peaks. The splitting only varies as we change the distance laterally between tip and atom. This effect can only be obtained for type-II Fe atoms, when approaching the type I Fe atoms with a Nc-tip no change in the STS can be observed.

### 5.6.3 Fe + Nc complex

After the Fe deposition, we could find some new features in the Nc layers. In the topography (Fig. 5.15 (a)) these structures appear as a half-moon or "bean" shape structure with a height of 4 Å above the Pb surface, or 50 pm above the Nc layer. The half-moon shape suggests that the Nc molecule is found on top, with some tilting with respect to the surface, exposing the side of one of its rings. We speculate that the Fe atom has migrated below the molecular layer after deposition. Similar structures were found on Nc layers and Ni atoms on Cu (100) [150]. In the following, we refer to this structure as Nc+Fe complex.

#### Tunneling spectra

The inset in Fig. 5.15 (a) shows one of these complexes. The measured tunnel spectrum on this feature is depicted in Fig. 5.15 (b). A small peak is visible at the usual bias of the inelastic spin excitation, but the signal is very weak compared to the usual spectra measured on the Nc layer. The height of the IETS peak varies between different Fe+Nc, but the signal is always drastically lower compared to

STS on Nc in the layer and, in some cases, the signal completely disappears. The STS is taken in the ±25.0 mV range, but no higher-bias signals are observed in the spectrum. Additionally, we observe that the superconducting coherence peaks at ±2.56 mV show some asymmetry.

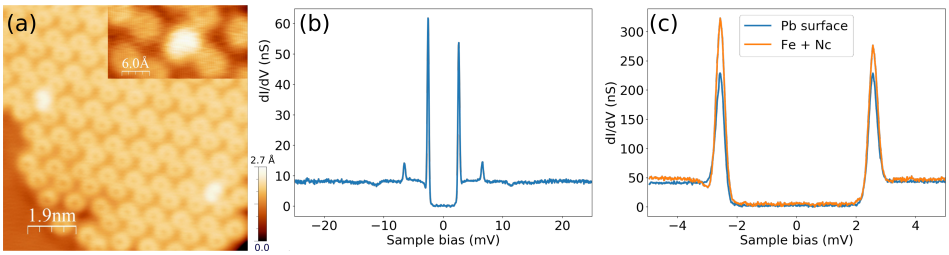


Figure 5.15: Fe+Nc complex found in a Nc molecular layer. (a) Constant current STM image of a paired Nc layer with two Fe+Nc complexes. Inset: Zoomed-in image of one of the structures, feed-back parameters $I = 30$ pA, $V = -20$ mV. (b) Tunnel spectra measured on the bright spot shown in the inset of (a) parameters $I = 20$ pA, $V = -30$ mV. (c) Superconducting gap measured on the Pb surface (blue) and on the Nc+Fe complex (orange).

We take a closer look at these two peaks: Figure 5.15 (c) shows a comparison of the superconducting gap measured on clean Pb surface (blue curve) and on the Fe+Nc complex (orange curve). We can see that the peaks of the two curves are found at a very similar sample bias, however the orange curve shows some degree of asymmetry. We can also see a drop in the $dI/dV$ at negative energy, right before the peak at −2.56 mV. These features point to the presence of a YSR state induced by the Fe + Nc complex in the Pb superconducting gap. Note that these features are found at a very different energy than the YSR states measured on single Fe type II atoms. Indicating that the magnetic interaction of the Nc+Fe complex is different from the one of single Fe adatoms.

### Contact measurements

Finally, we measure spectra on the Fe+Nc complex as we approach the Pb tip toward the sample. We first characterize the Nc+Fe junction with the tip. Figure 5.16 (a) shows the conductance versus tip displacement ($G(z)$) curve in a semilogarithmic scale obtained by approaching the superconducting tip toward the Fe+Nc complex. The small offset between forward and backward sweeps is due to a delay in data acquisition. The conductance increases exponentially up to close to one unit of conductance ($G_0$), and without big changes in the slope.

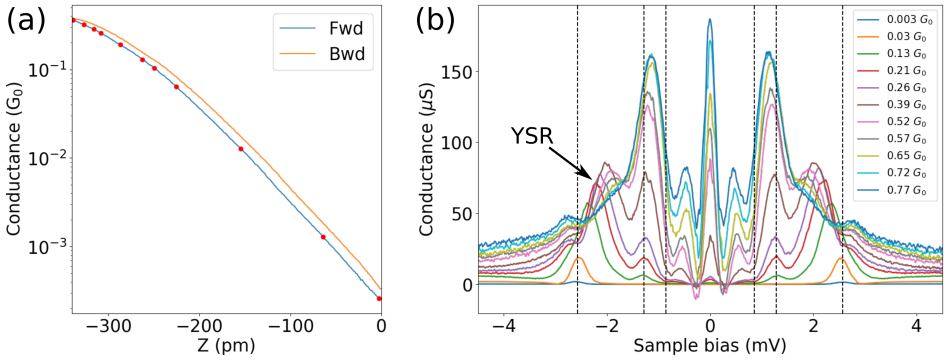


Figure 5.16: Contact measurements performed on a Fe+Nc complex. (a) Conductance versus tip displacement obtained by placing the STM tip on top of the Fe+Nc complex. (b) Measured spectra on the Fe+Nc as we increase the tunneling junction conductance. The black dashed lines indicate the expected position for MAR processes between the superconducting tip and Pb sample.

Figure 5.16 (b) shows the measured spectra, as we increase the current in the tunneling junction. The points where STS is acquired are marked with red points in the $G(z)$ curve in Fig. 5.16 (a). As the junction conductance increases, we can observe the YSR peaks shifting in to lower energies. Also, the asymmetry that we could observe in the tunneling spectra (Fig. 5.15 (b)), disappears. Additionally, as the conductance of the junction increases, low-resistance features appear in the spectra: two pairs of peaks below the energy of the YSR state which, in principle, we attribute to MAR processes, and a Josephson zero-bias peak that rapidly grows as we increase the set-point current. The black dashed lines indicate the expected energy position of the MAR ($2\Delta/n$).

For an increasing tunneling conductance the YSR peaks evolve as we explain in the following: starting from the coherence peaks (found at $\sim 2\Delta$), the peak starts to move to lower energies when tunneling conductance is higher than $0.1G_0$, from that point the peak keeps moving to lower energies. At a conductance of $0.6G_0$, the peak merges with the second-order Andreev reflection (pink curve). The merged peak is found at a sample bias below the expected $\Delta$ value, and stays at this energy for increasing junction conductance (up to $0.77G_0$).

A lower-energy peak is found at $\sim \pm 0.5$ mV, this peak does not match the expected bias for a third-order MAR process. The presence of YSR states together with MAR processes, makes the rationalization of the spectra in Fig. 5.16 (b) not a simple task. The interplay between the YSR states in the Fe+Nc complex and MAR in high conduction regime is still an ongoing study.

**Conclusions.** In the present chapter, we have studied nickelocene on a Pb (111) surface using superconducting STM tips. The deposited molecules create ordered molecular layers on the Pb surface. Nc presents robust magnetic properties that are conserved also on the Pb (111) surface. We measure a big inelastic signal, corresponding to a molecular spin-flip process. It constitutes a direct measurement of the magnetic anisotropy energy (MAE) of the system, for Pb (111) we found a value of $\sim 4$ meV. Similar to other metallic substrates [34], [35]. Thanks to the enhanced energy resolution granted by the Pb-coated superconducting tip, we were able to detect sub-meV energy variations in the MAE of molecules within the same layer.

The magnetic properties of Nc are also conserved when the molecule is transferred to the tip apex. Using a Nc-terminated tip, we were able to probe the MAE on the four different absorption sites. These measurements show a small dependence on the lateral position, the variation was found to be in the same range observed for the Nc layer. These results indicate that the small MAE variations recorded on the molecular layers have their origin on the position of the molecules on the Pb surface.

dI/dV maps of the molecular layers, give us more insight into the spatial distribution of the MAE variations. Using this information, we proposed a molecular supercell, combination of vertical and horizontal molecules. The resulting structure on the Pb (111) surface is in good agreement with the measured $dI/dV$ maps of the Nc layers. Additionally, DFT calculations point to a complex non-collinear arrangement of the spins in the molecular islands [36].

We also perform in-contact measurements with a Nc-terminated STM tip. In this regime, multiple Andreev reflections and the Josephson effect are measured as in-gap features. In our junction, we can resolve the MAR processes of order $n = 2, 3$. But we are not able to observe any YSR states for Nc on Pb (111). We fit the Josephson $I - V$ curves, allowing us to extract the effective temperature in the junction and the impedance resulting from Johnson noise of the system.

Finally, we investigate the interaction of Nc with single magnetic atoms by depositing Fe into the sample. We found that a minority of Fe (around 10 %) show YSR states in tunneling regimen. When we approach a Nc-tip to a single atom, the magnetic moment of the Fe splits the IETS peak, lifting the degeneracy of the doubly degenerated excited state of the molecular spin. When deposited on the molecular layers, Fe can migrate below the molecules, resulting in Nc + Fe complexes. These features show YSR states in the tunneling regimen that can be tuned by bringing the STM tip closer to the surface.

# 6 Conclusions and Outlook

Throughout this thesis, we have studied the physics of YSR states using theoretical and experimental approaches with the aim of understanding how these in-gap states can create MBS in spin chains.

Cr chains on $\beta$-$Bi_2Pd$ show drastically different YSR states depending on the chain's configuration. For the d - $\sqrt{2}a$ chains, we could find a good agreement between theory and experiments when the spin arrangement between the impurities is set as FM. The calculations on the d - $2a$ chain, initially assumed to have an AFM spin ordering, show a better match when a non-collinear spin arrangement is assumed. Calculations in longer chains point to the d - $\sqrt{2}a$ chain as a promising platform for MBS. We expect chains of less than 10 atoms to present localized MBS.

A first outlook of this work is to pursue our studies into assembling longer Cr spin chains on $\beta$-$Bi_2Pd$ superconductors, and compare with the theory presented here. Spin-polarized (SP-STM) measurements could give us more information about the chains' spin arrangement, in particular for the d - $2a$ configuration. Moreover, this thesis shows that a complex behavior of edge states can be found even in topological phases, that need to be characterized before concluding that a non-zero edge state has a topological origin.

For the unambiguous determination of MBS, it is important to evaluate topological invariants, such as the winding number, as set by the Hamiltonian of the system. Due to the efficient numerical calculations that can be performed by tailored BCS Green's functions, it is interesting to have a Hamiltonian that describes the same low-energy physics as the Green's function. We obtained an effective Hamiltonian, starting from the real-space Green's function, that describes a spin chain on a superconductor. From there, we could evaluate the system's winding number, allowing us to unambiguously identify the topological phase. Furthermore, we have shown that we can determine the winding number from solely numerical calculations.

Calculations for finite chains show an oscillatory behavior in the energy of edge states moving them away from zero and blurring the topological identification of the corresponding superconducting phase. The obtained period results from an emergent moiré pattern, product of two periods: The first one set by the discrete-

ness of the lattice and the second one by the spin-substrate interaction, governed by the Fermi wave vector, $k_F$. The significant dependence of the oscillations on these two parameters allows tuning the energy of edge states. In experiments, this can be achieved by varying the distance between the impurities.

We studied Nc on a Pb(111) crystal using superconducting tips. Their high-energy resolution allowed us to sense sub-meV magnetic variations between molecules within the same molecular island. Further information provided by dI/dV maps and DFT calculations allowed us to unravel the absorption of Nc on the Pb (111) surface.

Nc on Pb (111) was initially considered due to their potential application as a MBS platform. However, we could not find evidence of YSR in Nc on Pb (111), even in the contact regime, evidencing low magnetic exchange interaction between Nc and the Pb crystal. After adding Fe atoms to the sample, we found a new structure in the Nc layers. We speculate that Fe atoms migrate below the molecular layer, creating a Fe+Nc complex. The new structure shows YSR states in the tunneling regime, and their energy position can be tuned by approaching the tip.

Approaching the tip changes the conduction properties of the molecular junction. When the electrodes are superconducting, this leads to different regimes where Cooper-pair conduction and high-order single quasi-particle transmision can take place. Using Pb-coated tips with and without Nc molecules in the junction, we have been able to characterize the appearance of Josephson features due to the transmission of Cooper pairs and to study the interplay between multiple-Andreev-reflection (MAR) peaks and YSR states. This interesting work is still work in progress, with the aim to further study the interplay between MAR and YSR, in particular for the characterization of magnetic weak-links between superconductors.

# A Bloch theorem and BdG equations derivation

## A.1 Bloch theorem

In order to analyse the dispersion relation of the superconducting chain, we need to go to momentum space. For this, we can apply Bloch's theorem. It states that the wave function of a periodic system can be written as the product of a periodic function times a phase:

$$\psi_{n,k}(\vec{r}) = \psi_{n,k}(\vec{r}+\vec{R})e^{-i\vec{k}\cdot\vec{R}}. \tag{A.1}$$

Imagine we divide our crystal in unit cells, that are repeated periodically every $\vec{R}$. In each unit cell, we can define a local basis set, such that we can span the full Hilbert space, $\{\phi_\nu(\vec{r})\}$.

Let us start with the eigenvalue problem of the Schrödinger equation:

$$H\psi_{n,k}(\vec{r}) = \epsilon_{n,k}\psi_{n,k}(\vec{r}). \tag{A.2}$$

If we assume we have a finite basis of $N$ elements ($\nu \in \{1,\dots,N\}$), then the secular equation becomes:

$$\begin{bmatrix} \sum_R e^{i\vec{k}\cdot\vec{R}}\langle\phi_1(0)|H|\phi_1(R)\rangle & \dots & \sum_R e^{i\vec{k}\cdot\vec{R}}\langle\phi_1(0)|H|\phi_N(R)\rangle \\ \vdots & \dots & \vdots \\ \sum_R e^{i\vec{k}\cdot\vec{R}}\langle\phi_N(0)|H|\phi_1(R)\rangle & \dots & \sum_R e^{i\vec{k}\cdot\vec{R}}\langle\phi_N(0)|H|\phi_N(R)\rangle \end{bmatrix} \begin{bmatrix} C_1^{n,k} \\ \vdots \\ C_N^{n,k} \end{bmatrix} = \epsilon_{n,k} \begin{bmatrix} C_1^{n,k} \\ \vdots \\ C_N^{n,k} \end{bmatrix} \tag{A.3}$$

Where $C_\nu^{n,k}$ are the coefficients for the Bloch's wave function:

$$\psi_{n,k}(\vec{r}) = \sum_{\nu,i} C_\nu^{n,k}\phi_\nu(\vec{r}-\vec{R}_i)e^{i\vec{k}\cdot\vec{R}_i}. \tag{A.4}$$

This function abides by the Bloch theorem because

$$\psi_{n,k}(\vec{r}+\vec{R}) = \sum_{\nu,i} C_\nu^{n,k}\phi_\nu(\vec{r}-\vec{R}_i+\vec{R})e^{i\vec{k}\cdot\vec{R}_i}e^{i\vec{k}\cdot(\vec{R}-\vec{R})}, \tag{A.5}$$

Reshuffling the exponents and changing variables we get:

$$\psi_{n,k}(\vec{r}+\vec{R}) = \sum_{\nu,i} C_\nu^{n,k}\phi_\nu(\vec{r}-\vec{R}_i+\vec{R})e^{i\vec{k}\cdot(\vec{R}_i-\vec{R})}e^{i\vec{k}\cdot\vec{R}} = \psi_{n,k}(\vec{r})e^{i\vec{k}\cdot\vec{R}},$$

QED.

## A.2 BdG equations derivation

Starting from the Hamiltonian in Eq. 1.31, we want to calculate the commutation relations $[H, c_{i\sigma}^{(\dagger)}]$. Note that we can split the Hamiltonian and compute the commutators as: $[H, c_{i\sigma}^{(\dagger)}] = [H^0, c_{i\sigma}^{(\dagger)}] + [H^\Delta, c_{i\sigma}^{(\dagger)}]$. Where $H^0$ and $H^\Delta$ are the single-particle and coupling Hamiltonian respectively. We explicitly write the derivation for $[H, c_{i\uparrow}]$:

$$[H^0, c_{n\uparrow}] = -\sum_{ij\sigma}(t_{ij}+\delta_{ij}\mu)\underbrace{[c_{i\sigma}^\dagger c_{j\sigma}, c_{n\uparrow}]}_{*} \tag{A.6}$$

Using the anti-commutation relations for fermionic operators, $\{c_\nu, c_\mu\} = \{c_\nu^\dagger, c_\mu^\dagger\} = 0$ and $\{c_\nu, c_\mu^\dagger\} = 1$, we calculate:

$$\begin{aligned} * =& c_{i\sigma}^\dagger c_{j\sigma}c_{n\uparrow} - c_{n\uparrow}c_{i\sigma}^\dagger c_{j\sigma} \\ =& -(c_{i\sigma}^\dagger c_{n\uparrow}c_{j\sigma} + c_{n\uparrow}c_{i\sigma}^\dagger c_{j\sigma}) \\ =& -(c_{i\sigma}^\dagger c_{n\uparrow} + c_{n\uparrow}c_{i\sigma}^\dagger)c_{j\sigma} = \{c_{i\sigma}^\dagger, c_{n\uparrow}\}c_{j\sigma} = -\delta_{in}\delta_{\sigma\uparrow}c_{j\sigma} \end{aligned} \tag{A.7}$$

So that,

$$\begin{aligned} [H^0, c_{n\uparrow}] =& \sum_{ij\sigma}(t_{ij}+\delta_{ij}\mu)\delta_{in}\delta_{\sigma\uparrow}c_{j\sigma} \\ =& \sum_j (t_{nj}+\mu\delta_{tj})c_{j\uparrow} \end{aligned} \tag{A.8}$$

Similarly, we compute $[H^\Delta, c_{n\uparrow}]$:

$$[H^\Delta, c_{n\uparrow}] = \sum_i \left(\Delta_i \underbrace{[c_{i\uparrow}^\dagger c_{i\downarrow}^\dagger, c_{n\uparrow}]}_{**} + \Delta_i^*[c_{i\downarrow}c_{i\uparrow}, c_{n\uparrow}]\right) \tag{A.9}$$

The second term of the expression is zero, due to commutation properties of creation and annihilation operators. And we only need to calculate the first term:

$$\begin{aligned} ** =& c_{i\uparrow}^\dagger c_{i\downarrow}^\dagger c_{n\uparrow} - c_{n\uparrow}c_{i\uparrow}^\dagger c_{i\downarrow}^\dagger \\ =& -(c_{i\uparrow}^\dagger c_{n\uparrow}c_{i\downarrow}^\dagger + c_{n\uparrow}c_{i\uparrow}^\dagger c_{i\downarrow}^\dagger) \\ =& -\{c_{i\uparrow}^\dagger, c_{n\uparrow}\}c_{i\downarrow}^\dagger = -\delta_{in}c_{i\downarrow}^\dagger \end{aligned} \tag{A.10}$$

So that,

$$[H^{\Delta}, c_{n\uparrow}] = \sum_i \Delta_i(-\delta_{in}c^{\dagger}_{i\downarrow}) = \sum_n \Delta_n c^{\dagger}_{n\downarrow} \tag{A.11}$$

Finally, the total commutator writes:

$$[\hat{H}^{MF}, c_{i\uparrow}] = [\hat{H}^{0}, c_{i\uparrow}] + [\hat{H}^{\Delta}, c_{i\uparrow}] = \sum_j (t_{ij} + \delta_{ij}\mu)c_{j\uparrow} + \Delta_i c^{\dagger}_{i\downarrow} \tag{A.12}$$

The remaining commutators shown in Eq. 1.33 can be obtained similarly.

We next substitute the generalized Bogoliubov transformation form Eq. 1.32 into the commutators $[H, c^{(\dagger)}_{i\sigma}]$, we get:

$$\begin{aligned}
[H^{MF}, c_{i\uparrow}] &= \sum_{nj} \gamma_{n\uparrow}[(t_{ij} + \delta_{ij}\mu)u_{ni\uparrow} + \Delta_i v_{ni\downarrow}] + \gamma^{\dagger}_{n\downarrow}[(t_{ij} + \delta_{ij}\mu)v^{*}_{ni\uparrow} + \Delta_i u_{ni\downarrow}] \\
[H^{MF}, c_{i\downarrow}] &= \sum_{nj} \gamma_{n\downarrow}[(t_{ij} + \delta_{ij}\mu)u_{ni\downarrow} - \Delta_i v_{ni\uparrow}] + \gamma^{\dagger}_{n\uparrow}[(t_{ij} + \delta_{ij}\mu)v^{*}_{ni\downarrow} - \Delta_i u^{*}_{ni\uparrow}] \\
[H^{MF}, c^{\dagger}_{i\uparrow}] &= \sum_{nj} \gamma^{\dagger}_{n\uparrow}[-(t_{ij} + \delta_{ij}\mu)u^{*}_{ni\uparrow} - \Delta^{*}_i v_{ni\downarrow}] + \gamma_{n\downarrow}[-(t_{ij} + \delta_{ij}\mu)v_{ni\uparrow} - \Delta^{*}_i u_{ni\downarrow}] \\
[H^{MF}, c^{\dagger}_{i\downarrow}] &= \sum_{nj} \gamma^{\dagger}_{n\uparrow}[-(t_{ij} + \delta_{ij}\mu)v_{ni\downarrow} + \Delta^{*}_i u_{ni\uparrow}] + \gamma^{\dagger}_{n\downarrow}[-(t_{ij} + \delta_{ij}\mu)u^{*}_{ni\uparrow} + \Delta^{*}_i v^{*}_{ni\uparrow}]
\end{aligned} \tag{A.13}$$

We then, impose the $\gamma^{(\dagger)}_{n\sigma}$ operators to diagonalize the $H^{MF}$ Hamiltonian,

$$\hat{H}^{MF} = E_0 + \sum_n E_{n\uparrow}\gamma^{\dagger}_{n\uparrow}\gamma_{n\uparrow} + E_{n\downarrow}\gamma^{\dagger}_{n\downarrow}\gamma_{n\downarrow} \tag{A.14}$$

We compute, again the $[H, c^{(\dagger)}_{i\sigma}]$ for the diagonalized Hamiltonian in Eq. A.14. Applying the commutation relations:

$$[H^{MF}, \gamma_{n\sigma}] = -E_n\gamma_{n\sigma}, \quad [H^{MF}, \gamma^{\dagger}_{n\sigma}] = E_n\gamma^{\dagger}_{n\sigma} \tag{A.15}$$

We explicitly write the derivation for $[H, c_{i\uparrow}]$, using the generalized Bogoliubov transformation:

$$\begin{aligned}
[H^{MF}, c_{i\uparrow}] =& [H^{MF}, \sum_n (u_{ni\uparrow}\gamma_{n\uparrow} + v^{*}_{ni\uparrow}\gamma^{\dagger}_{n\downarrow})] \\
=& \sum_n (u_{ni\uparrow}[H^{MF}, \gamma_{n\uparrow}] + v^{*}_{ni\uparrow}[H^{MF}, \gamma^{\dagger}_{n\downarrow}]) \\
=& \sum_n (-u_{ni\uparrow}E_{n\uparrow}\gamma_{n\uparrow} + v^{*}_{ni\uparrow}E_{n\downarrow}\gamma^{\dagger}_{n\downarrow})
\end{aligned} \tag{A.16}$$

Proceeding similarly, for the rest of the $c_{i\sigma}^{(\dagger)}$ operators we find:

$$\begin{aligned}
[H^{MF}, c_{i\uparrow}] &= \sum_n (-E_{n\uparrow} u_{ni\uparrow} \gamma_{n\uparrow} + E_{n\downarrow} v_{ni\uparrow}^* \gamma_{n\downarrow}^\dagger) \\
[H^{MF}, c_{i\downarrow}] &= \sum_n (-E_{n\downarrow} u_{ni\downarrow} \gamma_{n\downarrow} + E_{n\uparrow} v_{ni\downarrow}^* \gamma_{n\uparrow}^\dagger) \\
[H^{MF}, c_{i\uparrow}^\dagger] &= \sum_n (E_{n\uparrow} u_{ni\uparrow}^* \gamma_{n\uparrow}^\dagger - E_{n\downarrow} v_{ni\uparrow} \gamma_{n\downarrow}) \\
[H^{MF}, c_{i\downarrow}^\dagger] &= \sum_n (E_{n\downarrow} u_{ni\downarrow}^* \gamma_{n\downarrow}^\dagger - E_{n\uparrow} v_{ni\downarrow} \gamma_{n\uparrow})
\end{aligned} \tag{A.17}$$

By comparing the $\gamma_{n\sigma}^{(\dagger)}$ coefficients from Eq. A.13 and A.17, we find the Bogoliubov equations written in the main text (Eq. 1.2.4), and a second set of BdG equations for the complex conjugate coefficients:

$$\begin{aligned}
v_{ni\uparrow}^* E_{n\downarrow} &= \sum_j (t_{ij} + \delta_{ij}\mu) v_{nj\uparrow}^* + \Delta_i u_{ni\downarrow}^* \\
v_{ni\downarrow}^* E_{n\uparrow} &= \sum_j (t_{ij} + \delta_{ij}\mu) v_{nj\downarrow}^* - \Delta_i u_{ni\uparrow}^* \\
u_{ni\uparrow}^* E_{n\uparrow} &= \sum_j -(t_{ij} + \delta_{ij}\mu) u_{nj\uparrow}^* - \Delta_i^* v_{ni\downarrow}^* \\
u_{ni\downarrow}^* E_{n\downarrow} &= \sum_j -(t_{ij+\delta_{ij}\mu}) u_{nj\downarrow}^* + \Delta_i^* v_{ni\uparrow}^*
\end{aligned} \tag{A.18}$$

Or under matrix form:

$$\begin{pmatrix} -h_\uparrow & 0 & 0 & \Delta_i \\ 0 & -h_\downarrow & -\Delta_i & 0 \\ 0 & -\Delta_i^* & h_\uparrow & 0 \\ \Delta_i^* & 0 & 0 & h_\downarrow \end{pmatrix} \begin{pmatrix} v_{ni\uparrow}^* \\ v_{ni\downarrow}^* \\ u_{ni\uparrow}^* \\ u_{ni\downarrow}^* \end{pmatrix} = E_n \begin{pmatrix} v_{ni\uparrow}^* \\ v_{ni\downarrow}^* \\ u_{ni\uparrow}^* \\ u_{ni\downarrow}^* \end{pmatrix} \tag{A.19}$$

Comparing these to set of BdG equations from the main text (Eq. 1.36), we observe that the two sets have the same expression, except for a minus sign. From this we can conclude: For every solution $(u_{n\uparrow}, u_{n\downarrow}, v_{n\uparrow} v_{n\downarrow})^T$ of Eq. 1.36 with eigen energy $E_n$. Automatically, there is a second solution, $(v_{n\uparrow}^*, v_{n\downarrow}^*, u_{n\uparrow}^*, u_{n\downarrow}^*)^T$ with eigen energy $-E_n$.

# B Some details on integrals and the Abrikosov-Gorkov equations

## B.1 Cauchy's expression

We have that:

$$\frac{1}{\omega + i\eta} = \frac{\omega}{\omega^2 + \eta^2} - i\frac{\eta}{\omega^2 + \eta^2} \tag{B.1}$$

By making the limit $\eta \to 0$. The real part simply becomes: $\frac{1}{\omega}$

In the imaginary part, we can see that it has the shape of a Lorentzian, in the limit this becomes a Dirac delta:

$$\lim_{\eta \to 0} \frac{\eta}{\omega^2 + \eta^2} = \pi\delta(\omega) \tag{B.2}$$

And so equation B.1 becomes:

$$\frac{p}{\omega} - i\pi\delta(\omega), \tag{B.3}$$

where $p$ stands for the principal part.

## B.2 Solving integrals

In order to evaluate the BCS Green's function, Eq. 2.28, we show here how to obtain Eqs. 2.26 and 2.27 that are the solutions to:

$$I_1 = \frac{1}{(2\pi^3)} \int \frac{e^{ik\mathbf{r}}\Delta}{\omega^2 - \xi_k^2 - \Delta^2} dk \tag{B.4}$$

$$I_2 = \frac{1}{(2\pi^3)} \int \frac{e^{ik\mathbf{r}}(\omega + \xi_k)}{\omega^2 - \xi_k^2 - \Delta^2} dk \tag{B.5}$$

To solve the first integral, we change the integration variables to spherical coordinates. And using the dispersion relation $\frac{k^2}{2m} - \mu = \xi_k$, where $\mu$ is the chemical potential or Fermi energy. We find that,

$$\int d^3k = \pi \int k^2 dk \int_{-1}^{1} dx = \pi \frac{N_0}{2} \int \xi_k \tag{B.6}$$

The new integration variables are $\xi_k$ and $x = \cos\theta_k$. Eq. B.4 becomes:

$$I_1 = \frac{N_0}{2} \int d\xi_k \int_{-1}^{1} dx \frac{\Delta e^{ikrx}}{\omega^2 - \xi_k^2 - \Delta^2}, \tag{B.7}$$

where $N_0$ is the normal-metal DOS at the Fermi energy. We first integrate $\xi_k$ for the case $\omega < \Delta$:

$$I = \int_{-\infty}^{\infty} d\xi_k \frac{e^{ikrx}}{(i\xi_k - \sqrt{\Delta^2 - \omega^2})(i\xi_k + \sqrt{\Delta^2 - \omega^2})} \tag{B.8}$$

Following the BCS approximations, we linearize the energy about the Fermi energy, which is equivalent to writing $k = k_F + \xi_k/v_F$. Then, the integral becomes:

$$I = \int_{-\infty}^{\infty} d\xi_k \frac{e^{i(k_F + \frac{\xi_k}{v_F})rx}}{(i\xi_k - \sqrt{\Delta^2 - \omega^2})(i\xi_k + \sqrt{\Delta^2 - \omega^2})} \tag{B.9}$$

To solve this integral, we move to the complex plane. We realize that it is equal to $2\pi$ the residue of the integrand. Changing variables to $z = i\xi_k$ gives us an overall negative sign and there is only one simple pole in the contour that makes the integral convergent:

$$I = -2\pi i \frac{e^{i(k_F rx + \frac{\sqrt{\Delta^2 - \omega^2}}{v_F} r|x|)}}{2i\sqrt{\Delta^2 - \omega^2}} \tag{B.10}$$

It is straight forward to integrate over $x$. After taking the limit $k_F \gg \frac{\sqrt{\Delta^2 - \omega^2}}{v_f}$, we obtain the result:

$$I_1 = -\frac{N_0 \pi sin(k_F r)}{k_F r \sqrt{\Delta^2 - \omega^2}} e^{-\frac{\sqrt{\Delta^2 - \omega^2}}{v_f} r}. \tag{B.11}$$

The second integral, $I_2$, needs to be renormalized to make it convergent. To do this, we apply a Lorentizan cutoff on the Debye frequency, $\omega_D$, as is customarily done in the BCS theory. The integral becomes:

$$I_2 = \frac{N_0}{2} \int d\xi_k \int_{-1}^{1} dx \frac{\xi_k e^{ikrx}}{\omega^2 - \xi_k^2 - \Delta^2} \frac{\omega_D^2}{\omega_D^2 + \xi_k^2}. \tag{B.12}$$

Following the same procedure as for $I_1$ and then taking the limits $k_F r \gg \frac{\omega_D r}{v_f} \gg 1$ as well as $k_F \gg \frac{\sqrt{\Delta^2 - \omega^2}}{v_f}$, we obtain the result:

$$I_2 = -\frac{N_0 \pi cos(k_F r)}{k_F r} e^{-\frac{\sqrt{\Delta^2 - \omega^2}}{v_f} r}. \tag{B.13}$$

These approximations lead to a discontinuity in $r$ when going from the spatially non-diagonal Green's function to the diagonal one as we saw in Chapter 2, since $r$ cannot be smaller than $1/k_F$.

## B.3 Lehmann representation using the Abrikosov-Gorkov equations

We explicitly calculate the term $I_1$ from Eq. 2.35, using Eq. 2.31:

$$I_1 = \sum_n \frac{e^{-\beta E_n}}{Z} \langle n| e^{\tau\mathcal{H}} \hat{c}_{i\uparrow} \underbrace{e^{-\tau\mathcal{H}} e^{\tau'\mathcal{H}}}_{=e^{-\mathcal{H}(\tau-\tau')}} \hat{c}^\dagger_{i\uparrow} e^{-\tau'\mathcal{H}} |n\rangle$$

And using the property that the trace of a matrix product is constant under cyclic permutations:

$$I_1 = \sum_n \frac{e^{-\beta E_n}}{Z} \langle n| e^{\mathcal{H}(\tau-\tau')} \hat{c}_{i\uparrow} e^{-\mathcal{H}(\tau-\tau')} \hat{c}^\dagger_{i\uparrow} |n\rangle = \sum_n \frac{e^{-\beta E_n}}{Z} \langle n| \hat{c}_{i\uparrow}(\tau-\tau') \hat{c}^\dagger_{i\uparrow}(0) |n\rangle$$

We now write the creation and annihilation operators using the Bogoliubov canonical transformation:

$$\hat{c}_{i\sigma} = \sum_n (u^n_{i\sigma} \hat{\gamma}_n - \sigma v^{n*}_{i\sigma} \hat{\gamma}^\dagger_n), \qquad \hat{c}^\dagger_{i\sigma} = \sum_n (u^{n*}_{i\sigma} \hat{\gamma}^\dagger_n - \sigma v^n_{i\sigma} \hat{\gamma}_n) \tag{B.14}$$

Where the $\hat{\gamma}^\dagger_n$ and $\hat{\gamma}_n$ operators creates and annihilates, respectively, a Bogoliubov quasiparticle in the state $n$.

$$I_1 = \sum_n \frac{e^{-\beta E_n}}{Z} \langle n| \sum_s (u^s_{i\uparrow} \hat{\gamma}_s(\tau-\tau') - v^{s*}_{i\uparrow} \hat{\gamma}^\dagger_s(\tau-\tau')) \sum_{s'} (u^{s'*}_{j\uparrow} \hat{\gamma}^\dagger_{s'} - v^{s'}_{j\uparrow} \hat{\gamma}_{s'}) |n\rangle$$

We now perform the product of the two sums in $s$ and $s'$, since we are evaluating the trace $\langle n| \dots |n\rangle$, only the components with $\gamma\gamma^\dagger$ and $\gamma^\dagger\gamma$ will be non-zero, so only the cross-products survive:

$$I_1 = \sum_n \frac{e^{-\beta E_n}}{Z} \langle n| \sum_{s,s'} (u^s_{i\uparrow} u^{s'*}_{j\uparrow} \hat{\gamma}_s(\tau-\tau') \hat{\gamma}^\dagger_{s'} + v^{s*}_{i\uparrow} v^{s'}_{j\uparrow} \hat{\gamma}^\dagger_s(\tau-\tau') \hat{\gamma}_{s'}) |n\rangle$$

We now need to write the time dependence of the Bogoliubov quasiparticle operators, however, these operators diagonalize the Hamiltonian of our system, so that the following commutation relations are verified:

$$[\gamma^\dagger_n, \mathcal{H}] = -E_n \gamma^\dagger_n, \qquad [\gamma_n, \mathcal{H}] = E_n \gamma_n \tag{B.15}$$

From this, it is easily shown that:

$$\gamma^\dagger_n(\tau) = \gamma^\dagger_n e^{E_n \tau/\hbar}, \qquad \gamma_n(\tau) = \gamma_n e^{-E_n \tau/\hbar} \tag{B.16}$$

So that the expression becomes:

$$I_1 = \sum_n \frac{e^{-\beta E_n}}{Z} \langle n| \sum_{s,s'} (e^{-E_s(\tau-\tau')/\hbar} u^s_{i\uparrow} u^{s'*}_{j\uparrow} \hat{\gamma}_s \hat{\gamma}^\dagger_{s'} + e^{E_s(\tau-\tau')/\hbar} v^{s*}_{i\uparrow} v^{s'}_{j\uparrow} \hat{\gamma}^\dagger_s \hat{\gamma}_{s'}) |n\rangle$$

We now use:

$$\sum_n \frac{e^{-\beta E_n}}{Z} \langle n| \gamma^\dagger_s \gamma_s |n\rangle = f(E_s), \qquad \sum_n \frac{e^{-\beta E_n}}{Z} \langle n| \gamma_s \gamma_s \dagger |n\rangle = f(-E_s) \tag{B.17}$$

Where $f(E)$ is the Fermi distribution. From the previous expression, we see that this results in a $\delta_{ss'}$, so the sum in $s'$ disspears and we end up with:

$$I_1 = \sum_s (e^{-E_s(\tau-\tau')/\hbar} u^s_{i\uparrow} u^{s*}_{j\uparrow} f(-E_s) + e^{E_s(\tau-\tau')/\hbar} v^{s*}_{i\uparrow} v^s_{j\uparrow} f(E_s))$$

Doing an analogous development, we find the second term to be:

$$I_2 = \sum_s (e^{E_s(\tau'-\tau)/\hbar} u^{s*}_{j\uparrow} u^s_{i\uparrow} f(E_s) + e^{-E_s(\tau'-\tau)/\hbar} v^s_{j\uparrow} v^{s*}_{i\uparrow} f(-E_s))$$

# C Rashba spin-orbit coupling

## C.1 Modelling the Rashba spin-orbit coupling in a discrete 2-D array

We recall here the Rashba Hamiltonian for a 2-D system (Eq. 2.53):

$$\hat{H}_{Rashba} = \frac{\alpha_R}{2a} \sum_{n,m} \left[ \big( |n+1,m\rangle\langle n,m| \times i\sigma_y \big) - \big( |n,m+1\rangle\langle n,m| \times i\sigma_x \big) \right] + h.c. \tag{C.1}$$

Where the index $n$, denotes the site in the $x$ spatial coordinate, and $m$ in the $y$ coordinate. $\sigma_x$ and $\sigma_y$ are the Pauli matrices acting on the two spin states $\uparrow$ and $\downarrow$. We want to find the explicit expression of Eq. C.1 and how to write the matrices in our 4-component Nambu base, $\Psi = (\psi_\uparrow \psi_\downarrow \psi_\uparrow^\dagger \psi_\downarrow^\dagger)^T$.

$$\hat{H}_{Rashba} = \frac{\alpha_R}{2a} \times \begin{pmatrix} 0 & \hat{p}_x - i\hat{p}_y & 0 & 0 \\ -\hat{p}_x - i\hat{p}_y & 0 & 0 & 0 \\ 0 & 0 & 0 & -\hat{p}_x - i\hat{p}_y \\ 0 & 0 & \hat{p}_x - i\hat{p}_y & 0 \end{pmatrix} \tag{C.2}$$

Where the upper block corresponds to the electron space and the lower block is the time-reversed or hole space. The time reversed Hamiltonian is obtained by taking the minus complex conjugate, $-\hat{H}^\dagger$. Nevertheless, when writing this matrix for a 2-dimensional superconducting array of dimension $N_x \times N_y$, we need to differentiate between the Rashba coupling in the $x$ and $y$ directions.

We explicitly write the matrix of the Rashba interaction, for the case where $N_x = 2$ and $N_y = 3$. The corresponding lattice is depicted in the following diagram. Each node is labelled with the corresponding state $|n,m\rangle$.

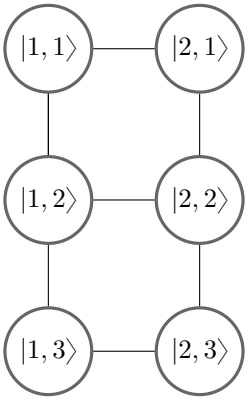


Figure C.1: Lattice with $N_x = 2$ and $N_y = 3$ resulting in a 6 sites lattice, labelled using the notation $|n, m\rangle$.

The resulting matrix will have total size $24 \times 24$ ($4N_xN_y \times 4N_xN_y$). Explicitly:

$$\hat{H}_{total} = \begin{array}{c} \\ \langle 1,1| \\ \langle 2,1| \\ \langle 1,2| \\ \langle 2,2| \\ \langle 1,3| \\ \langle 2,3| \end{array} \begin{array}{c} \begin{array}{cccccc} |1,1\rangle & |2,1\rangle & |1,2\rangle & |2,2\rangle & |1,3\rangle & |2,3\rangle \end{array} \\ \left[\begin{array}{c|c|c|c|c|c} & \hat{H}_x & \hat{H}_y & & & \\ \hline \hat{H}_x^\dagger & & & \hat{H}_y & & \\ \hline \hat{H}_y^\dagger & & & \hat{H}_x & \hat{H}_y & \\ \hline & \hat{H}_y^\dagger & \hat{H}_x^\dagger & & & \hat{H}_y \\ \hline & & \hat{H}_y^\dagger & & & \hat{H}_x \\ \hline & & & \hat{H}_y^\dagger & \hat{H}_x^\dagger & \end{array}\right] \end{array}$$

Each block in the previous matrix has size $4 \times 4$. As we can see, the Rashba Hamiltonian has been divided between $x$ and $y$ coupling. Note that the diagonal blocks are empty and given the state $|n, m\rangle$ only the sites where $n$ ($m$) differs in a unit, have Rashba coupling along $x$ ($y$) direction. The $\hat{H}_x$ and $\hat{H}_y$ are given:

$$\hat{H}_x = \frac{\alpha_R}{2a}\begin{pmatrix} 0 & 1 & 0 & 0 \\ -1 & 0 & 0 & 0 \\ 0 & 0 & 0 & -1 \\ 0 & 0 & 1 & 0 \end{pmatrix} \quad \hat{H}_y = \frac{\alpha_R}{2a}\begin{pmatrix} 0 & -i & 0 & 0 \\ -i & 0 & 0 & 0 \\ 0 & 0 & 0 & -i \\ 0 & 0 & -i & 0 \end{pmatrix} \tag{C.3}$$

# D dI/dV numerical calculation

## D.1 Convolution and dI/dV calculation

In this appendix, we explicitly write the expressions for the numerical evaluation of the $\partial I/\partial V$ signal between two superconductors. As shown in Eq. 4.5, there are three terms to evaluate:

$$\begin{aligned}(I) &= \int_{-\infty}^{\infty} d\epsilon \rho_s(\epsilon)\rho_t'(\epsilon - eV) f_t(\epsilon - eV) \\ (II) &= \int_{-\infty}^{\infty} d\epsilon \rho_s(\epsilon)\rho_t(\epsilon - eV) f_t'(\epsilon - eV) \\ (III) &= \int_{-\infty}^{\infty} d\epsilon \rho_s(\epsilon)\rho_t'(\epsilon - eV) f_s(\epsilon)\end{aligned} \tag{D.1}$$

The $\partial I/\partial V$ signal is proportional to $\partial I/\partial V \propto -(I) - (II) + (III)$. The three expressions in Eq. D.1, have the form of three convolutions[1]. Since our goal is to simulate the conductance between two superconductors, the expression used for $\rho_s(\epsilon)$ and $\rho_t(\epsilon)$ are given by Eq. 4.13. The derivative of this expression can be analytically obtained:

$$\frac{\partial \rho_{sc}(\epsilon)}{\partial \epsilon} = N_0 Re\Big[\frac{1}{\sqrt{(\epsilon + i\Gamma)^2 - \Delta^2}}\Big] - N_0 Re\Big[\frac{(\epsilon + i\Gamma)^2}{[(\epsilon + i\Gamma)^2 - \Delta^2]^{3/2}}\Big] \tag{D.2}$$

Similarly, we can obtain the derivative of the Fermi function:

$$\frac{\partial f(\epsilon, T)}{\partial \epsilon} = \frac{-1}{T} \frac{exp(\epsilon/T)}{\big(1 + exp(\epsilon/T)\big)^2} \tag{D.3}$$

The three expression in Eq. D.1 are evaluated numerically, we select the following parameters for the two electrodes of the junction: the normal electron density of the metal, $N_0$, the superconducting gap, $\Delta$, temperature, $T$, and the Dynes parameter, $\Gamma$. Figures 4.5 and D.1 shows some results that we can obtain with this numerical calculation. Figure D.1 (a) shows the result for a metallic tip and a superconducting sample, this can be easily achieved by setting $\rho_t \equiv cte$. The superconducting gap is set to be $\Delta = 1.35$ meV and temperature is $T = 4.0$ K.

[1] The convolution of two functions is defined as the integral of the product of the two functions after one is reversed and shifted, $f * g(t) := \int_{-\infty}^{\infty} f(\tau) g(t - \tau) d\tau$

The tunneling between two superconductors is plotted in Fig. D.1 (b), here the superconducting gaps are $\Delta_1 = 1.0$ meV and $\Delta_1 = 2.0$ meV, as discussed above, the thermally excited states appear at $|\Delta_1 - \Delta_2| = 1.0$ meV, and the tunneling through the quasi-particle peaks is visible at the peaks at $|\Delta_1 + \Delta_2|$.

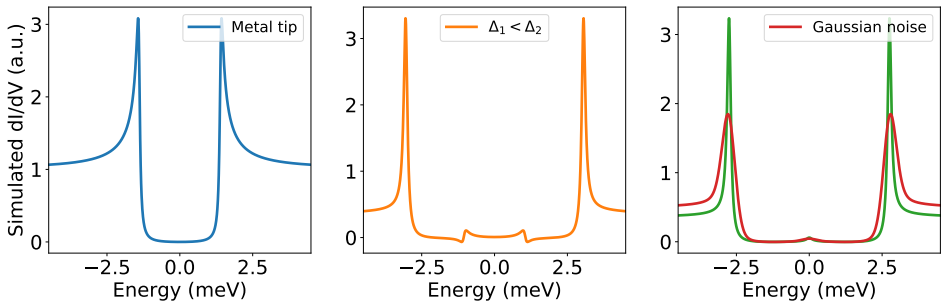


Figure D.1: Numerical $\partial I/\partial V$ simulations. (a) Metallic tip and superconducting sample with $\Delta = 1.35$ meV. (b) Superconducting sample and tip with $\Delta_1 = 1.0$ meV and $\Delta_2 = 2.0$ meV. (c) Superconducting tip and sample with $\Delta_1 = \Delta_2 = 1.35$ meV (green curve) adding Gaussian noise (red curve). Temperature is set to $T = 4.0$ K for all cases.

To add the noise effect of the electronics in the lock-in amplifier, we additionally make a convolution of the resulting signal with a Gaussian function. This allows to better fit the peaks' broadening in our measurements. Figure D.1 (c) we show the conductance signal with $\Delta_1 = \Delta_2 = 1.35$ meV (green curve), and then we add the effect of the noise by convolving the signal with a Gaussian function with $\sigma = 0.19$ meV (red curve).

# Bibliography


[1] J. Bardeen, L. N. Cooper, and J. R. Schrieffer, "Theory of superconductivity," *Phys. Rev.*, vol. 108, pp. 1175–1204, 5 Dec. 1957. DOI: 10.1103/PhysRev.108.1175. [Online]. Available: https://link.aps.org/doi/10.1103/PhysRev.108.1175.

[2] L. N. Cooper, "Bound electron pairs in a degenerate fermi gas," *Phys. Rev.*, vol. 104, pp. 1189–1190, 4 Nov. 1956. DOI: 10.1103/PhysRev.104.1189. [Online]. Available: https://link.aps.org/doi/10.1103/PhysRev.104.1189.

[3] L. Yu, "Bound state in superconductors with paramagnetic impurities," *Acta Phys. Sin*, vol. 21, no. 1, pp. 75–91, 1965.

[4] H. Shiba, "Classical Spins in Superconductors," *Progress of Theoretical Physics*, vol. 40, no. 3, pp. 435–451, Sep. 1968, ISSN: 0033-068X. DOI: 10.1143/PTP.40.435. eprint: https://academic.oup.com/ptp/article-pdf/40/3/435/5185550/40-3-435.pdf. [Online]. Available: https://doi.org/10.1143/PTP.40.435.

[5] A. I. Rusinov, "Superconductivity near a Paramagnetic Impurity," *Soviet Journal of Experimental and Theoretical Physics Letters*, vol. 9, p. 85, Jan. 1969.

[6] G. Binnig, H. Rohrer, C. Gerber, and E. Weibel, "Tunneling through a controllable vacuum gap," *Applied Physics Letters*, vol. 40, no. 2, pp. 178–180, 1982. DOI: 10.1063/1.92999. eprint: https://doi.org/10.1063/1.92999. [Online]. Available: https://doi.org/10.1063/1.92999.

[7] A. Yazdani, B. Jones, C. Lutz, M. Crommie, and D. Eigler, "Probing the local effects of magnetic impurities on superconductivity," English (US), *Science*, vol. 275, no. 5307, pp. 1767–1770, Mar. 1997, ISSN: 0036-8075. DOI: 10.1126/science.275.5307.1767.

[8] S. Nadj-Perge, I. K. Drozdov, B. A. Bernevig, and A. Yazdani, "Proposal for realizing majorana fermions in chains of magnetic atoms on a superconductor," *Phys. Rev. B*, vol. 88, p. 020 407, 2 Jul. 2013. DOI: 10.1103/PhysRevB.88.020407. [Online]. Available: https://link.aps.org/doi/10.1103/PhysRevB.88.020407.

[9] F. Pientka, L. I. Glazman, and F. von Oppen, "Topological superconducting phase in helical shiba chains," *Phys. Rev. B*, vol. 88, p. 155 420, 15 Oct. 2013. DOI: 10.1103/PhysRevB.88.155420. [Online]. Available: https://link.aps.org/doi/10.1103/PhysRevB.88.155420.

[10] E. Majorana, "Teoria simmetrica dell'elettrone e del positrone," *Il Nuovo Cimento (1924-1942)*, vol. 14, no. 4, p. 171, Sep. 2008, ISSN: 1827-6121. DOI: 10.1007/BF02961314. [Online]. Available: https://doi.org/10.1007/BF02961314.

[11] J. Alicea, "New directions in the pursuit of majorana fermions in solid state systems," *Reports on Progress in Physics*, vol. 75, no. 7, p. 076 501, Jun. 2012. DOI: 10.1088/0034-4885/75/7/076501. [Online]. Available: https://doi.org/10.1088%2F0034-4885%2F75%2F7%2F076501.

[12] B. Field and T. Simula, "Introduction to topological quantum computation with non-abelian anyons," *Quantum Science and Technology*, vol. 3, no. 4, p. 045 004, Jul. 2018. DOI: 10.1088/2058-9565/aacad2. [Online]. Available: https://doi.org/10.1088/2058-9565/aacad2.

[13] A. Y. Kitaev, "Unpaired majorana fermions in quantum wires," *Physics-Uspekhi*, vol. 44, no. 10S, pp. 131–136, Oct. 2001. DOI: 10.1070/1063-7869/44/10s/s29. [Online]. Available: https://doi.org/10.1070%2F1063-7869%2F44%2F10s%2Fs29.

[14] L. Fu and C. L. Kane, "Superconducting proximity effect and majorana fermions at the surface of a topological insulator," *Phys. Rev. Lett.*, vol. 100, p. 096 407, 9 Mar. 2008. DOI: 10.1103/PhysRevLett.100.096407. [Online]. Available: https://link.aps.org/doi/10.1103/PhysRevLett.100.096407.

[15] B. Braunecker, G. I. Japaridze, J. Klinovaja, and D. Loss, "Spin-selective peierls transition in interacting one-dimensional conductors with spin-orbit interaction," *Phys. Rev. B*, vol. 82, p. 045 127, 4 Jul. 2010. DOI: 10.1103/PhysRevB.82.045127. [Online]. Available: https://link.aps.org/doi/10.1103/PhysRevB.82.045127.

[16] J. Alicea, "Majorana fermions in a tunable semiconductor device," *Phys. Rev. B*, vol. 81, p. 125 318, 12 Mar. 2010. DOI: 10.1103/PhysRevB.81.125318. [Online]. Available: https://link.aps.org/doi/10.1103/PhysRevB.81.125318.

[17] J. D. Sau, R. M. Lutchyn, S. Tewari, and S. Das Sarma, "Generic new platform for topological quantum computation using semiconductor heterostructures," *Phys. Rev. Lett.*, vol. 104, p. 040 502, 4 Jan. 2010. DOI: 10.1103/PhysRevLett.104.040502. [Online]. Available: https://link.aps.org/doi/10.1103/PhysRevLett.104.040502.

[18] Y. Oreg, G. Refael, and F. von Oppen, "Helical liquids and majorana bound states in quantum wires," *Phys. Rev. Lett.*, vol. 105, p. 177 002, 17 Oct. 2010. DOI: 10.1103/PhysRevLett.105.177002. [Online]. Available: https://link.aps.org/doi/10.1103/PhysRevLett.105.177002.

[19] A. Kamlapure, L. Cornils, J. Wiebe, and R. Wiesendanger, "Engineering the spin couplings in atomically crafted spin chains on an elemental superconductor," *Nature Communications*, vol. 9, no. 1, p. 3253, Aug. 2018, ISSN: 2041-1723. DOI: 10.1038/s41467-018-05701-8. [Online]. Available: https://doi.org/10.1038/s41467-018-05701-8.

[20] S. Nadj-Perge, I. K. Drozdov, J. Li, *et al.*, "Observation of Majorana fermions in ferromagnetic atomic chains on a superconductor," en, *Science*, p. 1 259 327, Oct. 2014, ISSN: 0036-8075, 1095-9203. DOI: 10.1126/science.1259327. [Online]. Available: http://science.sciencemag.org/content/early/2014/10/01/science.1259327 (visited on 04/13/2017).

[21] S. Jeon, Y. Xie, J. Li, Z. Wang, B. A. Bernevig, and A. Yazdani, "Distinguishing a majorana zero mode using spin-resolved measurements," *Science*, vol. 358, no. 6364, pp. 772–776, 2017. DOI: 10.1126/science.aan3670. eprint: https://www.science.org/doi/pdf/10.1126/science.aan3670. [Online]. Available: https://www.science.org/doi/abs/10.1126/science.aan3670.

[22] R. Pawlak, M. Kisiel, J. Klinovaja, *et al.*, "Probing atomic structure and majorana wavefunctions in mono-atomic fe chains on superconducting pb surface," *Npj Quantum Information*, vol. 2, p. 16 035, Apr. 2016.

[23] H. Kim, A. Palacio-Morales, T. Posske, *et al.*, "Toward tailoring majorana bound states in artificially constructed magnetic atom chains on elemental superconductors," *Science Advances*, vol. 4, no. 5, 2018. DOI: 10.1126/sciadv.aar5251. [Online]. Available: http://advances.sciencemag.org/content/4/5/eaar5251.

[24] L. Schneider, P. Beck, T. Posske, *et al.*, "Topological Shiba bands in artificial spin chains on superconductors," en, *Nature Physics*, vol. 17, no. 8, pp. 943–948, Aug. 2021, Number: 8 Publisher: Nature Publishing Group, ISSN: 1745-2481. DOI: 10.1038/s41567-021-01234-y. [Online]. Available: https://www.nature.com/articles/s41567-021-01234-y (visited on 03/08/2022).

[25] F. Küster, S. Brinker, R. Hess, *et al.*, "Non-majorana modes in diluted spin chains proximitized to a superconductor," *Proceedings of the National Academy of Sciences*, vol. 119, no. 42, e2210589119, 2022. DOI: 10.1073/pnas.2210589119. eprint: https://www.pnas.org/doi/pdf/10.1073/pnas.2210589119. [Online]. Available: https://www.pnas.org/doi/abs/10.1073/pnas.2210589119.

[26] M. E. Flatté and J. M. Byers, "Local electronic structure of defects in superconductors," *Phys. Rev. B*, vol. 56, pp. 11 213–11 231, 17 Nov. 1997. DOI: 10.1103/PhysRevB.56.11213. [Online]. Available: https://link.aps.org/doi/10.1103/PhysRevB.56.11213.

[27] M. E. Flatté and D. E. Reynolds, "Local spectrum of a superconductor as a probe of interactions between magnetic impurities," *Phys. Rev. B*, vol. 61, pp. 14 810–14 814, 21 Jun. 2000. DOI: 10.1103/PhysRevB.61.14810. [Online]. Available: https://link.aps.org/doi/10.1103/PhysRevB.61.14810.

[28] D.-J. Choi, C. G. Fernández, E. Herrera, *et al.*, "Influence of magnetic ordering between cr adatoms on the yu-shiba-rusinov states of the $\beta-Bi_2Pd$ superconductor," *Phys. Rev. Lett.*, vol. 120, p. 167 001, 16 Apr. 2018. DOI: 10.1103/PhysRevLett.120.167001. [Online]. Available: https://link.aps.org/doi/10.1103/PhysRevLett.120.167001.

[29] P. Beck, L. Schneider, L. Rózsa, *et al.*, "Spin-orbit coupling induced splitting of yu-shiba-rusinov states in antiferromagnetic dimers," *Nature Communications*, vol. 12, no. 1, p. 2040, Apr. 2021, ISSN: 2041-1723. DOI: 10.1038/s41467-021-22261-6. [Online]. Available: https://doi.org/10.1038/s41467-021-22261-6.

[30] D. Sticlet, C. Bena, and P. Simon, "Spin and majorana polarization in topological superconducting wires," *Phys. Rev. Lett.*, vol. 108, p. 096 802, 9 Mar. 2012. DOI: 10.1103/PhysRevLett.108.096802. [Online]. Available: https://link.aps.org/doi/10.1103/PhysRevLett.108.096802.

[31] C. Mier, J. Hwang, J. Kim, *et al.*, "Atomic manipulation of in-gap states in the $\beta - Bi_2Pd$ superconductor," *Phys. Rev. B*, vol. 104, p. 045 406, 4 Jul. 2021. DOI: 10.1103/PhysRevB.104.045406. [Online]. Available: https://link.aps.org/doi/10.1103/PhysRevB.104.045406.

[32] C. Mier, D.-J. Choi, and N. Lorente, "Calculations of in-gap states of ferromagnetic spin chains on *s*-wave wide-band superconductors," *Phys. Rev. B*, vol. 104, p. 245 415, 24 Dec. 2021. DOI: 10.1103/PhysRevB.104.245415. [Online]. Available: https://link.aps.org/doi/10.1103/PhysRevB.104.245415.

[33] C. Mier, D.-J. Choi, and N. Lorente, "Moiré dispersion of edge states in spin chains on superconductors," *Phys. Rev. Res.*, vol. 4, p. L032010, 3 Jul. 2022. DOI: 10.1103/PhysRevResearch.4.L032010. [Online]. Available: https://link.aps.org/doi/10.1103/PhysRevResearch.4.L032010.

[34] M. Ormaza, N. Bachellier, M. N. Faraggi, *et al.*, "Efficient spin-flip excitation of a nickelocene molecule," *Nano Letters*, vol. 17, no. 3, pp. 1877–1882, 2017, PMID: 28199115. DOI: 10.1021/acs.nanolett.6b05204. eprint: https://doi.org/10.1021/acs.nanolett.6b05204. [Online]. Available: https://doi.org/10.1021/acs.nanolett.6b05204.

[35] G. Czap, P. J. Wagner, F. Xue, *et al.*, "Probing and imaging spin interactions with a magnetic single-molecule sensor," *Science*, vol. 364, no. 6441, pp. 670–673, 2019. DOI: 10.1126/science.aaw7505. eprint: https://www.science.org/doi/pdf/10.1126/science.aaw7505. [Online]. Available: https://www.science.org/doi/abs/10.1126/science.aaw7505.

[36] C. Mier, B. Verlhac, L. Garnier, *et al.*, "Superconducting scanning tunneling microscope tip to reveal sub-millielectronvolt magnetic energy variations on surfaces," *The Journal of Physical Chemistry Letters*, vol. 12, no. 11, pp. 2983–2989, 2021, PMID: 33730501. DOI: 10.1021/acs.jpclett.1c00328. eprint: https://doi.org/10.1021/acs.jpclett.1c00328. [Online]. Available: https://doi.org/10.1021/acs.jpclett.1c00328.

[37] M. T. Randeria, B. E. Feldman, I. K. Drozdov, and A. Yazdani, "Scanning josephson spectroscopy on the atomic scale," *Phys. Rev. B*, vol. 93, p. 161 115, 16 Apr. 2016. DOI: 10.1103/PhysRevB.93.161115. [Online]. Available: https://link.aps.org/doi/10.1103/PhysRevB.93.161115.

[38] M. Schirber, "Topological phases of matter," *Physics*, vol. 9, no. 116, 2016. [Online]. Available: https://physics.aps.org/articles/v9/116.

[39] M. Asorey, "Space, matter and topology," *Nature Physics*, vol. 12, no. 7, pp. 616–618, Jul. 2016, ISSN: 1745-2481. DOI: 10.1038/nphys3800. [Online]. Available: https://doi.org/10.1038/nphys3800.

[40] D. J. Thouless, M. Kohmoto, M. P. Nightingale, and M. den Nijs, "Quantized hall conductance in a two-dimensional periodic potential," *Phys. Rev. Lett.*, vol. 49, pp. 405–408, 6 Aug. 1982. DOI: 10.1103/PhysRevLett.49.405. [Online]. Available: https://link.aps.org/doi/10.1103/PhysRevLett.49.405.

[41] M. Sato and S. Fujimoto, "Majorana fermions and topology in superconductors," *Journal of the Physical Society of Japan*, vol. 85, no. 7, p. 072 001, 2016. DOI: 10.7566/JPSJ.85.072001. eprint: https://doi.org/10.7566/JPSJ.85.072001. [Online]. Available: https://doi.org/10.7566/JPSJ.85.072001.

[42] A. P. János K. Asbóth László Oroszlány, *A Short Course on Topological Insulators*. Springer, 2015.

[43] R. Aguado, "Majorana quasiparticles in condensed matter," *Rivista del Nuovo Cimento*, vol. 40, Oct. 2017. DOI: 10.1393/ncr/i2017-10141-9.

[44] M. Leijnse and K. Flensberg, "Introduction to topological superconductivity and majorana fermions," *Semiconductor Science and Technology*, vol. 27, no. 12, p. 124 003, Nov. 2012. DOI: 10.1088/0268-1242/27/12/124003. [Online]. Available: https://doi.org/10.1088/0268-1242/27/12/124003.

[45] T. E.-2. Collaboration, "Search for majorana neutrinos with the first two years of exo-200 data," *Nature*, vol. 510, no. 7504, pp. 229–234, Jun. 2014, ISSN: 1476-4687. DOI: 10.1038/nature13432. [Online]. Available: https://doi.org/10.1038/nature13432.

[46] I. Rivilla, B. Aparicio, J. M. Bueno, *et al.*, "Fluorescent bicolour sensor for low-background neutrinoless double $\beta$ decay experiments," *Nature*, vol. 583, no. 7814, pp. 48–54, Jul. 2020, ISSN: 1476-4687. DOI: 10.1038/s41586-020-2431-5. [Online]. Available: https://doi.org/10.1038/s41586-020-2431-5.

[47] J. K. Pachos, *Introduction to Topological Quantum Computation*. Cambridge University Press, 2012. DOI: 10.1017/CBO9780511792908.

[48] J. Alicea and A. Stern, "Designer non-abelian anyon platforms: From majorana to fibonacci," *Physica Scripta*, vol. 2015, no. T164, p. 014 006, Aug. 2015. DOI: 10.1088/0031-8949/2015/T164/014006. [Online]. Available: https://dx.doi.org/10.1088/0031-8949/2015/T164/014006.

[49] J.-X. Zhu, *Bogoliubov-de Gennes Method and Its Applications*. Switzerland: Springer, 2016.

[50] C. Chamon, R. Jackiw, Y. Nishida, S.-Y. Pi, and L. Santos, "Quantizing majorana fermions in a superconductor," *Phys. Rev. B*, vol. 81, p. 224 515, 22 Jun. 2010. DOI: 10.1103/PhysRevB.81.224515. [Online]. Available: https://link.aps.org/doi/10.1103/PhysRevB.81.224515.

[51] W. P. Su, J. R. Schrieffer, and A. J. Heeger, "Solitons in polyacetylene," *Phys. Rev. Lett.*, vol. 42, pp. 1698–1701, 25 Jun. 1979. DOI: 10.1103/PhysRevLett.42.1698. [Online]. Available: https://link.aps.org/doi/10.1103/PhysRevLett.42.1698.

[52] E. J. Meier, F. A. An, and B. Gadway, "Observation of the topological soliton state in the su–schrieffer–heeger model," *Nature Communications*, vol. 7, no. 1, p. 13 986, Dec. 2016, ISSN: 2041-1723. DOI: 10.1038/ncomms13986. [Online]. Available: https://doi.org/10.1038/ncomms13986.

[53] M. Atala, M. Aidelsburger, J. T. Barreiro, *et al.*, "Direct measurement of the zak phase in topological bloch bands," *Nature Physics*, vol. 9, no. 12, pp. 795–800, Dec. 2013, ISSN: 1745-2481. DOI: 10.1038/nphys2790. [Online]. Available: https://doi.org/10.1038/nphys2790.

[54] L. Thatcher, P. Fairfield, L. Merlo-Ramırez, and J. M. Merlo, "Experimental observation of topological phase transitions in a mechanical 1d-SSH model," *Physica Scripta*, vol. 97, no. 3, p. 035 702, Feb. 2022. DOI: 10.1088/1402-4896/ac4ed2. [Online]. Available: https://doi.org/10.1088/1402-4896/ac4ed2.

[55] S. D. Sarma, M. Freedman, and C. Nayak, "Majorana zero modes and topological quantum computation," *npj Quantum Information*, vol. 1, no. 1, p. 15 001, Oct. 2015, ISSN: 2056-6387. DOI: 10.1038/npjqi.2015.1. [Online]. Available: https://doi.org/10.1038/npjqi.2015.1.

[56] R. Wakatsuki, M. Ezawa, Y. Tanaka, and N. Nagaosa, "Fermion fractionalization to majorana fermions in a dimerized kitaev superconductor," *Phys. Rev. B*, vol. 90, p. 014 505, 1 Jul. 2014. DOI: 10.1103/PhysRevB.90.014505. [Online]. Available: https://link.aps.org/doi/10.1103/PhysRevB.90.014505.

[57] S. Ryu, A. P. Schnyder, A. Furusaki, and A. W. W. Ludwig, "Topological insulators and superconductors: Tenfold way and dimensional hierarchy," *New Journal of Physics*, vol. 12, no. 6, p. 065 010, Jun. 2010. DOI: 10.1088/1367-2630/12/6/065010. [Online]. Available: https://doi.org/10.1088/1367-2630/12/6/065010.

[58] C.-K. Chiu, J. C. Y. Teo, A. P. Schnyder, and S. Ryu, "Classification of topological quantum matter with symmetries," *Rev. Mod. Phys.*, vol. 88, p. 035 005, 3 Aug. 2016. DOI: 10.1103/RevModPhys.88.035005. [Online]. Available: https://link.aps.org/doi/10.1103/RevModPhys.88.035005.

[59] S. Tewari and J. D. Sau, "Topological invariants for spin-orbit coupled superconductor nanowires," *Phys. Rev. Lett.*, vol. 109, p. 150 408, 15 Oct. 2012. DOI: 10.1103/PhysRevLett.109.150408. [Online]. Available: https://link.aps.org/doi/10.1103/PhysRevLett.109.150408.

[60] H. Fröhlich, "Theory of the superconducting state. i. the ground state at the absolute zero of temperature," *Phys. Rev.*, vol. 79, pp. 845–856, 5 Sep. 1950. DOI: 10.1103/PhysRev.79.845. [Online]. Available: https://link.aps.org/doi/10.1103/PhysRev.79.845.

[61] M. Tinkham, *Introduction to Superconductivity*, 2nd ed. Dover Publications, Jun. 2004, ISBN: 0486435032. [Online]. Available: http://www.worldcat.org/isbn/0486435032.

[62] J. Annett, *Superconductivity, superfluids and condensates*, English. United Kingdom: Oxford University Press, 2004, ISBN: 0198507550.

[63] N. N. Bogoljubov, "On a new method in the theory of superconductivity," *Il Nuovo Cimento (1955-1965)*, vol. 7, no. 6, pp. 794–805, Mar. 1958, ISSN: 1827-6121. DOI: 10.1007/BF02745585. [Online]. Available: https://doi.org/10.1007/BF02745585.

[64] J. G. Valatin, "Comments on the theory of superconductivity," *Il Nuovo Cimento (1955-1965)*, vol. 7, no. 6, pp. 843–857, Mar. 1958, ISSN: 1827-6121. DOI: 10.1007/BF02745589. [Online]. Available: https://doi.org/10.1007/BF02745589.

[65] R. C. Dynes, V. Narayanamurti, and J. P. Garno, "Direct measurement of quasiparticle-lifetime broadening in a strong-coupled superconductor," *Phys. Rev. Lett.*, vol. 41, pp. 1509–1512, 21 Nov. 1978. DOI: 10.1103/PhysRevLett.41.1509. [Online]. Available: https://link.aps.org/doi/10.1103/PhysRevLett.41.1509.

[66] F. š. Herman and R. Hlubina, "Microscopic interpretation of the dynes formula for the tunneling density of states," *Phys. Rev. B*, vol. 94, p. 144 508, 14 Oct. 2016. DOI: 10.1103/PhysRevB.94.144508. [Online]. Available: https://link.aps.org/doi/10.1103/PhysRevB.94.144508.

[67] J.-B. Fu, B. Li, X.-F. Zhang, G.-Z. Yu, G.-Y. Huang, and M.-T. Deng, "Experimental review on majorana zero-modes in hybrid nanowires," *Science China Physics, Mechanics & Astronomy*, vol. 64, no. 10, p. 107 001, Sep. 2021, ISSN: 1869-1927. DOI: 10.1007/s11433-021-1737-4. [Online]. Available: https://doi.org/10.1007/s11433-021-1737-4.

[68] V. Mourik, K. Zuo, S. M. Frolov, S. R. Plissard, E. P. A. M. Bakkers, and L. P. Kouwenhoven, "Signatures of majorana fermions in hybrid superconductor-semiconductor nanowire devices," *Science*, vol. 336, no. 6084, pp. 1003–1007, 2012. DOI: 10.1126/science.1222360. eprint: https://www.science.org/doi/pdf/10.1126/science.1222360. [Online]. Available: https://www.science.org/doi/abs/10.1126/science.1222360.

[69] A. Das, Y. Ronen, Y. Most, Y. Oreg, M. Heiblum, and H. Shtrikman, "Zero-bias peaks and splitting in an al–inas nanowire topological superconductor as a signature of majorana fermions," *Nature Physics*, vol. 8, no. 12, pp. 887–895, Dec. 2012, ISSN: 1745-2481. DOI: 10.1038/nphys2479. [Online]. Available: https://doi.org/10.1038/nphys2479.

[70] L. P. Rokhinson, X. Liu, and J. K. Furdyna, "The fractional a.c. josephson effect in a semiconductor–superconductor nanowire as a signature of majorana particles," *Nature Physics*, vol. 8, no. 11, pp. 795–799, Nov. 2012, ISSN: 1745-2481. DOI: 10.1038/nphys2429. [Online]. Available: https://doi.org/10.1038/nphys2429.

[71] M. T. Deng, S. Vaitiekėnas, E. B. Hansen, *et al.*, "Majorana bound state in a coupled quantum-dot hybrid-nanowire system," *Science*, vol. 354, no. 6319, pp. 1557–1562, 2016. DOI: 10.1126/science.aaf3961. eprint: https://www.science.org/doi/pdf/10.1126/science.aaf3961. [Online]. Available: https://www.science.org/doi/abs/10.1126/science.aaf3961.

[72] K. Laubscher and J. Klinovaja, "Majorana bound states in semiconducting nanostructures," *Journal of Applied Physics*, vol. 130, no. 8, p. 081 101, 2021. DOI: 10.1063/5.0055997. eprint: https://doi.org/10.1063/5.0055997. [Online]. Available: https://doi.org/10.1063/5.0055997.

[73] J. Liu, A. C. Potter, K. T. Law, and P. A. Lee, "Zero-bias peaks in the tunneling conductance of spin-orbit-coupled superconducting wires with and without majorana end-states," *Phys. Rev. Lett.*, vol. 109, p. 267 002, 26 Dec. 2012. DOI: 10.1103/PhysRevLett.109.267002. [Online]. Available: https://link.aps.org/doi/10.1103/PhysRevLett.109.267002.

[74] D. I. Pikulin, J. P. Dahlhaus, M. Wimmer, H. Schomerus, and C. W. J. Beenakker, "A zero-voltage conductance peak from weak antilocalization in a majorana nanowire," *New Journal of Physics*, vol. 14, no. 12, p. 125 011, Dec. 2012. DOI: 10.1088/1367-2630/14/12/125011. [Online]. Available: https://dx.doi.org/10.1088/1367-2630/14/12/125011.

[75] R. Pawlak, S. Hoffman, J. Klinovaja, D. Loss, and E. Meyer, "Majorana fermions in magnetic chains," *Progress in Particle and Nuclear Physics*, vol. 107, pp. 1–19, 2019, ISSN: 0146-6410. DOI: https://doi.org/10.1016/j.ppnp.2019.04.004. [Online]. Available: https://www.sciencedirect.com/science/article/pii/S0146641019300316.

[76] M. F. Crommie, C. P. Lutz, and D. M. Eigler, "Confinement of electrons to quantum corrals on a metal surface," *Science*, vol. 262, no. 5131, pp. 218–220, 1993. DOI: 10.1126/science.262.5131.218. eprint: https://www.science.org/doi/pdf/10.1126/science.262.5131.218. [Online]. Available: https://www.science.org/doi/abs/10.1126/science.262.5131.218.

[77] Y. A. Bychkov and E. I. Rashba, "Oscillatory effects and the magnetic susceptibility of carriers in inversion layers," *Journal of Physics C: Solid State Physics*, vol. 17, no. 33, pp. 6039–6045, Nov. 1984. DOI: 10.1088/0022-3719/17/33/015. [Online]. Available: https://doi.org/10.1088/0022-3719/17/33/015.

[78] A. Manchon, H. C. Koo, J. Nitta, S. M. Frolov, and R. A. Duine, "New perspectives for rashba spin-orbit coupling," *Nature Materials*, vol. 14, p. 871, Aug. 2015, Review Article. [Online]. Available: http://dx.doi.org/10.1038/nmat4360.

[79] Y. Lin, W. Hao, M. Wang, J. Qian, and H. Guo, "Topological superconductors from one-dimensional periodically modulated majorana chains," *Scientific Reports*, vol. 7, no. 1, p. 9210, Aug. 2017, ISSN: 2045-2322. DOI: 10.1038/s41598-017-09160-x. [Online]. Available: https://doi.org/10.1038/s41598-017-09160-x.

[80] M. Cheng, R. M. Lutchyn, V. Galitski, and S. Das Sarma, "Splitting of majorana-fermion modes due to intervortex tunneling in a $p_x + ip_y$ superconductor," *Phys. Rev. Lett.*, vol. 103, p. 107 001, 10 Aug. 2009. DOI: 10.1103/PhysRevLett.103.107001. [Online]. Available: https://link.aps.org/doi/10.1103/PhysRevLett.103.107001.

[81] P. M. R. Brydon, S. Das Sarma, H.-Y. Hui, and J. D. Sau, "Topological yu-shiba-rusinov chain from spin-orbit coupling," *Phys. Rev. B*, vol. 91, p. 064 505, 6 Feb. 2015. DOI: 10.1103/PhysRevB.91.064505. [Online]. Available: https://link.aps.org/doi/10.1103/PhysRevB.91.064505.

[82] A. Heimes, D. Mendler, and P. Kotetes, "Interplay of topological phases in magnetic adatom-chains on top of a rashba superconducting surface," *New Journal of Physics*, vol. 17, no. 2, p. 023 051, Feb. 2015. DOI: 10.1088/1367-2630/17/2/023051. [Online]. Available: https://doi.org/10.1088/1367-2630/17/2/023051.

[83] P. Beck, L. Schneider, R. Wiesendanger, and J. Wiebe, *Effect of substrate spin-orbit coupling on the topological gap size of shiba chains*, 2022. DOI: 10.48550/ARXIV.2205.10062. [Online]. Available: https://arxiv.org/abs/2205.10062.

[84] P. Anderson, "Theory of dirty superconductors," *Journal of Physics and Chemistry of Solids*, vol. 11, no. 1, pp. 26–30, 1959, ISSN: 0022-3697. DOI: https://doi.org/10.1016/0022-3697(59)90036-8. [Online]. Available: https://www.sciencedirect.com/science/article/pii/0022369759900368.

[85] M. I. Salkola, A. V. Balatsky, and J. R. Schrieffer, "Spectral properties of quasiparticle excitations induced by magnetic moments in superconductors," *Physical Review B*, vol. 55, no. 18, pp. 12 648–12 661, May 1997. DOI: 10.1103/PhysRevB.55.12648. [Online]. Available: https://link.aps.org/doi/10.1103/PhysRevB.55.12648 (visited on 08/24/2017).

[86] R. M. Lutchyn, J. D. Sau, and S. Das Sarma, "Majorana fermions and a topological phase transition in semiconductor-superconductor heterostructures," *Phys. Rev. Lett.*, vol. 105, p. 077 001, 7 Aug. 2010. DOI: 10.1103/PhysRevLett.105.077001. [Online]. Available: https://link.aps.org/doi/10.1103/PhysRevLett.105.077001.

[87] M. H. Christensen, M. Schecter, K. Flensberg, B. M. Andersen, and J. Paaske, "Spiral magnetic order and topological superconductivity in a chain of magnetic adatoms on a two-dimensional superconductor," *Phys. Rev. B*, vol. 94, p. 144 509, 14 Oct. 2016. DOI: 10.1103/PhysRevB.94.144509. [Online]. Available: https://link.aps.org/doi/10.1103/PhysRevB.94.144509.

[88] J. Li, T. Neupert, Z. Wang, A. H. MacDonald, A. Yazdani, and B. A. Bernevig, "Two-dimensional chiral topological superconductivity in shiba lattices," *Nature Communications*, vol. 7, no. 1, p. 12 297, Jul. 2016, ISSN: 2041-1723. DOI: 10.1038/ncomms12297. [Online]. Available: https://doi.org/10.1038/ncomms12297.

[89] N. Sedlmayr, V. Kaladzhyan, and C. Bena, "Analytical and semianalytical tools to determine the topological character of shiba chains," *Phys. Rev. B*, vol. 104, p. 024 508, 2 Jul. 2021. DOI: 10.1103/PhysRevB.104.024508. [Online]. Available: https://link.aps.org/doi/10.1103/PhysRevB.104.024508.

[90] E. N. Economou, *Green's Functions in Quantum Physics*. Springer, 1979.

[91] E. Vernier, D. Pekker, M. W. Zwierlein, and E. Demler, "Bound states of a localized magnetic impurity in a superfluid of paired ultracold fermions," *Phys. Rev. A*, vol. 83, p. 033 619, 3 Mar. 2011. DOI: 10.1103/PhysRevA.83.033619. [Online]. Available: https://link.aps.org/doi/10.1103/PhysRevA.83.033619.

[92] J. Li, H. Chen, I. K. Drozdov, A. Yazdani, B. A. Bernevig, and A. H. MacDonald, "Topological superconductivity induced by ferromagnetic metal chains," *Phys. Rev. B*, vol. 90, p. 235 433, 23 Dec. 2014. DOI: 10.1103/PhysRevB.90.235433. [Online]. Available: https://link.aps.org/doi/10.1103/PhysRevB.90.235433.

[93] D.-J. Choi, N. Lorente, J. Wiebe, K. von Bergmann, A. F. Otte, and A. J. Heinrich, "Colloquium: Atomic spin chains on surfaces," *Rev. Mod. Phys.*, vol. 91, p. 041 001, 4 Oct. 2019. DOI: 10.1103/RevModPhys.91.041001. [Online]. Available: https://link.aps.org/doi/10.1103/RevModPhys.91.041001.

[94] J. Klinovaja, P. Stano, A. Yazdani, and D. Loss, "Topological superconductivity and majorana fermions in rkky systems," *Phys. Rev. Lett.*, vol. 111, p. 186 805, 18 Nov. 2013. DOI: 10.1103/PhysRevLett.111.186805. [Online]. Available: https://link.aps.org/doi/10.1103/PhysRevLett.111.186805.

[95] M. Schecter, K. Flensberg, M. H. Christensen, B. M. Andersen, and J. Paaske, "Self-organized topological superconductivity in a yu-shiba-rusinov chain," *Phys. Rev. B*, vol. 93, p. 140 503, 14 Apr. 2016. DOI: 10.1103/PhysRevB.93.140503. [Online]. Available: https://link.aps.org/doi/10.1103/PhysRevB.93.140503.

[96] F. Pientka, Y. Peng, L. Glazman, and F. von Oppen, "Topological superconducting phase and majorana bound states in shiba chains," *Physica Scripta*, vol. T164, p. 014 008, Aug. 2015. DOI: 10.1088/0031-8949/2015/t164/014008. [Online]. Available: https://doi.org/10.1088/0031-8949/2015/t164/014008.

[97] H. Bruus, K. Flensberg, and Ø. Flensberg, *Many-Body Quantum Theory in Condensed Matter Physics: An Introduction*, ser. Oxford Graduate Texts. OUP Oxford, 2004, ISBN: 9780198566335. [Online]. Available: https://books.google.es/books?id=v5vhg1tYLC8C.

[98] A. V. Balatsky, I. Vekhter, and J.-X. Zhu, "Impurity-induced states in conventional and unconventional superconductors," *Rev. Mod. Phys.*, vol. 78, pp. 373–433, 2 May 2006. DOI: 10.1103/RevModPhys.78.373. [Online]. Available: https://link.aps.org/doi/10.1103/RevModPhys.78.373.

[99] R. Žitko, "Quantum impurity models for magnetic adsorbates on superconductor surfaces," *Physica B: Condensed Matter*, vol. 536, pp. 230–234, 2018, ISSN: 0921-4526. DOI: https://doi.org/10.1016/j.physb.2017.08.019. [Online]. Available: https://www.sciencedirect.com/science/article/pii/S0921452617304969.

[100] F. von Oppen and K. J. Franke, "Yu-shiba-rusinov states in real metals," *Phys. Rev. B*, vol. 103, p. 205 424, 20 May 2021. DOI: 10.1103/PhysRevB.103.205424. [Online]. Available: https://link.aps.org/doi/10.1103/PhysRevB.103.205424.

[101] E. Liebhaber, L. M. Rütten, G. Reecht, *et al.*, "Quantum spins and hybridization in artificially-constructed chains of magnetic adatoms on a superconductor," *Nature Communications*, vol. 13, no. 1, p. 2160, Apr. 2022, ISSN: 2041-1723. DOI: 10.1038/s41467-022-29879-0. [Online]. Available: https://doi.org/10.1038/s41467-022-29879-0.

[102] G. C. Ménard, S. Guissart, C. Brun, *et al.*, "Coherent long-range magnetic bound states in a superconductor," *Nature Physics*, vol. 11, no. 12, pp. 1013–1016, Dec. 2015, ISSN: 1745-2481. DOI: 10.1038/nphys3508. [Online]. Available: https://doi.org/10.1038/nphys3508.

[103] D. Wang, J. Wiebe, R. Zhong, G. Gu, and R. Wiesendanger, "Spin-polarized yu-shiba-rusinov states in an iron-based superconductor," *Phys. Rev. Lett.*, vol. 126, p. 076 802, 7 Feb. 2021. DOI: 10.1103/PhysRevLett.126.076802. [Online]. Available: https://link.aps.org/doi/10.1103/PhysRevLett.126.076802.

[104] A. Sakurai, "Comments on Superconductors with Magnetic Impurities," *Progress of Theoretical Physics*, vol. 44, no. 6, pp. 1472–1476, Dec. 1970, ISSN: 0033-068X. DOI: 10.1143/PTP.44.1472. eprint: https://academic.oup.com/ptp/article-pdf/44/6/1472/5378530/44-6-1472.pdf. [Online]. Available: https://doi.org/10.1143/PTP.44.1472.

[105] B. W. Heinrich, J. I. Pascual, and K. J. Franke, "Single magnetic adsorbates on s-wave superconductors," *Progress in Surface Science*, vol. 93, no. 1, pp. 1–19, 2018, ISSN: 0079-6816. DOI: https://doi.org/10.1016/j.progsurf.2018.01.001. [Online]. Available: https://www.sciencedirect.com/science/article/pii/S0079681618300017.

[106] A. Costa, J. Fabian, and D. Kochan, "Connection between zero-energy yu-shiba-rusinov states and $0-\pi$ transitions in magnetic josephson junctions," *Phys. Rev. B*, vol. 98, p. 134 511, 13 Oct. 2018. DOI: 10.1103/PhysRevB.98.134511. [Online]. Available: https://link.aps.org/doi/10.1103/PhysRevB.98.134511.

[107] C.-K. Chiu and Z. Wang, "Yu-shiba-rusinov states in a superconductor with topological $\mathbb{Z}_2$ bands," *Phys. Rev. Lett.*, vol. 128, p. 237 001, 23 Jun. 2022. DOI: 10.1103/PhysRevLett.128.237001. [Online]. Available: https://link.aps.org/doi/10.1103/PhysRevLett.128.237001.

[108] Y. A. Bychkov and É. I. Rashba, "Properties of a 2D electron gas with lifted spectral degeneracy," *Soviet Journal of Experimental and Theoretical Physics Letters*, vol. 39, p. 78, Jan. 1984.

[109] C. R. Ast, J. Henk, A. Ernst, *et al.*, "Giant spin splitting through surface alloying," *Phys. Rev. Lett.*, vol. 98, p. 186 807, 18 May 2007. DOI: 10.1103/PhysRevLett.98.186807. [Online]. Available: https://link.aps.org/doi/10.1103/PhysRevLett.98.186807.

[110] K. Ishizaka, M. S. Bahramy, H. Murakawa, *et al.*, "Giant rashba-type spin splitting in bulk bitei," *Nature Materials*, vol. 10, no. 7, pp. 521–526, Jul. 2011, ISSN: 1476-4660. DOI: 10.1038/nmat3051. [Online]. Available: https://doi.org/10.1038/nmat3051.

[111] G. Metalidis, "Electronic transport in mesoscopic systems," Martin-Luther-Universität Halle-Wittenberg, 2007.

[112] Y. Kim, J. Zhang, E. Rossi, and R. M. Lutchyn, "Impurity-induced bound states in superconductors with spin-orbit coupling," *Phys. Rev. Lett.*, vol. 114, p. 236 804, 23 Jun. 2015. DOI: 10.1103/PhysRevLett.114.236804. [Online]. Available: https://link.aps.org/doi/10.1103/PhysRevLett.114.236804.

[113] G. M. Andolina and P. Simon, "Topological properties of chains of magnetic impurities on a superconducting substrate: Interplay between the shiba band and ferromagnetic wire limits," *Phys. Rev. B*, vol. 96, p. 235 411, 23 Dec. 2017. DOI: 10.1103/PhysRevB.96.235411. [Online]. Available: https://link.aps.org/doi/10.1103/PhysRevB.96.235411.

[114] K. Pöyhönen, A. Weststrom, J. Röntynen, and T. Ojanen, "Majorana states in helical shiba chains and ladders," *Phys. Rev. B*, vol. 89, p. 115 109, 11 Mar. 2014. DOI: 10.1103/PhysRevB.89.115109. [Online]. Available: https://link.aps.org/doi/10.1103/PhysRevB.89.115109.

[115] B. Braunecker and P. Simon, "Interplay between classical magnetic moments and superconductivity in quantum one-dimensional conductors: Toward a self-sustained topological majorana phase," *Phys. Rev. Lett.*, vol. 111, p. 147 202, 14 Oct. 2013. DOI: 10.1103/PhysRevLett.111.147202. [Online]. Available: https://link.aps.org/doi/10.1103/PhysRevLett.111.147202.

[116] M. M. Vazifeh and M. Franz, "Self-organized topological state with majorana fermions," *Phys. Rev. Lett.*, vol. 111, p. 206 802, 20 Nov. 2013. DOI: 10.1103/PhysRevLett.111.206802. [Online]. Available: https://link.aps.org/doi/10.1103/PhysRevLett.111.206802.

[117] Y. Peng, F. Pientka, L. I. Glazman, and F. von Oppen, "Strong localization of majorana end states in chains of magnetic adatoms," *Phys. Rev. Lett.*, vol. 114, p. 106 801, 10 Mar. 2015. DOI: 10.1103/PhysRevLett.114.106801. [Online]. Available: https://link.aps.org/doi/10.1103/PhysRevLett.114.106801.

[118] R. Hess, H. F. Legg, D. Loss, and J. Klinovaja, "Prevalence of trivial zero-energy subgap states in nonuniform helical spin chains on the surface of superconductors," *Phys. Rev. B*, vol. 106, p. 104 503, 10 Sep. 2022. DOI: 10.1103/PhysRevB.106.104503. [Online]. Available: https://link.aps.org/doi/10.1103/PhysRevB.106.104503.

[119] M. Mashkoori, S. Pradhan, K. Björnson, J. Fransson, and A. M. Black-Schaffer, "Identification of topological superconductivity in magnetic impurity systems using bulk spin polarization," *Phys. Rev. B*, vol. 102, p. 104 501, 10 Sep. 2020. DOI: 10.1103/PhysRevB.102.104501. [Online]. Available: https://link.aps.org/doi/10.1103/PhysRevB.102.104501.

[120] J. Li, S. Jeon, Y. Xie, A. Yazdani, and B. A. Bernevig, "Majorana spin in magnetic atomic chain systems," *Phys. Rev. B*, vol. 97, p. 125 119, 12 Mar. 2018. DOI: 10.1103/PhysRevB.97.125119. [Online]. Available: https://link.aps.org/doi/10.1103/PhysRevB.97.125119.

[121] M. Serina, D. Loss, and J. Klinovaja, "Boundary spin polarization as a robust signature of a topological phase transition in majorana nanowires," *Phys. Rev. B*, vol. 98, p. 035 419, 3 Jul. 2018. DOI: 10.1103/PhysRevB.98.035419. [Online]. Available: https://link.aps.org/doi/10.1103/PhysRevB.98.035419.

[122] M. M. Maśka and T. Domański, "Polarization of the majorana quasiparticles in the rashba chain," *Scientific Reports*, vol. 7, no. 1, p. 16 193, Nov. 2017, ISSN: 2045-2322. DOI: 10.1038/s41598-017-16323-3. [Online]. Available: https://doi.org/10.1038/s41598-017-16323-3.

[123] L. Cornils, A. Kamlapure, L. Zhou, *et al.*, "Spin-resolved spectroscopy of the yu-shiba-rusinov states of individual atoms," *Phys. Rev. Lett.*, vol. 119, p. 197 002, 19 Nov. 2017. DOI: 10.1103/PhysRevLett.119.197002. [Online]. Available: https://link.aps.org/doi/10.1103/PhysRevLett.119.197002.

[124] R. Wiesendanger, "Spin mapping at the nanoscale and atomic scale," *Rev. Mod. Phys.*, vol. 81, pp. 1495–1550, 4 Nov. 2009. DOI: 10.1103/RevModPhys.81.1495. [Online]. Available: https://link.aps.org/doi/10.1103/RevModPhys.81.1495.

[125] S. Nadj-Perge, I. K. Drozdov, B. A. Bernevig, and A. Yazdani, "Majorana fermions in chains of magnetic atoms on a superconductor," *Physical Review B*, vol. 88, no. 2, Jul. 2013, ISSN: 1098-0121, 1550-235X. DOI: 10.1103/PhysRevB.88.020407. [Online]. Available: http://arxiv.org/abs/1303.6363 (visited on 05/23/2014).

[126] M. Ruby *et al.*, "Tunneling processes into localized subgap states in superconductors," *Phys. Rev. Lett.*, vol. 115, p. 087 001, 8 Aug. 2015. DOI: 10.1103/PhysRevLett.115.087001.

[127] E. Liebhaber, L. M. Rütten, G. Reecht, *et al.*, *Quantum spins and hybridization in artificially-constructed chains of magnetic adatoms on a superconductor*, 2021. arXiv: 2107.06361 [cond-mat.mes-hall].

[128] L. Schneider, P. Beck, J. Neuhaus-Steinmetz, *et al.*, "Precursors of Majorana modes and their length-dependent energy oscillations probed at both ends of atomic Shiba chains," en, *Nature Nanotechnology*, pp. 1–6, Mar. 2022, Publisher: Nature Publishing Group, ISSN: 1748-3395. DOI: 10.1038/s41565-022-01078-4. [Online]. Available: https://www.nature.com/articles/s41565-022-01078-4 (visited on 03/08/2022).

[129] I. R. Shein and A. L. Ivanovskii, "Electronic band structure and fermi surface of tetragonal low-temperature superconductor bi2pd as predicted from first principles," *Journal of Superconductivity and Novel Magnetism*, vol. 26, no. 1, pp. 1–4, Jan. 2013, ISSN: 1557-1947. DOI: 10.1007/s10948-012-1776-x. [Online]. Available: https://doi.org/10.1007/s10948-012-1776-x.

[130] E. Herrera, I. Guillamón, J. A. Galvis, *et al.*, "Magnetic field dependence of the density of states in the multiband superconductor $\beta - Bi_2Pd$," *Phys. Rev. B*, vol. 92, p. 054 507, 5 Aug. 2015. DOI: 10.1103/PhysRevB.92.054507. [Online]. Available: https://link.aps.org/doi/10.1103/PhysRevB.92.054507.

[131] S. V. Eremeev, I. P. Rusinov, I. A. Nechaev, and E. V. Chulkov, "Rashba split surface states in BiTeBr," *New Journal of Physics*, vol. 15, no. 7, p. 075 015, Jul. 2013. DOI: 10.1088/1367-2630/15/7/075015. [Online]. Available: https://doi.org/10.1088/1367-2630/15/7/075015.

[132] M. Steinbrecher, R. Rausch, K. T. That, *et al.*, "Non-collinear spin states in bottom-up fabricated atomic chains," *Nature Communications*, vol. 9, no. 1, p. 2853, Jul. 2018, ISSN: 2041-1723. DOI: 10.1038/s41467-018-05364-5. [Online]. Available: https://doi.org/10.1038/s41467-018-05364-5.

[133] L. Schneider, P. Beck, J. Wiebe, and R. Wiesendanger, "Atomic-scale spin-polarization maps using functionalized superconducting probes," *Science Advances*, vol. 7, no. 4, eabd7302, 2021. DOI: 10.1126/sciadv.abd7302. eprint: https://www.science.org/doi/pdf/10.1126/sciadv.abd7302. [Online]. Available: https://www.science.org/doi/abs/10.1126/sciadv.abd7302.

[134] M. Schecter, K. Flensberg, M. H. Christensen, B. M. Andersen, and J. Paaske, "Self-organized topological superconductivity in a yu-shiba-rusinov chain," *Phys. Rev. B*, vol. 93, p. 140 503, 14 Apr. 2016. DOI: 10.1103/PhysRevB.93.140503. [Online]. Available: https://link.aps.org/doi/10.1103/PhysRevB.93.140503.

[135] Z. Wang and S.-C. Zhang, "Strongly correlated topological superconductors and topological phase transitions via green's function," *Phys. Rev. B*, vol. 86, p. 165 116, 16 Oct. 2012. DOI: 10.1103/PhysRevB.86.165116. [Online]. Available: https://link.aps.org/doi/10.1103/PhysRevB.86.165116.

[136] A. Kobiałka, N. Sedlmayr, and A. Ptok, "Majorana bound states in a superconducting rashba nanowire in the presence of antiferromagnetic order," *Phys. Rev. B*, vol. 103, p. 125 110, 12 Mar. 2021. DOI: 10.1103/PhysRevB.103.125110. [Online]. Available: https://link.aps.org/doi/10.1103/PhysRevB.103.125110.

[137] T. Ojanen, "Topological $\pi$ josephson junction in superconducting rashba wires," *Phys. Rev. B*, vol. 87, p. 100 506, 10 Mar. 2013. DOI: 10.1103/PhysRevB.87.100506. [Online]. Available: https://link.aps.org/doi/10.1103/PhysRevB.87.100506.

[138] M. Kjaergaard, K. Wölms, and K. Flensberg, "Majorana fermions in superconducting nanowires without spin-orbit coupling," *Phys. Rev. B*, vol. 85, p. 020 503, 2 Jan. 2012. DOI: 10.1103/PhysRevB.85.020503. [Online]. Available: https://link.aps.org/doi/10.1103/PhysRevB.85.020503.

[139] S. Das Sarma, J. D. Sau, and T. D. Stanescu, "Splitting of the zero-bias conductance peak as smoking gun evidence for the existence of the majorana mode in a superconductor-semiconductor nanowire," *Phys. Rev. B*, vol. 86, p. 220 506, 22 Dec. 2012. DOI: 10.1103/PhysRevB.86.220506. [Online]. Available: https://link.aps.org/doi/10.1103/PhysRevB.86.220506.

[140] J. Klinovaja and D. Loss, "Composite majorana fermion wave functions in nanowires," *Phys. Rev. B*, vol. 86, p. 085 408, 8 Aug. 2012. DOI: 10.1103/PhysRevB.86.085408. [Online]. Available: https://link.aps.org/doi/10.1103/PhysRevB.86.085408.

[141] A. Theiler, K. Björnson, and A. M. Black-Schaffer, "Majorana bound state localization and energy oscillations for magnetic impurity chains on conventional superconductors," *Phys. Rev. B*, vol. 100, p. 214 504, 21 Dec. 2019. DOI: 10.1103/PhysRevB.100.214504. [Online]. Available: https://link.aps.org/doi/10.1103/PhysRevB.100.214504.

[142] C. Bena, "Friedel oscillations: Decoding the hidden physics," *Comptes Rendus Physique*, vol. 17, no. 3, pp. 302–321, 2016, Physique de la matière condensée au XXIe siècle: l'héritage de Jacques Friedel, ISSN: 1631-0705. DOI: https://doi.org/10.1016/j.crhy.2015.11.006. [Online]. Available: https://www.sciencedirect.com/science/article/pii/S1631070515002236.

[143] G. Binnig, H. Rohrer, C. Gerber, and E. Weibel, "Surface studies by scanning tunneling microscopy," *Phys. Rev. Lett.*, vol. 49, pp. 57–61, 1 Jul. 1982. DOI: 10.1103/PhysRevLett.49.57. [Online]. Available: https://link.aps.org/doi/10.1103/PhysRevLett.49.57.

[144] G. Binnig, H. Rohrer, C. Gerber, and E. Weibel, "7 × 7 reconstruction on si(111) resolved in real space," *Phys. Rev. Lett.*, vol. 50, pp. 120–123, 2 Jan. 1983. DOI: 10.1103/PhysRevLett.50.120. [Online]. Available: https://link.aps.org/doi/10.1103/PhysRevLett.50.120.

[145] G. Binnig, C. F. Quate, and C. Gerber, "Atomic force microscope," *Phys. Rev. Lett.*, vol. 56, pp. 930–933, 9 Mar. 1986. DOI: 10.1103/PhysRevLett.56.930. [Online]. Available: https://link.aps.org/doi/10.1103/PhysRevLett.56.930.

[146] J. Bardeen, "Tunnelling from a many-particle point of view," *Phys. Rev. Lett.*, vol. 6, pp. 57–59, 2 Jan. 1961. DOI: 10.1103/PhysRevLett.6.57. [Online]. Available: https://link.aps.org/doi/10.1103/PhysRevLett.6.57.

[147] J. Tersoff and D. R. Hamann, "Theory of the scanning tunneling microscope," *Phys. Rev. B*, vol. 31, pp. 805–813, 2 Jan. 1985. DOI: 10.1103/PhysRevB.31.805. [Online]. Available: https://link.aps.org/doi/10.1103/PhysRevB.31.805.

[148] B. Voigtländer, *Scanning Probe Microscopy Atomic Force Microscopy and Scanning Tunneling Microscopy*. Springer, 2015. DOI: https://doi.org/10.1007/978-3-662-45240-0.

[149] B. C. Stipe, M. A. Rezaei, and W. Ho, "Single-molecule vibrational spectroscopy and microscopy," *Science*, vol. 280, no. 5370, pp. 1732–1735, 1998. DOI: 10.1126/science.280.5370.1732. eprint: https://www.science.org/doi/pdf/10.1126/science.280.5370.1732. [Online]. Available: https://www.science.org/doi/abs/10.1126/science.280.5370.1732.

[150] N. Bachellier, B. Verlhac, L. Garnier, *et al.*, "Vibron-assisted spin excitation in a magnetically anisotropic molecule," *Nature Communications*, vol. 11, no. 1, p. 1619, Apr. 2020, ISSN: 2041-1723. DOI: 10.1038/s41467-020-15266-0. [Online]. Available: https://doi.org/10.1038/s41467-020-15266-0.

[151] J. Homberg, A. Weismann, T. Markussen, and R. Berndt, "Resonance-enhanced vibrational spectroscopy of molecules on a superconductor," *Phys. Rev. Lett.*, vol. 129, p. 116 801, 11 Sep. 2022. DOI: 10.1103/PhysRevLett.129.116801. [Online]. Available: https://link.aps.org/doi/10.1103/PhysRevLett.129.116801.

[152] J.-P. Gauyacq, N. Lorente, and F. D. Novaes, "Excitation of local magnetic moments by tunneling electrons," *Progress in Surface Science*, vol. 87, no. 5, pp. 63–107, 2012, ISSN: 0079-6816. DOI: https://doi.org/10.1016/j.progsurf.2012.05.003. [Online]. Available: https://www.sciencedirect.com/science/article/pii/S0079681612000068.

[153] M. Ternes, "Spin excitations and correlations in scanning tunneling spectroscopy," *New Journal of Physics*, vol. 17, no. 6, p. 063 016, Jun. 2015. DOI: 10.1088/1367-2630/17/6/063016. [Online]. Available: https://dx.doi.org/10.1088/1367-2630/17/6/063016.

[154] A. J. Heinrich, J. A. Gupta, C. P. Lutz, and D. M. Eigler, "Single-atom spin-flip spectroscopy," *Science*, vol. 306, no. 5695, pp. 466–469, 2004. DOI: 10.1126/science.1101077. eprint: https://www.science.org/doi/pdf/10.1126/science.1101077. [Online]. Available: https://www.science.org/doi/abs/10.1126/science.1101077.

[155] C. F. Hirjibehedin, C.-Y. Lin, A. F. Otte, *et al.*, "Large magnetic anisotropy of a single atomic spin embedded in a surface molecular network," *Science*, vol. 317, no. 5842, pp. 1199–1203, 2007. DOI: 10.1126/science.1146110. eprint: https://www.science.org/doi/pdf/10.1126/science.1146110. [Online]. Available: https://www.science.org/doi/abs/10.1126/science.1146110.

[156] N. Agraıt, J. G. Rodrigo, and S. Vieira, "Transition from the tunneling regime to point contact and proximity-induced josephson effect in lead–normal-metal nanojunctions," *Phys. Rev. B*, vol. 46, pp. 5814–5817, 9 Sep. 1992. DOI: 10.1103/PhysRevB.46.5814. [Online]. Available: https://link.aps.org/doi/10.1103/PhysRevB.46.5814.

[157] S. H. Pan, E. W. Hudson, and J. C. Davis, "Vacuum tunneling of superconducting quasiparticles from atomically sharp scanning tunneling microscope tips," *Applied Physics Letters*, vol. 73, no. 20, pp. 2992–2994, 1998. DOI: 10.1063/1.122654. eprint: https://doi.org/10.1063/1.122654. [Online]. Available: https://doi.org/10.1063/1.122654.

[158] S.-H. Ji, T. Zhang, Y.-S. Fu, *et al.*, "High-resolution scanning tunneling spectroscopy of magnetic impurity induced bound states in the superconducting gap of pb thin films," *Phys. Rev. Lett.*, vol. 100, p. 226 801, 22 Jun. 2008. DOI: 10.1103/PhysRevLett.100.226801. [Online]. Available: https://link.aps.org/doi/10.1103/PhysRevLett.100.226801.

[159] J. Wiebe, A. Wachowiak, F. Meier, *et al.*, "A 300mk ultra-high vacuum scanning tunneling microscope for spin-resolved spectroscopy at high energy resolution," *Review of Scientific Instruments*, vol. 75, no. 11, pp. 4871–4879, 2004. DOI: 10.1063/1.1794431. eprint: https://doi.org/10.1063/1.1794431. [Online]. Available: https://doi.org/10.1063/1.1794431.

[160] G. Webb, F. Marsiglio, and J. Hirsch, "Superconductivity in the elements, alloys and simple compounds," *Physica C: Superconductivity and its Applications*, vol. 514, pp. 17–27, 2015, Superconducting Materials: Conventional, Unconventional and Undetermined, ISSN: 0921-4534. DOI: https://doi.org/10.1016/j.physc.2015.02.037. [Online]. Available: https://www.sciencedirect.com/science/article/pii/S0921453415000647.

[161] J. P. Ibe, P. P. Bey, S. L. Brandow, *et al.*, "On the electrochemical etching of tips for scanning tunneling microscopy," *Journal of Vacuum Science & Technology A*, vol. 8, no. 4, pp. 3570–3575, 1990. DOI: 10.1116/1.576509. eprint: https://doi.org/10.1116/1.576509. [Online]. Available: https://doi.org/10.1116/1.576509.

[162] C. Brun, I.-P. Hong, F. ç. Patthey, *et al.*, "Reduction of the superconducting gap of ultrathin pb islands grown on si(111)," *Phys. Rev. Lett.*, vol. 102, p. 207 002, 20 May 2009. DOI: 10.1103/PhysRevLett.102.207002. [Online]. Available: https://link.aps.org/doi/10.1103/PhysRevLett.102.207002.

[163] J. M. Rowell and L. Kopf, "Tunneling measurements of phonon spectra and density of states in superconductors," *Phys. Rev.*, vol. 137, A907–A916, 3A Feb. 1965. DOI: 10.1103/PhysRev.137.A907. [Online]. Available: https://link.aps.org/doi/10.1103/PhysRev.137.A907.

[164] J. Jandke, P. Hlobil, M. Schackert, W. Wulfhekel, and J. Schmalian, "Coupling to real and virtual phonons in tunneling spectroscopy of superconductors," *Phys. Rev. B*, vol. 93, p. 060 505, 6 Feb. 2016. DOI: 10.1103/PhysRevB.93.060505. [Online]. Available: https://link.aps.org/doi/10.1103/PhysRevB.93.060505.

[165] A. F. Andreev, "The thermal conductivity of the intermediate state in superconductors," *Soviet Physics-JETP*, vol. 19, pp. 1228–1232, 5 1964.

[166] G. E. Blonder, M. Tinkham, and T. M. Klapwijk, "Transition from metallic to tunneling regimes in superconducting microconstrictions: Excess current, charge imbalance, and supercurrent conversion," *Phys. Rev. B*, vol. 25, pp. 4515–4532, 7 Apr. 1982. DOI: 10.1103/PhysRevB.25.4515. [Online]. Available: https://link.aps.org/doi/10.1103/PhysRevB.25.4515.

[167] J. C. Cuevas and W. Belzig, "Full counting statistics of multiple andreev reflections," *Phys. Rev. Lett.*, vol. 91, p. 187 001, 18 Oct. 2003. DOI: 10.1103/PhysRevLett.91.187001. [Online]. Available: https://link.aps.org/doi/10.1103/PhysRevLett.91.187001.

[168] B. D. Josephson, "Possible new effects in superconductive tunnelling," *Physics Letters*, vol. 1, no. 7, pp. 251–253, 1962, ISSN: 0031-9163. DOI: https://doi.org/10.1016/0031-9163(62)91369-0. [Online]. Available: https://www.sciencedirect.com/science/article/pii/0031916362913690.

[169] B. D. Josephson, "The discovery of tunnelling supercurrents," *Rev. Mod. Phys.*, vol. 46, pp. 251–254, 2 Apr. 1974. DOI: 10.1103/RevModPhys.46.251. [Online]. Available: https://link.aps.org/doi/10.1103/RevModPhys.46.251.

[170] P. W. Anderson and J. M. Rowell, "Probable observation of the josephson superconducting tunneling effect," *Phys. Rev. Lett.*, vol. 10, pp. 230–232, 6 Mar. 1963. DOI: 10.1103/PhysRevLett.10.230. [Online]. Available: https://link.aps.org/doi/10.1103/PhysRevLett.10.230.

[171] O. Naaman, W. Teizer, and R. C. Dynes, "Fluctuation dominated josephson tunneling with a scanning tunneling microscope," *Phys. Rev. Lett.*, vol. 87, p. 097 004, 9 Aug. 2001. DOI: 10.1103/PhysRevLett.87.097004. [Online]. Available: https://link.aps.org/doi/10.1103/PhysRevLett.87.097004.

[172] Z.-F. Xu, Y. Xie, W.-L. Feng, and H. F. Schaefer, "Systematic investigation of electronic and molecular structures for the first transition metal series metallocenes m(c5h5)2 (m = v, cr, mn, fe, co, and ni)," *The Journal of Physical Chemistry A*, vol. 107, no. 15, pp. 2716–2729, Apr. 2003, ISSN: 1089-5639. DOI: 10.1021/jp0219855. [Online]. Available: https://doi.org/10.1021/jp0219855.

[173] T. J. Kealy and P. L. Pauson, "A new type of organo-iron compound," *Nature*, vol. 168, no. 4285, pp. 1039–1040, Dec. 1951, ISSN: 1476-4687. DOI: 10.1038/1681039b0. [Online]. Available: https://doi.org/10.1038/1681039b0.

[174] S. A. Miller, J. A. Tebboth, and J. F. Tremaine, "114. dicyclopentadienyl-iron," *J. Chem. Soc.*, pp. 632–635, 0 1952. DOI: 10.1039/JR9520000632. [Online]. Available: http://dx.doi.org/10.1039/JR9520000632.

[175] C. Waldfried, D. Welipitiya, C. W. Hutchings, *et al.*, "Preferential bonding orientations of ferrocene on surfaces," *The Journal of Physical Chemistry B*, vol. 101, no. 47, pp. 9782–9789, 1997. DOI: 10.1021/jp972496l. eprint: https://doi.org/10.1021/jp972496l. [Online]. Available: https://doi.org/10.1021/jp972496l.

[176] C. M. Woodbridge, D. L. Pugmire, R. C. Johnson, N. M. Boag, and M. A. Langell, "Hreels and xps studies of ferrocene on ag(100)," *The Journal of Physical Chemistry B*, vol. 104, no. 14, pp. 3085–3093, 2000. DOI: 10.1021/jp993235+. eprint: https://doi.org/10.1021/jp993235+. [Online]. Available: https://doi.org/10.1021/jp993235+.

[177] C. N. Borca, D. Welipitiya, P. A. Dowben, and N. M. Boag, "Bonding configurations for nickelocene on ag(100) and steric effects in thermal desorption," *The Journal of Physical Chemistry B*, vol. 104, no. 5, pp. 1047–1049, 2000. DOI: 10.1021/jp993086v. eprint: https://doi.org/10.1021/jp993086v. [Online]. Available: https://doi.org/10.1021/jp993086v.

[178] D. L. Pugmire, C. M. Woodbridge, S. Root, and M. A. Langell, "Nickelocene adsorption on single-crystal surfaces," *Journal of Vacuum Science & Technology A*, vol. 17, no. 4, pp. 1581–1586, 1999. DOI: 10.1116/1.581854. eprint: https://doi.org/10.1116/1.581854. [Online]. Available: https://doi.org/10.1116/1.581854.

[179] D. Welipitiya, C. Borca, C. Waldfried, *et al.*, "The adsorption of nickelocene part 1: Molecular bonding on ag(100)," *Surface Science*, vol. 393, no. 1, pp. 34–46, 1997, ISSN: 0039-6028. DOI: https://doi.org/10.1016/S0039-6028(97)00500-1. [Online]. Available: https://www.sciencedirect.com/science/article/pii/S0039602897005001.

[180] M. Ormaza, P. Abufager, N. Bachellier, *et al.*, "Assembly of ferrocene molecules on metal surfaces revisited," *The Journal of Physical Chemistry Letters*, vol. 6, no. 3, pp. 395–400, 2015, PMID: 26261954. DOI: 10.1021/jz5026118. eprint: https://doi.org/10.1021/jz5026118. [Online]. Available: https://doi.org/10.1021/jz5026118.

[181] N. Bachellier, M. Ormaza, M. Faraggi, *et al.*, "Unveiling nickelocene bonding to a noble metal surface," *Phys. Rev. B*, vol. 93, p. 195 403, 19 May 2016. DOI: 10.1103/PhysRevB.93.195403. [Online]. Available: https://link.aps.org/doi/10.1103/PhysRevB.93.195403.

[182] R. Sessoli, D. Gatteschi, A. Caneschi, and M. A. Novak, "Magnetic bistability in a metal-ion cluster," *Nature*, vol. 365, no. 6442, pp. 141–143, Sep. 1993, ISSN: 1476-4687. DOI: 10.1038/365141a0. [Online]. Available: https://doi.org/10.1038/365141a0.

[183] B. Verlhac, N. Bachellier, L. Garnier, *et al.*, "Atomic-scale spin sensing with a single molecule at the apex of a scanning tunneling microscope," *Science*, vol. 366, no. 6465, pp. 623–627, 2019. DOI: 10.1126/science.aax8222. eprint: https://www.science.org/doi/pdf/10.1126/science.aax8222. [Online]. Available: https://www.science.org/doi/abs/10.1126/science.aax8222.

[184] N. Mohammadi, A. Ganesan, C. T. Chantler, and F. Wang, "Differentiation of ferrocene d5d and d5h conformers using ir spectroscopy," *Journal of Organometallic Chemistry*, vol. 713, pp. 51–59, 2012, ISSN: 0022-328X. DOI: https://doi.org/10.1016/j.jorganchem.2012.04.009. [Online]. Available: https://www.sciencedirect.com/science/article/pii/S0022328X12002082.

[185] M. Ormaza, P. Abufager, B. Verlhac, *et al.*, "Controlled spin switching in a metallocene molecular junction," *Nature Communications*, vol. 8, no. 1, p. 1974, Dec. 2017, ISSN: 2041-1723. DOI: 10.1038/s41467-017-02151-6. [Online]. Available: https://doi.org/10.1038/s41467-017-02151-6.

[186] M. Mohr, M. Gruber, A. Weismann, *et al.*, "Spin dependent transmission of nickelocene-cu contacts probed with shot noise," *Phys. Rev. B*, vol. 101, p. 075 414, 7 Feb. 2020. DOI: 10.1103/PhysRevB.101.075414. [Online]. Available: https://link.aps.org/doi/10.1103/PhysRevB.101.075414.

[187] M. Ormaza, R. Robles, N. Bachellier, P. Abufager, N. Lorente, and L. Limot, "On-surface engineering of a magnetic organometallic nanowire," *Nano Letters*, vol. 16, no. 1, pp. 588–593, 2016, PMID: 26650920. DOI: 10.1021/acs.nanolett.5b04280. eprint: https://doi.org/10.1021/acs.nanolett.5b04280. [Online]. Available: https://doi.org/10.1021/acs.nanolett.5b04280.

[188] L. Garnier, B. Verlhac, P. Abufager, N. Lorente, M. Ormaza, and L. Limot, "The kondo effect of a molecular tip as a magnetic sensor," *Nano Letters*, vol. 20, no. 11, pp. 8193–8199, 2020, PMID: 33119321. DOI: 10.1021/acs.nanolett.0c03271. eprint: https://doi.org/10.1021/acs.nanolett.0c03271. [Online]. Available: https://doi.org/10.1021/acs.nanolett.0c03271.

[189] B. Verlhac, "Atomic-scale spin-sensing with a single molecule at the apex of a scanning tunneling microscope," Ph.D. dissertation, Université de Strasbourg, 2019.

[190] M. T. Vieyra-Eusebio and A. Rojas, "Vapor pressures and sublimation enthalpies of nickelocene and cobaltocene measured by thermogravimetry," *Journal of Chemical & Engineering Data*, vol. 56, no. 12, pp. 5008–5018, 2011. DOI: 10.1021/je200815v. eprint: https://doi.org/10.1021/je200815v. [Online]. Available: https://doi.org/10.1021/je200815v.

[191] P. Gambardella, S. Stepanow, A. Dmitriev, *et al.*, "Supramolecular control of the magnetic anisotropy in two-dimensional high-spin fe arrays at a metal interface," *Nature Materials*, vol. 8, no. 3, pp. 189–193, Mar. 2009, ISSN: 1476-4660. DOI: 10.1038/nmat2376. [Online]. Available: https://doi.org/10.1038/nmat2376.

[192] M. G. Cuxart, M. A. Valbuena, R. Robles, *et al.*, "Molecular approach for engineering interfacial interactions in magnetic/topological insulator heterostructures," *ACS Nano*, vol. 14, no. 5, pp. 6285–6294, 2020, PMID: 32293865. DOI: 10.1021/acsnano.0c02498. eprint: https://doi.org/10.1021/acsnano.0c02498. [Online]. Available: https://doi.org/10.1021/acsnano.0c02498.

[193] R. Raval, "Molecular assembly at surfaces: Progress and challenges," *Faraday Discuss.*, vol. 204, pp. 9–33, 0 2017. DOI: 10.1039/C7FD90072D. [Online]. Available: http://dx.doi.org/10.1039/C7FD90072D.

[194] H. I. Li, K. J. Franke, J. I. Pascual, L. W. Bruch, and R. D. Diehl, "Origin of moiré structures in $C_{60}$ on pb(111) and their effect on molecular energy levels," *Phys. Rev. B*, vol. 80, p. 085 415, 8 Aug. 2009. DOI: 10.1103/PhysRevB.80.085415. [Online]. Available: https://link.aps.org/doi/10.1103/PhysRevB.80.085415.

[195] L. Farinacci, G. Ahmadi, G. Reecht, *et al.*, "Tuning the coupling of an individual magnetic impurity to a superconductor: Quantum phase transition and transport," *Phys. Rev. Lett.*, vol. 121, p. 196 803, 19 Nov. 2018. DOI: 10.1103/PhysRevLett.121.196803. [Online]. Available: https://link.aps.org/doi/10.1103/PhysRevLett.121.196803.

[196] K. J. Franke, G. Schulze, and J. I. Pascual, "Competition of superconducting phenomena and kondo screening at the nanoscale," *Science*, vol. 332, no. 6032, pp. 940–944, 2011. DOI: 10.1126/science.1202204. eprint: https://www.science.org/doi/pdf/10.1126/science.1202204. [On-

line]. Available: https://www.science.org/doi/abs/10.1126/science.1202204.

[197] L. Malavolti, M. Briganti, M. Hänze, *et al.*, "Tunable spin–superconductor coupling of spin 1/2 vanadyl phthalocyanine molecules," *Nano Letters*, vol. 18, no. 12, pp. 7955–7961, 2018, PMID: 30452271. DOI: 10.1021/acs.nanolett.8b03921. eprint: https://doi.org/10.1021/acs.nanolett.8b03921. [Online]. Available: https://doi.org/10.1021/acs.nanolett.8b03921.

[198] R. Prins, J. van Voorst, and C. Schinkel, "Zero-field splitting in the triplet ground state of nickelocene," *Chemical Physics Letters*, vol. 1, no. 2, pp. 54–55, 1967, ISSN: 0009-2614. DOI: https://doi.org/10.1016/0009-2614(67)80067-8. [Online]. Available: https://www.sciencedirect.com/science/article/pii/0009261467800678.

[199] B. W. Heinrich, L. Braun, J. I. Pascual, and K. J. Franke, "Protection of excited spin states by a superconducting energy gap," *Nature Physics*, vol. 9, no. 12, pp. 765–768, Dec. 2013, ISSN: 1745-2481. DOI: 10.1038/nphys2794. [Online]. Available: https://doi.org/10.1038/nphys2794.

[200] I. G. Rau, S. Baumann, S. Rusponi, *et al.*, "Reaching the magnetic anisotropy limit of a 3d metal atom," *Science*, vol. 344, no. 6187, pp. 988–992, 2014. DOI: 10.1126/science.1252841. eprint: https://www.science.org/doi/pdf/10.1126/science.1252841. [Online]. Available: https://www.science.org/doi/abs/10.1126/science.1252841.

[201] F. Donati, S. Rusponi, S. Stepanow, *et al.*, "Magnetic remanence in single atoms," *Science*, vol. 352, no. 6283, pp. 318–321, 2016. DOI: 10.1126/science.aad9898. eprint: https://www.science.org/doi/pdf/10.1126/science.aad9898. [Online]. Available: https://www.science.org/doi/abs/10.1126/science.aad9898.

[202] J. A. Stroscio and R. J. Celotta, "Controlling the dynamics of a single atom in lateral atom manipulation," *Science*, vol. 306, no. 5694, pp. 242–247, 2004. DOI: 10.1126/science.1102370. eprint: https://www.science.org/doi/pdf/10.1126/science.1102370. [Online]. Available: https://www.science.org/doi/abs/10.1126/science.1102370.

[203] G. Kresse and J. Furthmüller, "Efficient iterative schemes for ab initio total-energy calculations using a plane-wave basis set," *Phys. Rev. B*, vol. 54, pp. 11 169–11 186, 16 Oct. 1996. DOI: 10.1103/PhysRevB.54.11169. [Online]. Available: https://link.aps.org/doi/10.1103/PhysRevB.54.11169.

[204] C. Mier, B. Verlhac, L. Garnier, *et al.*, *Molecular templates of spin textures on superconducting surfaces*, 2020. DOI: 10.48550/ARXIV.2009.00501. [Online]. Available: https://arxiv.org/abs/2009.00501.

[205] Y. Harada, H. Takayanagi, and A. A. Odintsov, "Cooper-pair tunneling in small junctions with tunable josephson coupling," *Phys. Rev. B*, vol. 54, pp. 6608–6613, 9 Sep. 1996. DOI: 10.1103/PhysRevB.54.6608. [Online]. Available: https://link.aps.org/doi/10.1103/PhysRevB.54.6608.

[206] J. B. Johnson, "Thermal agitation of electricity in conductors," *Phys. Rev.*, vol. 32, pp. 97–109, 1 Jul. 1928. DOI: 10.1103/PhysRev.32.97. [Online]. Available: https://link.aps.org/doi/10.1103/PhysRev.32.97.

[207] H. Nyquist, "Thermal agitation of electric charge in conductors," *Phys. Rev.*, vol. 32, pp. 110–113, 1 Jul. 1928. DOI: 10.1103/PhysRev.32.110. [Online]. Available: https://link.aps.org/doi/10.1103/PhysRev.32.110.

[208] S. Y. Song and J. Seo, "Observation of enhanced superconductivity in the vicinity of ar-induced nano-cavities in pb(111)," *Scientific Reports*, vol. 7, no. 1, p. 12 177, Sep. 2017, ISSN: 2045-2322. DOI: 10.1038/s41598-017-12505-1. [Online]. Available: https://doi.org/10.1038/s41598-017-12505-1.

[209] M. Müller, N. Néel, S. Crampin, and J. Kröger, "Lateral electron confinement with open boundaries: Quantum well states above nanocavities at pb(111)," *Phys. Rev. Lett.*, vol. 117, p. 136 803, 13 Sep. 2016. DOI: 10.1103/PhysRevLett.117.136803. [Online]. Available: https://link.aps.org/doi/10.1103/PhysRevLett.117.136803.

[210] K. M. Bastiaans, D. Cho, D. Chatzopoulos, M. Leeuwenhoek, C. Koks, and M. P. Allan, "Imaging doubled shot noise in a josephson scanning tunneling microscope," *Phys. Rev. B*, vol. 100, p. 104 506, 10 Sep. 2019. DOI: 10.1103/PhysRevB.100.104506. [Online]. Available: https://link.aps.org/doi/10.1103/PhysRevB.100.104506.

[211] Y. H. Jiang, W. D. Xiao, L. W. Liu, *et al.*, "Self-assembly of metal phthalocyanines on pb(111) and au(111) surfaces at submonolayer coverage," *The Journal of Physical Chemistry C*, vol. 115, no. 44, pp. 21 750–21 754, 2011. DOI: 10.1021/jp203462f. eprint: https://doi.org/10.1021/jp203462f. [Online]. Available: https://doi.org/10.1021/jp203462f.